Modelling and optimisation of mass transfer in CO2 electrolysers

Blake, J.W.

DOI

Publication date
2025

Document Version
Final published version

Citation (APA)

Important note
To cite this publication, please use the final published version (if applicable).
Please check the document version above.

MODELLING AND OPTIMISATION OF MASS TRANSFER IN CO_2 ELECTROLYSERS

MODELLING AND OPTIMISATION OF MASS TRANSFER IN CO_2 ELECTROLYSERS

Dissertation

for the purpose of obtaining the degree of doctor
at Delft University of Technology,
by the authority of the Rector Magnificus Prof. dr. ir. T. H. J. J. van der Hagen,
chair of the Board of Doctorates
to be publicly defended on
Thursday the 6th of February 2025 at 12:30

by

Joseph William BLAKE

Master of Science in Mathematics and Physics,
University of Warwick, United Kingdom,
born in Hornchurch, United Kingdom.

This dissertation has been approved by the promotors

promotor: prof. dr. ir. J.T. Padding
copromotor: dr. ir. J.W. Haverkort

Composition of the doctoral committee:

Rector Magnificus,	chairman
Prof. dr. ir. J.T. Padding,	Delft University of Technology, promotor
Dr. ir. J.W. Haverkort,	Delft University of Technology, copromotor

Independent members:

Prof. dr. ir. W. de Jong,	Delft University of Technology
Dr. L. Botto,	Delft University of Technology
Prof. dr. T. Breugelmans,	University of Antwerp, Belgium
Prof. dr. ir. A.W. Vreman,	Eindhoven University of Technology
Prof.dr. R. Pecnik,	Delft University of Technology, reserve member

Non-independent members:

Dr. ir. D.A. Vermaas,	Delft University of Technology

I apologise for the long thesis:
I did not have the time to write a short one.

Blaise Pascal, 1656, *(paraphrased)*

CONTENTS

SUMMARY

In this thesis, analytical and computational models have been created for the electroreduction of CO_2 in gas-diffusion electrodes. It initially covers the creation of a 1D analytical model of CO_2 mass transport and reaction in a gas-diffusion electrode catalyst layer in an electrolyser with a flowing catholyte layer. This model balances the diffusion of CO_2 through the porous media against the reaction of CO_2. Both electrochemical conversion, with concentration dependent Tafel kinetics, and chemical reaction with OH^- in the bicarbonate buffer system, rapidly consume CO_2. It shows that the OH^- produced in the reduction reaction and competing hydrogen evolution reaction lead to an alkalinity problem, in which large fractions CO_2 are converted to bicarbonate and carbonate instead of the intended electroreduction product. This problem is pervasive in the catalyst layer environment, and the rising pH further causes significant increases in local carbonate concentrations, limiting the CO_2 solubility through the salting-out effect. The carbonate concentrations can approach the solubility limit in the electrolyte and precipitate with cations into solid carbonate crystals in the pore structure.

Rudimentary optimisation is performed on this 1D system, and it determines that the effectiveness of a catalyst layer is governed to an extent by the Thiele modulus. Furthermore, a thick catalyst layer is usually underutilised when there is insufficient CO_2 partial pressure in the gas feed or excessive cathode potential. In these cases, the regions of the catalyst furthest from the gas supply perform very little CO_2 electroreduction, but still perform hydrogen evolution. This hydrogen evolution produces OH^- ions that further consume CO_2 and consumes electricity that would ideally instead be used to produce the more valuable products of CO_2 reduction.

The 1D model necessarily used averaged values for components that depend on the perpendicular flow direction, namely the flowing catholyte channel and the reactant gas CO_2 channel. We note that this treatment is insufficient to describe the whole electrolyser, as CO_2 conversion to carbonate and OH^- production create a developing concentration boundary layer. Similarly, the partial pressure of the gas channel CO_2 will vary along the electrolyser as it reacts away.

To address these issues, the model is converted into a computational 2D system, solved in COMSOL Multiphysics. This also permits the inclusion of some of the more convoluted effects of ionic strength and temperature on the system. Homogeneous reaction rates, anodic and cathodic reaction rates, pH, and reaction equilibrium potentials and constants are all corrected in this way. This gives a more detailed representation of the physical processes, but given the complicated forms of the corrections it becomes far more difficult to interpret the interactions behind observed phenomena when compared to the analytical model. With some additional computational methods of domain decomposition and variable recasting, the model is applied to both a small lab-scale scenario and an upscaled metre-long channel, to demonstrate the scaling relations and limitations of a typical CO_2 electrolyser with flowing catholyte. It shows that the reaction environ-

ment at the inlet is far more favourable than further down the stream, as the reactant partial pressure is higher, the local catalyst layer pH is lower, the local CO_2 solubility is higher, the catholyte is purer, and the catholyte concentration boundary layer is thinner. The model allows us to see that the majority of reactant and current utilisation limitations come from unabated hydrogen evolution in the poorly utilised regions, similar to what was found in the perpendicular direction in the 1D model. We propose some methods to mitigate these limitations. One of these methods is the selective removal of catalyst in these poorly utilised areas, to ensure that limiting kinetics and limiting mass transport share similar values and hydrogen evolution only occurs where necessary.

With the rudimentary hypothesis of selective catalyst removal showing some promising results, we return to a readily optimisable 1D system in the flow-wise direction of both a simple flow-through reactor and a gas-diffusion electrode with flowing catholyte. We find that variable catalyst loading can act as a modifier of the dimensionless Damköhler number that typically governs the performance of such a system. The effect is more profound in a gas-diffusion electrode however, so we create a numerical framework in which we can perform functional optimisation to find ideal loading profiles for a range of electrolyser setups and operational loads. We found that high single-pass conversion is associated with lower reaction selectivity, and subsequently constructed a more robust financial cost weighted metric. This metric reveals that many electrolyser setups can be improved by reducing the amount of catalyst used further down the channels, as the reduced cost of electricity spent on the hydrogen evolution reaction far outweighs the reduction in product yield and reactant utilisation. Furthermore, the optimisation process reveals that the most economically feasible setups for contemporary costs are categorically those that operate at minimal cell voltage and single-pass conversion, as electrolysis cost is dominant, even in cells with optimised catalyst loading. This high electrolysis cost, exceeds reactant cost and separation costs, so a low single-pass conversion is preferable to maintain a high reactant availability for efficient electrolysis in the catalyst layer, even if this leads to higher product stream separation costs due to more unreacted CO_2 in the outlet. We conclude with a recommendation for a focus on minimising electrolysis cost and maximising long-term stability and scalability, with less of a focus on reactant utilisation and intensive upstream or downstream processing, as the former attributes are of greater financial significance.

SAMENVATTING

In dit proefschrift zijn analytische en numerieke modellen ontwikkeld voor de elektroreductie van CO_2 in gasdiffusie-elektroden. Allereerst wordt een één-dimensionaal analytisch model van het massatransport en consumptie van CO_2 in de katalysatorlaag van een gasdiffusie-elektrode in een elektrolyser met stromende katholyt. Dit model beschrijft de diffusie van CO_2 door de poreuze media en de reacties waarin CO_2 betrokken is. Zowel de elektrochemische reductie met concentratie-afhankelijke Tafel-kinetiek, als de chemische reactie met OH^- in de bicarbonaat bufferreactie consumeren CO_2 in een hoog tempo. Het model laat zien dat de OH^- geproduceerd door de reductiereactie en de concurrerende waterstof evolutie reactie zorgen voor een te hoge pH-waarde, waardoor een groot deel van de CO_2 reageert tot bicarbonaat en carbonaat in plaats van het beoogde elektroreductieproduct. Dit probleem is vind plaats in het gehele milieu in de katalysatorlaag, en de stijgende pH zorgt verder voor een grote toename van de lokale carbonaatconcentratie, waardoor door het uitzoutingseffect de oplosbaarheid van CO_2 wordt verlaagd. De carbonaatconcentratie kan in de buurt van de maximale oplosbaarheid komen wat neerslag van het zout tot vaste kristallen kan veroorzaken in de poriën van de katalysatorlaag.

Dit één-dimensionale systeem is eenvoudig geoptimaliseerd, wat laat zien dat de effectiviteit van de katalysatorlaag gedeeltelijk wordt bepaald door de Thiele-modulus. Bovendien wordt een dikke katalysatorlaag vaak slecht benut wanneer de gasvoeding een te lage partiële druk van CO_2 heeft of bij excessief hoge kathodepotentialen. In deze gevallen vind er erg weinig CO_2 elektroreductie plaats in katalysatorlaag verder van de gasvoeding, maar wordt op deze plekken wel nog waterstof geproduceerd. Deze waterstofproductie genereert meer OH^- ionen die meer CO_2 consumeren, en gebruikt elektriciteit die idealiter voor de meer waardevolle producten van CO_2 reductie gebruikt zou worden.

Dit één-dimensionale model gebruikt noodzakelijkerwijs gemiddelde waarden voor componenten die afhangen van de haakse stromingsrichting, namelijk het stromende katholytkanaal en het CO_2 gaskanaal. We merken op dat deze aanpak onvoldoende is om een gehele elektrolyser te beschrijven, omdat CO_2 conversie naar carbonaat en OH^- productie zorgen voor een ontwikkelende grenslaag in de concentratie. Op gelijke manier neemt de partiële druk van CO_2 in het gaskanaal af terwijl het reageert langs de elektrolyser.

Om deze problemen aan te pakken is het model aangepast naar een tweedimensionaal numeriek systeem, opgelost met COMSOL Multiphysics. Dit maakt ook de opname van een aantal van de ingewikkeldere effecten van ionische sterkte en temperatuur op het systeem mogelijk. De snelheden van de homogene reacties, de anodische en cathodische reactiesnelheden, pH, en evenwichtspotentialen van de reacties zijn allen op deze manier gecorrigeerd. Dit geeft een meer gedetailleerde representatie van de fysische processen, maar door de ingewikkelde formulatie van de correcties wordt het moeilijker om

de onderliggende interacties achter de geobserveerde fenomenen te intrepeteren. Met behulp van enkele aanvullende rekenmethoden voor domeinontleding en herformulering van variabelen, wordt het model toegepast zowel op een kleine lab-schaal opstelling, als een opgeschaald kanaal van een meter lang, om de schaalrelaties en beperkingen van een typische CO_2 elektrolyser met stromend katholyt te demonstreren. Dit laat zien dat het reactiemilieu aan de ingang veel gunstiger is dan verder stroomafwaarts, omdat de partiële druk van de reactant hoger is, de lokale pH in de katalysatorlaag lager is, de lokale oplosbaarheid van CO_2 hoger is, het katholyt puurder is, en de concentratiegrenslaag in het katholyt dunner is. Met dit model laten we zien dat het merendeel van de beperkingen op het gebied van reactant en stroomgebruik voortkomen uit de ongebreidelde waterstofontwikkeling in de slecht benutte regio's van de katalysatorlaag, vergelijkbaar met wat met het één-dimensionale model in de richting loodrecht op de stroming werd aangetroffen. We stellen een aantal methoden voor om deze limitaties te beperken. Een van deze methoden is het selectief verwijderen van katalysator in deze slecht benutte regio's, om ervoor te zorgen dat de kinetiek en het massatransport vergelijkbaar beperkt zijn, en waterstofproductie alleen plaatsvind waar het onvermijdelijk is.

Met deze veelbelovende hypothese van het selectief verwijderen van katalysator, keren we terug naar een eenvoudig te optimaliseren één-dimensionaal systeem in de stromingsrichting voor beide een simpele doorstroomreactor als een gasdiffusie-elektrode met stromend katholyt. We ontdekken dat een variabele katalysatorbelading kan fungeren als een modificator van het dimensieloze Damköhler-getal dat doorgaans de prestaties van een dergelijk systeem bepaalt. Omdat dit effect is groter bij een gasdiffusie-elektrode, hebben we een numeriek raamwerk gecreëerd waarmee we functionele optimisatie kunnen uitvoeren om de ideale beladingsprofielen te vinden voor een groot bereik van elektrolyser-opstellingen en operationele lasten. We vinden dat een hoge conversie in een enkele doorgang geassocieerd is met lagere selectiviteit, en hebben vervolgens een meer robuuste kostengewogen maatstaf ontwikkeld. Deze maatstaf onthult dat veel elektrolyser-opstellingen kunnen worden verbeterd door de hoeveelheid katalysator geleidelijk te verminderen in de stroomrichting van het katholyt, omdat de verminderde kosten van elektriciteit gebruikt voor waterstofproductie veel zwaarder weegt dan de afname in opbrengst van product en gebruik van reactant. Bovendien onthult het optimalisatieproces dat de meest economisch aantrekkelijke opstellingen voor hedendaagse kosten categorisch gezien die zijn die werken op minimaal celpotentiaal en single-pass conversie, omdat de kosten gerelateerd aan elektrolyse dominant zijn, zelfs in cellen met geoptimaliseerde katalysatorbelading. Deze hoge elektrolysekosten overtreffen de kosten van reactanten en scheidingskosten. Daarom heeft een lage conversie in één doorgang voorkeur, omdat dit een hoge beschikbaarheid van reactant behoud voor effectieve elektrolyse in de katalysatorlaag, zelfs als dit leidt tot hogere kosten voor scheiding van meer niet-gereageerd CO_2 in het uitlaatgas. We sluiten af met een aanbeveling om te richten op het minimaliseren van de kosten van elektrolyse en het maximaliseren van schaalbaarheid en stabiliteit op de lange termijn met minder nadruk op de conversiegraad van de reactanten en intensievere voor- en nabehandeling van de voedingsstromen, omdat de eerstgenoemde factoren van groter financieel belang zijn.

NOMENCLATURE

Abbreviations

AEM   Anion exchange membrane

BPM   Bipolar membrane

CEM   Cation exchange membrane

CL   Catalyst layer

COER CO_2 electroreduction reaction

FE   Faradaic efficiency

GDE   Gas-diffusion electrode

GDL   Gas-diffusion layer

HER   Hydrogen evolution reaction

MEA   Membrane electrode assembly

MPL   Microporous layer

Constants and coefficients

α Charge transfer coefficient, -

ϵ Porosity, -

κ Permeability, m^2

$\mathscr{H}$ Henry's constant, $mol\,m^{-3}\,Pa^{-1}$

μ Dynamic viscosity, $kg\,m^{-1}\,s^{-1}$

σ Conductivity, $S\,m^{-1}$

a_v Volumetric surface area, m^{-1}

b Tafel slope, V

i_0 Exchange current density, $A\,m^{-2}$

D   Diffusion coefficient, $mol\,m^{-2}\,s^{-1}$

E_0 Electrochemical equilibrium potential, V

F   Faraday's constant, s A mol^{-1}

K   Chemical equilibrium constant, m^3 mol^{-1}

k   Chemical reaction rate, s^{-1} or m^3 s^{-1} mol^{-1}

R   Ideal gas constant, J mol^{-1} K^{-1}

Dimensionless numbers

Da   Damköhler number, -

M_T Thiele modulus, -

Re   Reynolds number, -

Sc   Schmidt number, -

Sh   Sherwood number, -

Variables and parameters

J Mass flux, kg m^{-2} s^{-1}

N Molar flux, mol m^{-2} s^{-1}

δ Boundary layer thickness, m

η Overpotential, V

$\mathscr{E}$ Effectiveness factor, -

Φ Electrode potential, V

ϕ Electrolyte potential, V

ρ Density, kg m^{-3}

Θ Cumulative catalyst loading, -

θ Local catalyst loading, -

c Concentration, mol m^{-3}

h_i Sechenov coefficient for species i, m^3 s^{-1}

i Superficial current density, A m^{-2}

j Geometric current density, A m^{-2}

n Electron transfer number, -

p Pressure (partial), Pa

Q Flow rate, m^3 s^{-1}

R Volumetric reaction rate, mol m^{-3} s^{-1}

r Particle radius, m

s_j^i Stoichiometric coefficient of reaction i in reaction j, -

U Flow velocity, m s^{-1}

V_{cell} Cell potential, V

x_i Mole fraction of species, i, -

z Ionic charge, -

T   Temperature, K

1

INTRODUCTION

If fossil fuels are so bad, why do we keep using them? The two main answers are that: fossil fuels are "great"; that is to say, decades upon decades of propagandising and proliferation have led to heavy dependence and desensitisation to their limitations, and secondly: fossil fuels are *great*; they are ubiquitous, energy dense, multipurpose, and cheap, and have revolutionised everything from agriculture and medicine to transport and energy[1]. To many people, fossil fuels have connotations of power generation and transport, and while the majority of fossil fuel use is in those sectors, it is also important to look from the other side at how how dependent an industry is on fossil fuels. In the EU, energy is around 80% dependent on fossil fuels [32], transport is around 92% [12], but practically all plastic [50] or fertiliser [42] production requires fossil fuels. This disparity in defossilisation readiness is a great issue. Renewable energy sources are relatively advanced compared to the sustainable technologies that intend to utilise them.

1.1. PROBLEMS IN A DEFOSSILISED FUTURE

1.1.1. INTERMITTENCY

Many renewable energy sources are dependent on global cycles, from seasonal, to meteorological and daily. These fluctuations in supply are compounded by large daily variations in energy demands, as is seen in Fig. 1.1, which shows that the slack of renewable sources is usually picked up by fossil fuel power plants. Seasonal variations further complicate this, with short winter days and unreliable lulls in the wind mean that large power sources can be mostly useless for large parts of the year. Few renewable energy sources can be described as reliable, even disregarding inherent intermittency, and it is conceivable that in the future of extreme weather even hydroelectric power may lose this title. Despite this, the capacity for renewable power generation can easily satisfy modern and future demands as long as it can be stored to compensate for these issues.

---

[1]The revolutionary effect on global politics has been respectfully omitted from this list

1
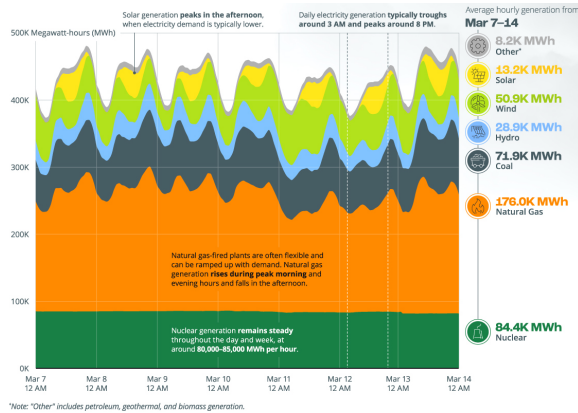
Figure 1.1: Power source distribution across the US for one week in March 2023. Source: DecarbonizationReport.com

1.1.2. STORAGE AND TRANSPORT

The capacity of large-scale energy storage is tragically far lower than that necessary to compensate the daily, let alone seasonal variations in renewable energy sources. The energy density of batteries, the most stereotypical energy storage devices, pale in comparison to that of fossil fuels (Fig. 1.2), and the promising alternative renewable fuels like hydrogen still require huge increases in infrastructural support before they can compete with fossil fuels. This low cost high energy density is why fossil fuels continue to dominate the transport sector. For roaming vehicles, this higher density represents a greater range, shorter refuelling times. Moreover, a more energy dense fuel is easier to transport, making it more preferable for use in isolated locations.

1.1.3. INDUSTRY

Industries that depend strongly on fossil fuels do not always have strong alternatives. Plastic use can be reduced in packaging for instance, but disposable plastics in medicine are vital. Building materials like steel, concrete and tarmac depend on fossil fuels and alternative production methods are extremely inefficient by comparison. The chemical industry in general is also highly dependent on fossil fuels, although arguably out of historical expediency rather than necessity [2], as the basic building blocks in the synthesis of important chemicals are hydrocarbons obtained from or derived from fossil fuels. Hydrocarbon building blocks are derived from fossil fuels like benzene (C_6H_6) from oil or coal distillation [37], ethylene (C_2H_4) and propylene (C_3H_6) from oil refining and thermal cracking [41], or methanol (H_3COH) from synthetic gas, a mixture of hydrogen (H_2) and carbon monoxide (CO) produced through the steam reforming of methane (CH_4) from natural gas [9]. For a defossilised future, alternative sources must be realised for these building block hydrocarbons.

---

[2]A wide range of byproducts resulting from the primary refinement of fossil fuels were unsuitable for use as fuel, causing their widespread adoption as chemical building blocks
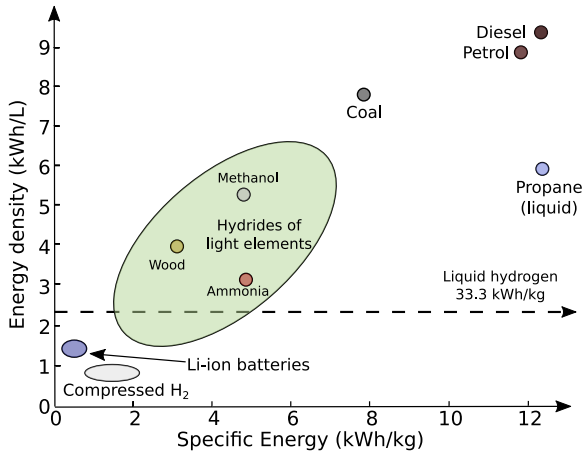
Figure 1.2: Energy density and specific energy of various energy storage materials, based on the work of Sartbaeva et al. [47] Note that Uranium-235 is not included in this plot, but if it was it would be about 180 km to your right hand side.

1.2. PROSPECTIVE SOLUTIONS

As hinted at in Fig. 1.1, significant headway has already been made in one method: biomass conversion. Through the CO_2 conversion technology already present in plants, photosynthesis, and the resultant creation of different forms of plant biomass or waste and excrement, it is possible to convert atmospheric CO_2 and solar energy into a hydrocarbon source. While biomass as an energy source is already being strongly adopted in the EU renewable energy market [2], its diverse nature leads to issues when attempting to upgrade or trade it. Upgrading through gasification, pyrolysis, liquefaction, or torrefaction is necessary to attain chemical building blocks, and the cost of processing is dependent on specific biomass stock and can be comparable to or even more than the final product value. Furthermore, for future demands to be met, biomass must be cultivated entirely for energy purposes, leading to debates over land use, especially in the context of the dilemma of *food versus fuel* [45]. As such, biomass is a viable and effective energy source, but is neither versatile nor scalable enough to solve the wider issues in a defossilised future alone.

Alternatively, natural CO_2 conversion can be eschewed in favour of direct thermal or electrochemical conversion. While complicated in theory, only a select few chemicals would necessarily need to be mass-produced before they could form a basis for the ubiquitous petrochemical processes on which the industry has built for decades. Furthermore, direct CO_2 conversion can be tailored to rely on renewable energy sources, exploiting cheap electricity at peak production hours and scaling down when production is low. In the case of extreme renewable energy intermittency or remoteness, CO_2 can even be converted into fuels, providing long term scaleable CO_2-neutral energy storage [38]. The CO_2 can be sourced from clean direct carbon capture sources [51] or from cheaper but less pure industrial emissions [52]. In the former case, promising research shows that it is feasible to perform electrochemical processes directly on the carbon capture liquid, still
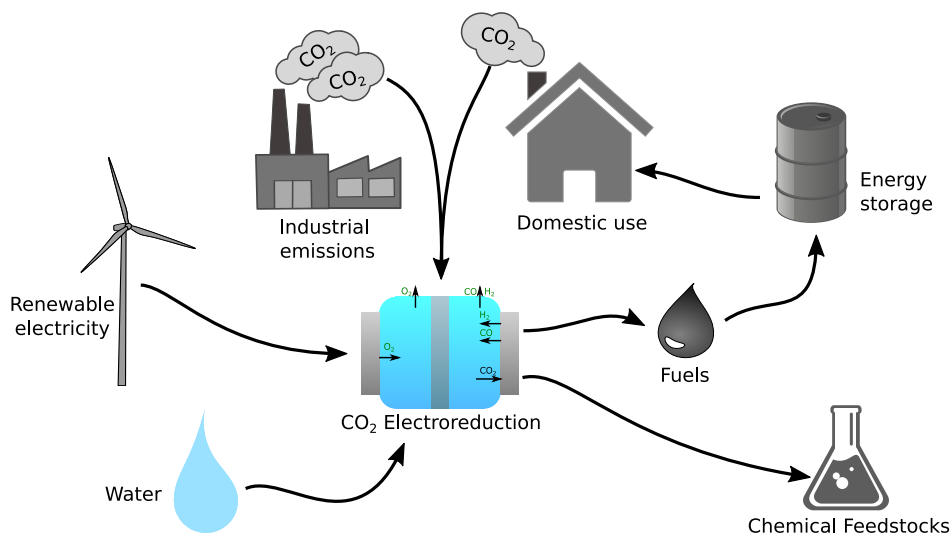
Figure 1.3: Typical carbon cycle for electrochemical CO_2 conversion, with renewable energy converting waste CO_2 into chemical feedstocks.

in dissolved carbonate form, circumventing the need for CO_2 pressurisation. [28].

Fig. 1.3 shows a typical electrochemical process cycle. Note that within the supply of renewable electricity and water there is also an implicit supply of H_2 generated from water electrolysis, as many of the multi-step processes to chemical feedstocks similarly require renewably sourced H_2 to remain carbon neutral. In the simplest case of reduction on a silver catalyst, CO_2 is converted into CO in a two electron process through $CO_2 + 2e^- + H_2O \longrightarrow CO + 2OH^-$. This CO can then be combined with H_2 to form methanol or higher order (C-C) hydrocarbons in the Fischer-Tropsch process [44, 19]. With both the CO and H_2 produced electrochemically with renewable energy, the need for fossil CH_4 reforming is entirely circumvented.

While electroreduction to CO is relatively advanced [36], different catalysts, usually copper, Cu, can produce more complicated chemicals, such has the relatively valuable formate (HCOOH) or even ethylene or methane directly. In the latter case, methane can simply be used as a fuel, allowing for long-term scaleable energy storage, with relatively low energy efficiencies offset by the existence of broad infrastructural support for its use [49].

1.3. ELECTROCHEMICAL CO_2 REDUCTION

1.3.1. OVERVIEW

Electrochemical conversion of CO_2 centres on the cathodic electroreduction of CO_2, involving a reaction with either protons (H^+) or water (H_2O), through the two reactions,

$$CO_2 + 2e^- + 2H^+ \longrightarrow CO + H_2O$$
$$CO_2 + 2e^- + H_2O \longrightarrow CO + 2OH^-.$$
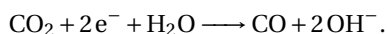
These usually takes place in aqueous media, with the former reaction with H^+ being more favourable in relatively H^+ abundant acidic or near-neutral media, and the latter being favoured in alkaline media. The product may either be in the liquid phase, like HCOOH, or predominantly gas phase phase, like CO or CH_4, escaping as bubbles. The specific product or spectrum of products depends on the nature of the catalytic reaction sites: in addition to Ag (silver) and Cu (copper), elemental catalysts of Au (gold), Pd (palladium), and Sn (tin) have been utilised, showing selectivity towards CO and HCOOH [48], and more complex catalysts also show promising results, such as tandem or alloyed Ag-Cu catalysts [8, 18] and metal-organic frameworks (MOFs) [40].

As the reaction requires electrons to be consumed at the cathode, a counter-reaction takes place at the opposite electrode, or anode, in which electrons are produced. The reaction at the anode is typically a generic oxygen evolution reaction (OER), as the reactant, H_2O is abundant [33]. This process, while well-understood, is practically worthless when producing O_2, so promising new anodic processes are currently being investigated, like ethylene glycol or glucose oxidation to valuable HCOOH [3, 58]. In aqueous media, the common cathodic counterpart to OER also occurs: the hydrogen evolution reaction (HER). Similar to OER, the produced H_2 is much less valuable than the products of CO_2 reduction, so this reaction is generally unwanted and it is usually preferable to minimise. However, HER occurs at similar potentials to CO_2 reduction, and is difficult to prevent [22, 16]. The ratio between amount that effectively goes to reducing CO_2 and the total electricity spent on electrolysis and the is known as Faradaic efficiency (FE), and is one of the key metrics in field.

CO_2 is generally supplied through the aqueous phase, but in the presence of H_2O this dissolved CO_2 partially reacts into bicarbonate (HCO_3^-) and carbonate (CO_3^{2-}), through the carbonate buffer reactions:

$$CO_2 + H_2O \longleftrightarrow HCO_3^- + H^+$$
$$HCO_3- \longleftrightarrow CO_3^{2-} + H^+,$$

or in alkaline media,

$$CO_2 + OH^- \longleftrightarrow HCO_3^-$$
$$HCO_3^- + OH^- \longleftrightarrow CO_3^{2-} + H_2O.$$
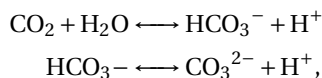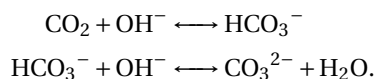
While some setups utilise this phenomenon to circumvent the specific need for CO_2 [24, 29], in others it can lead to complications. The H^+ consumed or OH^- generated from the CO_2 reduction reaction causes these buffer reactions to move to the right hand side, aggressively converting the CO_2 to the less useful HCO_3^- and CO_3^{2-}, which themselves can be problematic for the reactors [11, 21, 15]. Both are negatively charged, promoting migration and crossover to the anode side and allowing the formation and precipitation of carbonate salts, causing pathway blockage in the porous structures, and loss of hydrophobicity. The supply of CO_2 to the cathode is limited by its solubility and diffusivity. In a simple configuration, such as in Fig. 1.4, aqueous phase CO_2 is supplied in the electrolyte and must diffuse to the cathode. The solubility of CO_2 in standard conditions is around 34 mol m^{-3} for typical electrolytes, so without any method of enhancing CO_2 mass transfer the limiting current density for planar electrodes sits at a meagre 35 mA cm^{-2} [57,
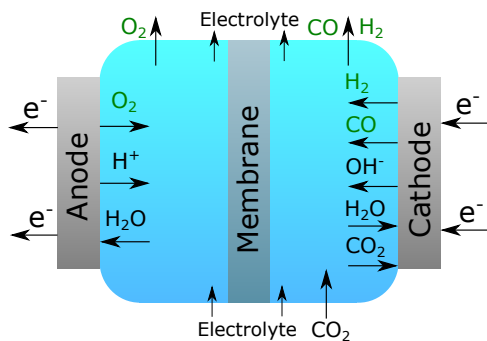
Figure 1.4: An gap configuration for CO_2 reduction. The anode at the left performs OER, converting H_2O to O_2. The cathode at the right converts CO_2 to CO (or other products) and H_2O to H_2 in the unwanted HER side reaction.

7]. This is far too low to be economically feasible, even neglecting the impact of the bicarbonate buffer reactions [36]. To compensate for this, gas-diffusion electrodes (GDEs) that supply gas-phase CO_2 are used.
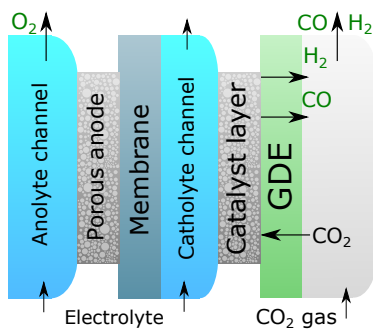
Figure 1.5: A gas-diffusion electrode (GDE) setup. CO_2 is provided as a gas in a separate gas channel, from which it can diffuse through the porous diffusion layer to reach the porous catalyst layer in and react. The gas phase products can then escape back into the gas channel.

GDEs exploit porous structures to allow the electrolyte to penetrate into a porous medium with extremely high internal surface area, and are commonly used in fuel cells [43, 59]. Fig. 1.5 shows a typical setup, in which the cathode and anode have both been replaced with porous media. In the case of the anode, a porous medium allows the anolyte channel to be moved to the other side, reducing the inter-electrode distance and thus cell potential [14]. The cathode is replaced with a GDE, comprising of multiple layers, depicted in Fig. 1.6: a catalyst layer (CL) with suspended catalyst particles, a microporous layer (MPL) with hydrophobic properties that prevent liquid breakthrough, and a gas-diffusion layer (GDL) that provides diffusive pathways for CO_2 while maintaining electrical conductivity [25].

By allowing the CO_2 to remain a gas until it is very close to the reaction sites, GDEs yield a huge increase in limiting current density, with characteristic aqueous diffusive pathway
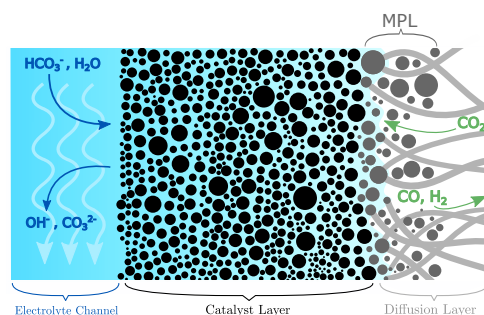
Figure 1.6: A zoomed in schematic of the GDE. The catalyst layer (CL) is in contact with both aqueous electrolyte and the gas filled microporous layer (MPL), allowing for extremely short aqueous diffusion lengths for the gas phase CO_2 that enters through the gas-diffusion layer (GDL).

lengths dropping from roughly 50 μm to under 50 nm [7]. While theoretically allowing a thousand-fold increase in current density, the extreme local environments present in these cells mean that this increase is unrealised, and contemporary electrolysers only see a ten-fold increase [6]. The room for improvement is great, but there are many issues that must be addressed before the technology becomes feasible at large scales [23].

1.3.2. ISSUES IN CO_2 REDUCTION

Referring back to Fig. 1.3 shows that CO_2 reduction is governed by the input of CO_2 and electricity and the output of valuable chemicals, so any performance analysis should include interactions with upstream and downstream processes [1]. CO_2 and electricity are not free, so their utilisation must be maximised, and upstream and downstream processing costs should ideally be minimised. Furthermore, the electrolysers must operate at sufficient current densities and be scaleable enough to be relevant in the face of industry demands, and must be stable for years of operation. Many targets have been put forward, like the often quoted target of a current density of ≥ 200 mA cm^{-2} [7], which has also increased to around 500 mA cm^{-2} in the case of reduction to CO [54], or a maximum cell potential of 3 V to remain energy efficient [46].

Maximising Faradaic efficiency is primarily a case of minimising unnecessary hydrogen evolution, but when multiple reduction products are present it can also be a case of maximising selectivity towards a single desired product. To minimise hydrogen evolution, many electrolysers utilise high pH electrolytes to minimise the availability of aqueous protons that promote acidic hydrogen evolution [53]. However, these electrolytes rapidly react with CO_2, leading to a decrease in CO_2 available for reduction, and hence a reduction in partial current density towards CO_2 reduction products [10]. Furthermore, the reacted CO_2 will first form HCO_3^-, which can act as a proton donor and allow unabated HER [35].

The consumption of CO_2 reactant by alkaline electrolytes is exacerbated by the inherent increase in local pH associated with both HER and the CO_2 reduction reaction, either through the removal of H^+ or the generation of OH^-. Both HER and reduction to CO produce two OH^- per product molecule, leading to pH shifts that theoretically

(a) A membrane electrode assembly (MEA) type cell, operating with an anion exchange membrane (AEM).

(b) A cell with a flowing catholyte channel. These cells do not necessarily require a membrane, but often include one at the anode side.
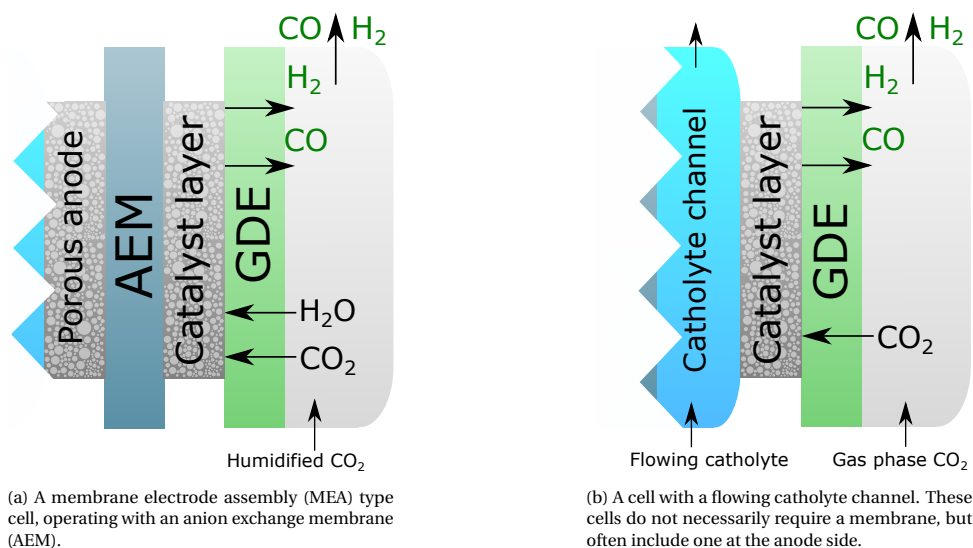
Figure 1.7: Two of the most promising CO_2 electrolyser setups

consume one molecule of reactant CO_2 each, and more in the case of products requiring more electron transfers [26]. This formation of HCO_3^- and CO_3^{2-} not only constitutes a local loss of reactant, but also contributes to the precipitation of carbonate salts in the fragile CL and MPL [11], which can further lead to blockage in diffusion pathways, loss of hydrophobicity, and electrode flooding [56, 31]. Flooding theoretically should be mitigated by the MPL, but that often fails under the pressure differences present between the catholyte flow channel and gas feed [4]. Furthermore, the formed HCO_3^- and CO_3^{2-} can cross over to the anode, at which they evolve as gaseous CO_2 in the O_2 product stream [21]. Recovering the CO_2 from this CO_2/O_2 mixture is expensive [1] and for some conditions even economically infeasible, meaning that this crossover constitutes a large loss of reactant or additional separation cost. Depending on the setup, up to 70% of reactant CO_2 can cross over in this manner [34].

The leading operational cost is practically always the cost of electrolysis [39]. FE is maximised to minimise unnecessary electrolysis cost, but it is often more beneficial to lower total electrolysis cost by reducing the cell potential. Reducing the inter-electrode distance and using a highly conductive electrolyte, like concentrated KOH, can reduce the potential drop across the cell, and more advanced catalysts can reduce the overpotential necessary to reach high current densities. However, reduced inter-electrode distance and concentrated KOH exacerbate the problems of non-electrochemical consumption and crossover of CO_2. While acidic electrolytes can also provide high conductivity, the high availability of H^+ leads to large HER current densities and large drops in FE, making them unfeasible without significant advances in HER suppression. Alarmingly, even strongly acidic electrolytes may not be sufficient to prevent salt precipitation due to high inhomogeneity in reaction environment and high pH near and in the CL [5].

Figs. 1.7a and 1.7b show a membrane electrode assembly (MEA) type cell and a flowing

catholyte channel cell respectively. The former eschews the use of a liquid catholyte in favour of a humidified CO_2 gas stream, to minimise the inter-electrode distance with an anion exchange membrane (AEM) in direct contact with both electrodes. The close electrodes allow lower cell potentials and the lack of circulating catholyte removes complicated pressure balance issues associated with electrolyte pumping, making upscaling simple [17]. However, the AEM allows the transport of the HCO_3^- and CO_3^{2-} anions as well as OH^-, and combined with the lower inter-electrode distance this leads to very large rates of CO_2 crossover to and evolution at the anode. As OER requires 4 electrons transferred per O_2 produced, this means that charge transferred with HCO_3^- or CO_3^{2-} would lead to an anode outlet CO_2 fraction of 80% or 66%, respectively [27]. Despite this, AEMs are still not selective enough to prevent all cations from migrating to the cathode and allowing carbonate salt precipitation. Furthermore, if the HCO_3^- and CO_3^{2-} ions replace OH^- as the primary charge carriers then the H^+ generated at the anode is not neutralised and the anolyte can become acidified unless regularly refreshed.

The flowing liquid catholyte in Fig. 1.7b helps to prevent these issues, but at the cost of a higher cell potential [55] and pumping and pressure balance complications [4, 30]. This configuration is more compatible with bipolar membranes (BPMs) and cation exchange membranes (CEMs) that can greatly, though still not entirely, inhibit crossover [13]. However, CEMs promote cation migration and carbonate accumulation and can induce salt precipitation, whereas BPMs have poor conductivity, and CO_2 may evolve as insulating bubbles at the membrane surface and further increase cell potential [13].

1.4. THESIS OUTLINE

The closely interlinked physical phenomena at play make CO_2 reduction on GDEs a difficult field to make experimental progress in. It can be difficult to tell without deep and laborious investigation what the source, or often sources, of an observed effect truly are. An increase in galvanostatic cell potential could be due to bubble resistance, deterioration of electrolyte, change in catalyst, or many other problems, and the relevance of these effects can vary under different operational loads and with different electrode materials.

To peer deeper into the underlying interactions and processes, this thesis focuses on analytical, numerical, and computational modelling of mass transfer within a GDE cell. Analytical models use scaling analyses to neglect irrelevant processes in favour of capturing only phenomena relevant to the current operating conditions. For example, an analytical model can note that the characteristic mass transfer **through** a CL is orders of magnitude more important than mass transfer **along** a CL, due to the enormous difference in characteristic length, from μm scale to cm scale. These scaling relations are often useful and recognised in a more generalised sense as named dimensionless numbers, for instance, the ratio of reaction rate to mass transfer, the Damköhler number (Da).

When a model is expressed in these terms, the interactions between characteristic processes become more clear and results become more generally applicable to a range of situations. For example, if a solution is valid for a high Da, then it is valid for all systems with disproportionately high reaction rates, or high flow rates, or small length scales. In this way an analytical model can represent a whole range of systems simultaneously, while an experimental setup or computational model can only represent one single system at a

1

time. These solutions usually give insight into which underlying mechanisms are relevant at different scales, as irrelevant elements are readily discarded when their impacts are negligible.

Not all systems are readily tractable in this approach however. Even with purely analytical inroads, solutions can arrive in the form of non-elementary functions, whose resulting values are not immediately clear, or forms that are too complicated to be useful. In these cases it can be useful to implement numerical processes. For example, some analytical solutions contain equations of the form, $xe^x = y$, whose solution, the Lambert W function, is inexpressible in terms of elementary functions. The options that remain are to formulate (excellent but scale-dependent) approximations [20], or rely on arbitrarily precise numerical calculation. Similarly, as will be seen in Chapter 4, an analytical system can arise that, while presumably perfectly soluble, would be laborious and fruitless to solve, as the long-winded and complicated form of the solution would obfuscate any useful underlying relationships. In these cases it is again preferable to solve numerically.

Somewhat of a distinction is made between numerical and computational modelling here. The analytical and numerical models are resultant from *a priori* assumptions about the systems at hand, making informed decisions about which phenomena are relevant. Computational modelling, in this case, is less targeted, and aims to broadly cover a much wider range of scenarios without discrimination. This thesis utilises such models frequently, but notes that they alone do not provide meaningful information in and of themselves, and should be viewed as closer related to experimental work than analysis. Nonetheless, they are a valuable resource in validation of analytical assumptions and in exploring hypotheses.

Returning to the topic of this thesis, these tools will be used to make predictions and recommendations for general design and operation of GDE based CO_2 electrolysers with a flowing catholyte. To some extent, optimisation is the art of finding and eliminating bottlenecks: it is the goal of this thesis to find which process or cost limits the performance of the system and determine how to alleviate that limitation. This ideally constitutes finding such a limitation and providing a method by which to improve the underlying physical process, but in many cases such a process is limited by some more fundamental property, such as diffusivity, rather than some operational construct. In the case of CO_2 electrolysers, factors from parasitic consumption from buffer reactions, to activation overpotential, to aqueous diffusivity, to gas supply partial pressure can all become limiting in different setups, so the goal is to provide a rough framework of which factors become limiting in which scenarios.

1.4.1. RESEARCH QUESTIONS

While theses usually set out to answer a few key questions, it is important to note that, like many analytical and modelling studies, this thesis follows the construction of a framework of models whose explicit implementation only covers a few cases. These cases comprise of a relevant but small subset of the domain of the models, and it is encouraged for the interested reader to seek the models at the links listed in 5.5. As such, the research questions take more of a form of observations made during the construction of these models, but nonetheless, this thesis aims to answer the following questions

(RQ1) When does a thicker catalyst layer lead to a higher current density? (Chapter 2)

(RQ2) Can a buffering catholyte effectively prevent parasitic reaction with OH^- in the catalyst layer? (Chapters 2-4)

(RQ3) How do selectivity and current density scale and vary with electrolyser length? (Chapter 3)

(RQ4) Is the presence of available catalyst always beneficial in a realistic electrolyser? (Chapters 3, 4)

(RQ5) What are the main operational costs in a CO_2 electrolyser and how do they compare to each other? (Chapter 4)

BIBLIOGRAPHY

[1] Théo Alerte et al. "Downstream of the CO2 Electrolyzer: Assessing the Energy Intensity of Product Separation". In: *ACS Energy Letters* 6.12 (2021), pp. 4405–4412.

[2] Manjola Banja et al. "Biomass for energy in the EU – The support framework". In: *Energy Policy* 131 (2019), pp. 215–228. ISSN: 0301-4215.

[3] Ifra Bashir et al. "Sustainable Formate Synthesis: Integrating Ethylene Glycol Oxidation with Carbon Dioxide Electrocatalysis Using Redox-Stabilized Earth-Abundant Electrodes". In: *ACS Sustainable Chemistry & Engineering* 12.12 (2024), pp. 4795–4802.

[4] Lorenz M. Baumgartner et al. "Narrow Pressure Stability Window of Gas Diffusion Electrodes Limits the Scale-Up of CO_2 Electrolyzers". In: *ACS Sustainable Chemistry & Engineering* 10.14 (2022), pp. 4683–4693.

[5] Francesco Bernasconi et al. "Operando Observation of (Bi)carbonate Precipitation during Electrochemical CO_2 Reduction in Strongly Acidic Electrolytes". In: *ACS Catalysis* 0.0 (0), pp. 8232–8237.

[6] Joseph W. Blake et al. "Inhomogeneities in the Catholyte Channel Limit the Upscaling of CO2 Flow Electrolysers". In: *ACS Sustainable Chemistry & Engineering* 11.7 (2023), pp. 2840–2852.

[7] Thomas Burdyny and Wilson A. Smith. "CO_2 reduction on gas-diffusion electrodes and why catalytic performance must be assessed at commercially-relevant conditions". In: *Energy Environ. Sci.* 12 (5 2019), pp. 1442–1453.

[8] Zhizhou Cai et al. "Hierarchical Ag-Cu interfaces promote C-C coupling in tandem CO2 electroreduction". In: *Applied Catalysis B: Environmental* 325 (2023), p. 122310. ISSN: 0926-3373.

[9] Gabriele Centi and Siglinda Perathoner. "Chemistry and energy beyond fossil fuels. A perspective view on the role of syngas from waste sources". In: *Catalysis Today* 342 (2020). SI: Syngas Convention 3, pp. 4–12. ISSN: 0920-5861.

[10] Chubai Chen, Yifan Li, and Peidong Yang. "Address the alkalinity problem in CO_2 electrolysis with catalyst design and translation". In: *Joule* 5.4 (2021), pp. 737–742. ISSN: 2542-4785.

[11] Emiliana R. Cofell et al. "Investigation of Electrolyte-Dependent Carbonate Formation on Gas Diffusion Electrodes for CO_2 Electrolysis". In: *ACS Applied Materials & Interfaces* 13.13 (2021). PMID: 33764731, pp. 15132–15142.

[12] Romeo Danielis, Mariangela Scorrano, and Marco Giansoldati. "Decarbonising transport in Europe: Trends, goals, policies and passenger car scenarios". In: *Research in Transportation Economics* 91 (2022). Decarbonising transport, p. 101068. ISSN: 0739-8859.

[13] Bert De Mot et al. "Insight in the behavior of bipolar membrane equipped carbon dioxide electrolyzers at low electrolyte flowrates". In: *Chemical Engineering Journal* 428 (2022), p. 131170. ISSN: 1385-8947.

[14] Guillermo Díaz-Sainz et al. "Coupling continuous CO2 electroreduction to formate with efficient Ni-based anodes". In: *Journal of Environmental Chemical Engineering* 11.1 (2023), p. 109171. ISSN: 2213-3437.

[15] S. Erbach et al. "CO_2 Enrichment in Anode Loop and Correlation with CO Poisoning of Low Pt Anodes in PEM Fuel Cells". In: *Fuel Cells* 18.5 (2018), pp. 613–618.

[16] Sahil Garg et al. "Advances and challenges in electrochemical CO_2 reduction processes: an engineering and design perspective looking beyond new catalyst materials". In: *J. Mater. Chem. A* 8 (4 2020), pp. 1511–1544.

[17] Lei Ge et al. "Electrochemical CO2 reduction in membrane-electrode assemblies". In: *Chem* 8.3 (2022), pp. 663–692.

[18] Peiqi Guo et al. "Perspectives on Cu–Ag Bimetallic Catalysts for Electrochemical CO2 Reduction Reaction: A Mini-Review". In: *Energy & Fuels* 38.7 (2024), pp. 5659–5675.

[19] Pavan K Gupta, Vineet Kumar, and Sudip Maity. "Renewable fuels from different carbonaceous feedstocks: a sustainable route through Fischer–Tropsch synthesis". In: *Journal of Chemical Technology & Biotechnology* 96.4 (2021), pp. 853–868.

[20] JW Haverkort et al. "An analytical flow-by capacitive deionization model". In: *Desalination* (2024), p. 117408.

[21] Juan Herranz et al. "Co-electrolysis of CO_2 and H_2O: From electrode reactions to cell-level development". In: *Current Opinion in Electrochemistry* 23 (2020), pp. 89–95. ISSN: 2451-9103.

[22] Y. Hori. "Electrochemical CO_2 Reduction on Metal Electrodes". In: *Modern Aspects of Electrochemistry* (2008), pp. 89–189.

[23] Matthew Jouny, Wesley Luc, and Feng Jiao. "General Techno-Economic Analysis of CO_2 Electrolysis Systems". In: *Industrial & Engineering Chemistry Research* 57.6 (2018), pp. 2165–2177.

[24] Recep Kas et al. "Modeling the Local Environment within Porous Electrode during Electrochemical Reduction of Bicarbonate". In: *Industrial & Engineering Chemistry Research* 61.29 (2022), pp. 10461–10473.

[25] Ahmad El-kharouf et al. "Ex-situ characterisation of gas diffusion layers for proton exchange membrane fuel cells". In: *Journal of Power Sources* 218 (2012), pp. 393–404. ISSN: 0378-7753.

[26] Gastón O. Larrazábal, Ming Ma, and Brian Seger. "A Comprehensive Approach to Investigate CO_2 Reduction Electrocatalysts at High Current Densities". In: *Accounts of Materials Research* 2.4 (2021), pp. 220–229.

[27] Gastón O. Larrazábal et al. "Analysis of Mass Flows and Membrane Cross-over in CO2 Reduction at High Current Densities in an MEA-Type Electrolyzer". In: *ACS Applied Materials & Interfaces* 11.44 (2019). PMID: 31603302, pp. 41281–41288.

[28] Geonhui Lee et al. "CO2 electroreduction to multicarbon products from carbonate capture liquid". In: *Joule* 7.6 (2023), pp. 1277–1288.

[29] Eric W. Lees et al. "Electrodes Designed for Converting Bicarbonate into CO". In: *ACS Energy Letters* 5.7 (2020), pp. 2165–2173.

[30] Ulrich Legrand et al. "Product Crossflow through a Porous Gas Diffusion Layer in a CO2 Electrochemical Cell with Pressure Drop Calculations". In: *Industrial & Engineering Chemistry Research* 60.19 (2021), pp. 7187–7196.

[31] Mclain Leonard et al. "Investigating Electrode Flooding in a Flowing Electrolyte, Gas-Fed Carbon Dioxide Electrolyzer". In: *ChemSusChem* 13 (Nov. 2019), pp. 400–411.

[32] Raymond Li and Guy C.K. Leung. "The relationship between energy prices, economic growth and renewable energy consumption: Evidence from Europe". In: *Energy Reports* 7 (2021), pp. 1712–1719. ISSN: 2352-4847.

[33] Jing Lin et al. "Electroreduction of CO2 toward High Current Density". In: *Processes* 10.5 (2022). ISSN: 2227-9717.

[34] Ming Ma et al. "Insights into the carbon balance for CO2 electroreduction on Cu using gas diffusion electrode reactor designs". In: *Energy Environ. Sci.* 13 (3 2020), pp. 977–985.

[35] Giulia Marcandalli, Akansha Goyal, and Marc T. M. Koper. "Electrolyte Effects on the Faradaic Efficiency of CO2 Reduction to CO on a Gold Electrode". In: *ACS Catalysis* 11.9 (2021). PMID: 34055454, pp. 4936–4945.

[36] Richard I. Masel et al. "An industrial perspective on catalysts for low-temperature CO2 electrolysis". In: *Nature Nanotechnology* 16.2 (2021), pp. 118–128. ISSN: 1748-3395.

[37] Qinglei Meng et al. "Sustainable production of benzene from lignin". In: *Nature Communications* 12.1 (2021), p. 4534. ISSN: 2041-1723.

[38] Emanuele Moioli, Robin Mutschler, and Andreas Züttel. "Renewable energy storage via CO2 and H2 conversion to methane and methanol: Assessment for small scale applications". In: *Renewable and Sustainable Energy Reviews* 107 (2019), pp. 497–506. ISSN: 1364-0321.

[39] Thomas Moore et al. "Electrolyzer energy dominates separation costs in state-of-the-art CO2 electrolyzers: Implications for single-pass CO2 utilization". In: *Joule* 7.4 (2023), pp. 782–796. ISSN: 2542-4351.

[40] Dae-Hyun Nam et al. "Intermediate Binding Control Using Metal–Organic Frameworks Enhances Electrochemical CO2 Reduction". In: *Journal of the American Chemical Society* 142.51 (2020). PMID: 33319985, pp. 21513–21521.

[41] Basil J. Nikolau et al. "Platform biochemicals for a biorenewable chemical industry". In: *The Plant Journal* 54.4 (2008), pp. 536–545.

[42] Bas Paris et al. "Energy use in open-field agriculture in the EU: A critical review recommending energy efficiency measures and renewable energy sources adoption". In: *Renewable and Sustainable Energy Reviews* 158 (2022), p. 112098. ISSN: 1364-0321.

1

[43]   Nagappan Ramaswamy et al. "Carbon Support Microstructure Impact on High Current Density Transport Resistances in PEMFC Cathode". In: *Journal of The Electrochemical Society* 167.6 (2020), p. 064515.

[44]   Quirina I. Roode-Gutzmer, Doreen Kaiser, and Martin Bertau. "Renewable Methanol Synthesis". In: *ChemBioEng Reviews* 6.6 (2019), pp. 209–236.

[45]   Frank Rosillo-Calle. "A review of biomass energy – shortcomings and concerns". In: *Journal of Chemical Technology & Biotechnology* 91.7 (2016), pp. 1933–1945.

[46]   Danielle Salvatore and Curtis P. Berlinguette. "Voltage Matters When Reducing CO2 in an Electrochemical Flow Cell". In: *ACS Energy Letters* 5.1 (2020), pp. 215–220.

[47]   A. Sartbaeva et al. "Hydrogen nexus in a sustainable energy future". In: *Energy Environ. Sci.* 1 (1 2008), pp. 79–85.

[48]   Mark Sassenburg et al. "Characterizing CO2 Reduction Catalysts on Gas Diffusion Electrodes: Comparing Activity, Selectivity, and Stability of Transition Metal Catalysts". In: *ACS Applied Energy Materials* 5.5 (2022), pp. 5983–5994.

[49]   Armin Sedighian Rasouli et al. "CO2 Electroreduction to Methane at Production Rates Exceeding 100 mA/cm2". In: *ACS Sustainable Chemistry & Engineering* 8.39 (2020), pp. 14668–14673.

[50]   Paul Stegmann et al. "Plastic futures and their CO2 emissions". In: *Nature* 612.7939 (2022), pp. 272–276. ISSN: 1476-4687.

[51]   Ian Sullivan et al. "Coupling electrochemical CO2 conversion with CO2 capture". In: *Nature Catalysis* 4.11 (2021), pp. 952–958. ISSN: 2520-1158.

[52]   Di Tian, Zhiguo Qu, and Jianfei Zhang. "Electrochemical condition optimization and techno-economic analysis on the direct CO2 electroreduction of flue gas". In: *Applied Energy* 351 (2023), p. 121787. ISSN: 0306-2619.

[53]   Ana Sofia Varela. "The importance of pH in controlling the selectivity of the electrochemical CO2 reduction". In: *Current Opinion in Green and Sustainable Chemistry* 26 (2020), p. 100371. ISSN: 2452-2236.

[54]   Sumit Verma et al. "A Gross-Margin Model for Defining Technoeconomic Benchmarks in the Electroreduction of CO_2". In: *ChemSusChem* 9.15 (2016), pp. 1972–1979.

[55]   Sumit Verma et al. "The effect of electrolyte composition on the electroreduction of CO_2 to CO on Ag based gas diffusion electrodes". In: *Phys. Chem. Chem. Phys.* 18 (10 2016), pp. 7075–7084.

[56]   Kailun Yang et al. "Role of the Carbon-Based Gas Diffusion Layer on Flooding in a Gas Diffusion Electrode Cell for Electrochemical CO_2 Reduction". In: *ACS Energy Letters* 6.1 (2021), pp. 33–40.

[57]   Wenjun Zhang et al. "Progress and Perspective of Electrocatalytic CO2 Reduction for Renewable Carbonaceous Fuels and Chemicals". In: *Advanced Science* 5.1 (2018), p. 1700275.

[58] Runyao Zhao et al. "Coupling electrocatalytic CO2 reduction with glucose oxidation for concurrent production of formate with high efficiency". In: *Chemical Engineering Journal* 486 (2024), p. 150280. ISSN: 1385-8947.

[59] A. Zlotorowicz et al. "Tailored porosities of the cathode layer for improved polymer electrolyte fuel cell performance". In: *Journal of Power Sources* 287 (2015), pp. 472–477. ISSN: 0378-7753.

1

2

ANALYTICAL MODELLING OF CO_2 REDUCTION IN GAS-DIFFUSION ELECTRODE CATALYST LAYERS

The electrochemical reduction of CO_2 on planar electrodes is limited by its prohibitively low diffusivity and solubility in water. Gas-diffusion electrodes (GDEs) can be used to reduce these limitations, and facilitate current densities orders of magnitude higher than the limiting current densities of planar electrodes. These improvements are accompanied by increased variation in the local environment within the cathode, with significant effect on Faradaic efficiency. By developing a simple and freely available analytical model of a cathodic catalyst layer configured for the production of CO, we investigate the relationships between electrode reaction kinetics, cell operation conditions, catholyte composition and cell performance. Analytical methods allow us to cover parameter ranges that are intractable for numerical and experimental studies. We validate our findings against experimental and numerical results and provide a derivation and implementation of the analytical model.

2

2.1. INTRODUCTION

The electrochemical reduction of CO_2 has seen much attention in recent years for its potential as a panacea solution to the limitations of renewable energy sources [59, 41, 3, 45]. Electrochemical CO_2 reduction (CO2R) can yield a variety of products such as formate [57, 1], syngas [18] and ethylene [2], which can serve as carbon-neutral feedstock for the chemical industry or as scalable chemical energy storage [11]. However, the process is prohibited by the low solubility [35] ($\lesssim$ 30 mM) and diffusivity of CO_2 in aqueous electrolytes at ambient conditions, the low Faradaic efficiency, and the poor utilisation of supplied CO_2, resulting in the limiting CO2R current density on planar electrodes (10-30 mA cm^{-2}) [8] being far lower than the economically viable minimum. These limitations have been addressed in recent years through the adoption of gas-diffusion electrodes (GDEs) [28], which greatly reduce the boundary layer thickness and enable current densities orders of magnitude higher than what is possible on planar electrodes.

Despite historical success [36] in the development of GDE structures for use in proton exchange membrane fuel cells (PEMFCs) [56], there are many design parameters that must be optimised for GDEs in CO2R cells [5]. A GDE consists of a dry macroporous gas-diffusion layer (GDL) through which the CO_2 diffuses and electronic current can flow, a thin hydrophobic microporous layer (MPL) that acts as a bed for the catalyst layer while preventing electrolyte flooding into the GDL [63], and a catalyst layer (CL) in which embedded catalyst particles provide active sites for electrochemical reduction. The CL usually consists of catalyst particles deposited onto the (MPL), creating a thin microporous structure into which both electrolyte and CO_2 can enter. However, the performance of a true GDE is seldom attained, as in practice the CL commonly becomes highly saturated with liquid electrolyte. The three-phase interface retreats to the MPL and can in places even break through into the GDL in flooding events.

Full cell setups also vary outside of the cathode. This work covers a flow cell, in which electrolyte flows between a cathode performing CO2R, in competition with a simultaneous hydrogen evolution reaction (HER), and an anode performing the oxygen evolution reaction. Following PEMFC setups, it is common to include an ion exchange membrane between the anode and cathode. Experiments have been performed with bipolar, anion, and cation exchange membranes, as well as with full membrane electrode assemblies replacing one or both of the aqueous electrolyte channels. These different setups can better control the transport of ions, but can lead to issues with conductivity and water management. Although the catalysts and designs may vary for the oxygen evolution reaction taking place at the anode, these variations are often neglected as a non-limiting process with no effect on cathodic FE. Different catalysts can, however, lead to different reactions at the cathode, which may have a distribution of gas or liquid products.

There are a number of factors limiting the performance of the CL. Despite a large reduction in mass-transfer resistance compared to planar electrodes, the CO_2 concentration drop within a CL fully flooded with electrolyte remains large at high current densities [6]. Although the resistance can be further reduced by maintaining gas channels within the CL itself [49], the multiphase boundaries are difficult to control as flooding resistance has been shown to vary with current density [29]. Furthermore, the Faradaic efficiency (FE) towards desired products is impacted negatively by the hydrogen evolution reaction
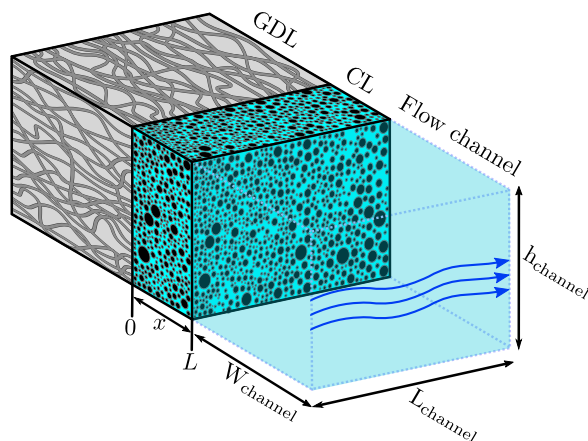
Figure 2.1: 3D section of the cathode, showing the electrolyte flow channel and flooded CL next to the dry GDL. The numerical CL domain considered spans from $x = 0$ at the GDL boundary to $x = L$ at the flow channel boundary, where L is the CL thickness (not to scale).

on the electrode [12]. The competing HER is suppressed in high pH electrolytes [25], but high OH$^-$ concentrations drive the carbonate equilibrium reactions to chemically consume CO_2 to form bicarbonate and carbonate at a rate comparable to that of the electrode reaction. At high current densities this parasitic chemical loss of dissolved CO_2 can account for over 50% of the total CO_2 consumption. This reduces reactant utilisation and leads to a reduction in CO_2 solubility due to the salting-out effect in the resulting high ionic-strength electrolyte [40]. High concentrations of carbonate can also lead to salt precipitation and loss of hydrophobicity in the MPL and GDL, leading to detrimental liquid breakthrough and flooding. In cells with an anion-exchange membrane, it is also possible for carbonate to cross over to the anode, along with a significant portion of the liquid products [61], and re-evolve [19, 10].

In this work we derive an analytical approximation of cathodic CL dynamics and use it to determine the effect of carbonate on cell performance and how the state of the equilibrium reactions can be influenced by cell parameters. The model uses Ag catalyst particles as their high selectivity towards CO and H_2 [62, 13, 48, 47] allows us to neglect products of further reduction that require additional reaction parameters [22]. The benefit of analytical predictions is in their versatility: one can cover vast parameter spaces with ease and parametric studies do not require long computational or experimental time investments.

2.2. MODEL

2.2.1. THEORY

The CL is modeled as a 1D domain in the plane-perpendicular direction, with mass-transfer boundary conditions determined by the electrolyte channel properties and GDL gas phase interface. The porous medium is assumed to be homogeneous and fully flooded with electrolyte at a liquid fraction of ϵ. Although earlier studies proposed that

the reaction takes place only at a triple-phase boundary [58, 31], recent studies have determined that it is more likely to occur at a solid-liquid boundary [33], and flooded CLs can still exhibit high current densities. Local variation in structure is difficult to categorise and is neglected, though studies show that the effects of variation can be significant. [37, 64, 16]. The volumetric reactive surface area, a, is assumed constant throughout the CL and can be correlated with further CL structure properties (2.5.3). Diffusion of aqueous species through the medium is corrected for porosity and tortuosity through the Bruggeman relation $D_{\text{eff}} = D\epsilon^{\frac{3}{2}}$. We assume that all species remain in an aqueous state within the CL, neglecting the effects of bubble formation and bubble-induced voltage instability [27].
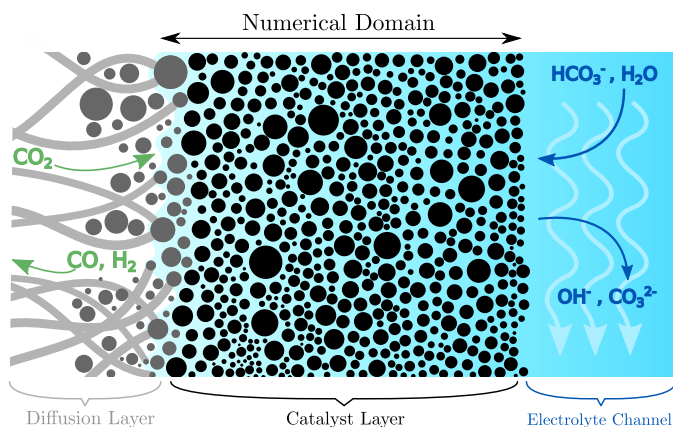
Figure 2.2: The numerical model covers a 1D plane-perpendicular domain of the catalyst layer, with boundaries at the microporous layer and GDL (left) and electrolyte flow channel (right). The blue-filled domains represent liquid phase portions and clear domain represents gas phase. At the far right side of the electrolyte channel will be a membrane and anode surface.

The GDL acts as a source of CO_2 at pressure p_{CO_2}. Other gaseous species in the GDL are neglected, and while CO and H_2 products can escape freely into both the GDL and the electrolyte channel they are assumed to have negligible effect on CO_2 transport and chemical equilibria. As an important limiting factor, the transport of CO_2 from the GDL to the CL is based on Henry's Law with the solubility of CO_2 in the electrolyte corrected for ionic content through the Schumpe [50] extension to the Sechenov [40] equation. The electrolyte channel consists of a potassium bicarbonate ($KHCO_3$) solution in a plane-parallel Poisueille flow with average velocity v, with carbonate equilibria determined from the electroneutrality condition and carbon conservation and corrected for ionic strength and temperature. In-plane effects have been shown to be significant enough to lead to a drop in current density in the streamwise direction, from 450 mA cm^{-2} to <300 mA cm^{-2}, in addition to large streamwise pH gradients [24]. Although this cannot be fully captured in a 1D model, we expect the majority of the variation to be due to the development of the electrolyte ionic concentration profiles, namely OH$^-$, bicarbonate and carbonate, from a thin developing concentration boundary layer near the inlet of the electrolyte

channel to a fully developed concentration profile downstream. This variation, along with the possibility for a developing flow profile, is accounted for in the determination of electrolyte boundary conditions. More information on the solubility and boundary conditions can be found in 2.5.6

As Ag catalysts are highly selective towards CO and H_2, we neglect other electrode reactions. Furthermore, the cathodic potentials at relevant current densities are sufficient for us to discard anodic branches of the electrode reactions and assume Tafel kinetics, with a first-order dependence on CO_2 concentration for the CO evolution reaction [21] and a concentration independent basic reaction pathway for HER [9] for constant water content.

$$CO_2 + H_2O + 2e^- \longrightarrow CO + 2OH^-, \qquad\qquad E_{CO}^0 = -0.11 \text{ V},$$
$$2H_2O + 2e^- \longrightarrow H_2 + 2OH^-, \qquad\qquad E_{H_2}^0 = 0 \text{ V},$$
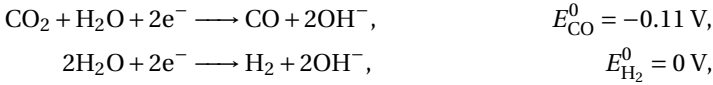
with current densities

$$i_{CO2R} = -i_{0,CO2R} \frac{[CO_2]}{[CO_2]_{ref}} \exp\left(\frac{-\eta_{CO2R}}{b_{CO2R}}\right) \qquad (2.1)$$

$$i_{HER} = -i_{0,HER} \exp\left(\frac{-\eta_{HER}}{b_{HER}}\right), \qquad (2.2)$$

where i_0, η and b are the exchange current densities, overpotentials and Tafel slopes respectively. The Tafel slope is related to the charge transfer coefficient α by $b = \frac{RT}{F\alpha}$ where F and R are Faraday's constant and the universal gas constant respectively. Geometric current densities; that is, current density per unit external CL area, can be determined by integrating the superficial current densities described in (2.1) and (2.2) along the thickness of the CL and multiplying by the volumetric surface area, a. Our domain consists of only a single CL, so the ohmic drops across the remainder of the cell are not included here. Furthermore, the Wagner number in the CL, which is the ratio of solution and polarisation resistance, is small ($Wa = \frac{\kappa b}{i_0 L} \approx 10^4$) for typical values of the electrolyte conductivity κ, meaning that ohmic drops are negligible and the majority of the ohmic drop of the full cell occurs outside of the CL. The assumptions of Tafel kinetics are generally valid when the total Butler-Volmer current density significantly exceeds the exchange current density, which is true for both considered reactions at relevant CO current densities of $> 1 \text{ mA cm}^{-2}$. Furthermore, any effect on local reaction environment in the low overpotential regime would be outweighed by the buffering effect of the homogeneous chemical reactions. These alkaline carbonate equilibrium reactions are modelled kinetically in the CL, closed with the assumption of arbitrarily fast water dissociation,

$$CO_2 + OH^- \underset{k_{-1}}{\overset{k_1}{\rightleftharpoons}} HCO_3^-, \qquad\qquad K_1 = 10^{7.69} \text{ M}^{-1}, \qquad (2.3)$$

$$HCO_3^- + OH^- \underset{k_{-2}}{\overset{k_2}{\rightleftharpoons}} H_2O + CO_3^{2-} \qquad\qquad K_2 = 10^4 \text{ M}^{-1}, \qquad (2.4)$$

$$H_2O \longrightarrow H^+ + OH^- \qquad\qquad K_w = 10^{-14} \text{ M}^2, \qquad (2.5)$$

where k_n and k_{-n} are the forwards and backwards rate coefficients respectively, and $K_n = \frac{k_n}{k_{-n}}$ are the equilibrium constants. The acidic carbonate equilibrium reactions are considered kinetically in the numerical model, but are neglected in the analytical model.

2.2.2. NUMERICAL METHOD

A numerical model was created in COMSOL Multiphysics, solving species transport and tertiary current distribution through the Nernst-Planck equation. Steady state solutions were determined using the MUMPS solver with geometrically scaled node spacing to improve resolution at the boundaries. Electrode geometry and operational parameters, were chosen to mimic the experimental setup of Verma et. al. [47]. The electrolyte carbonate equilibrium state was determined from experimentally reported pH and concentration.

2.2.3. ANALYTICAL SOLUTION

The main contribution of this work is an approximate analytical solution. This solution was determined by decoupling ionic species from CO_2, solving the reaction-diffusion equation for CO_2 along the CL. Ionic concentrations were averaged within the CL, whereas the CO_2 concentration was determined by solving the reaction-diffusion equation,

$$[CO_2] = [CO_2]_{DL} \frac{\cosh\left(M_T(1 - \frac{x}{L})\right)}{\cosh(M_T)}, \tag{2.6}$$

$$M_T = \sqrt{\frac{L^2 k}{D_{CO_2}^{eff}}}, \tag{2.7}$$

$$k = \epsilon k_1 [OH^-] + \frac{a}{2F} \frac{i_{0,CO2R}}{[CO_2]_{ref}} \exp\left(\frac{-\eta_{CO2R}}{b_{CO2R}}\right) \tag{2.8}$$

where $[CO_2]_{DL}$ is the CO_2 concentration at the GDL-CL boundary, M_T is the Thiele [43] modulus and k is the total volumetric CO_2 reaction rate, which is the sum of volumetric electrode reaction rate determined from the current density in (2.1) and chemical reaction rate (2.3).

By only considering average ionic concentrations we arrive at a simple mass balance equation, equating the boundary flux from the electrolyte channel with the total chemical reaction rate in the CL and, in the case of OH^-, electrode reaction rate. However, the nonlinear dependencies of OH^- on the Nernstian equilibrium potential and of ion concentrations on CO_2 solubility and thus $[CO_2]_{DL}$ led to an analytically intractable system of equations, so the ionic system was decoupled and solved approximately to then be recombined with the Thiele solution. A derivation and method of reproduction can be found in 2.7.2.

Parameter	Value	Unit	Ref.
α_{CO}	0.44	[-]	[15]
α_{H_2}	0.36	[-]	[15]
E^0_{CO}	-0.11	V	[34]
$E^0_{H_2}$	0	V	[34]
L	3.81×10^{-6}	m	[51]
a	3×10^7	m^{-1}	[42]
ϵ	0.5	[-]	
T	293.15	K	
p_{CO_2}	1	atm	
$w_{channel}$	1.5×10^{-3}	m	[53]
$L_{channel}$	0.02	m	[53]
$h_{channel}$	5×10^{-3}	m	[53]
q_{flow}	0.5	$ml\,min^{-1}$	[46]

2.3. RESULTS

The following analytical plots were generated using the analytical model and verified against further numerical simulations. Fig. 2.3 shows a comparison between the CO current densities predicted by the analytical approximation and the numerical and experimental results. Between -0.4 V and -0.8 V we see an exponential relationship between potential and current, indicating a kinetically (activation overpotential) limited regime governed predominantly by the Tafel equation. The flattening curve with more negative potential is indicative of the drop in aqueous CO_2 concentration, with the peak current density being attained when the parasitic chemical reaction (2.3) and CO_2 transfer limitations combine to outweigh increasing overpotential. At post-peak potentials, unhindered HER leads to a high ionic strength catholyte with poor solubility, which readily consumes CO_2 to reduce the pH.

The approximation is an excellent match for the numerical model, with small discrepancies arising only at -0.7 V and in the neighbourhood of the peak current density. These discrepancies are due to term neglections in the simplified homogeneous reactions used to predict pH in Eq. 2.57 and degradation of the approximation of carbonate concentration in Eq. 2.82 respectively. The latter error remains small for potentials less negative than the potential at peak current density but can increase at very negative potentials, as is observable in the -1.4 to -1.5 V vs RHE range in Fig. 2.3. The analytical solution begins to degrade for parameter combinations that allow ion concentrations large enough to necessitate inclusion of more detailed ionic effects, or for parameter combinations that allow large ion concentration gradients to develop within the CL, which prohibit the use of concentration averages in the model. The former can arise at potentials lower than -1.4 V vs RHE or with low electrolyte flow rate (<0.5 $ml\,min^{-1}$) and the latter can arise for large CL thicknesses (>100 μm) when paired with low electrolyte flow rates.

In Figure 2.4a we plot CO current density against CL thickness at multiple cathode potentials (coloured lines) and at the optimal potential (dashed black line): the thickness
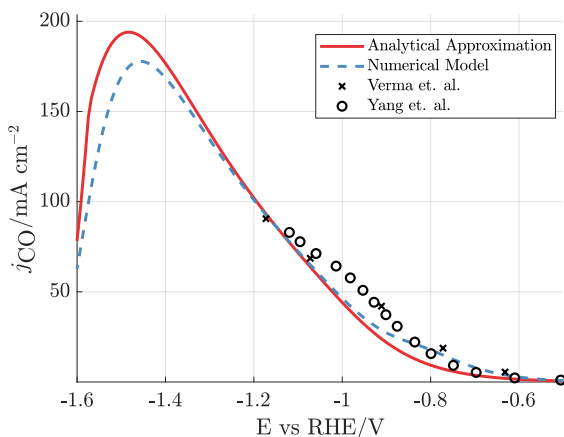
Figure 2.3: Numerical and analytical models compared to experimental data from Verma et. al. [47] for a KHCO$_3$ concentration of 1 M and flow rate of 0.5 ml min^{-1}. Here, j_{CO} is the geometric CO current density, derived by integrating the superficial current density i_{CO2R} across the CL and multiplying by the volumetric surface area, a. Electrolyte species concentrations were determined directly from experimentally reported pH rather than determined through the analytical model. An additional set of experimental data from Yang [60] is included, in which a similar experimental setup is used. More information can be found in 2.12
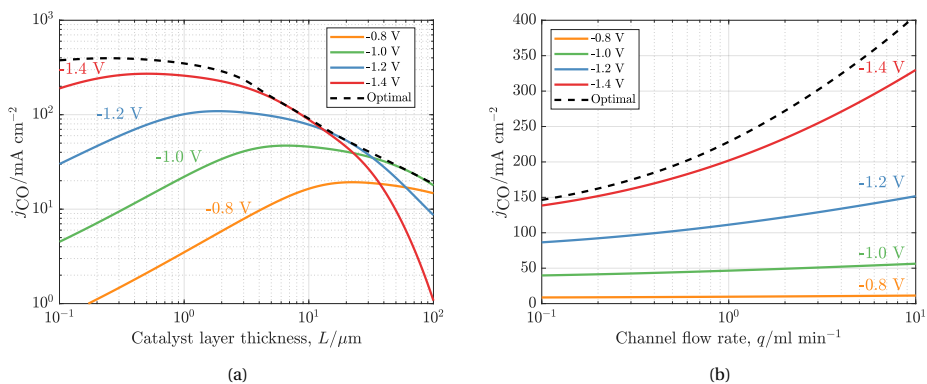
Figure 2.4: Analytical CO current density against CL length for fixed electrolyte flow rate 0.5 ml min^{-1} (a), and against electrolyte flow rate (b), with curves for different potentials ranging from -0.8 to -1.4 V vs RHE. Dashed black lines indicate the maximum current density predicted by the model for the chosen parameters. Note that for all addressed CL thicknesses there is a potential at which its performance exceeds all other thicknesses, and vice versa. Details of flow channel geometry are available in Table 1, with which one can convert to flow velocity or flow rate for a channel with different cross-sectional area.

dependent potential which achieves maximum CO current density. This optimal potential is also seen to be dependent on the electrolyte channel flow rate in Figure 2.4b, and in general is dependent on every parameter in Table 1. This optimum can be clearly seen to vary in Figure 2.4a as it intersects the other potential curves for different thicknesses. The specific value of the optimal potential is most easily extracted by applying a simple root

finding method to the data sets provided by the analytical approximation. We assume that the ohmic drop is small compared to the Tafel slope for the considered CL thicknesses so that mass transfer determines optimal performance [17]. Thicker CLs have more surface area available for reaction, but suffer from poorer mass transfer due to longer diffusion distances. A thick CL exhibits relatively high current densities at weak potentials but poor peak current density, as the mass transfer limitations begin to occur at lower current densities and are more severe. By contrast, a thin CL benefits from a shorter diffusion distance, meaning that aqueous CO_2 concentrations can remain relatively high at high current densities. As the Tafel slope of the CO2R reaction is lower than that of HER, this allows for much improved Faradaic efficiency for the same CO current density in a thinner CL, albeit at a more negative potential. The combined reduction in OH^- generation from HER and increase in CO2R overpotential lead to higher CO_2 utilisation and lower ionic strength compared to a thicker CL. This delays the onset of solubility and parasitic reaction limitations, allowing the thinner CLs in Fig. 2.4a to attain higher limiting CO densities.

Fig. 2.4b shows the impact of electrolyte flow rate on current density for a range of potentials. We reflect literature trends by utilising flow rate as an independent variable, but it is important to note that the electrolyte boundary conditions are also dependent on channel geometry. Nonetheless, Fig. 2.4b shows the importance of flow rate in attaining high current densities in regimes limited by salting out effects. The flow channel boundary mass transfer is improved at higher flow rates, facilitating faster removal of OH^- and carbonate while replenishing bicarbonate, all of which serve to decrease the pH in the CL. This improves CO_2 solubility and reduces parasitic reaction rate, increasing CO_2 concentration and current density. By contrast, increasing flow rate has only a small effect at -0.8 V and -1 V in Fig. 2.4b, as in both cases current density is limited by a small activation overpotential and neither mass transfer limitations nor ionic effects play a significant role.

(a) (b)
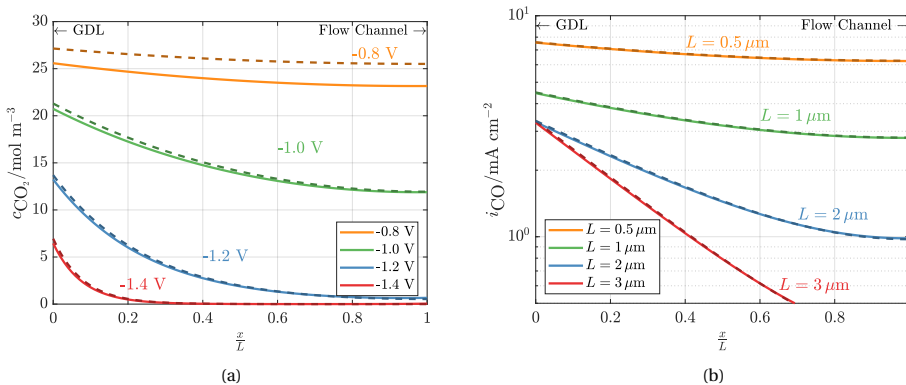
Figure 2.5: Analytical (dashed) and numerical (lined) concentration plots for CO_2 along the length of the CL at varying potentials (a), and local current density distributions at a geometric current density of 100 mA cm^{-2} for different CL thicknesses (b). The analytical prediction of CO_2 concentration variation within the CL is shown to be an excellent match with numerical results at large potentials and similarly for the analytic current density distribution at 100 mA cm^{-2}.

2

Fig. 2.5a further shows how closely the analytical approximation of CO_2 concentration matches the numerical concentration. The deviation at -0.8 V is due to the analytical assumption of zero CO_2 flux through the electrolyte boundary. This discrepancy consequently shows precisely how much CO_2 concentration is reduced through direct loss to the electrolyte channel and how this loss has a negligible effect at relevant potentials. However, this loss is positively correlated with electrolyte flow rate, so at potentials lower than -0.8 V an increase in flow rate can cause a large enough CO_2 loss to the channel to lead to a reduction in current density and CO_2 utilisation.

Due to the low variation of overpotential within the CL, the local superficial current density distribution follows the CO_2 concentration. Fig. 2.5b shows that for the same geometric current density, thinner CLs will have more uniform current density distributions, whereas thicker CLs will exhibit a much less uniform distribution, with the majority of the reaction taking place close to the GDL boundary.

The average chemical species concentrations in the CL are shown in 2.6a, where more negative potentials lead to increasing pH and carbonate concentration with a corresponding drop in CO_2 and bicarbonate concentration. For all potentials considered this way the equilibrium reaction (2.4) remains in equilibrium, while reaction (2.3) is forced out of equilibrium at high current densities by rapid depletion of bicarbonate. This causes the back reaction of (2.3) to be negligible and it becomes practical to view and analytically approximate the parasitic chemical reaction as a direct conversion of CO_2 to carbonate, consuming $2OH^-$, rather than a two-step process. Influent bicarbonate and CO_2 are both consumed increasingly rapidly as pH increases, producing increasing amounts of carbonate.

The latter effects are shown in Fig. 2.6b, where at large negative potentials up to 45% of CO_2 entering the CL is not reduced to CO. As determined earlier and shown in 2.5a, the loss of CO_2 to the electrolyte channel is negligible at these potentials, so this loss of CO_2 can be directly attributed to chemical reaction with OH^-. The corresponding increase in ionic strength leads to a large reduction in solubility. This solubility reduction is observable in Fig. 2.5a, as it is the primary cause of the reduction in CO_2 concentration at the GDL boundary, and at potentials more negative than -1.5 V in Fig. 2.3, where it is the cause of the fall in CO_2 current density as the system becomes entirely mass transfer limited. It is possible for solubility to be reduced to such a degree that even the carbonate concentration begins to peak and fall at further negative potentials, as less CO_2 is available for consumption. The analytical approximation degrades in this regime and underestimates the carbonate concentration, as evinced earlier in the current density discrepancy in Fig. 2.3 at -1.5 V. The CO_2 utilisation also reaches a minimum, despite continually increasing pH, as the decreasing Faradaic efficiency indicates that the HER is beginning to dominate. Due to the difference in Tafel slopes, at more negative potentials HER will never produce enough OH^- to consume CO_2 faster than the electrode, and CO_2 utilisation will converge to 100%, despite the FE converging to 0%. Although the FE prediction is a reasonable match to the experimental data at small potentials, the decrease at potentials lower than -1 V is not seen experimentally. This is most likely due to the suppression of HER at high pH [25], which is not included in the Tafel kinetics implemented in the model.
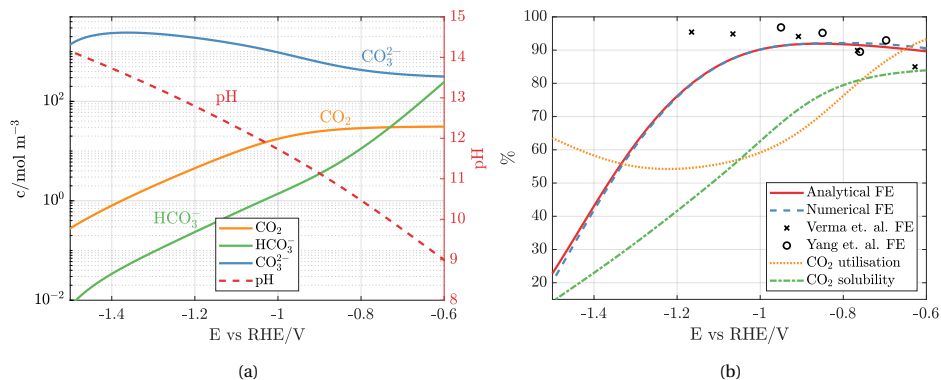
Figure 2.6: Analytical plots against cathode potential of Faradaic efficiency, defined as the percentage of electrons used to reduce CO_2 to CO, along with the Faradaic efficiencies corresponding to the experimental results in Fig. 2.3 (a), and analytical CL averaged aqueous concentrations as a function of potential(b). Additionally plotted in (a) are curves for CO_2 utilisation, defined as the percentage of CO_2 entering from the GDL that is converted to CO, and CO_2 solubility in the CL catholyte, expressed as a percentage of CO_2 solubility in the bulk flow channel electrolyte.

2.4. CONCLUSIONS

In this work we have developed an analytical approximation of CO_2 reduction in the cathodic CL. By assuming approximately homogeneous electrolyte potential in the CL and reducing the simplified mass transport of ions within the CL to a system of concentration averaged mass balance equations, we derived a simple system of equations that capture the effects of the chemical reaction of CO_2 with OH^-, the carbonate equilibrium reactions, the concentration dependent CO_2 electroreduction kinetics, and the CO_2 solubility reduction at high ionic strengths. The accuracy of the model was demonstrated through comparison to experimental and numerical results for CO current density and spatial CO_2 concentration variation respectively. The model was shown to correctly predict CL performance in both activation overpotential limited regimes and mass-transfer limited regimes, and transition smoothly between the two. The model predicts limiting current densities from mass-transfer and homogeneous reaction limitations, though it must be noted that these predictions may exceed attainable current densities in cells prone to liquid breakthrough, precipitation, or other stability issues, with additional limitations addressed in 2.11.

Transport and reaction interplay in the CL has been covered by a number of numerical studies, but with this work we demonstrated that this behaviour can be approximated analytically to a similar degree of complexity. This should motivate future numerical studies to focus either on including more detailed physics within the CL or expanding the scope to include more influence from the diffusion medium or electrolyte channel. For instance, we assume that the MPL remains entirely dry at all potentials, despite the adjacent CL being entirely flooded, and this lets the model predict high current densities that may not be possible for a physical cell to achieve without flooding.

We assumed simple kinetics for the heterogeneous reactions, and although this is still

common, the model of Weng et al. [52] utilises a more involved description for kinetic parameters and better captures the suppression of the HER at high pH. We expect that the inclusion of such an effect would better the agreement of the model with the Faradaic efficiencies reported in Fig. 2.6b. Similarly, the Smith group note that catalyst studies are often performed in conditions that are unrealistic for commercial use[5], such as weak electrolytes or low current densities, and as such modelling studies are forced to broadly extrapolate from kinetic data. Future endeavours to extract kinetic parameters from experimental data should also similarly account for this influence of local environment on activation energy.

Although it has been commonplace to restrict numerical studies to the through-plane dimension, we herein predict that the variation of electrolyte channel concentration boundary layers alone is sufficient reason to merit the inclusion of flow-wise dimension, such as in the work of Kas et al. [24]. Weber and coworkers have already demonstrated the positive impact of pH buffering electrolytes on the limiting current density[14] and we herein show that these improvements can be magnified by increasing flow rate. Increasing buffer strength will increase CO_2 utilisation and limiting current density, but the corresponding decrease in CO_2 solubility will lead to a decrease in current density unless counteracted with increased partial pressure, and higher ionic strengths could lead to earlier onset of precipitation events. It would be of great use to future numerical studies if experimental studies would report channel dimensions along with flow-rates, as the latter alone are insufficient to determine boundary layer profiles. Like other studies we predict significant carbonate formation in the CL, so further work should investigate the effect of the migration of this carbonate to the anode and how it could accumulate in a re-cycled electrolyte. Carbonate crossover is difficult to prevent, and research from the Chiu group has shown that the anion-exchange membranes exhibit a strong bias towards the transport of carbonate[26], due to its higher valence, and their resistances also increase as a consequence[55]. At high current densities we also predict an increase in electrolyte ionic strength, the effects of which are manifold. Most of these effects are neglected in this approximation and many other numerical studies, but the large effect of salting-out alone shows that, in agreement with the recommendations of Nesbitt and Smith [32], high ionic strength effects are imperative to include in future studies, particularly with regards to solubility and chemical activity. Ionic strength corrections are often entirely empirical or complicated in form, necessitating numerical approaches. If they are neglected then full numerical modelling is likely to be unnecessary because, as we have shown in this work, the system will likely be analytically approximable.

The versatility of the analytical model allowed us to perform parametric studies over large ranges of CL thicknesses and electrolyte channel flow rates. It was shown that minimising transport resistances in both the CL and the electrolyte channel is crucial in attaining optimal CO current densities. The benefit of shorter diffusion distances and increased Faradaic efficiencies in thin CLs was shown to outweigh the reduction in reactive surface area, yielding higher CO current densities than thicker CLs at more negative potentials. The benefit of increased flow rate was also shown, as catholyte regulation is governed by electrolyte boundary mass transfer and is essential in maintaining a low pH and ionic strength within the CL. We have also given context to these results, showing that such parameter recommendations are only valid in mass transfer limited regimes and can

be detrimental at less negative potentials. By providing a freely accessible spreadsheet containing the model we facilitate further independent analytical studies and hope to motivate further work in the development of practical analytical approximations for GDE design and optimisation for CO_2 reduction.

2.5. NUMERICAL MODEL

2.5.1. SCOPE & ASSUMPTIONS

The numerical results are determined using a numerical model of the catalyst layer (CL) in the cathode of a gas-diffusion electrode half-cell. The CL is situated between the gas diffusion layer (GDL) and a flowing electrolyte channel, with Ag catalyst particles and a porous matrix fully flooded with electrolyte.

The numerical model makes a number of assumptions, the applicability of which will be discussed in section 2.11.

2.5.2. GDL

The GDL is modelled through a well-defined stationary phase boundary at the edge of the CL domain. The gas supplied by the GDL is assumed to be pure CO_2 and neither impurities in supplied gas nor gas products are considered.

2.5.3. CL

The CL is assumed to be a uniformly microporous structure with uniformly distributed catalyst. The correction for diffusivity in the medium will be determined in this case using the Bruggeman relation [44], but this can be readily replaced with a more detailed relation or experimental results. The solid phase is again assumed to have negligible electronic resistance. The remaining volume is assumed to be fully flooded with stationary electrolyte. Variance in the plane parallel direction is assumed small, and is neglected. Electric double layer effects are not considered and the electrolyte within the CL is assumed to maintain electroneutrality. Transport within the CL is modeled using the Nernst-Planck equation, assuming species are dilute and all species remain in liquid phase: neither precipitates nor bubbles are included in the model. Ionic mobility is determined by the Einstein relation. Water content within the CL is assumed constant.

Electrode reactions are modeled using concentration dependent Tafel kinetics. CO_2 reduction and acidic hydrogen evolution are modeled with a first-order concentration dependence and alkaline hydrogen evolution with dependence only on the constant water concentration. Reduction potentials are corrected with the Nernst equation.

Chemical reactions are treated as kinetic equations, with the forward and backward reaction rates calculated individually for each of the reactions, including water self-ionisation. The formation of H_2CO_3 is assumed to be an intermediary step and is neglected.

Volumetric surface area can be correlated with average particle radius in a number of ways. Here we assume sphere packing, where the volumetric surface area of each sphere of radius r is given by $\frac{3}{r}$, and the resulting volumetric surface area of the CL is $\frac{3(1-\epsilon)}{r}$.

2.5.4. ELECTROLYTE CHANNEL

The flowing electrolyte is assumed to be in full equilibrium, independent of the flux of ions from the CL and is hence treated as constant along the flow channel. It is assumed that there are also no bubbles or precipitates entering the channel. Potentials are measured against a reversible hydrogen electrode (RHE), where we mimic experiments by measuring RHE against a virtual reference electrode placed upstream of the electrochemically active region. This electrode is assumed to be sufficiently far that the pH is that of the bulk electrolyte and it is unaffected by cell operation.

2.5.5. EQUATIONS: BULK

We will adopt the following superscript notation for dissolved species concentrations:

$$[CO_2] = c^0, \tag{2.9}$$

$$[OH^-] = c^1, \tag{2.10}$$

$$[CO_3^{2-}] = c^2, \tag{2.11}$$

$$[HCO_3^-] = c^3, \tag{2.12}$$

$$[H^+] = c^4, \tag{2.13}$$

$$[K^+] = c^5, \tag{2.14}$$

as subscripts are often commandeered in the governing equations. If a constant or variable is specific to an ionic species, the corresponding superscript will be used. Transport within the CL is governed by the Nernst-Planck equation:

$$N^i = -D^i \frac{\partial c^i}{\partial x} - \frac{D^i z^i F c^i}{RT} \frac{\partial \phi}{\partial x}, \tag{2.15}$$

$$\frac{\partial N^i}{\partial x} = R_E^i + R_C^i, \tag{2.16}$$

where diffusivity D^i is given by the Bruggeman correction $D^i = D_0^i \epsilon^{\frac{3}{2}}$, z^i is ionic charge, which is zero for CO_2, and R_E^i and R_C^i refer to the total volumetric electrode and chemical reaction rates for species respectively, all for species i.

The electrode reactions are:

$$2H^+ + 2e^- \longrightarrow H_2, \tag{2.17}$$

$$2H_2O + 2e^- \longrightarrow H_2 + 2OH^-, \tag{2.18}$$

$$CO_2 + H_2O + 2e^- \longrightarrow CO + 2OH^-, \tag{2.19}$$
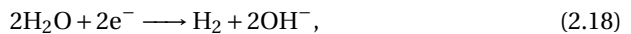
with current densities expressed using Butler-Volmer equations [51] in

$$i_A = -i_{0,A} \frac{c^4}{c^4_{\text{ref}}} \exp\left(\frac{-\eta_A}{b_A}\right), \tag{2.20}$$

$$i_B = -i_{0,B} \exp\left(\frac{-\eta_B}{b_B}\right), \tag{2.21}$$

$$i_C = -i_{0,C} \frac{c^0}{c^0_{\text{ref}}} \exp\left(\frac{-\eta_C}{b_C}\right), \tag{2.22}$$

$$\tag{2.23}$$

respectively, where subscripts A and B correspond to acidic and basic pathways for hydrogen evolution, and subscript C corresponds to CO_2 reduction. It is assumed in (2.20) that the Tafel step is not the rate determining step and the determining step is either the Volmer or Heyrovsky step, both of which are first order in H^+ concentration. In Eq. (2.21) the reaction modelled as concentration independent as it is assumed that the concentration of the governing species, water, does not vary. The activation overpotential for the electrode reactions are determined by reduction potential and Nernst correction by

$$\eta_k = \phi - E_{0,k} + \frac{RT}{F} \ln(c^1), \tag{2.24}$$

where $E_{0,k}$ is the equilibrium potential of reduction reaction k. The corresponding volumetric reaction rates are given by

$$R_E^i = \sum_k \frac{a s_k^i i_k}{n_k F}, \tag{2.25}$$

where s_k^i is the stoichiometric coefficient for species i in reaction k. Stoichiometric coefficients can be directly extracted from the reduction reaction expressions in Eqs. (2.17), (2.18), and (2.19), for example: $s_k^i = -2$ for $i = 4, k = A$ and $s_k^i = 2$ for $i = 1, k = C$.

The chemical reactions are

$$K_1 : CO_2 + OH^- \underset{k^1_{\leftarrow}}{\overset{k^1_{\rightarrow}}{\rightleftarrows}} HCO_3^-, \tag{2.26}$$

$$K_2 : HCO_3^- + OH^- \underset{k^2_{\leftarrow}}{\overset{k^2_{\rightarrow}}{\rightleftarrows}} H_2O + CO_3^{2-}, \tag{2.27}$$

$$K_3 : CO_2 + H_2O \underset{k^3_{\leftarrow}}{\overset{k^3_{\rightarrow}}{\rightleftarrows}} HCO_3^- + H^+, \tag{2.28}$$

$$K_4 : HCO_3^- \underset{k^4_{\leftarrow}}{\overset{k^4_{\rightarrow}}{\rightleftarrows}} CO_3^{2-} + H^+, \tag{2.29}$$

$$K_w : H_2O \underset{k^w_{\leftarrow}}{\overset{k^w_{\rightarrow}}{\rightleftarrows}} H^+ + OH^-, \tag{2.30}$$
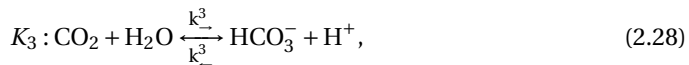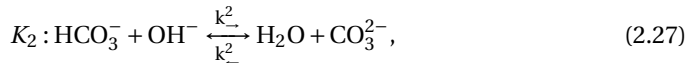
with total volumetric chemical reaction rate for each species given by

$$R_C^i = \epsilon \sum_n s_n^i \left(k_{\rightarrow}^n \prod_{s_n^j > 0}^j c^j - k_{\leftarrow}^n \prod_{s_n^j < 0}^j c^j \right). \tag{2.31}$$

The system is closed with the electroneutrality assumption:

$$\sum_i z^i c^i = 0. \tag{2.32}$$

2.5.6. EQUATIONS: BOUNDARY CONDITIONS

The electrolyte current is zero at the GDL boundary and potential is zero at the flow channel boundary. The GDL boundary is determined using Henry's Law to find the equilibrium concentration for dissolved CO_2. The Sechenov (salting out) effect [40] is incorporated into a corrected solubility (Henry) constant dependent on ion concentrations,

$$\mathcal{H} = \mathcal{H}_0 \prod_j e^{-h^j c^j}, \tag{2.33}$$

where h^j are the combined ion-specific and CO_2-specific constants for the Schumpe form of the solubility correction [50]. The CO_2 flux at the GDL boundary is then determined by the concentration drop from the corrected equilibrium concentration through

$$N^0 = K_{DL}(\mathcal{H}p^0 - c^0), \tag{2.34}$$

in which the concentration difference between equilibrium concentration from Henry's Law and the dissolved CO_2 concentration at the GDL boundary drives flux. GDL flux is heavily simplified by assuming a characteristic diffusive length scale based on average pore radius, $K_{DL} = \frac{D^0}{r}$. This length scale can be altered if more realistic diffusive length scales are determined from experimental results. There is no flux to the GDL for the other modelled species.

The species flux through the CL boundary with the electrolyte can be expressed in a number of ways depending on the flow profile. The general form remains the same:

$$N^i = K^i_{EL}(c^i - c^i_{EL}), \tag{2.35}$$

but if we assume that the geometry will lead to Poiseuille flow there are certain regimes we must address to determine K^i_{EL}.

- **Developing** flow profile, **developing** concentration profile

- *Developed* flow profile, **developing** concentration profile

- **Developing** flow profile, *developed* concentration profile

- *Developed* flow profile, *developed* concentration profile

Figure 2.7 shows the first two of these regimes, as well as the final boundary layer (BL) thickness used. fAs the Schmidt number, the ratio of viscous and molecular diffusion rates $\frac{v}{D}$, of the catholyte is high, we can safely discard the third regime, as the flow profile will always be developed before the concentration profile. In many flow channel configurations there will be an electrochemically inactive region before the catalyst, which is usually of sufficient length that the flow profile will be fully developed before contact with the catalyst. However, if there is no inactive region then within the hydrodynamic entrance length,

usually of the order of $L_{\text{entrance}} \approx 0.01 \text{Re} W_{\text{channel}}$ [54], we can use Reynolds-Sherwood-Schmidt mass transfer described in Ref. [51]. The Sherwood number Sh is the ratio of convective and diffusive mass transfer rates, $\text{Sh}^i = \frac{K_{\text{EL}}^i L_{\text{channel}}}{D^i}$, and is expressed here as a function of the Reynolds and Schmidt numbers,

$$\text{Sh}^i = 0.664 \text{Re}^{\frac{1}{2}} \text{Sc}^{\frac{1}{3}} = 0.664 \left(\frac{U L_{\text{channel}}}{\nu} \right)^{\frac{1}{2}} \left(\frac{\nu}{D^i} \right)^{\frac{1}{3}} \tag{2.36}$$

$$N^i = \frac{D^i}{L_{\text{channel}}} \text{Sh}^i (c^i - c_{\text{EL}}^i), \tag{2.37}$$

in the developing flow region. Once the flow has fully developed, we can use the Lévêque approximation [20, 30] of linearised Poiseuille flow to express the averaged boundary layer thickness along the channel length as

$$\delta^i = 1.607 \frac{3}{4} \sqrt[3]{\frac{W_{\text{channel}} D^i L_{\text{channel}}}{U}}, \tag{2.38}$$

and use

$$K_{\text{EL}}^i = \frac{D^i}{\delta^i}. \tag{2.39}$$

Once both the flow and concentration profiles are fully developed, we can use a Sherwood number for laminar flow between parallel plates in Eq. (2.37),

$$\text{Sh} = \frac{13}{35}, \tag{2.40}$$

determined from an analogous result for the Nusselt number in heat transfer[38]. In many cases, only the form of (2.38) is necessary, as the hydrodynamic entrance length often coincides with an electrochemically inactive region of the flow channel and the flow channel is often too short for the concentration boundary layer to fully develop. However, fully developed concentration profiles may occur in larger industrially relevant lengthscales, and if multiple regimes are present in the flow channel then we use an expression to correlate their respective boundary layer thicknesses through the equation [7]

$$\delta_{\text{eff}}^i = \left(\frac{1}{N} \sum_{n=1}^{N} (\delta_n^i)^{-2} \right)^{-\frac{1}{2}}, \tag{2.41}$$

where δ_n are the respective boundary layer thicknesses, normalised by N, the number of correlated thicknesses. This correlation chooses the thinnest boundary layer while accounting for comparable boundary layer thicknesses from the other regimes.

Boundary mass transfer coefficients will be henceforth denoted as K_{DL} for the diffusion layer and K_{EL}^i for species i where $K_{\text{EL}}^i = \frac{D^i}{\delta_{\text{eff}}^i}$ at the electrolyte flow channel boundary. This includes transport of CO_2 through the electrolyte boundary, both outward and, at higher current densities, inward fluxes.
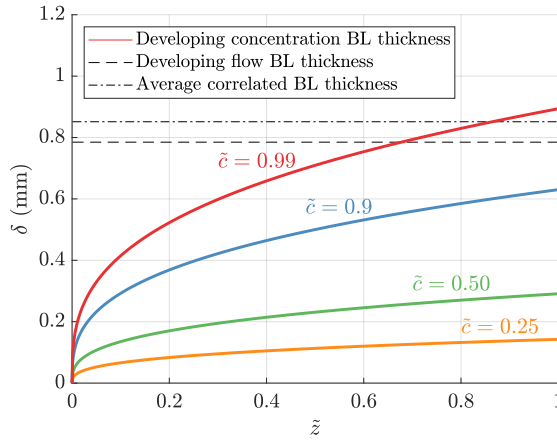
Figure 2.7: The respective boundary layer thicknesses for the Leveque approximation at varying concentration limits along the flow channel dimension, $\tilde{z} = \frac{z}{L_{\text{channel}}}$, and the respective single-valued boundary layer thicknesses of developing flow, developed parallel plate flow and the correlation of those two thicknesses with the average Leveque approximation thickness for $\tilde{c} = 0.99$ where $\tilde{c} = \frac{c^i}{c^i_{\text{EL}}}$.

2.6. ANALYTICAL MODEL

2.6.1. FURTHER ASSUMPTIONS

Further simplification is necessary to construct an analytically solvable problem. Firstly, as a high pH is expected within the CL, acidic phenomena are excluded. Specifically, this means we neglect both the H$^+$ dependent H$_2$ evolution pathway and the H$^+$ dependent chemical reaction pathways. Furthermore, the water self-ionisation is assumed to be fully equilibrated at all times, as opposed to kinetically modelled in (2.30).

One can demonstrate that acidic equilibrium reactions become negligible at high pH by comparing the reaction rate coefficients for the acidic and alkaline reactions. Considering that the equilibrium constants for the acidic pathways differ by a factor of K_w to the alkaline equilibrium constants, we know that the ratio between alkaline and acidic forward reaction rates will be the same as the ratio between the backward reaction rates, and can be determined from Eq. (2.31) to be

$$\frac{k^1_{\rightarrow} c^0 c^1}{k^3_{\rightarrow} c^0} \approx 10^{\text{pH}-9.22}, \tag{2.42}$$

which succinctly shows that the alkaline reaction will begin to dominate above pH = 9.22 in reaction K_1. Similar analysis can be done for the remaining reaction to get pH$_{K1}$ = 9.22 and pH$_{K2}$ = 6, for the respective reactions. This means that whenever we consider high current densities and their corresponding high pH values, we can reasonably neglect acidic reactions.

At low current densities where the pH remains closer to neutral, this argument no longer holds up. However, this is inconsequential, as the chemical equilibrium reactions are not a limiting factor in this regime.g The primary reason that the system begins to

chemically consume CO_2 is in an attempt to buffer the system, so it stands to reason that the only time this should occur is when the pH begins to rise.

It is assumed that there is zero flux of CO_2 at the electrolyte flow channel boundary. This includes the small amount of dissolved CO_2 that would diffuse in from the flowing electrolyte. We also assume a negligible variation in electrode and electrolyte potential along the length of the CL.

To simplify the chemical reaction terms we take averaged values of ion species within the CL, and consequently neglect the difference in flux at the electrolyte flow channel boundary due to boundary ion concentration differing from the the average ion concentration. We also assume that in the parasitic chemical consumption of CO_2, in reaction (2.26), the forward reaction rate heavily outweighs the backward reaction rate, with the latter being neglected entirely in the approximation.

2.7. Analytical method

2.7.1. CO_2

By assuming averaged ion concentrations and zero flux at the electrolyte boundary for CO_2 we can heavily simplify the CO_2 conservation in the Nernst-Planck equation (2.15), as the reaction rate is now uniformly dependent on CO_2 concentration:

$$-D^0 \frac{d^2 c^0}{dx^2} = \frac{a i_C^*}{2F} \frac{c^0}{c_{ref}^0} \exp\left(\frac{-\eta_C}{b_C}\right) + \epsilon k_{\rightarrow}^1 c^0 \langle c^1 \rangle, \tag{2.43}$$

whose solution is commonly expressed using the Thiele modulus, M, the ratio of reaction and diffusion rates. The resulting solution for the linear case is as follows:

$$c^0 = c_{DL}^0 \frac{\cosh\left(M(1 - \frac{x}{L})\right)}{\cosh(M)}, \tag{2.44}$$

$$M = \sqrt{\frac{L^2 k}{D^0}}, \tag{2.45}$$

$$k = \epsilon k_{\rightarrow}^1 \langle c^1 \rangle + \frac{a}{2F} \frac{i_C^*}{c_{ref}^0} \exp\left(\frac{-\eta_C}{b_C}\right). \tag{2.46}$$

This solution can also be integrated to find the average CO_2 concentration,

$$\langle c^0 \rangle = \frac{1}{L} \int_0^L c_{DL}^0 \frac{\cosh\left(M(1 - \frac{x}{L})\right)}{\cosh(M)} dx = c_{DL}^0 \frac{\tanh(M)}{M}. \tag{2.47}$$

As we have assumed CO_2 flux at the electrolyte boundary is zero, we can determine the value of c_{DL}^0 by equating the flux at the GDL boundary with the total reaction rate along the CL:

$$K_{DL}(\mathcal{H} p^0 - c_{DL}^0) = k L c_{DL}^0 \frac{\tanh(M)}{M} \implies c_{DL}^0 = \frac{\mathcal{H} p^0 K_{DL} M}{k L \tanh(M) + K_{DL} M}. \tag{2.48}$$

We now write

$$\mathcal{E}^{CL} = \frac{\tanh(M)}{M} \text{ and } \mathcal{E}^{DL} = \frac{K_{DL}}{k L} \tag{2.49}$$

as diffusive/reactive effectiveness factors for the CL and GDL respectively, and write the average CO_2 concentration as

$$\langle c^0 \rangle = \mathcal{H} p^0 \mathcal{E}^{tot}, \tag{2.50}$$

where

$$\frac{1}{\mathcal{E}^{tot}} = \frac{1}{\mathcal{E}^{CL}} + \frac{1}{\mathcal{E}^{DL}}. \tag{2.51}$$

2.7.2. IONS

We utilise the conservation equation in the CL to determine ionic concentrations. The continuity equation,

$$\int_{\delta\Omega} \mathbf{j}^i \cdot \mathbf{n} \, d\mathrm{A} = \mathrm{R}^i_{tot}, \tag{2.52}$$

simply states that in a steady state the species flux through the CL boundaries must be equal to the species source in the CL volume. To greatly simplify the problem, we assume that the ionic concentrations at the boundaries are sufficiently close to the average concentrations along the entire CL that an average concentration can be taken for all terms. As no ionic species escape into the GDL, we can integrate over (2.16) and reduce this to

$$K^i_{EL}(c^i - c^i_{EL}) = L(\mathrm{R}^i_C + \mathrm{R}^i_E). \tag{2.53}$$

We will be dropping the concentration average notation as all concentrations are averages from here on, including the c^0 determined in Eq. (2.47). Writing out Eq. (2.53) for HCO_3^- and inserting Eq. (2.31) ,

$$K^3_{EL}(c^3 - c^3_{EL}) = \epsilon L(k^1_{\rightarrow} c^0 c^1 - k^1_{\leftarrow} c^3 - k^2_{\rightarrow} c^1 c^3 + k^2_{\leftarrow} c^2), \tag{2.54}$$

and similarly for OH^- with the term from (2.25),

$$K^1_{EL}(c^1 - c^1_{EL}) = \epsilon L(-k^1_{\rightarrow} c^0 c^1 + k^1_{\leftarrow} c^3 - k^2_{\leftarrow} c^1 c^3 + k^2_{\leftarrow} c^2) + L\mathrm{R}^1_E. \tag{2.55}$$

We can subtract these equations to eliminate the CO_3^{2-} buffer terms and get

$$K^1_{EL}(c^1 - c^1_{EL}) - K^3_{EL}(c^3 - c^3_{EL}) = 2\epsilon L(-k^1_{\rightarrow} c^0 c^1 + k^1_{\leftarrow} c^3) + L\mathrm{R}^1_E, \tag{2.56}$$

and rearrange to make OH^- concentration the subject:

$$c^1 = \frac{K^1_{EL} c^1_{EL} + K^3_{EL}(c^3 - c^3_{EL}) + \epsilon L k^1_{\leftarrow} c^3 + L\mathrm{R}^1_E}{K^1_{EL} + 2\epsilon L k^1_{\rightarrow} c^0}. \tag{2.57}$$

We have already mentioned that we expect HCO_3^- to be depleted at high current densities. Due to this we expect its contribution to salting-out and the parasitic reaction (2.26) to be small, and will now be neglected. Its boundary flux contribution remains important, but unlike other species it is predominantly inward flux whose magnitude tends towards and is bounded above by $K^3_{EL} c^3_{EL}$. Due to this, we only need to approximate the transition between high HCO_3^- concentration at low current density and low HCO_3^- concentration at high current density, as we know that before this transition $c^1 \approx c^1_{EL}$ and afterwards

$K^3_{\text{EL}}(c^3 - c^3_{\text{EL}}) \approx -K^3_{\text{EL}}c^3_{\text{EL}}$. As the HCO_3^- depletion is caused by reaction with OH^-, we can approximate

$$-K^3_{\text{EL}}(c^3 - c^3_{\text{EL}}) \approx N^3_{\text{EL}}, \quad \text{where} \quad \frac{1}{N^3_{\text{EL}}} = \frac{1}{LR^1_{\text{E}}} + \frac{1}{K^3_{\text{EL}}c^3_{\text{EL}}}, \tag{2.58}$$

which becomes small at low current densities and tends to $K^3_{\text{EL}}c^3_{\text{EL}}$ at high current densities. This approximation is however not entirely sufficient as it neglects the possibility for outward flux of HCO_3^-, which is present at very low current densities due to excess CO_2 from the GDL pushing the K_1 chemical reaction forward without a corresponding effect from OH^- increase in the K_2 reaction that we see at high current densities. To this end we insert (2.58) into the OH^- conservation equation (2.57) to form

$$c^1 \approx c^1_{\text{EL}} + \frac{K^1_{\text{EL}}c^1_{\text{EL}} - N^3_{\text{EL}} + LR^1_{\text{E}}}{K^1_{\text{EL}} + 2\epsilon L k^1_\to c^0}, \tag{2.59}$$

where we have neglected the HCO_3^- back reaction and appended the electrolyte OH^- concentration instead to account for the initial equilibrium state.

Approximating CO_3^{2-} concentration is trickier, as it is heavily linked with the non-linear salting-out effect. However, we can still form an expression based on mass balance,

$$K^2_{\text{EL}}(c^2 - c^2_{\text{EL}}) = \epsilon L(k^2_\to c^1 c^3 - k^2_\leftarrow c^2), \tag{2.60}$$

and again combine with the HCO_3^- conservation equation to get

$$K^2_{\text{EL}}(c^2 - c^2_{\text{EL}}) + K^3_{\text{EL}}(c^3 - c^3_{\text{EL}}) = \epsilon L(k^1_\to c^0 c^1 - k^1_\leftarrow c^3). \tag{2.61}$$

In this case however, the CO_3^{2-} concentration is only relevant at high current density when the salting-out effect becomes large. This means that we simplify this expression assuming high current density and thus depleted HCO_3^-, and rearrange to get

$$c^2 = \frac{K^3_{\text{EL}}c^3_{\text{EL}} + K^2_{\text{EL}}c^2_{\text{EL}} + \epsilon L k^1_\to c^0 c^1}{K^2_{\text{EL}}}. \tag{2.62}$$

Although we know c^1 in terms of c^0, c^0 is also implicitly a function of c^2 through the salting-out effect, leading to an equation involving the Lambert-W function. This will be solved in the following section.

2.7.3. SALTING-OUT

At low current densities the effect of salting-out is small, and at high current densities the H^+ and HCO_3^- ions are heavily depleted, so we neglect their contributions entirely. We also utilise the electroneutrality condition to determine that $c^5 = c^1 + 2c^2$, to get

$$\mathscr{H} = \mathscr{H}_0 \exp\left(-h^1 c^1 - h^2 c^2 - (c^1 + 2c^2)h^5\right), \tag{2.63}$$

where h^i are the CO_2-ion salting-out constants for OH^-, CO_3^{2-} and K^+ respectively.

2.8. STEP-BY-STEP GUIDE

2.8.1. SOLVE WITHOUT EQUILIBRIUM REACTIONS

As it is infeasible to immediately solve for CO_2 including all the effects described so far, we instead determine the CO_2 profile for a simple system neglecting equilibrium reactions, ionic effects, Nernst correction and CO_2 loss into the electrolyte channel. We will however, include the correction for mass transport limitations at the DL boundary. The later effects will then be approximated using the solutions to this simplified system, denoted with a subscript 0, which has been highlighted in blue to distinguish the solution iterations steps from the superscripts. The previous solution can be extended to

$$\eta_C = \Phi - E_{0,C}, \tag{2.64}$$

$$k_0 = \frac{a}{2F} \frac{i_C^*}{c_{ref}^0} \exp\left(-\frac{\eta_C}{b_C}\right), \tag{2.65}$$

$$M_0 = \sqrt{\frac{k_0 L^2}{D^0}}, \tag{2.66}$$

$$c_0^0 = \mathcal{H}_0 p^0 \frac{K_{DL}^0 \tanh(M_0)}{K_{DL}^0 M_0 + k_0 L \tanh(M_0)} = \mathcal{H}_0 p^0 \mathcal{E}_0^{tot}. \tag{2.67}$$

where

$$\frac{1}{\mathcal{E}_0^{tot}} = \frac{1}{\mathcal{E}_0^{DL}} + \frac{1}{\mathcal{E}_0^{CL}}, \tag{2.68}$$

and

$$\mathcal{E}_0^{CL} = \frac{\tanh(M_0)}{M_0} \text{ and } \mathcal{E}_0^{DL} = \frac{K_{DL}}{k_0 L}. \tag{2.69}$$

2.8.2. ESTIMATING OH^- CONCENTRATION

With an approximation for average CO_2 concentration, we can now determine the OH^- production from CO_2 reduction, combined with hydrogen evolution,

$$R_{E,0}^1 = R_{CO,0}^1 + R_{H_2}^1, \tag{2.70}$$

where

$$R_{CO,0}^1 = 2k_0 c_0^0, \tag{2.71}$$

and

$$R_{H_2}^1 = \frac{ai_B^*}{F} \exp\left(-\frac{\eta_B}{b_B}\right), \tag{2.72}$$

and the HCO_3^- flux approximation

$$\frac{1}{N_{EL,0}^3} = \frac{1}{LR_{E,0}^1} + \frac{1}{K_{EL}^3 c_{EL}^3} \tag{2.73}$$

we can estimate the average OH^- concentration with

$$c^1 = c_{EL}^1 + \frac{K_{EL}^1 c_{EL}^1 - N_{EL,0}^3 + LR_{E,0}^1}{K_{EL}^1 + 2\epsilon L k_{\rightarrow}^1 c_0^0}. \tag{2.74}$$

2.8.3. ESTIMATING CO_3^{2-} CONCENTRATION

First, we can update the previous CO_2 concentration with the new OH^- to account for parasitic loss of CO_2 to the equilibrium reactions:

$$k_1 = k_0 + \epsilon k_{\rightarrow}^1 c^1, \tag{2.75}$$

$$M_1 = \sqrt{\frac{k_1 L^2}{D^0}}, \tag{2.76}$$

$$c_1^0 = \mathcal{H}_0 p^0 \frac{K_{DL}^0 \tanh(M_1)}{K_{DL}^0 M_1 + k_1 L \tanh(M_1)} = \mathcal{H}_0 p^0 \mathcal{E}_1^{tot}, \tag{2.77}$$

$$R_{CO,1}^1 = 2k_0 c_1^0, \tag{2.78}$$

where we increment the subscripts (highlighted in blue) to indicate a subsequent iteration of a variable. Note that k_0 in the last line is not incremented, but the c_1^0 is. Keeping these variables separate instead of collapsing them into one step is useful as it allows us to view the individual magnitude of each subsequent step on their values. Solving for the CO_3^{2-} concentration is more complicated so we will split up the relevant terms in preparation for input into the Lambert-W function:

$$A = \frac{2K_{EL}^2 c_{EL}^2 + K_{EL}^3 c_{EL}^3 + K_{EL}^1 c_{EL}^1 + LR_{H_2}^1 - K_{EL}^1 c^1}{2K_{EL}^2}, \tag{2.79}$$

$$B = \frac{LR_{CO,1}^1}{2K_{EL}^2} \exp\big(-c^1(h_{OH^-} + h_{K^+})\big), \tag{2.80}$$

$$C = h_{CO_3^{2-}} + 2h_{K^+}. \tag{2.81}$$

We now solve for CO_3^{2-} concentration:

$$c^2 = A + \frac{1}{C} \mathcal{W}(BCe^{-AC}) \approx A + \frac{1}{C} \ln\left(1 + \frac{BCe^{-AC}}{1 + \ln\sqrt{1 + BCe^{-AC}}}\right), \tag{2.82}$$

and determine the corresponding chemical reaction and salting-out corrected CO_2 concentration:

$$c_2^0 = \mathcal{E}_1^{tot} \mathcal{H}_0 p^0 \exp\left(-c^1 h_{OH^-} - c^2 h_{CO_3^{2-}} - (c^1 + 2c^2) h_{K^+}\right). \tag{2.83}$$

In Eq. (2.82) we have used one of the many analytical approximations of the positive-real domain of the Lambert-W function [23]. The error is small for small arguments ($< 2.5\%$) and in this case the argument remains small (< 1) for most current densities and only usually exceeds unity in the neighbourhood of the peak current density.

2.8.4. OPTIONAL HIGHER PRECISION

In the close neighbourhood of the limiting current density of a given geometry, the error of the Lambert-W approximation may increase in (2.82), especially when compounded with small discrepancies due to the approximations used to determine OH^- concentration. In such cases it is possible for the model to predict an erroneous negative CO_3^{2-} concentration and an overestimation of performance. These cases only arise in particularly effective

or ineffective electrodes and for general use the above method will suffice. However, if negative CO_3^{2-} concentrations do arise, two further steps can be taken to restore accuracy:

- Inspect the predicted CO_3^{2-} concentration and forbid negative values

- Introduce an additional step to account for any CO_3^{2-} corrections due to the previous step

In practical terms, this means rewriting (2.82) as

$$c_0^2 = A_0 + \frac{1}{C}\mathscr{W}(B_0 C e^{-A_0 C}) \approx \max\left\{0, A_0 + \frac{1}{C}\ln\left(1 + \frac{B_0 C e^{-A_0 C}}{1 + \ln\sqrt{1 + B_0 C e^{-A_0 C}}}\right)\right\}, \quad (2.84)$$

and after determining the corresponding CO_2 concentration as c_2^0, proceed to recalculate OH^- using the new value in (2.74)

$$c_1^1 = c_{EL}^1 + \frac{K_{EL}^1 c_{EL}^1 - N_{EL,1}^3 + LR_{E,1}^1}{K_{EL}^1 + 2\epsilon L k_\rightarrow^1 c_2^0}, \quad (2.85)$$

and repeat steps (2.79)-(2.83) again, utilising the new CO_2 and OH^- concentrations to develop a new CO_3^{2-} and final CO_2 value.

2.9. DERIVED VALUES & PLOTTING

2.9.1. POTENTIAL

From here on, an unsubscripted variable is used to represent the final value attained from the previous section. As the Nernst correction for electrode reaction potential is not included in the above, we similarly decouple it and add it in later. When plotting curves against potential, one need only make a change of variable from

$$\Phi \rightarrow \Phi - \frac{RT}{F}\ln\left(\frac{c^1}{c_{EL}^1}\right). \quad (2.86)$$

Current densities of hydrogen evolution and CO_2 reduction can be calculated by inserting this corrected potential along with the above approximations into

$$i_B = i_B^* \exp\left(-\frac{\eta_B}{b_B}\right), \quad (2.87)$$

$$i_C = \frac{c^0 i_C^*}{c_{ref}^0} \exp\left(-\frac{\eta_C}{b_C}\right), \quad (2.88)$$

per absolute surface area or multiplying by aL for outer electrode surface area. We can also now form expressions for products, as electrode reaction rates for CO and H_2 are given by

$$R_{CO} = \frac{a}{2F} i_C, \quad (2.89)$$

$$R_{H_2} = \frac{a}{2F} i_B. \quad (2.90)$$

2.9.2. EFFECTIVENESS

Some measures can be derived for cathode effectiveness. The Faradaic efficiency can similarly be determined by

$$\text{FE (\%)}_{\text{CO}} = \frac{R_{\text{CO}}}{R_{\text{CO}} + R_{\text{H}_2}} = \frac{1}{1 + \frac{i_B^* c_{\text{ref}}^0}{i_C^* c^0} \exp\left(\frac{\eta_C}{b_C} - \frac{\eta_B}{b_B}\right)}. \tag{2.91}$$

As we only consider two products, product selectivity follows directly from Faradaic efficiency. We can also write CO_2 utilisation as

$$\text{Util.\%} = \frac{k_0}{k}. \tag{2.92}$$

2.9.3. ENERGY EFFICIENCY

It is common to define an energy efficiency as follows

$$\text{EE(\%)} = \text{VE} \times \text{FE}, \tag{2.93}$$

where FE is faradaic efficiency and

$$\text{VE} = \frac{V_{\text{equilibrium}}}{V_{\text{cell}}}, \tag{2.94}$$

the voltage efficiency defined as the ratio of equilibrium potential to cell potential. This is sufficient for a full-cell, but is not unique for a half-cell as the ratio must still depend on a reference potential. To clarify, in a full cell one attains

$$\text{VE} = \frac{(V_{\text{eq}}^a - V_{\text{ref}}) - (V_{\text{eq}}^c - V_{\text{ref}})}{(V^a - V_{\text{ref}}) - (V^c - V_{\text{ref}})}, \tag{2.95}$$

and the reference potentials all cancel, whereas in a half-cell we only have

$$\text{VE} = \frac{V_{\text{eq}}^c - V_{\text{ref}}}{V^c - V_{\text{ref}}}, \tag{2.96}$$

and now the choice of reference electrode affects the voltage efficiency, and with no non-arbitrary choice, Eq. 2.94 must suffice. Nevertheless, the results are not without relevance and are included in Figure 2.8

2.10. EXAMPLE PLOTS
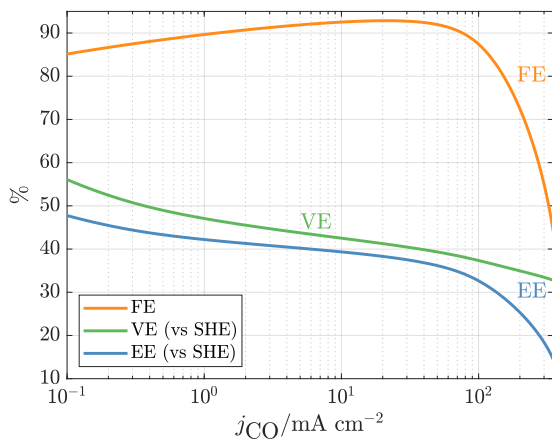
Figure 2.8: FE, VE, and their product EE vs SHE against current density for 0.5 M KHCO$_3$ at a flow rate of 5 ml min^{-1}. Energy efficiency is low due to low voltage efficiency at all current densities, but the variation is primarily due to change in Faradaic efficiency.
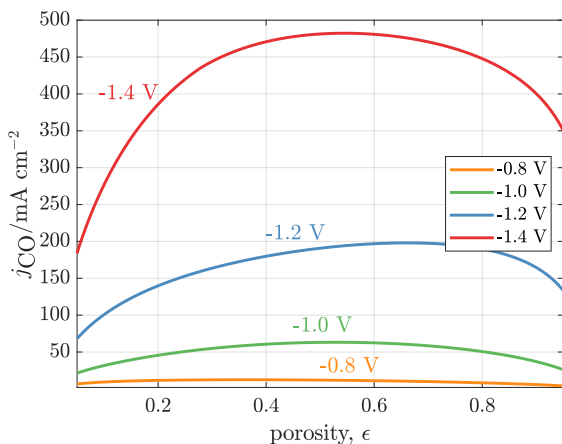
Figure 2.9: Effect of porosity on current density across a range of potentials for 0.5 M KHCO$_3$ at a flow rate of 5 ml min^{-1}. At less negative potentials, volumetric surface area is more valuable than improved transport, so lower porosity is favoured. At more negative potentials, the process is limited by transport so increased porosity yields higher current densities as a result of better transport. At extreme potentials the balance shifts back towards 0.5 slightly, as the consumption of CO_2 is more heavily contested by high OH^- concentrations, and increased volumetric surface area improves CO_2 utilisation.

2.11. LIMITATIONS

2.11.1. ELECTROLYTE

By only considering a 1D domain, we neglect variation in the electrolyte along the flow channel. It is expected that weak electrolytes with slow flow rates in long channels would experience large variations in ionic content, with a large corresponding drop in current density downstream. This variation could potentially become more of an issue when precipitation and flooding are included, as conditions necessary to prevent them will vary along the flow channel.

Similarly, increasing the flow rate has no consequence in the model: that is to say, the loss of dissolved CO_2 and other costs of maintaining a high flow rate are neglected in the analytical model and as such the model should not be used to investigate extreme flow rates.

2.11.2. ACTIVITY CORRECTIONS

The equilibrium constants used are valid only for ionic strengths < 0.7M, and although this assumption can be valid for particularly weak electrolytes such as the 0.5M $KHCO_3$ used here, it is invalid within the catalyst layer for any appreciable current density due to the large carbonate generation. To model such behaviour would require activity corrections for both water and carbonate equilibria, which would also cause a correction to pH and all of the associated electrode potentials and reaction terms.

Furthermore, the depletion of bicarbonate within the catalyst layer leads to parasitic reaction (2.26) being so far out of equilibrium that it is modelled kinetically. Although activity corrections are available for equilibrium constants, kinetic rate constants for carbonate equilibria are measured primarily in seawater and are only available at relatively low ionic strength and pH. Although water activity corrections are expected to alleviate a number of these problems, it is infeasible to include such corrections in any concise analytical approximation as methods of activity correction are empirical and related primarily to ionic strength, which requires all species concentrations to be known in advance. Furthermore, such activity corrections are still often only valid over a small range of ionic strengths and will likely be insufficient at high current densities where the catholyte becomes highly ionic.

2.11.3. ELECTRODE REACTION

The kinetics of both electrode reactions are heavily simplified. The most important source of error, and often confusion in literature, is the alkaline nature of the electrode reactions. It is common for the alkaline and acidic/neutral forms of the reactions to be erroneously used interchangeably, leading to errors regarding the equilibrium potential of the alkaline CO2ER and the pH dependence of the alkaline HER.

2.11.4. DIFFUSION MEDIUM

While it is not uncommon for the CL to become flooded at higher current densities, the actual true value of the liquid phase saturation across the GDL may be more complicated. Firstly, due to inhomogeneities in the CL it is possible that the medium will exhibit a residual non-wetting phase saturation, meaning that some portion of gas phase pathways

may survive maximal flooding and contribute positively to CO_2 transport. By contrast however, we assume an entirely dry MPL and GDL, which may not be the case in situations in which the CL is flooded. Higher liquid saturation in these layers can reduce permeability and inhibit CO_2 transport to the CL.

Similarly, the model does not account for variations in CO_2 transport in the diffusion medium, for both the in and through plane directions. To account for both this and the DL saturation, one could tune the K_{DL} coefficient to an effective value more suited to their level of flooding and CO_2 depletion.

2.12. PARAMETERS

Electrolyte concentrations are calculated using a rudimentary solver, contained in the attached spreadsheet. For high ionic strengths it is recommended to use more detailed solvers or experimental reports.

2.12.1. ADDITIONAL EXPERIMENTAL COMPARISON

The experimental results of Yang et. al. [60] are included in Figures 2.3 and 2.6b. It should be noted that the experimental conditions differ from those of Verma et. al. [47] by the inclusion of a proton exchange membrane, a thinner CL (300 nm), and a higher flow rate (5 ml min^{-1}). The thin CL, as shown in Fig. 2.4a, should lead to lower current densities at small cathode potentials but higher current densities at larger negative potentials. Similarly, Fig. 2.4b predicts that increasing flow rate will have little impact on current density at small potentials. In alignment with this, the Yang et. al. results predict lower current densities at below -0.8 V but begin to overtake the Verma et. al. current densities at more negative potentials. This similarly leads to a higher Faradaic efficiency in the Yang et. al. results, as CO_2 concentration can remain high throughout the entirety of the thin CL.

2

Parameter	Value	Unit	Reference
Diffusion			
D_{CO_2}	1.91×10^{-9}	m^2/s	[34]
$D_{HCO_3^-}$	0.923×10^{-9}	m^2/s	[34]
$D_{CO_3^{2-}}$	1.18×10^{-9}	m^2/s	[34]
D_{OH^-}	5.293×10^{-9}	m^2/s	[34]
D_{H^+}	9.311×10^{-9}	m^2/s	[34]
D_K	1.96×10^{-9}	m^2/s	[34]
D_{CO}	2.03×10^{-9}	m^2/s	[34]
D_{H_2}	4.5×10^{-9}	m^2/s	[34]
Electrode reaction			
$i_{0,CO}$	2.355×10^{-5}	A/m^2	[15]
i_{0,H_2}^A	1.16×10^{-5}	A/m^2	[15]
i_{0,H_2}^B	4.268×10^{-11}	A/m^2	[15]
α_{CO}	0.44	-	[15]
$\alpha_{H_2}^A$	0.36	-	[15]
$\alpha_{H_2}^B$	0.27	-	[15]
E_{CO}^0	-0.11	V	[34]
$E_{H_2}^0$	0	V	[34]
Chemical reaction			
K_1	4.266×10^5	m^3/mol	[39]
K_2	4.786	m^3/mol	[39]
K_w	1×10^{-8}	m^6/mol^2	[4]
$k_{\rightarrow}^1$	2.23	$m^3/(s\ mol)$	[39]
$k_{\leftarrow}^1$	4.5×10^{-5}	$1/s$	[39]
$k_{\rightarrow}^2$	6×10^6	$m^3/(s\ mol)$	[39]
$k_{\leftarrow}^2$	6×10^5	$1/s$	[39]
$k_{\rightarrow}^3$	0.0371	$1/s$	[39]
$k_{\leftarrow}^3$	86.91	$m^3/(s\ mol)$	[39]
$k_{\rightarrow}^4$	59.44	$1/s$	[39]
$k_{\leftarrow}^4$	1.24×10^9	$m^3/(s\ mol)$	[39]
Electrode geometry			
L	3.81×10^{-6}	m	[51]
r	5×10^{-8}	m	[42]
a	3×10^7	$1/m$	[42]
ϵ	0.5	-	-

2

Parameter	Value	Unit	Reference
Operation conditions			
T	293.15	K	-
p_{CO_2}	1	atm	-
Channel Geometry			
$w_{channel}$	1.5×10^{-3}	m	[53]
$L_{channel}$	0.02	m	[53]
$h_{channel}$	5×10^{-3}	m	[53]
q_{flow}	0.5	ml/min	[46]
Concentrations			
c_{EL}^0	13.8	mol/m^3	-
c_{EL}^1	1.42×10^{-3}	mol/m^3	-
c_{EL}^2	13.8	mol/m^3	-
c_{EL}^3	972	mol/m^3	-
$c_{electrolyte}$	1000	mol/m^3	-
Salting-out			
h^1	6.67×10^{-5}	m^3/mol	[50]
h^2	1.25×10^{-4}	m^3/mol	[50]
h^3	7.95×10^{-5}	m^3/mol	[50]
h^5	7.5×10^{-5}	m^3/mol	[50]

BIBLIOGRAPHY

[1] Arun S. Agarwal et al. "The Electrochemical Reduction of Carbon Dioxide to Formate/Formic Acid: Engineering and Economic Feasibility". In: *ChemSusChem* 4.9 (2011), pp. 1301–1310.

[2] Enrico Andreoli. "CO_2-to-ethylene electroreduction gets a boost". In: *Nature Catalysis* 4.1 (2021), pp. 8–9. ISSN: 2520-1158.

[3] Svetlana van Bavel et al. "Integrating CO_2 Electrolysis into the Gas-to-Liquids–Power-to-Liquids Process". In: *ACS Energy Letters* 5.8 (2020), pp. 2597–2601.

[4] John D Bernal and Ralph H Fowler. "A theory of water and ionic solution, with particular reference to hydrogen and hydroxyl ions". In: *The Journal of Chemical Physics* 1.8 (1933), pp. 515–548.

[5] Thomas Burdyny and Wilson A. Smith. "CO_2 reduction on gas-diffusion electrodes and why catalytic performance must be assessed at commercially-relevant conditions". In: *Energy Environ. Sci.* 12 (5 2019), pp. 1442–1453.

[6] Yikai Chen, Nathan S. Lewis, and Chengxiang Xiang. "Modeling the Performance of A Flow-Through Gas Diffusion Electrode for Electrochemical Reduction of CO or CO_2". In: *Journal of The Electrochemical Society* 167.11 (2020), p. 114503.

[7] S. W. Churchill and R. Usagi. "A general expression for the correlation of rates of transfer and other phenomena". In: *AIChE Journal* 18.6 (1972), pp. 1121–1128.

[8] Charles Delacourt, Paul L. Ridgway, and John Newman. "Mathematical Modeling of CO_2 Reduction to CO in Aqueous Electrolytes". In: *Journal of The Electrochemical Society* 157.12 (2010), B1902.

[9] Nicolas Dubouis and Alexis Grimaud. "The hydrogen evolution reaction: from material to interfacial descriptors". In: *Chem. Sci.* 10 (40 2019), pp. 9165–9181.

[10] S. Erbach et al. "CO_2 Enrichment in Anode Loop and Correlation with CO Poisoning of Low Pt Anodes in PEM Fuel Cells". In: *Fuel Cells* 18.5 (2018), pp. 613–618.

[11] M. Gattrell, N. Gupta, and A. Co. "Electrochemical reduction of CO_2 to hydrocarbons to store renewable electrical energy and upgrade biogas". In: *Energy Conversion and Management* 48.4 (2007), pp. 1255–1265. ISSN: 0196-8904.

[12] Akansha Goyal et al. "Competition between CO_2 Reduction and Hydrogen Evolution on a Gold Electrode under Well-Defined Mass Transport Conditions". In: *Journal of the American Chemical Society* 142.9 (2020), pp. 4154–4161.

[13] Akansha Goyal et al. "Competition between CO_2 Reduction and Hydrogen Evolution on a Gold Electrode under Well-Defined Mass Transport Conditions". In: *Journal of the American Chemical Society* 142.9 (2020), pp. 4154–4161.

2

[14] Hiroshi Hashiba et al. "Effects of Electrolyte Buffer Capacity on Surface Reactant Species and the Reaction Rate of CO_2 in Electrochemical CO_2 Reduction". In: *The Journal of Physical Chemistry C* 122.7 (2018), pp. 3719–3726.

[15] Toru Hatsukade et al. "Insights into the electrocatalytic reduction of CO_2 on metallic silver surfaces". In: *Phys. Chem. Chem. Phys.* 16 (27 2014), pp. 13814–13819.

[16] Tatsuya Hattori et al. "Porosity and Pt content in the catalyst layer of PEMFC: Effects on diffusion and polarization characteristics". In: *International Journal of Electrochemical Science* 5 (Dec. 2010), pp. 2221–2229.

[17] J. W. Haverkort. "A theoretical analysis of the optimal electrode thickness and porosity". In: *Electrochimica Acta* 295 (2019), pp. 846–860. ISSN: 0013-4686.

[18] Simelys Hernández et al. "Syngas production from electrochemical reduction of CO_2: current status and prospective implementation". In: *Green Chem.* 19 (10 2017), pp. 2326–2346.

[19] Juan Herranz et al. "Co-electrolysis of CO_2 and H_2O: From electrode reactions to cell-level development". In: *Current Opinion in Electrochemistry* 23 (2020), pp. 89–95. ISSN: 2451-9103.

[20] E. Holzbecher and Weierstrass. "Numerical Solutions for the Lévêque Problem of Boundary Layer Mass or Heat Flux". In: *COMSOL Conference 2008 Hannover* (2008).

[21] Y. Hori. "Electrochemical CO_2 Reduction on Metal Electrodes". In: *Modern Aspects of Electrochemistry* (2008), pp. 89–189.

[22] Yoshio Hori et al. "Electrochemical Reduction of CO at a Copper Electrode". In: *The Journal of Physical Chemistry B* 101.36 (1997), pp. 7075–7081.

[23] Roberto Iacono and John Boyd. "New approximations to the principal real-valued branch of the Lambert W-function". In: *Advances in Computational Mathematics* 43 (2017).

[24] Recep Kas et al. "Along the Channel Gradients Impact on the Spatioactivity of Gas Diffusion Electrodes at High Conversions during CO_2 Electroreduction". In: *ACS Sustainable Chemistry & Engineering* 9.3 (2021), pp. 1286–1296.

[25] Byoungsu Kim et al. "Influence of dilute feed and pH on electrochemical reduction of CO_2 to CO on Ag in a continuous flow electrolyzer". In: *Electrochimica Acta* 166 (2015), pp. 271–276. ISSN: 0013-4686.

[26] Andrew M. Kiss et al. "Carbonate and Bicarbonate Ion Transport in Alkaline Anion Exchange Membranes". In: *Journal of The Electrochemical Society* 160.9 (2013), F994–F999.

[27] ChungHyuk Lee et al. "Bubble Formation in the Electrolyte Triggers Voltage Instability in CO_2 Electrolyzers". In: *iScience* 23.5 (2020), p. 101094. ISSN: 2589-0042.

[28] Mi-Young Lee et al. "Current achievements and the future direction of electrochemical CO_2 reduction: A short review". In: *Critical Reviews in Environmental Science and Technology* 50.8 (2020), pp. 769–815.

[29] Mclain Leonard et al. "Investigating Electrode Flooding in a Flowing Electrolyte, Gas-Fed Carbon Dioxide Electrolyzer". In: *ChemSusChem* 13 (Nov. 2019), pp. 400–411.

[30] André Lévêque. "Les lois de la transmission de chaleur par convection". PhD thesis. Faculté des Sciences de Paris, 1928.

[31] Jun Li et al. "Efficient electrocatalytic CO_2 reduction on a three-phase interface". In: *Nature Catalysis* 1.8 (2018), pp. 592–600. ISSN: 2520-1158.

[32] Nathan Nesbitt and Wilson Smith. *Water Activity Regulates CO_2 Reduction in Gas-Diffusion Electrodes*. 2021.

[33] Nathan T. Nesbitt et al. "Liquid–Solid Boundaries Dominate Activity of CO_2 Reduction on Gas-Diffusion Electrodes". In: *ACS Catalysis* 10.23 (2020), pp. 14093–14106.

[34] John Newman and Karen E Thomas-Alyea. *Electrochemical systems*. John Wiley & Sons, 2012.

[35] Daniel Pabsch, Christoph Held, and Gabriele Sadowski. "Modeling the CO_2 Solubility in Aqueous Electrolyte Solutions Using ePC-SAFT". In: *Journal of Chemical & Engineering Data* 65.12 (2020), pp. 5768–5777.

[36] M. Paidar, V. Fateev, and K. Bouzek. "Membrane electrolysis—History, current status and perspective". In: *Electrochimica Acta* 209 (2016), pp. 737–756. ISSN: 0013-4686.

[37] Nagappan Ramaswamy et al. "Carbon Support Microstructure Impact on High Current Density Transport Resistances in PEMFC Cathode". In: *Journal of The Electrochemical Society* 167.6 (2020), p. 064515.

[38] T. L. S. Rao and W. D. Morris. "Paper 40: Superimposed Laminar Forced and Free Convection between Vertical Parallel Plates when One Plate is Uniformly Heated and the Other is Thermally Insulated". In: *Proceedings of the Institution of Mechanical Engineers, Conference Proceedings* 182.8 (1967), pp. 374–381.

[39] Kai Schulz et al. "Determination of the rate constants for the carbon dioxide to bicarbonate inter-conversion in pH-buffered seawater systems". In: *Marine Chemistry* 100 (Jan. 2006), pp. 53–65.

[40] M. Sechenov. "On the behavior of salt solutions based on their relation to carbon dioxide". In: *Z. Phys. Chem.* (1889), pp. 117–125.

[41] Wilson A. Smith et al. "Pathways to Industrial-Scale Fuel Out of Thin Air from CO_2 Electrolysis". English. In: *Joule* 3.8 (2019), pp. 1822–1834. ISSN: 2542-4351.

[42] Tatyana Soboleva et al. "On the Micro-, Meso-, and Macroporous Structures of Polymer Electrolyte Membrane Fuel Cell Catalyst Layers". In: *ACS Applied Materials & Interfaces* 2.2 (2010), pp. 375–384.

[43] E. W. Thiele. "Relation between Catalytic Activity and Size of Particle". In: *Industrial & Engineering Chemistry* 31.7 (1939), pp. 916–920.

2

[44] Bernhard Tjaden et al. "On the origin and application of the Bruggeman correlation for analysing transport phenomena in electrochemical systems". In: *Current Opinion in Chemical Engineering* 12 (2016). Nanotechnology / Separation Engineering, pp. 44–51. ISSN: 2211-3398.

[45] Harry L. Tuller. "Solar to fuels conversion technologies: a perspective". In: *Materials for Renewable and Sustainable Energy* 6.1 (2017), p. 3. ISSN: 2194-1467.

[46] Sumit Verma et al. "Insights into the Low Overpotential Electroreduction of CO_2 to CO on a Supported Gold Catalyst in an Alkaline Flow Electrolyzer". In: *ACS Energy Letters* 3.1 (2018), pp. 193–198.

[47] Sumit Verma et al. "The effect of electrolyte composition on the electroreduction of CO_2 to CO on Ag based gas diffusion electrodes". In: *Phys. Chem. Chem. Phys.* 18 (10 2016), pp. 7075–7084.

[48] James W. Vickers, Dominic Alfonso, and Douglas R. Kauffman. "Electrochemical Carbon Dioxide Reduction at Nanostructured Gold, Copper, and Alloy Materials". In: *Energy Technology* 5.6 (2017), pp. 775–795.

[49] Qinian Wang et al. "Enhanced performance of gas diffusion electrode for electrochemical reduction of carbon dioxide to formate by adding polytetrafluoroethylene into catalyst layer". In: *Journal of Power Sources* 279 (2015), pp. 1–5. ISSN: 0378-7753.

[50] S. Weisenberger and A. Schumpe. "Estimation of gas solubilities in salt solutions at temperatures from 273 K to 363 K". In: *Aiche Journal* 42 (1996), pp. 298–300.

[51] Lien-Chun Weng, Alexis T. Bell, and Adam Z. Weber. "Modeling gas-diffusion electrodes for CO_2 reduction". In: *Phys. Chem. Chem. Phys.* 20 (25 2018), pp. 16973–16984.

[52] Lien-Chun Weng, Alexis T. Bell, and Adam Z. Weber. "Towards membrane-electrode assembly systems for CO_2 reduction: a modeling study". In: *Energy Environ. Sci.* 12 (6 2019), pp. 1950–1968.

[53] Devin T. Whipple, Eryn C. Finke, and Paul J. A. Kenis. "Microfluidic Reactor for the Electrochemical Reduction of Carbon Dioxide: The Effect of pH". In: *Electrochemical and Solid-State Letters* 13.9 (2010), B109.

[54] Janusz Wojtkowiak and Czeslaw Popiel. "Inherently Linear Annular-Duct-Type Laminar Flowmeter". In: *Journal of Fluids Engineering-transactions of The Asme - J FLUID ENG* 128 (2006).

[55] Jacob A. Wrubel et al. "Predicting the Effects of Carbon Dioxide on the Conductivity of Electrospun Anion Exchange Membranes". In: *Journal of The Electrochemical Society* 166.14 (2019), F1047–F1054.

[56] D. Wu. "Review of System Integration and Control of Proton Exchange Membrane Fuel Cells". In: *Electrochem. Energ. Rev. 3* (2020), pp. 466–505.

[57] Hang Xiang et al. "Production of formate by CO_2 electrochemical reduction and its application in energy storage". In: *Sustainable Energy Fuels* 4 (1 2020), pp. 277–284.

[58] T. Yamamoto et al. "Electrochemical reduction of CO_2 in micropores". In: *Advances in Chemical Conversions for Mitigating Carbon Dioxide* (1998). Ed. by T. Inui et al., pp. 585–588. ISSN: 0167-2991.

[59] Zhifei Yan et al. "Renewable electricity storage using electrolysis". In: *Proceedings of the National Academy of Sciences* 117.23 (2020), pp. 12558–12563. ISSN: 0027-8424.

[60] Kailun Yang et al. "Role of the Carbon-Based Gas Diffusion Layer on Flooding in a Gas Diffusion Electrode Cell for Electrochemical CO_2 Reduction". In: *ACS Energy Letters* 6.1 (2021), pp. 33–40.

[61] Jie Zhang, Wen Luo, and Andreas Züttel. "Crossover of liquid products from electrochemical CO_2 reduction through gas diffusion electrode and anion exchange membrane". In: *Journal of Catalysis* 385 (2020), pp. 140–145. ISSN: 0021-9517.

[62] Shuo Zhao, Renxi Jin, and Rongchao Jin. "Opportunities and Challenges in CO_2 Reduction by Gold- and Silver-Based Electrocatalysts: From Bulk Metals to Nanoparticles and Atomically Precise Nanoclusters". In: *ACS Energy Letters* 3.2 (2018), pp. 452–462.

[63] J. Zhou et al. "Analysis of the role of the microporous layer in improving polymer electrolyte fuel cell performance". In: *Electrochimica Acta* 268 (2018), pp. 366–382. ISSN: 0013-4686.

[64] A. Zlotorowicz et al. "Tailored porosities of the cathode layer for improved polymer electrolyte fuel cell performance". In: *Journal of Power Sources* 287 (2015), pp. 472–477. ISSN: 0378-7753.

2

3

CATHOLYTE INHOMOGENEITIES LIMIT UPSCALING OF CO$_2$ FLOW ELECTROLYSERS

The use of gas diffusion electrodes that supply gaseous CO$_2$ directly to the catalyst layer has greatly improved the performance of electrochemical CO$_2$ conversion. However, reports of high current densities and Faradaic efficiencies primarily come from small lab scale electrolysers. Such electrolysers typically have a geometric area of 5 cm^2, while an industrial electrolyser would require an area closer to 1 m^2. The difference in scales means that many limitations that manifest only for larger electrolysers are not captured in lab scale setups. We develop a 2D computational model of both a lab scale and upscaled CO$_2$ electrolyser to determine performance limitations at larger scales and how they compare to the performance limitations observed at the lab scale. We find that for the same current density larger electrolysers exhibit much greater reaction and local environment inhomogeneity. Increasing catalyst layer pH and widening concentration boundary layers of the KHCO$_3$ buffer in the electrolyte channel lead to higher activation overpotential and increased parasitic loss of reactant CO$_2$ to the electrolyte solution. We show that a variable catalyst loading along the direction of the flow channel may improve the economics of a large scale CO$_2$ electrolyser.

3.1. INTRODUCTION

CO_2 from atmospheric or industrial sources can be electrochemically converted to valuable chemicals and fuels, leading to carbon neutral energy storage solutions and chemical feedstocks. The use of gas-diffusion electrodes (GDEs) allows the problems of low CO_2 solubility and diffusivity in aqueous electrolytes to be minimised, leading to high current density lab scale electrolysers [20]. However, the industrial realisation of this technology is hindered by poor understanding of how these processes work in industrially relevant conditions. A rough benchmark of a minimum current density of 200 mA cm^{-2} has been reported for commercial feasibility [28, 58, 53], and this current density must be achieved at industrial scales. The typical lab scale cell has a geometric surface area around 5 cm^2 but an industrial scale cell would be significantly larger: Verma et al. proposed a surface area of 400 cm^2 per cell [58], while analyses that make comparisons to alkaline water electrolysis propose even surface areas from 1000 cm^2 to 1 m^2 and above [2, 55].

However, upscaling in the flow direction leads to issues that negatively affect the performance of larger electrolysers. The high pH gradients, which have little impact on short lab scale electrolysers, lead to excessive pH increase in the extended flow direction. This high pH induces a Nernstian potential shift and depletes CO_2 through the carbonate equilibrium reactions, leading to reduced current density, Faradaic efficiency (FE), and reactant utilisation. However, the lack of experimental upscaling studies means the mechanisms behind these issues and the severity of their effects are poorly understood. In this paper we investigate the effect of scale by developing a 2D model of a typical lab scale CO_2 electrolysis cell and compare it to models that extend the geometry in the flow direction to 1 m. We identify the causes and magnitude of the performance loss, and provide strategies to minimise the issues.

3.2. THEORY

Figure 3.1 shows a schematic diagram of an electrolyser setup [64, 65] for CO_2 electrolysis flow cell with a liquid electrolyte channel. This channel is sometimes replaced with a membrane-electrode assembly (MEA) [17, 63], and similarly it is not unusual for an anion-exchange membrane (AEM) [14, 13, 35] to be used in place of the bipolar membrane (BPM) shown [40, 57, 49, 12, 46]. Gaseous CO_2 enters through the gas channel and passes through the macroporous gas diffusion layer (GDL) and microporous layer (MPL) to enter the liquid catholyte in the porous catalyst layer (CL), in which the heterogeneous electrochemical reaction takes place on the catalyst particles suspended in ionomer in the CL. The porous structures in the cell are modelled as macrohomogeneous domains characterised by porosity, ϵ, permeability κ, and volumetric surface area a_v. While it is possible for the exact location of the gas-liquid interface to vary in the neighbourhood of the CL-MPL boundary when hydrophobic CLs are used [66, 19], it is assumed in the model that the CL remains fully saturated with liquid electrolyte while the MPL and GDL remain entirely dry at all times. This allows the combination of the GDL and MPL into one effective diffusion layer, a practice which is common in the determination of bulk properties of commercial GDLs supplied with preprinted MPLs.
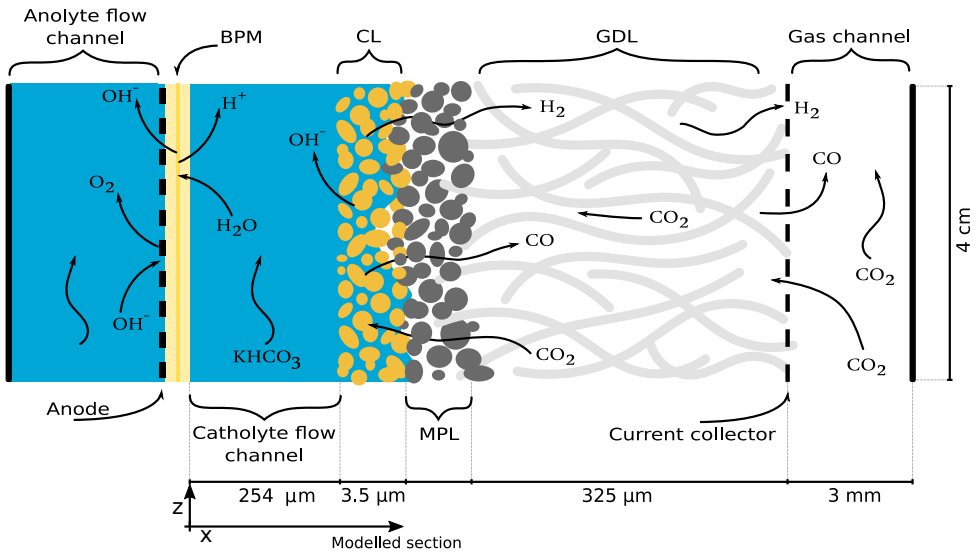
Figure 3.1: A diagram of a typical electrolysis cell (not to scale). From right to left: the gas channel, which supplies gas phase CO_2; the gas-diffusion layer (GDL), a dry macroporous structure through which CO_2 can permeate; the microporous layer (MPL), a thin hydrophobic layer which prevents electrolyte leakage into the gas-diffusion layer while allowing CO_2 dissolution into the liquid phase; the catalyst layer (CL), in which liquid electrolyte and catalyst particles embedded in the porous structure facilitate the electrochemical reaction with the dissolved CO_2; the catholyte flow channel, through which liquid electrolyte is supplied; a bipolar membrane (BPM), in which water dissociation supplies H^+ and OH^- ions to the respective sides; the anode, on which the counter reaction is performed; and the anolyte flow channel.

3.2.1. REACTIONS

The ionomer in the CL is considered to be impregnated with evenly distributed Ag catalyst particles that facilitate heterogeneous reactions, and due to the high Faradaic efficiency (FE) of Ag catalysts towards CO, we consider only the reduction of CO_2 to CO

$$CO_2 + H_2O + 2e^- \longrightarrow CO + 2OH^-, \tag{3.1}$$
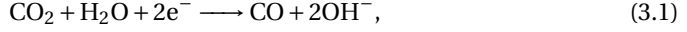
and the competing hydrogen evolution reaction (HER),

$$2H_2O + 2e^- \longrightarrow H_2 + 2OH^-. \tag{3.2}$$
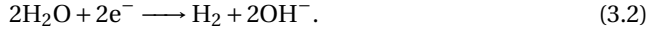
While there is an argument for the HER pathways involving H^+ and HCO_3^- to be included, these pathways are prevalent in near-neutral pH environments [18], and previous modelling studies predict that the CL environment will be very basic at current densities greater than 100 mA cm^{-2} [62] and that this pH will only increase in the flow-wise direction [29]. On the anode the oxygen evolution reaction (OER),

$$4OH^- \longrightarrow O_2 + 2H_2O + 4e^-, \tag{3.3}$$
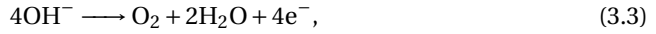
takes place.

A major complication distinguishing CO_2 electroreduction from similar technologies arises from the homogeneous reaction of CO_2 with OH^- to form bicarbonate and carbonate. These reactions can take both acidic and basic pathways, neither of which can be neglected. The basic

$$CO_2 + OH^- \underset{k_{-1}}{\overset{k_1}{\rightleftharpoons}} HCO_3^- \tag{3.4}$$

$$HCO_3^- + OH^- \underset{k_{-2}}{\overset{k_2}{\rightleftharpoons}} H_2O + CO_3^{2-} \tag{3.5}$$

and acidic

$$CO_2 + H_2O \underset{k_{-3}}{\overset{k_3}{\rightleftharpoons}} H^+ + HCO_3^- \tag{3.6}$$

$$HCO_3^- \underset{k_{-4}}{\overset{k_4}{\rightleftharpoons}} H^+ + CO_3^{2-} \tag{3.7}$$
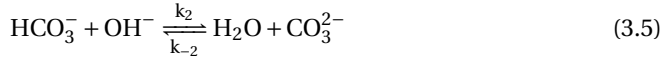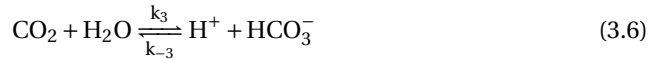
reactions have the same ratios of CO_2, HCO_3^- and CO_3^{2-} at equilibrium for a given pH due to their coupling in the water self-ionisation reaction

$$H_2O \underset{k_{-w}}{\overset{k_w}{\rightleftharpoons}} H^+ + OH^-. \tag{3.8}$$

Furthermore, the equilibrium constants, $K_i = \frac{k_i}{k_{-i}}$, for the acidic reactions are related to the basic reactions through $K_3 = K_1 K_w$ and $K_4 = K_2 K_w$. However, the reactions have different kinetic rates, and as such are each modelled individually.

The reaction rates per unit volume for species i in heterogeneous reaction r are given by

$$R_{ct,i} = \sum_r \frac{j_r v_{i,r} a_v}{n_r F}, \tag{3.9}$$

where j_r is the local current density of reaction r, $v_{i,r}$ is the stoichiometric coefficient of species i in reaction r, a_v is the volumetric surface area, n_r is the number of electrons transferred in reaction r and F is Faraday's constant. The local current densities at the anode and cathode are determined using the anodic and cathodic branches of the Butler-Volmer equation, respectively, in the forms of

$$j_{\text{OER}} = j_{0,\text{OER}} e^{\frac{\eta_{\text{OER}}}{b_{\text{OER}}}}, \tag{3.10}$$

$$j_{\text{HER}} = -j_{0,\text{HER}} e^{-\frac{\eta_{\text{HER}}}{b_{\text{HER}}}}, \tag{3.11}$$

$$j_{\text{COER}} = -\frac{c_{\text{CO}_2}}{c_{\text{ref}}} j_{0,\text{COER}} e^{-\frac{\eta_{\text{COER}}}{b_{\text{COER}}}}, \tag{3.12}$$

where $j_{0,r}$ are the exchange current densities, b_r are the Tafel slopes, and η_r are the activation overpotentials. The COER equation includes the concentration dependence on CO_2 with respect to a reference concentration c_{ref}, but the other two reactions are assumed to have a constant reactant source of water, and as such no explicit concentration dependence is necessary. In this case, c_{ref} should refer to the equilibrium concentration, but in some derivations of kinetics a different reference concentration, such as 1 M [62], is used, leading to a correspondingly altered derived value of exchange current density. The Tafel slopes are given by

$$b_r = \frac{RT}{\alpha_r F}, \tag{3.13}$$

where α_r are the charge transfer coefficients for their respective Tafel branches and R is the ideal gas constant. The activation overpotentials η_r are defined as

$$\eta_r = \phi_s - \phi_l - E_{\text{eq},r} \tag{3.14}$$

where ϕ_s and ϕ_l are the electrode and electrolyte potentials respectively and $E_{\text{eq},r}$ is the equilibrium potential of reaction r, corrected for the local pH through the a simplified Nernst equation assuming water and solute activities are near unity,

$$E_{\text{eq},r} = E_{0,r} - \frac{\ln(10)RT}{F}\text{pH}. \tag{3.15}$$

Nesbitt et al. noted that this form of the Nernst equation is determined using the assumption of an acidic or near neutral electrolyte in which the reaction equation reads

$$CO_2 + 2H^+ + 2e^- \longrightarrow CO + H_2O, \tag{3.16}$$
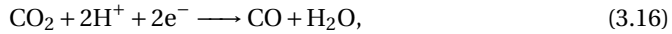
and the rate-determining step is the second protonation by H_2O [48], but it is often assumed without verification that this remains the rate-determining step for the reaction pathway in alkaline media, Eq. 3.1. Noting that the pH dependency in Eq. 3.15 is roughly -0.0591pH, they give simplified Nernst equations for acidic/neutral electrolytes and alkaline electrolytes,

$$E_{\text{CO}_2/\text{CO}} = -0.106 - 0.0591 \text{ pH (V)} \qquad \text{acidic/neutral}, \tag{3.17}$$

$$E_{\text{CO}_2/\text{CO}} = -0.933 - 0.0591 \text{ pH (V)} \qquad \text{alkaline}, \tag{3.18}$$
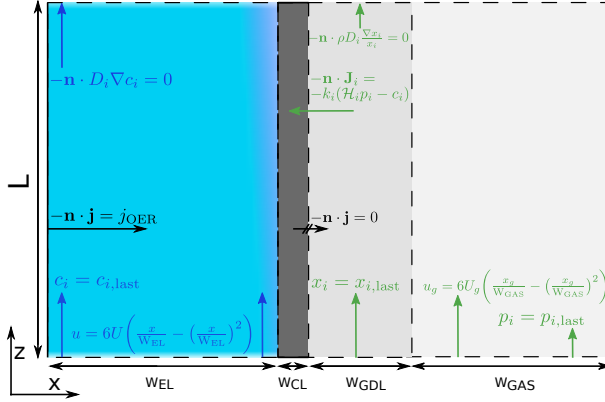
Figure 3.2: A schematic of the model equations and domains. The z-axis follows the flow along the catholyte channel of length L. The x-axis passes through the catholyte channel of width W_{EL}, the CL of width W_{CL}, the GDL of width W_{GDL} and into the gas channel of width W_{GAS}. In black, the electrolyte current boundary conditions denote the anodic current source on the left and insulating condition on the right. In the liquid phase, blue equations denote the inlet condition on concentration, the open boundary outlet condition, and the Poiseuille flow velocity distribution in Eq. (3.27). In the gas phase, green equations denote the inlet conditions on partial pressures and mole fractions, the open boundary outlet condition, the liquid-gas mass transfer rate in Eq. (3.28), and the initial Poiseuille gas velocity distribution in the gas channel, where x_g denotes coordinate within the gas channel and U_g is the initial average gas velocity for the simulation.

and note a common misnomer in literature in which Eq. 3.1 is associated with Eq. 3.17. Reaction kinetics determined under these assumptions are frequently used in literature [62] and while the resulting current density-potential curves may give results similar to experiments, further experimental verification of the reaction mechanism in alkaline media and subsequent recalculation of kinetic parameters are necessary to describe the dependence of the reaction on local activities. The reaction rates from the homogeneous chemical reactions, $R_{H,i}$, are given by

$$R_{H,i} = \epsilon \sum_n \nu_{i,n} \Big(k_n \prod_{\nu_{j,n}>0}^{j} c_j - k_{-n} \prod_{\nu_{j,n}<0}^{j} c_j \Big), \tag{3.19}$$

where $\nu_{i,n}$ are the stoichiometric coefficients of species i in homogeneous reaction n, and $k_{\pm n}$ are the forward and backward reaction rates of reaction n.

3.2.2. TRANSPORT

The gas phase consists of 99.99% pure CO_2 at the inlet (0.01% N_2) with additional CO and H_2 components at the outlet. Transport in the gas phase from the gas channel through the GDL and MPL is modelled with Darcy's law and a mixture averaged diffusion model approximation requiring only binary diffusion coefficients [31, 47]. Darcy's law reads

$$\mathbf{v} = -\frac{\kappa}{\mu_g} \nabla p, \tag{3.20}$$

where $\mathbf{v}$ is the gas velocity field, κ is the permeability of the porous medium, μ_g is the dynamic viscosity of the gas and p is the pressure. The flow is assumed incompressible and density variations are neglected. The diffusive mass flux is assumed to be proportional to the mole fraction gradient through

$$\mathbf{J}_i = -\rho_i D_i \frac{\nabla x_i}{x_i} \tag{3.21}$$

where $\mathbf{J}_i$ is the mass flux of species i relative to the average fluid velocity $\mathbf{v}$, ρ_i is the species density, D_i is the porosity and finite pore size corrected mixture-averaged diffusion coefficient and x_i is the mole fraction. The mixture-averaged diffusion coefficients are determined from the binary diffusion coefficients in

$$D_i = \frac{1 - x_i}{\sum_{j \neq i} \frac{x_j}{D_{i,j}^{\text{eff}}}}, \tag{3.22}$$

where D_i^{eff} are the effective binary diffusion coefficients corrected for porosity and tortuosity through the Bruggeman correlation [56],

$$D_{i,j}^{\text{eff}} = \epsilon^{\frac{3}{2}} D_{i,j}. \tag{3.23}$$

Gas transport is usually slightly poorer in the MPL than in the GDL because MPLs typically have lower permeabilities and porosities than GDLs, but this reduction is small compared to the effect that electrolyte intrusion would have on the GDL. Regardless, it is common for manufacturers to supply GDLs with MPLs already applied, and provide the averaged values of transport properties of the final bilayer structure rather than of the individual components. We thus elect to model the GDL and MPL as one numerical domain with uniform porosity and permeability.

In the liquid phase there is bulk flow in the electrolyte channel, but the effect of change in permeability on transition into the porous CL is sufficient that flow in the CL can be neglected [5]. Transport of species is modelled by assuming that concentrations remain small enough to be treated as a dilute solution and using the Nernst-Planck equation:

$$\mathbf{N}_i = -D_i^{\text{eff}} \nabla c_i - D_i^{\text{eff}} \frac{F z_i}{RT} c_i \nabla \phi_l + c_i \mathbf{u}, \tag{3.24}$$

where $\mathbf{u}$ is the liquid velocity and z_i is the species charge number. Species conservation in the steady state is ensured by

$$\nabla \cdot \mathbf{N}_i = R_{\text{H},i} + R_{\text{ct},i}, \tag{3.25}$$

and electroneutrality is ensured by

$$\sum_i z_i c_i = 0, \tag{3.26}$$

allowing the transport equations in Eq. 3.24 and 3.25 to be solved for all but one of the species, with the final concentration determined through the electroneutrality condition in Eq. 3.26. The local liquid velocity $\mathbf{u}$ is determined assuming a Poiseuille flow profile,

$$\mathbf{u} = 6U\left(\frac{x}{W_{\text{EL}}} - \left(\frac{x}{W_{\text{EL}}}\right)^2\right)\hat{\mathbf{z}}, \tag{3.27}$$

where U is the average velocity. A similar method is used for the inlet gas velocity but with W_{GAS} instead of W_{EL} and U_g prescribed based on target single pass conversion. At the liquid-gas phase interface the flux is described by

$$-\mathbf{n} \cdot \mathbf{J}_i = -k_i(\mathcal{H}_i p_i - c_i),\tag{3.28}$$

where $\mathcal{H}_i$ is the Henry constant for species i, p_i is the partial pressure of that species and k_i is a characteristic cross phase mass transfer coefficient determined for CO_2 adsorption into the CL ionomer by Kas et al. [29]. The Henry constant is further corrected for ionic concentrations within the electrolyte (see Eq. 6 in SI) following the Sechenov equation [51, 50, 61]. The solubilities of the remaining gas species are around two orders of magnitude lower than that of CO_2, so their Henry constants are negligible and they cannot enter the CL, only exit. CO_2 entering the liquid phase causes p_{CO_2} to progressively decrease along the flow channel, subsequently decreasing the flux in Eq. (3.28).

3.3. COMPUTATIONAL MODEL

The equations for the liquid phase are altered slightly to yield approximate expressions that prove significantly easier to resolve computationally. The homogeneous reactions are problematic due to the extreme magnitudes of the rate coefficients, so we use the assumption that the local environment will be alkaline in the vicinity of the cathodic reaction and acidic in the vicinity of the BPM to selectively neglect the alkaline pathways, K_1 and K_2, in the BPM half of the electrolyte channel and the acidic pathways, K_3 and K_4, in the cathodic half of the channel. Due to the coupling of their equilibrium constants we are assured that there is no significant discontinuity in net reaction rates at this halfway point so long as the concentration boundary layers do not extend further than half of the channel width. Furthermore, for numerical stability we adopt a logarithmic form of the transport equations in the liquid,

$$\mathbf{N}_i = -e^{C_i} D_i^{\text{eff}} \nabla C_i - D_i^{\text{eff}} \frac{Fz_i}{RT} e^{C_i} \nabla \phi_l + e^{C_i} \mathbf{u},\tag{3.29}$$

where $c_i = e^{C_i}$. C_i can now take any real value and the relation ensures that c_i is strictly positive. This entirely precludes the possibility of negative concentrations in the solution, which is otherwise a common computational issue in systems with high reaction rates and reactant depletion. Another limitation is the computational cost of the effect of local ionic strength variation on ϕ_l in Eq. (3.24). Extremely high homogeneous reaction rate coefficients lead to high species concentration sensitivities even in regions with smooth solutions, leading to stiffness in the system. However, we can do little more to alleviate this without sacrificing significant detail in the homogeneous reactions. An approximation is made to remove the dependence of the migration term on concentration and instead use an iterative non-uniform electrolyte conductivity, given by

$$\sigma_l = \frac{F^2}{RT} \sum_i z_i^2 D_i c_i^*,\tag{3.30}$$

where c_i^* is the average concentration in the previous iteration of the numerical solver. This effectively decouples ϕ_l from Eq. (3.29) by determining it from Ohm's law,

$$\mathbf{i} = -\sigma_l \nabla \phi_l,\tag{3.31}$$

and the state of the previous iteration, and allowing Eq. (3.29) to solve for C_i without simultaneously solving for ϕ_l.

Despite these simplifications, the scale of the system is still too large for reasonable computation. To this end the cell model is decomposed into the subcells shown in Fig. 3.3. We take one initial short (4 cm) basis cell and find a stationary solution, and then solve a second subcell with the downstream outlet of the previous subcell used as the inlet condition. This approximation requires that the flow be sufficiently fast that transport against the flow direction can be neglected. This condition can be written as a necessarily high bulk Péclet number, the ratio of advective to diffusive transport rates. While there is no flow at the channel walls and in the CL, these regions are fully within the concentration boundary layer and the flow-wise concentration gradient is too small for diffusion to play a non-negligible role. Instead the flow wise variation in the CL is almost entirely determined by the concentration development in the adjacent electrolyte channel and in the gas phase, in what amounts to a locally 1D model, which is to be expected of a domain whose in plane dimension is four orders of magnitude greater than the through plane dimension. In the 4 cm model with no subcell decomposition it was already found that in plane diffusion was negligible in the CL, and it is expected that it would become even less important when the length scale is increased.

Similarly we require that electrolyte potential varies little in the flow-wise direction. The characteristic length of a subcell far exceeds the thickness of the channel, so the flow-wise current density, j_z, will be negligible with respect to the flow-perpendicular current density j_x. The variation of electrolyte potential in the flow-wise direction depends on the variation of electrode reaction kinetics, and while this can be large due to high pH gradients, it is still small compared to the potential drop across the channel. While the subcells allow us to reduce the size of the computed domain in favour of iteration, the above requirements still motivate us to take as long a subcell as feasible, but the size of 4 cm is chosen out of expediency. While domain decomposition and variable transformations are not uncommon in numerical modelling they are underutilised in the field, with most models of electrochemical CO_2 reduction resorting to 1D [62, 21, 63, 7], simplifying the homogeneous reactions [34], investigating only low current densities [52], or only modelling small electrolysers [29]. Table 3.1 shows the geometric and operational parameters of the electrolyser, with unreferenced parameters measured from an in-house experimental setup.

3
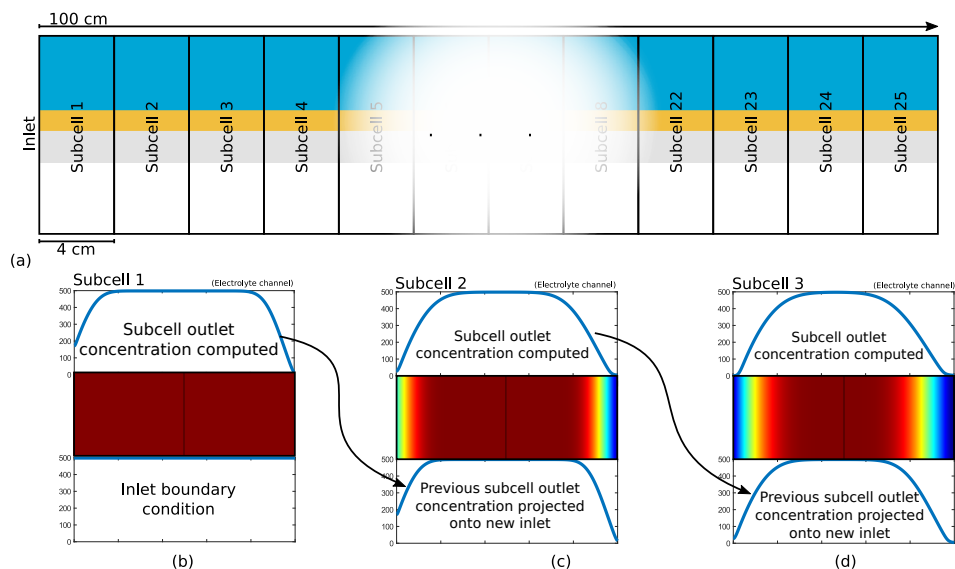
Figure 3.3: The simulation sequentially solves subcells divided in the flow direction. (a) shows the decomposition of the 100 cm cell into 25 adjacent 4 cm subcells. The initial and final subcells are coupled to inlet and outlet regions, respectively, and each internal subcell is coupled to the boundary values of the adjacent subcells. (b) shows that the inlet HCO_3^- profile is projected onto the inlet of the first subcell, solved along the length of the subcell, then projected from the outlet onto the inlet of (c), which is subsequently solved and projected onto the inlet of (d) and so on. The other concentration and potential profiles at the top of each subcell catholyte channel and CL are projected onto the inlets of each subsequent subcell. The same method is applied between subsequent GDL and gas flow channel inlets, projecting the mole fractions and pressures in the gas phase. The numerical conditions are shown in Fig. 3.2.

Parameter	Description	Value	Unit	Ref.
p_{abs}	Gas pressure	1	atm	-
T	Temperature	293.15	K	-
c_{KHCO_3}	Catholyte concentration	500	mM	-
Re	Reynolds number	200	-	-
L	Flow channel length	4	cm	-
W	Flow channel thickness	0.254	mm	-
W_{CL}	CL thickness	3.5	µm	[62]
W_{GDL}	GDL thickness	325	µm	[32]
W_{GAS}	Gas channel thickness	3	mm	-
H	Flow channel height	5	mm	-
ϵ_{CL}	CL porosity	0.5	-	-
ϵ_{GDL}	GDL porosity	0.53	-	[32]
κ	GDL permeability	1.72×10^{-11}	m^2	[32]

Table 3.1: Geometric and operational parameters for the base model. For a description of all parameters see Table S2. Flow rate and channel length in the validation cases are adjusted accordingly, with standard temperature and pressure. Channel parameters are based on an in-house experimental setup with dimensions similar to that of Wu et al. [65]

3.4. RESULTS

3.4.1. MODEL VALIDATION

Figure 3.4, shows experimental comparisons of partial current density against cathode potential and FE against total current density, for the parameters in Table S2. The match between computational and experimental results is good, only slightly overestimating partial current density. It is expected that the deviation arises from phenomena outside of the scope of the model, such as significant bubble formation near the CL-electrolyte channel interface or liquid breakthrough in the MPL. Both of these phenomena would result in a reduction in cell performance due to reduced access to reaction sites [38] and increased diffusion pathway lengths [33] and are both present primarily at higher current densities. As the liquid breakthrough would lead to a significant reduction in FE [41], which is not observed in Fig. 3.4b, the bubble formation explanation is favoured. Despite the short length of the validation case electrolyser, the difference between the presented 2D model and the 1D model of Weng et al. is stark. The use of one operation-independent boundary layer thickness in the Weng model leads to prohibitively low mass transfer between the electrolyte channel and CL at low current densities where the boundary layer should be thinner, and unrealistically high mass transfer at high current densities where the boundary layer should be thicker. By contrast the analytical model of Blake et al. predicts the development of the concentration boundary layer in the channel and takes an average value for its thickness, but neglects the effect that the buffer of the $KHCO_3$ catholyte will have on this development. This leads to an overestimation of boundary layer thicknesses and a lower prediction for CO_2 current density as a result. It is possible to verify against analytical mathematical approximations of scaling relations that can be extrapolated to larger length scales. Fig 3.5 shows that the computational results match the predicted trends well, such as the cubic root length scaling of the boundary layer thicknesses and the hyperbolic cosine shape of the CO_2 distribution in the CL. The quality of the agreement with these results is the best validation that the circumstances permit.

3.4.2. UPSCALING

UPSCALING STUDY

To determine how local reaction environments change for longer electrolysers, we compare a 4 cm long electrolyser model with a 100 cm long electrolyser model. For this ratio of lengths, we chose to model the 100 cm electrolyser receiving a 25 times higher CO_2 flow rate in the gas channel, due to it being 25 times longer. Despite this, the pressure drop in the gas phase remains small compared to the liquid pressure drop. The liquid flow rate between models is held constant. Depending on the flow geometry, this can lead to large pressure drops in the liquid phase that far exceed the pressure drops in the gas phase, up to the order of hundreds of millibars for thin single channels. Although this could lead to many problems, from mechanical stability to local liquid breakthrough when pressure variations exceed the stability window of the GDL [3], these effects are outside of the scope of this work and are not modelled. The gas flow rate was varied to give insight into how different single pass conversions affect cell performance.

Given the focus on higher current densities (>100 mA cm^{-2}), we normalise reactant consumption by gas phase reactant supply only, as the overwhelming majority of CO_2
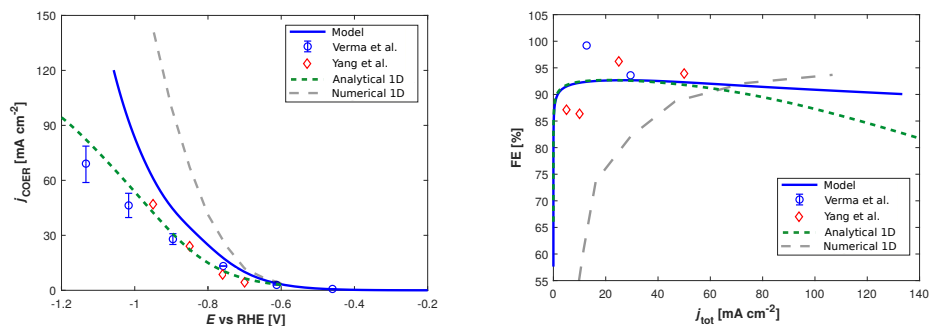
(a) Partial CO_2 current density, j_{COER} as a function of cathode potential from the model.

(b) Faradaic efficiency (FE) as a function of total current density, j_{tot}.

Figure 3.4: Model validation against experimental results from experimental results from Verma et al.[59] as well as experimental results from a similar experimental setup from Yang et al.[68], and a computational model developed by Weng et al.[62] and an analytical model developed by Blake et al. [7] based on the electrolyser properties of the Verma et al. experiments. (a) shows the partial CO_2 current density against cathode potential and (b) shows the Faradaic efficiency against total current density. The line plot for the computational model is for the experimental case of a 15 mm long flow electrolyser with a 0.5 M unsaturated $KHCO_3$ liquid electrolyte with a liquid flow rate corresponding to Re = 2.6 and an excess gas feed.

from the liquid flow channel is expected to be consumed in buffer reactions before reaching the CL for current densities above 40 mA cm^{-2} [30]. If the yield was normalised around the total influent CO_2 from both gas and liquid phase then it would become a relatively low percentage that is dependent on the ratio of channel flow rates. This electrolyte contribution to the reaction is similar to the operational method of a bicarbonate reactor, but such reactors seldom reach high current densities and when they do, they require high electrolyte concentrations [39]. We furthermore disambiguate between the usage of consumption and conversion following the convention of Larrázabal et al. [36], defining consumption as the percentage of gas phase CO_2 that enters and is consumed in the electrolyser and conversion as the percentage of influent gas phase CO_2 converted specifically into CO. These choices are further motivated by the results of the lab-scale electrolyser model in Figure 3.6.

CO_2 CONVERSION

At the low current density in Fig. 3.6a, the carbonate buffer reaction in Eq. (3.5) occurs almost entirely within the CL and HCO_3^- concentration remains high at the edge of the CL, indicating that the pH within the CL remains well buffered and the aqueous CO_2 concentration is high enough for the reaction to be performed in both bicarbonate electrolyser mode and gas supplied mode. However, at higher current densities in Figs. 3.6c and 3.6d, HCO_3^- is depleted by the reaction in Eq. (3.5) before reaching the CL, and the buffering reaction takes place in a concentration boundary layer outside the CL, showing that the reaction can no longer be performed in bicarbonate electrolyser mode. Despite this, when tracking the total HCO_3^- consumed this way we still find that the majority of the reaction takes place within the CL, implying that the buffering effect is actually due to the reaction of gas-supplied CO_2 to HCO_3^- through Eq. (3.4) and then CO_3^{2-} through
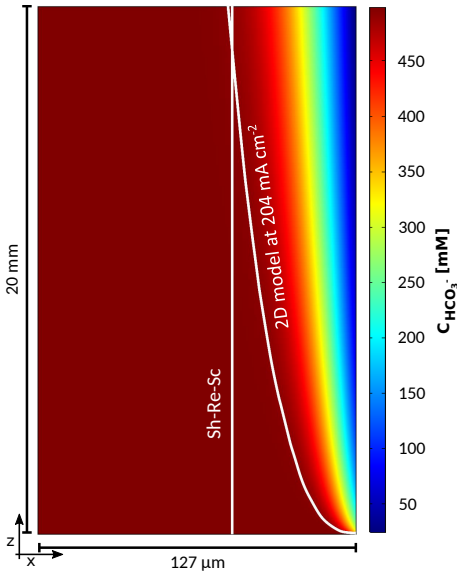
(a) HCO_3^- boundary layer thickness, δ_{bl,HCO_3^-}, at which concentration reaches 99% of the bulk concentration, compared to the Sherwood-Reynolds-Schmidt correlation (Eq. S2) used by Weng et al. for a 20 mm long electrolyser.
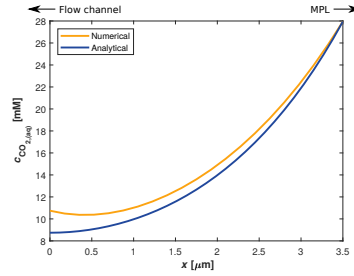
(b) Comparison of CO_2 distribution in the CL to an analytical approximation derived from the reaction-diffusion equation in 1D
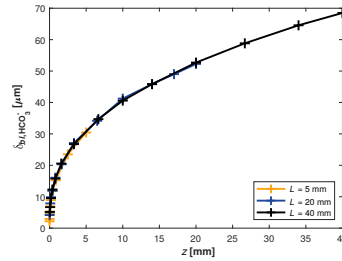
(c) Comparison of boundary layer thickness, δ_{bl,HCO_3^-}, for increasing electrolyser lengths.

Figure 3.5: Analytical results for flow-wise development of concentration boundary layer thickness, compared to numerical results. To quantify the numerical boundary layer thickness, HCO_3^- is used as the characteristic species to quantify the buffering effect, rather than CO_2. In (a) the boundary layer develops from negligible thickness to a thickness greater than that of the Sherwood-Reynolds-Schmidt correlation (Eq. S2), which does support its validity as an average approximation, but also highlights how unreasonable it is to take such an average near the inlet. In (b) the CO_2 distribution in the CL from the model follows $\cosh\left(\frac{x}{W_{CL}}\right)$ as is expected of a 1D reaction-diffusion system [54, 7]. More information on the analytical approximations can be found in SI Section 1.2. In (c) the boundary layer thicknesses exhibit a dependence on $z^{\frac{1}{3}}$ as is expected of Poiseuille flow for boundary layers much thinner than the half-channel width. [6, 22]
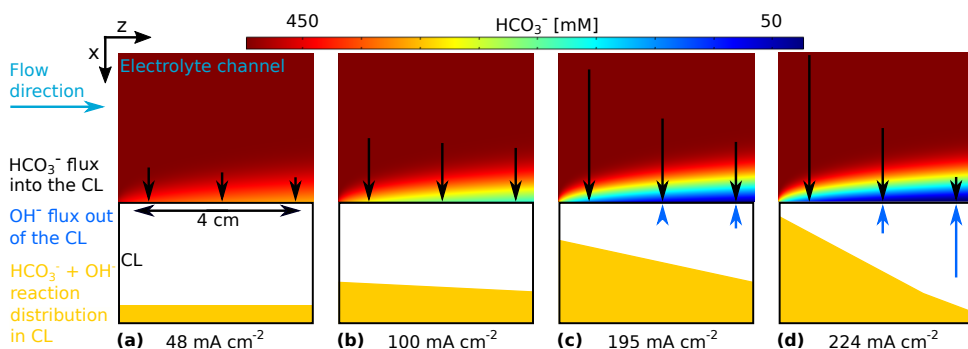
Figure 3.6: Profiles of HCO$_3^-$ just outside the CL at increasing total current densities, along with the respective distributions of the reaction in Eq. 3.5 of HCO$_3^-$ ions with OH$^-$ in the CL. The yellow shape shows the distribution of the homogeneous reaction within the CL. In (a) and (b) relatively little carbonate buffering takes place due to low OH$^-$ generation, and this reaction is quite uniform and almost exclusively takes place within the CL (>99%). For (c) and (d), however the reaction rate is relatively high, occurs predominantly close to the inlet where CO$_2$ availability and OH$^-$ generation are highest, and increasingly takes place in the buffer layer outside of the CL, with 10% in (c) and 30% in (d). This increasing reaction outside of the CL is due to the combined transport of buffer into the CL and CO$_2$ gas supply together being insufficient to buffer the generated OH$^-$, which is now able to diffuse out into the electrolyte channel before reacting with the bulk buffer solution.
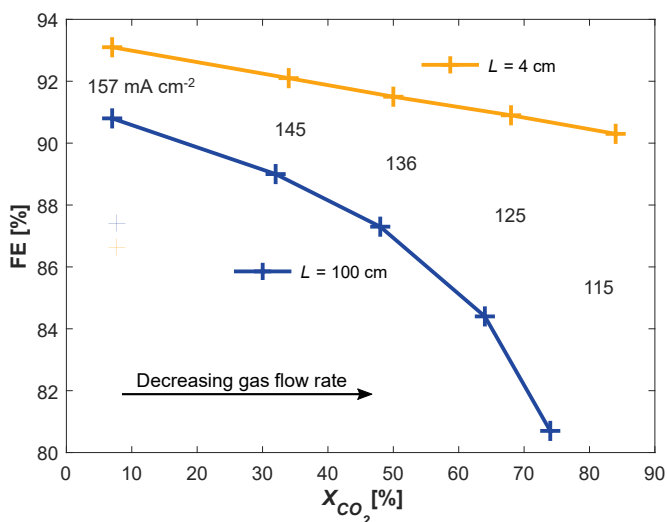
Figure 3.7: The effect of increasing single pass conversion, X_{CO_2} on Faradaic efficiency in the 4 cm and 100 cm electrolysers. The 100 cm electrode is maintained at 3.1 V, leading to a progressive reduction in average j_{tot} as flow rate is reduced to emulate increasing single pass conversion. The 4 cm electrolyser cell potential is adjusted from 2.98 V to 2.94 V to match the average j_{tot} at each corresponding gas flow rate. While FE decreases when single pass conversion is increased, the drop is more severe in the 100 cm case.
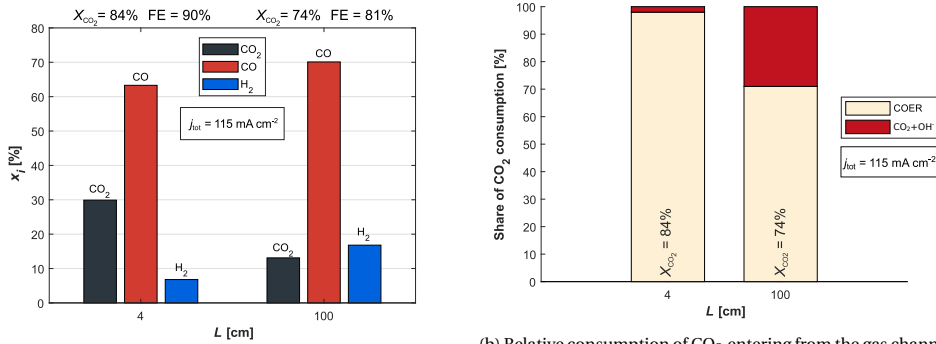
(a) Gas channel outlet composition for the two cases at j_{tot} = 115 mA cm^{-2}.

(b) Relative consumption of CO_2 entering from the gas channel in the electrolysis reaction and homogeneous reaction with OH$^-$ at j_{tot} = 115 mA cm^{-2}.

Figure 3.8: (a) shows the molar composition of the gas channel outlets in the two cases. Despite lower total CO_2 conversion and higher H_2 mole fraction, the 100 cm case exhibits a higher CO mole fraction in the gas outlet. (b) shows the relative magnitude of reaction sinks for CO_2 entering the CL from the gas phase. This explains (a), as 30% of the total CO_2 consumed is converted to HCO_3^- through the reaction with OH$^-$ instead of being converted to CO, leading to a higher total consumption of CO_2 and a lower resultant CO_2 fraction in the outlet stream. It is thus the loss of reactant rather than improvement in conversion that seemingly improves the outlet composition.

Eq. (3.5).

The performances at different single pass conversions are shown in Fig. 3.7. At low conversions, the supply of CO_2 is not limiting and so both cases exhibit high FE, with the small reduction in the 100 cm electrolyser FE arising only from the increase in average boundary layer thickness, following the trend of the 4 cm case in Fig. 3.5c. As conversion increases, the reduction in FE is far more severe in the 100 cm electrolyser than the 4 cm, as the reactant CO_2 is increasingly consumed by the parasitic reaction with OH$^-$ in the regions where the boundary layer is too thick to effectively buffer the OH$^-$ produced in the CL. This can be seen directly in Fig. 3.8b, in which 30% of the total consumed CO_2 is converted into HCO_3^- and CO_3^{2-} instead of CO. This high consumption can be easily erroneously interpreted as a high conversion, as in Fig. 3.8a in which the outlet ratio of CO_2 and CO seems much improved in the 100 cm case over the 4 cm case. It is instead the loss of reactant rather than increase in product that skews this ratio.

Experimental studies often report significantly higher consumption of reactant than is found in Fig. 3.8b due to conversion to CO_3^{2-} as well as crossover of this CO_3^{2-} through the membrane. The reports of exceptionally high crossover mainly come from electrolysers with AEMs [45], but BPMs inhibit transport of the carbon carrying anions [40] so we would expect lower crossover in our case. However, our assumption that BPMs entirely prevent this ion transport may not be realistic, as unwanted crossover has still been reported in BPM electrolysers [8, 9]. There is also an argument that, purely by the stoichiometry of Eqs. 3.1, 3.4 and 3.5 and balancing the local production and consumption of CO_2 and OH$^-$, the minimum fraction of reactant CO_2 converted to CO_3^{2-} should be 50% [36]. This argument assumes fast equilibrium reactions though, and Weng et al. showed that the CO_2 utilisation efficiency is dependent on k_1 from Eq. 3.4 [63], and we also found that

3
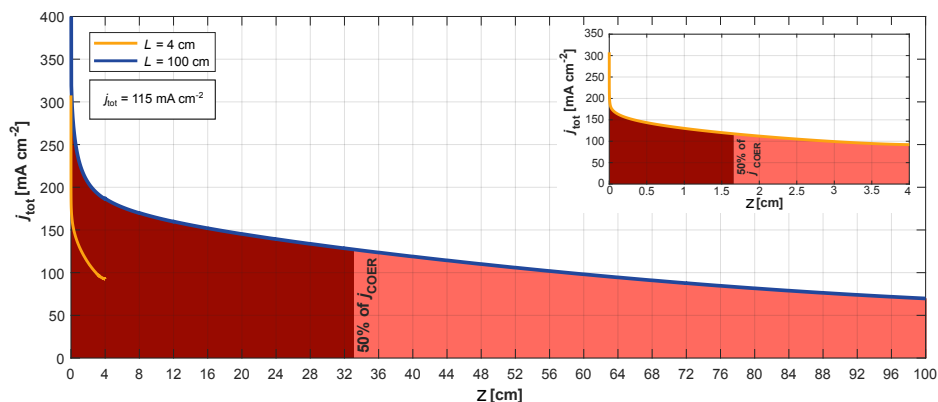
Figure 3.9: The local values of j_{tot} in the two electrolyser cases for an average total current density of $j_{tot} =$ 115 mA cm^{-2}. The 100 cm reaches a higher value of j_{tot} near the inlet due to the higher cell potential (3.1 V) than the 4 cm case (2.94 V) necessary for the same average j_{tot}, but falls to a lower value near the outlet due to the larger pH increase in the CL.

the kinetic treatment is necessary as Eq. 3.4 is out of equilibrium. The 50% minimum estimate is most valid for KOH electrolytes, due to their high pH and capacity for CO$_2$. We instead use a CO$_2$ saturated KHCO$_3$ electrolyte with a high buffer capacity, and although we do observe a large reaction between CO$_2$ and OH$^-$ a significant portion of this comes from the catholyte supplied CO$_2$ while we only consider CO$_2$ sourced from the gas phase in Fig. 3.8b.

The impact of the chemical consumption of CO$_2$ by the reaction with OH$^-$ depends on the relative costs of the gas channel upstream and downstream processes. If the cost of separation of CO from the product stream is relatively high, then the excess CO$_2$ consumption actually improves the economics due to the higher CO outlet portion in the 100 cm electrolyser. Assuming that the anolyte and catholyte streams are recombined and recirculated through the cell this chemically reacted CO$_2$ will be converted back from CO$_3^{2-}$ and HCO$_3^-$ when the acidic anolyte stream shifts the pH back to the initial value and the CO$_2$ can be recovered from the solution. This means that the reaction with OH$^-$ need not be considered as a true loss of reactant, rather as an inhibiting process that reduces j_{CO} and single pass conversion.

REACTION INHOMOGENEITY

The variation of j_{tot} is also greater in the 100 cm case. Fig. 3.9 shows j_{tot} near the inlet, in the vicinity of which the boundary layers are thin and the CL is very well buffered. At the inlet, j_{tot} is far greater than j at the outlet, where both poorer buffering and reduced reactant supply. This ideal inlet region is limited only by overpotential and as such reaches a higher value of j_{tot} in the 100 cm case due to the higher cell potential necessary to reach an average of 115 mA cm^{-2}. Despite this increased potential, j_{tot} at the outlet drops below the 4 cm case, because the pH is far higher in the 100 cm case. This inhomogeneity of the reaction distribution leads to the half of the total CO$_2$ reduction reaction taking place in only the first third of the electrolyser. Additional discussion of the pH gradients in the CL

and catholyte channel can be found in SI Section 2.

The inhomogeneity of the reaction distribution and failure of the buffering effect also causes a wide range of pH values to be present along the CL. The well-buffered inlet will retain a pH equal to that of the influent electrolyte, but the poorly buffered CL near the outlet will have a far higher pH unless the current density is very low or the gas phase CO_2 supply is very high. This increase in pH leads to a larger equilibrium potential correction through Eq. (3.15), a greater parasitic reaction rate and a chemical shift towards CO_3^{2-}. The electroneutrality condition requires that the high CO_3^{2-} concentration be paired with a high K^+ concentration, which together facilitate the precipitation of K_2CO_3 on the solid phase, leading to a reduction in diffusion pathways for CO_2 and potential damage to the porous structure as the K_2CO_3 crystals obstruct pores in the CL and MPL [11, 41]. These precipitates are also hydrophilic and can, along with the high pH, alter the potential of zero charge and thus electrowetting properties of the solid-liquid boundary, leading to loss of effective hydrophobicity in the MPL. This allows electrolyte breakthrough into the GDL and gas channel, leading to a negative impact on FE and stability. The penetrating electrolyte increases the diffusion pathway length for CO_2 as it blocks pores, leading to a reduction in j_{CO} while allowing HER to continue unmitigated. This pervasive issue is one of the main causes of performance loss over time, and mitigation strategies currently focus on temporal variation in reactor operation or low electrolyte strengths [67, 15].

3.4.3. DISCUSSION

By modelling the flow parallel direction as well as the through plane direction we overcome the limitations of 1D models that require empirical or simplified analytical expressions to attempt to capture flow-wise variation. The work of Yang et al. [69] includes the flow channel in 2D but neglects variation in pH in the electrolyte. This is at odds with this work and the work of Kas et al. [29], which both predict large variations in local pH. While this could be roughly justified by the use of high pH KOH electrolyte, it would still have a large impact on the local homogeneous reaction rates and the total loss of reactant to carbonate formation. This is not reported on, despite carbonate crossover being a serious issue [45, 40, 8, 9], and despite the homogeneous reaction kinetics they report being significantly faster than the heterogeneous kinetics for such a high pH. This assumption of pH homogeneity also hampers the upscaling analysis, as homogeneous properties are indifferent to scale, giving overambitious positive predictions for scalability. By contrast, the experimental scalability analysis of Jeanty et al. [27] highlights the more fundamental issues of electrolyte breakthrough and salt precipitation. Both of these support our conclusion of the importance of quantifying local pH and its effect on the carbonate equilibrium reactions as the perspired electrolyte has a pH value of 10 compared to that of the neutral K_2SO_4 catholyte and the precipitate comprised of carbonate salts for which the carbon could only have been sourced from the CO_2 feed. They also find similar trends for FE, in which the upscaled electrolyser suffered larger reduction in FE when lowering feed gas CO_2 supply. The most interesting result is the drastic improvement when implementing the circulating pump in the scaled up cell which, despite lowering the average CO_2 concentration, leads to a much more uniform concentration profile and a break up of the boundary layer. We identify an analogous issue in the catholyte channel with non-uniform pH and thick boundary layer development as a primary concern in

scalability, and the experimental success in reducing the effect in the gas channel is reassuring.

Stability

The extension of the 4 cm model to the 100 cm model shows deterioration in conversion, FE, and necessary cell potential, and the model indicates that these issues will only be exacerbated with further elongation of the flow channel. While these performance losses could be in some cases surmountable, the extreme variation in local reaction environment that comes with them would lead to further issues outside of the scope of the model. While liquid breakthrough in generalised porous media is well understood, electrolyte breakthrough in the electrolytic cell is related to precipitation and electrowetting. Precipitation would require stochastic modelling and electrowetting effects are poorly understood at interfaces where charge transfer reactions take place, so both are out of the scope of the model. However, we can note that both are dependent on the local ionic concentrations and pH, the latter due to the shift in potential of zero charge, and comment that by determining the general trends in pH and ionic strength we can predict that the upscaled model will be more susceptible to breakthrough closer to the outlet. In the future, when better descriptions of these phenomena are available, it will be possible to bridge the gap between local environment scalability and pressure stability studies [3, 4] to create a full description of breakthrough.

If the Reynolds number of the electrolyte flow channel is held constant, then the pressure drop along the channel will increase linearly with electrolyser length. The pressure variation in the liquid phase can lead to electrolyte or gas breakthrough when out of balance with the gas pressure drop, so it is ideal to scale one flow rate to ensure the differential pressures remain within MPL stability ranges. If particularly thin flow channels, such as those used in lab scale electrolysers, are required to minimise ohmic losses then the pressure drop can become excessively large. Without sufficiently pressure resistant MPLs this could lead to liquid breakthrough. Both the hydrophobicity and the mechanical stability of CLs are dependent on ionomer type and loading, which vary between experimental studies and are the subject of independent optimisation. Furthermore, it becomes an issue to mechanically support a flow channel under such conditions, potentially necessitating additional structural supports in the flow channel, which could cause the Poiseuille flow to transition into plug flow. Plug flow boundary layers scale with $z^{\frac{1}{2}}$, rather than the $z^{\frac{1}{3}}$ of Poiseuille flow [42], and as such can grow more rapidly. Specifically, we can take the ratio of the Lévêque approximation for plug flow and Poiseuille flow concentration boundary layer thicknesses,

$$\delta_{\text{plug}} = 3.643\sqrt{\frac{Dz}{U}}, \text{ and } \delta_{\text{Poiseuille}} = 1.607\sqrt[3]{\frac{lDz}{U}}, \tag{3.32}$$

where the concentration at the edge of the boundary layer is 99% of the bulk concentration. Plug flow will lead to thicker boundary layers when

$$z > \left(\frac{1.607}{3.643}\right)^6 \frac{UL^2}{D}, \tag{3.33}$$

which in our case for the diffusivity of HCO_3^- is roughly after only 11 cm. Widening the channel leads to increasing ohmic drop in across the electrolyte, so a balance must be

struck between electrolyte flow rate, pressure drop, and ohmic drop. For small lab scale electrolysers this balance usually favours thin channels due to the short flow channels exhibiting small pressure drops and little variation in the local pH and boundary layer, but as electrolyser length increases the benefit of lower ohmic drop will be outweighed by the cost of reduced GDL stability and increase in boundary layer thickness. This trade-off between flow velocity, flow channel length and ohmic drop is an optimisation problem that will remain relevant even in a full-scale stack implementing short channels.

PERFORMANCE LOSS MINIMISATION

With the sources of the performance losses isolated, it is possible to propose potential solutions. The primary issue is the lack of effective buffering due to thick concentration boundary layers, and so reducing the boundary layer thickness is paramount. This could be done by introducing static mixers or altering the geometry in the electrolyte channel to induce chaotic mixing [37] and break up the developing boundary layer, and although this could worsen carbonate and product crossover [16, 70], product crossover is only likely to be an issue when producing primarily liquid products [60, 43]. A similar issue would arise from the use of a stronger base such as KOH, in which the high pH would lead to unavoidable loss of CO_2 feed reactant to carbonate. When averaging across the entire CL for 115 mA cm^{-2} we find a dissolved CO_2 concentration of $\sim$ 5 mol m^{-3}, so as a rough estimate we can replace our predicted pH of $\sim$ 12.5 with 14 for KOH to find from Eqs. (3.9) and (3.19) that the percentage of total reacted CO_2 reacting with OH$^-$ rises from $\sim$ 30%, in Fig. 3.8b, to $\sim$ 80%. This chemical reaction with OH$^-$ would be significantly greater than the electrochemical production of OH$^-$, leading to a decreased pH boundary layer forming in the flow, in which the gas CO_2 feed is used primarily to buffer the KOH. This boundary layer would be comprised of carbonate and bicarbonate and suffer from lower conductivity, and in a recirculated electrolyte would eventually react with enough feed CO_2 to effectively become KHCO3. In this case the share of CO_2 converted to CO would actually be improved by increasing overpotential at the cost of FE.

Circumvention of scaling issues can be preferable to prevention, so alternative parallelised geometries can be employed to retain short channels and high performance. Splitting one long channel into multiple shorter channels would require each shorter channel to maintain a comparable flow rate to and thus pressure drop to achieve greater performance, so it would be preferable to use entirely distinct shorter channels with separate inlets and outlets. While techno-economic assessments often consider MEAs without catholyte buffers, Badgett et al. showed that the inclusion of a catholyte buffer layer improves performance [10] and only requires an increase in the capital cost of the system by around 1% [1]. The supply of catholyte at sufficient flow rates to multiple channels within a cell or stack could necessitate additional equipment and, from a holistic perspective, could complicate full-scale stack designs.

Alternatively, the problem can be addressed at the source: the high production rate of OH$^-$ ions. While the production of OH$^-$ due to the reduction reaction (Eq. (3.1)) is necessary and unavoidable, the low FE shows that the HER (Eq. (3.2)) rate is unnecessarily high, especially in the regions with low j_{CO}. The low j_{CO} is due to reactant limitation, not lack of available reaction sites, so by reducing the catalyst loading further along the electrolyser the zeroth order HER would be reduced linearly but the COER would be impacted less as it would remain reactant limited. This would cause an overall reduction in

single pass conversion, but an improvement in FE and reduction in parasitic consumption as the lowered OH^- production from HER would lower the pH in the CL. Variable catalyst loading the flow direction will be discussed in more depth in a forthcoming paper, and a brief demonstration of the efficacy of the proposed solution can be found in SI Section 3.

3.5. CONCLUSION

We have developed a large scale 2D computational model of a CO_2 reduction flow cell, and showed through comparison of a 4 cm lab scale model and a 100 cm upscaled model that the performance metrics of FE, conversion, and voltage efficiency decrease with electrolyser length. We found that poor electrolyte buffering due to increasing boundary layer thickness in the flow channel leads to reaction inhomogeneity in the flow direction and poor utilisation of the outlet regions of the electrolyser, resulting in a system that struggles to match performance benchmarks set in lab scale electrolysers. While some mitigation strategies have been suggested, such as electrolyte mixing, catalyst loading variation and flow channel optimisation, it is recommended that future experimental studies test these strategies and acknowledge that not only will the necessary current densities for industrial realisation be greater than those commonly assumed in lab scale studies, but the local reaction environments will be far less favourable than those present in typical lab scale electrolysers.

3.6. ADDITIONAL THEORY

3.6.1. CENTRAL CHANNEL CONTINUITY

As the electrolyte flow channel is decomposed into two subchannels, the boundaries must be specified. It is assumed that the boundary layer thicknesses at each side of the channel are sufficiently less than half the channel width so that the electrolyte is fully equilibrated at the centre and the electrolytic composition in the neighbourhoods of the mid-channel divide are equal. In the case where boundary layer thicknesses are comparable to the half-channel width, the computational domains can be slightly reshaped as the boundary layer development at the membrane will differ from that at the catalyst layer boundary due to it being dependent on different species with different diffusivities: CO_2 and H^+ at the membrane and CO_3^{2-} and OH^- at the catalyst layer. Continuity at the mid-channel divide is simply given by

$$c_{i,\text{left}} = c_{i,\text{right}}, \tag{3.34}$$

and as the acidic and alkaline homogeneous reaction pathways share equilibrium constants this should be trivially true provided the boundary layers do not approach the divide.

3.6.2. ANALYTICAL COMPARISON

In Fig. 5(a) in the main text, the Reynolds-Sherwood-Schmidt correlation [26] used for the mass transfer boundary by Weng et al. in Ref. [62] is given by

$$k_{\text{MT}} = 0.664 \frac{D}{L} \left(\frac{\rho_l U L}{\mu_l} \right)^{\frac{1}{2}} \left(\frac{\mu_l}{\rho_l D} \right)^{\frac{1}{3}}, \tag{3.35}$$

and is a similarity solution, original derived for heat transfer, in co-developing momentum and diffusion boundary layers. It is questionably relevant for the flows we consider, as the hydrodynamic entrance length is small and often comparable to the flow inlet region, so the momentum boundary layer is likely only co-developing for a small portion of the channel length. The computational model however, follows a curve closely matching the Lévêque approximation [6, 42], which is derived from the advection-diffusion equation neglecting co-flow diffusion, and is given by

$$\delta = 1.607\left(\frac{W_{\text{EL}}Dz}{U}\right)^{\frac{1}{3}} \tag{3.36}$$

for Poiseuille flow. This roughly leads to the $z^{\frac{1}{3}}$ dependence seen in Fig. 5(a) and Fig. 5(c) in the main text. However, the advection-diffusion equation does not include the effect of homogeneous reactions. A more detailed description of this can be found in Lin et al. [44] in which a bicarbonate buffer system is included through a modified Graetz-Lévêque approach leading to a modified Lévêque scaling for Sherwood number multiplied by a stoichiometry dependent reaction factor ($\frac{1}{2}$ in the diffusion limited regime) in parallel with the surface reaction Damköhler number. For diffusion limited regimes, this means that $z^{\frac{1}{3}}$ scaling should be retained, but we do not attempt to include more details due to the differences in geometry, with the analytical model more closely representing an H-cell than a gas-diffusion electrode, and the incomplete treatment of the buffer ion transport. This work does not include electromigration however. The analytical approximation in Fig. 5(b) in the main text comes from the solution to the 1D reaction-diffusion equation laid out in Blake et al. [7],

$$-D\frac{\partial^2 c}{\partial x^2} = \frac{a_{\text{v}}i}{2F}\frac{c}{c_{\text{ref}}}\exp\left(\frac{-\eta}{b}\right) + \epsilon k_1 c\langle c_{\text{OH}^-}\rangle, \tag{3.37}$$

in which only the fast homogeneous forward reaction between OH^- and CO_2 and the heterogeneous reaction are considered. Collapsing the reaction rate terms into a single first order reaction rate constant k, the solution can be written as

$$c = c_0 \frac{\cosh M_{\text{T}}(1 - \frac{x}{W_{\text{CL}}})}{\cosh M_{\text{T}}} \tag{3.38}$$

where $M_{\text{T}} = \sqrt{\frac{kW_{\text{CL}}^2}{D_{\text{CO}_2}}}$ is known as the Thiele modulus and

$$k = \frac{a_{\text{v}}i}{2F}\frac{1}{c_{\text{ref}}}\exp\left(\frac{-\eta}{b}\right) + \epsilon k_1\langle c_{\text{OH}^-}\rangle \tag{3.39}$$

. While in the original work, the OH^- concentration is simultaneously determined analytically, in this work we simply insert the computationally determined average OH^- concentration to yield the analytical CO_2 profile in the CL.

3.6.3. SALTING-OUT

The Sechenov equation effectively modifies Henry's constant, $\mathcal{H}_{\text{CO}_2,0}$ in the presence of high ion concentrations, and can be written as

$$\mathcal{H}_{\text{CO}_2} = 10^{-\left(S_{\text{KHCO}_3} c_{\text{HCO}_3^-} + S_{\text{K}_2\text{CO}_3} c_{\text{CO}_3^{2-}} + S_{\text{KOH}} c_{\text{OH}^-}\right)}\mathcal{H}_{\text{CO}_2,0} \tag{3.40}$$

where the values of S_i can be determined from measurements and methods detailed by Schumpe et al. [61]. This formulation builds on the one used in [7], correcting a misuse of the natural logarithm, but attaining similar trends for ionic strengths at which the equation is valid.

Salt	$S\,[\mathrm{m^3\,kmol^{-1}}]$
$KHCO_3$	0.1579
K_2CO_3	0.2802
KOH	0.1451

Table 3.2: Values of S for the three salts in the electrolyte

3.7. ADDITIONAL PLOTS

The pH within the CL develops exceptionally quickly in the 100 cm case due to the increased potential, as seen in Fig. 3.10, leading to a pH gradient in excess of the entire 4 cm case within the first subcell. While the pH stabilises further along the electrolyser, this
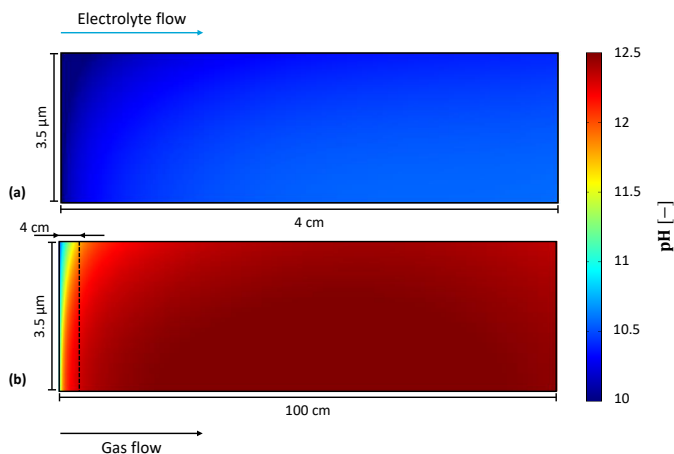
Figure 3.10: The pH within the CL for (a), the 4 cm case, and (b), the 100 cm case. The local j_{tot} in the first 4 cm of the 100 cm model far far exceeds that of the 4 cm model, and as such the pH increase is far greater. The combined effects of the Nernstian potential shift and increased reaction with OH^- lead to a lower j_{tot} across the rest of the of the electrolyser.

has to be qualified with the knowledge that the CO_2 current density is rapidly decreasing over the same length. This reduction in current density should lead to a reduction in OH^- generation and pH, but the depletion of the buffer and thickening of the concentration boundary layer prohibit this, as seen in Fig. 3.11. In the 100 cm case the pH increase is so severe that the variation in pH passes through the half channel line. It is urgent to note that, while the channel is divided into two sections for the purposes of modelling, this does not mean that the pH profile stops developing past this point. The diffusion, migration, and homogeneous reactions of species still occur, but the pathway for homogeneous kinetic reaction rate is determined by an acidic pathway (i.e. reaction with H^+) rather
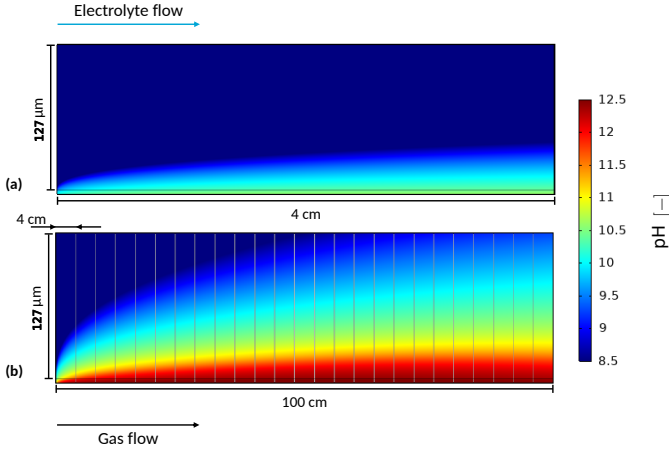
Figure 3.11: The pH within the cathode half of the catholyte channel for (a), the 4 cm case, and (b), the 100 cm case, with the subcells indicated in the 100 cm case. The 4 cm model only reaches a low pH and is short enough that the boundary layer only spans a small portion of the channel thickness. However, the 100 cm model pH boundary layer again grows far more rapidly even in the first 4 cm subcell, and continues to do so until the pH change begins to reach the half-channel divide.

than alkaline. This only has an effect on the results when the reaction of CO_2 to HCO_3^- is out of equilibrium, which only occurs in the CL or at the BPM. At the half channel mark, the pH is sufficiently close to neutral that homogeneous reactions remain in equilibrium, and so the trespass of the pH boundary layer over the channel midpoint is not expected to cause any error.

The concentration overpotential can be written by collapsing the reactant term into the exponent and normalising by the Tafel slope, b, to arrive at

$$i_{COER} = i_{0,COER} \exp\left\{ \frac{b \ln \frac{c}{c_0} - \eta}{b} \right\}, \tag{3.41}$$

where η is the activation overpotential and c and c_0 are the local and equilibrium concentrations of CO_2, not to be confused with the reference concentration of 1 M used in the Tafel equation concentration dependence. This is simply a consequence of the way the kinetics were derived, and the solution is to re-scale the exchange current density by a the ratio of the reference and equilibrium concentrations. The equilibrium concentration in this case in this case is set to the equilbrium value given by the Henry constant above (roughly 34 mM). We can further separate out these terms into the Nernstian shift in overpotential at the bulk electrolyte pH,

$$V_{N,0} = E_{0,COER} - \frac{\ln(10)RT}{F} pH_{bulk} \tag{3.42}$$

the Nernstian shift in overpotential at the local electrolyte pH

$$V_N = E_{0,COER} - \frac{\ln(10)RT}{F} pH, \tag{3.43}$$

and the effect of reactant depletion, normalised as a potential,

$$V_{CO_2} = b \ln \frac{c}{c_0}. \tag{3.44}$$

The negatives of these are plotted in Fig. 3.12 and Fig. 3.13, both for the region of the CL closest to the electrolyte channel (x = 0) and for the region of the CL closest to the MPL (x = W_{CL} We find that for high conversions the largest variation in overpotential is invariably from V_{CO_2} as reactant is depleted along the electrolyser. However, for the 100 cm case, the change in pH within the first few centimetres is so large that it exceeds the effects of concentration overpotential for the majority of the length of the electrolyser.
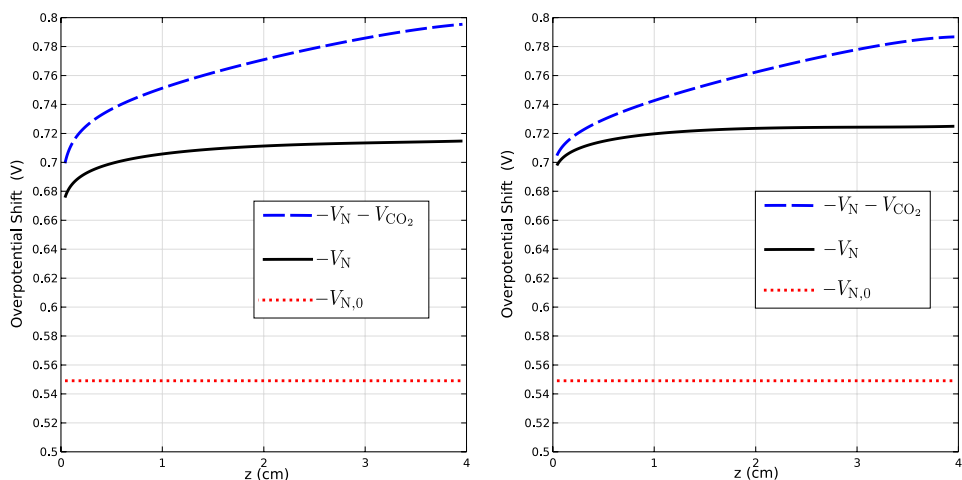
(a) Overpotential contributions at x = 0 in the 4 cm electrolyser model.

(b) Overpotential contributions at the at x = W_{CL} in the 4 cm electrolyser model.

Figure 3.12: Comparisons of overpotential contributions and development along the 4 cm long electrolyser model at 115 mA cm^{-2} and X_{CO_2} = 84% at (a), the channel-CL boundary, and (b), the CL-MPL boundary. The contribution of V_{CO_2} to the total overpotential is greater at the channel than at the MPL boundary due to depletion through the CL. In both cases however, the increase in V_{CO_2} exceeds the increase in V_{Nernst} before at most 1 cm of the electrolyser length, showing that performance losses are almost always dominated by reactant supply at high conversions.

In the 100 cm case it can be seen that the pH and Nernstian potential both decrease slightly towards the outlet. Despite the widening boundary layer, the decrease in available gas-supplied CO_2 at high conversion causes a decrease in the amount of OH^- produced in the CO_2 electroreduction reaction. As we find a figure of only 30% non-electrochemical consumption of the CO_2 gas stream, this means that a reduction in available CO_2 leads to a net reduction in OH^- production. For example, a simplified scenario neglecting buffering catholytes and mass transport would see two CO_2 molecules entering the CL, one being reduced to CO and producing two OH^-, while the other reacting with two OH^- to form HCO_3^- then CO_3^{2-}. In this case the increase or reduction of CO_2 supply has no effect on pH. However, in our case only 30% of the gas-supplied CO_2 reacts with OH^-, so the same two CO_2 molecules would instead lead to one 1.4 CO ions and 0.6 CO_3^{2-} ions,
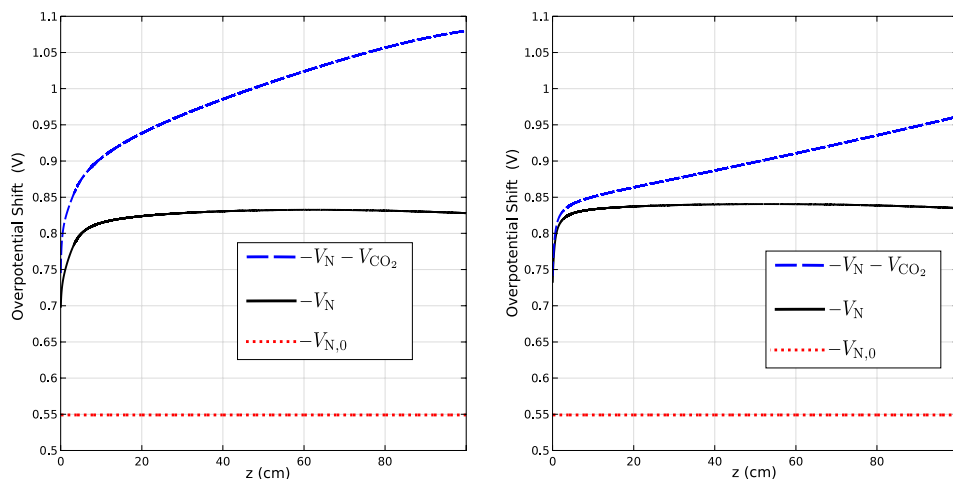
(a) Overpotential contributions at x = 0 in the 100 cm electrolyser model.

(b) Overpotential contributions at x = W_{CL} in the 100 cm electrolyser model.

Figure 3.13: Comparisons of overpotential contributions and development along the 100 cm long electrolyser model at 115 mA cm^{-2} and X_{CO_2} = 74% at (a), the channel-CL boundary, and (b), the CL-MPL boundary. Similarly to Fig. 3.12, the profile for shows V_{CO_2} quickly dominates near x = 0. However, the variation in pH over the first few centimetres is so high that the contribution to V_{Nernst} exceeds that of V_{CO_2} for over half of the electrolyser.

leaving behind 1.6 OH$^-$ ions. This possible as, despite the large concentration boundary layer, the excess OH$^-$ is still buffered away by the HCO$_3^-$ diffusing towards the CL.

The local Faradaic efficiency is shown in Fig. 3.14. While the drop in FE for the 4 cm case is almost entirely due to gas phase reactant depletion, the drop in the 100 cm case is also due to the significant parasitic consumption of reactant through the homogeneous reaction with OH$^-$ at the higher local pH. While this parasitic reaction is still small compared to that observed in high pH catholytes or unbuffered systems, it is compounded by the higher potential necessary to reach the same current density, allowing higher rates of hydrogen evolution to continue unabated in the poorly utilised CL near the outlet. While the potential necessary to achieve the same average current density is higher in the 100 cm case, this only allows it to exceed the current density and FE of the 4 cm case directly at the inlet, z = 0. The resulting change in pH causes some odd behaviour in the FE profile, as we observe a Nernstian shift and a fast transition from a bicarbonate reactor operation mode to a gas-diffusion operation mode. In the 100 cm case this is all resolved within the first 4 cm subcell so subsequent subcells exhibit FEs that develop in a smoother manner, but in the 4 cm case the the lower current density at the inlet means that the pH gradients are small compared to the effect of reactant depletion and the FE develops smoothly throughout. The reactant depletion necessary for high conversion is why the FE after 4 cm is lower in the 4 cm case than the 100 cm, as the latter case has a correspondingly upscaled gas flow rate: a fairer comparison is shown in the insert in Fig. 3.14.
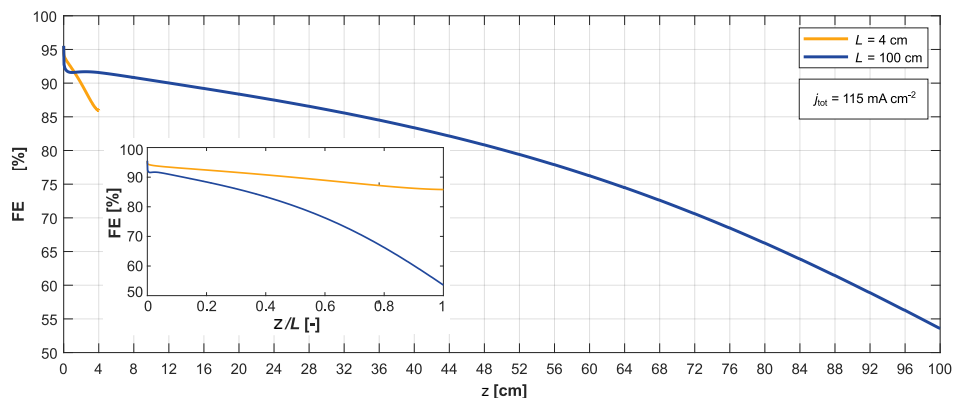
Figure 3.14: FE as function of the electrolyser length, FE(z), at 115 mA cm^{-2} for the 4 cm and 100 cm cases, with an embedded length normalised plot. While the 4 cm case exhibits a rapid drop in FE, this is due to the high conversion ($X_{CO_2} = 84\%$) and consequent depletion of reactant. When normalised by channel length we see that the drop in FE for the 100 cm case is far more dramatic, despite lower conversion ($X_{CO_2} = 74\%$).

3.8. VARIABLE CATALYST LOADING

One of the proposed methods of performance loss mitigation is to vary the catalyst loading in the flow direction. While the desired effect is to improve FE by reducing the amount of catalyst used predominantly for hydrogen evolution in the reactant limited regions in the latter half of the electrolyser, this has the secondary effect of reducing the pH through decreasing the OH$^-$ production in both HER and COER. This reduction in pH reduces the Nernst potential shift and reduces homogeneous reaction rates, leading to a sublinear drop in COER rate with respect to catalyst loading. A schematic of the demonstrative simulation can be found in Fig. 3.15, in which catalyst loading is linearly varied from unity at the inlet to 20% of inlet value in a 10 cm cell. This is achieved by linearly decreasing the exchange current densities of COER and HER, $i_{0,COER}$ and $i_{0,HER}$ respectively, linearly down to 20% of the value listed in the parameter table. In Fig. 3.16 the results show the improvement that even a simple unoptimised implementation of variable catalyst loading can achieve. At relevant current densities, where the reaction becomes reactant limited, the reduced loading case exceeds the CO_2ER current density at a higher FE, and with only 60% of the catalyst used in the control case. This improvement is expected to become even more pronounced in longer cells with lower flow rates, in which reaction inhomogeneity and low FE are more severe.
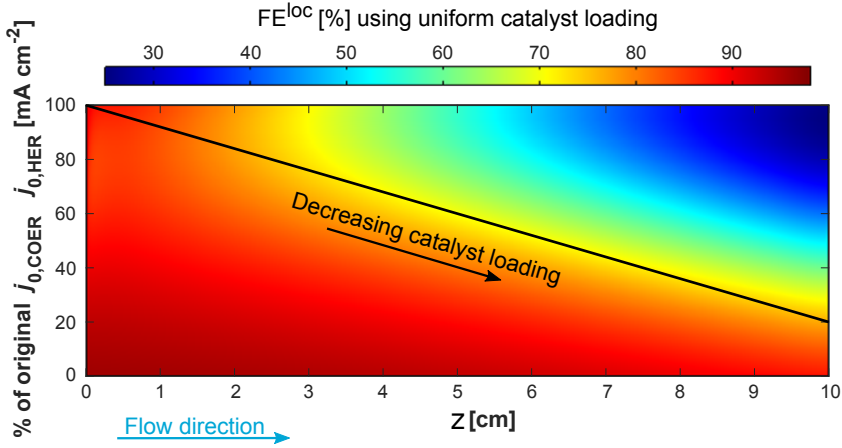
Figure 3.15: In a 10 cm the Faradaic efficiency is highest near the MPL-CL boundary and near the well-buffered inlet region of the electrolyser. Near the outlet and the flow-channel boundary however the high pH and low reactant concentration cause a drop in Faradaic efficiency to below 30%. To circumvent this issue we propose linearly decreasing catalyst loading down to 20% of the initial loading to reduce unnecessary HER and OH^- production in the poorly performing regions.
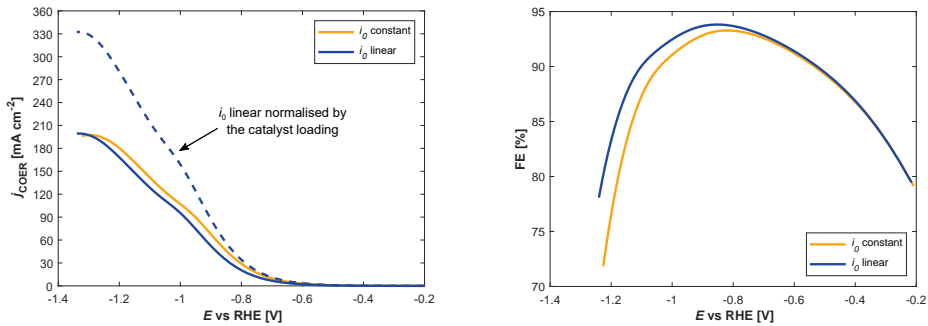
(a) CO_2ER current density against potential for constant catalyst loading and linearly decreasing catalyst loading.

(b) Faradaic efficiency against potential for constant catalyst loading and linearly decreasing catalyst loading.

Figure 3.16: (a) shows the negligible loss of CO_2ER current density in the linearly reducing catalyst loading case. Given that the linear catalyst loading uses 40% less catalyst, we can normalise the CO_2ER current density by total catalyst used. This normalised current density far exceeds that of the constant catalyst loading. (b) shows that the improvement of the linearly decreasing catalyst loading becomes larger with potential as the reactant depletion becomes the limiting factor.

3.9. Parameters

3

Parameter	Description	Value	Unit	Ref.
Operational				
p_{abs}	Gas pressure	1	atm	-
T	Temperature	293.15	K	-
c_{KHCO_3}	Catholyte concentration	500	mM	-
Re	Reynolds number	200	-	-
Geometry				
L	Flow channel length	20	mm	-
W_{EL}	Flow channel thickness	0.254	mm	-
W_{CL}	CL thickness	3.5	μm	[62]
W_{GDL}	GDL thickness	325	μm	[32]
W_{GAS}	Gas channel thickness	3	mm	-
H	Flow channel height	5	mm	-
Electrolyte				
ρ_l	Electrolyte density	998	$kg\,m^{-3}$	[25]
μ_l	Electrolyte dynamic viscosity	1×10^{-3}	Pa s	[25]
$D_{CO_2,(aq)}$	CO_2 diffusion coefficient	1.910×10^{-9}	$m^2\,s^{-1}$	[62]
$D_{HCO_3^-}$	HCO_3^- diffusion coefficient	1.185×10^{-9}	$m^2\,s^{-1}$	[62]
$D_{CO_3^{2-}}$	CO_3^{2-} diffusion coefficient	9.230×10^{-9}	$m^2\,s^{-1}$	[62]
D_{OH^-}	OH^- diffusion coefficient	5.293×10^{-9}	$m^2\,s^{-1}$	[62]
D_{H^+}	H^+ diffusion coefficient	9.311×10^{-9}	$m^2\,s^{-1}$	[62]
GDL Properties				
ϵ_{GDL}	GDL porosity	0.53	-	[32]
σ_{GDL}	GDL conductivity	220	$S\,m^{-1}$	[62]
κ	GDL permeability	1.72×10^{-11}	m^2	[32]
λ	GDL average pore radius	2×10^{-6}	m	[29]
Gas Properties				
ρ_g	Gas density	1.839	$kg\,m^{-3}$	[24]
μ_g	Gas dynamic viscosity	1.469×10^{-5}	Pa s	[24]
$D_{CO_2,CO}$	CO_2/CO binary diffusion coefficient	1.52×10^{-5}	$m^2\,s^{-1}$	[62]
D_{CO_2,H_2}	CO_2/H_2 binary diffusion coefficient	6.46×10^{-5}	$m^2\,s^{-1}$	[62]
D_{CO,H_2}	CO/H_2 binary diffusion coefficient	7.43×10^{-5}	$m^2\,s^{-1}$	[62]
D_{CO_2,N_2}	CO_2/N_2 binary diffusion coefficient	1.65×10^{-5}	$m^2\,s^{-1}$	[62]
D_{CO,N_2}	CO/N_2 binary diffusion coefficient	2.02×10^{-5}	$m^2\,s^{-1}$	[62]
D_{H_2,N_2}	H_2/N_2 binary diffusion coefficient	7.79×10^{-5}	$m^2\,s^{-1}$	[62]

Parameter	Description	Value	Unit	Ref.
CL Properties				
$H_{CO_2,ref}$	Henry's constant for CO_2 in water	3.4×10^{-4}	$mol\,m^{-3}\,Pa^{-1}$	[50]
ϵ_{CL}	CL porosity	0.5	-	-
a_v	CL volumetric surface area	3.75×10^7	m^{-1}	[62]
$\sigma_{s,CL}$	CL conductivity	25	$S\,m^{-1}$	[29]
r_{np}	CL average pore radius	4×10^{-8}	m^{-1}	[62]
k_{CO_2}	MPL-CL CO_2 mass transfer coefficient	1.56×10^{-2}	$m\,s^{-1}$	[29]
Electrochemistry				
E^0_{COER}	CO_2 electroreduction potential	-0.11	V	[23]
$i_{0,COER}$	COER exchange current density	4.71×10^{-4}	$mA\,cm^{-2}$	[62]
α_{COER}	COER charge transfer coefficient	0.44	-	[62]
E^0_{HER}	HER electroreduction potential	0	V	[23]
$i_{0,HER}$	HER exchange current density	1.16×10^{-6}	$mA\,cm^{-2}$	[62]
α_{HER}	HER charge transfer coefficient	0.36	-	[62]
E^0_{OER}	OER electroreduction potential	1.23	V	[63]
$i_{0,OER}$	OER exchange current density	6.21×10^{-5}	$mA\,cm^{-2}$	[63]
α_{OER}	OER charge transfer coefficient	1.5	-	[63]
	(for simplified fitted reaction kinetics)			

Table 3.3: Full list of model parameters

3.10. NUMERICAL METHODS

The computational model was solved in COMSOL Multiphysics 5.6, using coupled transport of diluted species and secondary current distribution physics interfaces in the liquid phase, secondary current distribution in the solid phase, and coupled Darcy flow and transport of concentrated species in the gas phase. Dissolved species concentrations in the liquid phase are replaced with logarithmic variables, through $c_i = e^{C_i} \iff C_i = \log(c_i)$, to ensure positivity. Element sizes are scaled by computational region, with priority given to thin regions with high gradients, namely the CL and electrolyte channel, with element density increasing near interfaces and boundaries. Element volumes (2D) range from 10^{-11} m² in and around the CL to 10^{-8} m² in the gas channel. A preliminary stationary solver was ramped from open circuit potential up to the working potential in the inlet subcell, which was then used as the initial conditions for the full cell model.

BIBLIOGRAPHY

[1] Alex Badgett et al. "An economic analysis of the role of materials, system engineering, and performance in electrochemical carbon dioxide conversion to formate". In: *Journal of Cleaner Production* 351 (2022), p. 131564. ISSN: 0959-6526.

[2] Fazele Karimian Bahnamiri et al. "Techno-economic assessment of a novel power-to-liquid system for synthesis of formic acid and ammonia, based on CO_2 electroreduction and alkaline water electrolysis cells". In: *Renewable Energy* 187 (2022), pp. 1224–1240. ISSN: 0960-1481.

[3] Lorenz M. Baumgartner et al. "Narrow Pressure Stability Window of Gas Diffusion Electrodes Limits the Scale-Up of CO_2 Electrolyzers". In: *ACS Sustainable Chemistry & Engineering* 10.14 (2022), pp. 4683–4693.

[4] Lorenz M. Baumgartner et al. "When Flooding Is Not Catastrophic-Woven Gas Diffusion Electrodes Enable Stable CO_2 Electrolysis". In: *ACS Applied Energy Materials* 5.12 (2022), pp. 15125–15135.

[5] Gordon S. Beavers and Daniel D. Joseph. "Boundary conditions at a naturally permeable wall". In: *Journal of Fluid Mechanics* 30.1 (1967), pp. 197–207.

[6] Ali Belhocine and Wan Zaidi Wan Omar. "Similarity solution and Runge Kutta method to a thermal boundary layer model at the entrance region of a circular tube". In: *World Journal of Engineering* 10 (2018), pp. 1–10.

[7] J.W. Blake, J.T. Padding, and J.W. Haverkort. "Analytical modelling of CO_2 reduction in gas-diffusion electrode catalyst layers". In: *Electrochimica Acta* 393 (2021), p. 138987. ISSN: 0013-4686.

[8] Marijn A. Blommaert et al. "Orientation of a bipolar membrane determines the dominant ion and carbonic species transport in membrane electrode assemblies for CO_2 reduction". In: *J. Mater. Chem. A* 9 (18 2021), pp. 11179–11186.

[9] Marijn A. Blommaert et al. "Reduced Ion Crossover in Bipolar Membrane Electrolysis via Increased Current Density, Molecular Size, and Valence". In: *ACS Applied Energy Materials* 3.6 (2020), pp. 5804–5812.

[10] Yingying Chen et al. "A Robust, Scalable Platform for the Electrochemical Conversion of CO_2 to Formate: Identifying Pathways to Higher Energy Efficiencies". In: *ACS Energy Letters* 5.6 (2020), pp. 1825–1833.

[11] Emiliana R. Cofell et al. "Investigation of Electrolyte-Dependent Carbonate Formation on Gas Diffusion Electrodes for CO_2 Electrolysis". In: *ACS Applied Materials & Interfaces* 13.13 (2021). PMID: 33764731, pp. 15132–15142.

[12] Bert De Mot et al. "Insight in the behavior of bipolar membrane equipped carbon dioxide electrolyzers at low electrolyte flowrates". In: *Chemical Engineering Journal* 428 (2022), p. 131170. ISSN: 1385-8947.

[13] B. Endrődi et al. "High carbonate ion conductance of a robust PiperION membrane allows industrial current density and conversion in a zero-gap carbon dioxide electrolyzer cell". In: *Energy Environ. Sci.* 13 (11 2020), pp. 4098–4105.

[14] B. Endrődi et al. "Multilayer Electrolyzer Stack Converts Carbon Dioxide to Gas Products at High Pressure with High Efficiency". In: *ACS Energy Letters* 4.7 (2019). PMID: 31328172, pp. 1770–1777.

[15] B. Endrődi et al. "Operando cathode activation with alkali metal cations for high current density operation of water-fed zero-gap carbon dioxide electrolysers". In: *Nature Energy* 6.4 (2021), pp. 439–448. ISSN: 2058-7546.

[16] S. Erbach et al. "CO_2 Enrichment in Anode Loop and Correlation with CO Poisoning of Low Pt Anodes in PEM Fuel Cells". In: *Fuel Cells* 18.5 (2018), pp. 613–618.

[17] Christine M. Gabardo et al. "Continuous Carbon Dioxide Electroreduction to Concentrated Multi-carbon Products Using a Membrane Electrode Assembly". In: *Joule* 3.11 (2019), pp. 2777–2791. ISSN: 2542-4351.

[18] Akansha Goyal et al. "Competition between CO_2 Reduction and Hydrogen Evolution on a Gold Electrode under Well-Defined Mass Transport Conditions". In: *Journal of the American Chemical Society* 142.9 (2020), pp. 4154–4161.

[19] Kentaro U. Hansen and Feng Jiao. "Hydrophobicity of CO_2 gas diffusion electrodes". In: *Joule* 5.4 (2021), pp. 754–757. ISSN: 2542-4351.

[20] Kohjiro Hara et al. "High Efficiency Electrochemical Reduction of Carbon Dioxide under High Pressure on a Gas Diffusion Electrode Containing Pt Catalysts". In: *Journal of The Electrochemical Society* 142.4 (1995), pp. L57–L59.

[21] Hiroshi Hashiba et al. "Effects of Electrolyte Buffer Capacity on Surface Reactant Species and the Reaction Rate of CO_2 in Electrochemical CO_2 Reduction". In: *The Journal of Physical Chemistry C* 122.7 (2018), pp. 3719–3726.

[22] E. Holzbecher and Weierstrass. "Numerical Solutions for the Lévêque Problem of Boundary Layer Mass or Heat Flux". In: *COMSOL Conference 2008 Hannover* (2008).

[23] Y. Hori. "Electrochemical CO_2 Reduction on Metal Electrodes". In: *Modern Aspects of Electrochemistry* (2008), pp. 89–189.

[24] https://webbook.nist.gov/cgi/cbook.cgi?ID=124-38-9; *NIST Chemistry WebBook, Carbon dioxide.*

[25] https://webbook.nist.gov/cgi/cbook.cgi?ID=C7732185. *NIST Chemistry WebBook, Water.*

[26] FP Incropera and DP Dewitt. "Fundamentals of Heat and Mass Transfer, John Wiley & Sons Inc". In: *New-york, p A5 A* 7 (1990).

[27] Philippe Jeanty et al. "Upscaling and continuous operation of electrochemical CO_2 to CO conversion in aqueous solutions on silver gas diffusion electrodes". In: *Journal of CO_2 Utilization* 24 (2018), pp. 454–462. ISSN: 2212-9820.

[28] Matthew Jouny, Wesley Luc, and Feng Jiao. "General Techno-Economic Analysis of CO_2 Electrolysis Systems". In: *Industrial & Engineering Chemistry Research* 57.6 (2018), pp. 2165–2177.

[29] Recep Kas et al. "Along the Channel Gradients Impact on the Spatioactivity of Gas Diffusion Electrodes at High Conversions during CO_2 Electroreduction". In: *ACS Sustainable Chemistry & Engineering* 9.3 (2021), pp. 1286–1296.

[30] Recep Kas et al. "Modeling the Local Environment within Porous Electrode during Electrochemical Reduction of Bicarbonate". In: *Industrial & Engineering Chemistry Research* 61.29 (2022), pp. 10461–10473.

[31] Robert J. Kee, Michael E. Coltrin, and Peter Glarborg. *Chemically Reacting Flow, Theory and Practice.* English. Wiley, 2003.

[32] Ahmad El-kharouf et al. "Ex-situ characterisation of gas diffusion layers for proton exchange membrane fuel cells". In: *Journal of Power Sources* 218 (2012), pp. 393–404. ISSN: 0378-7753.

[33] Ying Kong et al. "Visualisation and quantification of flooding phenomena in gas diffusion electrodes (GDEs) used for electrochemical CO_2 reduction: A combined EDX/ICP–MS approach". In: (2022).

[34] Yosra Kotb et al. "Modeling of a Microfluidic Electrochemical Cell for the Electro-Reduction of CO_2 to CH_3OH". In: *Journal of The Electrochemical Society* 164.13 (2017), E391–E400.

[35] Robert B. Kutz et al. "Sustainion Imidazolium-Functionalized Polymers for Carbon Dioxide Electrolysis". In: *Energy Technology* 5.6 (2017), pp. 929–936.

[36] Gastón O. Larrazábal, Ming Ma, and Brian Seger. "A Comprehensive Approach to Investigate CO_2 Reduction Electrocatalysts at High Current Densities". In: *Accounts of Materials Research* 2.4 (2021), pp. 220–229.

[37] Chia-Yen Lee et al. "Microfluidic Mixing: A Review". In: *International Journal of Molecular Sciences* 12.5 (2011), pp. 3263–3287. ISSN: 1422-0067.

[38] ChungHyuk Lee et al. "Bubble Formation in the Electrolyte Triggers Voltage Instability in CO_2 Electrolyzers". In: *iScience* 23.5 (2020), p. 101094. ISSN: 2589-0042.

[39] Eric W. Lees et al. "Electrodes Designed for Converting Bicarbonate into CO". In: *ACS Energy Letters* 5.7 (2020), pp. 2165–2173.

[40] Eric W. Lees et al. "Gas diffusion electrodes and membranes for CO2 reduction electrolysers". In: *Nature Reviews Materials* 7.1 (2022), pp. 55–64. ISSN: 2058-8437.

[41] Mclain Leonard et al. "Investigating Electrode Flooding in a Flowing Electrolyte, Gas-Fed Carbon Dioxide Electrolyzer". In: *ChemSusChem* 13 (Nov. 2019), pp. 400–411.

[42] André Lévêque. "Les lois de la transmission de chaleur par convection". PhD thesis. Faculté des Sciences de Paris, 1928.

[43] Yuguang C. Li et al. "Bipolar Membranes Inhibit Product Crossover in CO_2 Electrolysis Cells". In: *Advanced Sustainable Systems* 2.4 (2018), p. 1700187.

[44] Tiras Y. Lin et al. "Analysis of the Reactive CO_2 Surface Flux in Electrocatalytic Aqueous Flow Reactors". In: *Industrial & Engineering Chemistry Research* 60.31 (2021), pp. 11824–11833.

3

[45] Ming Ma et al. "Insights into the carbon balance for CO_2 electroreduction on Cu using gas diffusion electrode reactor designs". In: *Energy Environ. Sci.* 13 (3 2020), pp. 977–985.

[46] Ming Ma et al. "Role of ion-selective membranes in the carbon balance for CO_2 electroreduction via gas diffusion electrode reactor designs". In: *Chem. Sci.* 11 (33 2020), pp. 8854–8861.

[47] R. J. Millington and J. P. Quirk. "Permeability of porous solids". In: *Trans. Faraday Soc.* 57 (0 1961), pp. 1200–1207.

[48] Nathan T. Nesbitt and Wilson A. Smith. "Water and Solute Activities Regulate CO_2 Reduction in Gas-Diffusion Electrodes". In: *The Journal of Physical Chemistry C* 125.24 (2021), pp. 13085–13095.

[49] Danielle A. Salvatore et al. "Designing anion exchange membranes for CO2 electrolysers". In: *Nature Energy* 6.4 (2021), pp. 339–348. ISSN: 2058-7546.

[50] R. Sander. "Compilation of Henry's law constants (version 4.0) for water as solvent". In: *Atmospheric Chemistry and Physics* 15.8 (2015), pp. 4399–4981. ISSN: 16807324.

[51] M. Sechenov. "On the behavior of salt solutions based on their relation to carbon dioxide". In: *Z. Phys. Chem.* (1889), pp. 117–125.

[52] Omnia A. El-Shafie et al. "Modeling and Numerical Investigation of the Performance of Gas Diffusion Electrodes for the Electrochemical Reduction of Carbon Dioxide to Methanol". In: *Industrial & Engineering Chemistry Research* 59.47 (2020), pp. 20929–20942.

[53] Joshua M. Spurgeon and Bijandra Kumar. "A comparative technoeconomic analysis of pathways for commercial electrochemical CO_2 reduction to liquid products". In: *Energy Environ. Sci.* 11 (6 2018), pp. 1536–1551.

[54] E. W. Thiele. "Relation between Catalytic Activity and Size of Particle". In: *Industrial & Engineering Chemistry* 31.7 (1939), pp. 916–920.

[55] Robert Tichler et al. *Power-to-Gas: Technology and Business Models.* Jan. 2014. ISBN: 978-3-319-03994-7.

[56] Bernhard Tjaden et al. "On the origin and application of the Bruggeman correlation for analysing transport phenomena in electrochemical systems". In: *Current Opinion in Chemical Engineering* 12 (2016). Nanotechnology / Separation Engineering, pp. 44–51. ISSN: 2211-3398.

[57] Ramato Ashu Tufa et al. "Towards highly efficient electrochemical CO2 reduction: Cell designs, membranes and electrocatalysts". In: *Applied Energy* 277 (2020), p. 115557. ISSN: 0306-2619.

[58] Sumit Verma et al. "A Gross-Margin Model for Defining Technoeconomic Benchmarks in the Electroreduction of CO_2". In: *ChemSusChem* 9.15 (2016), pp. 1972–1979.

[59] Sumit Verma et al. "The effect of electrolyte composition on the electroreduction of CO_2 to CO on Ag based gas diffusion electrodes". In: *Phys. Chem. Chem. Phys.* 18 (10 2016), pp. 7075–7084.

[60] Ning Wang et al. "Suppressing the liquid product crossover in electrochemical CO_2 reduction". In: *SmartMat* 2.1 (2021), pp. 12–16.

[61] S. Weisenberger and A. Schumpe. "Estimation of gas solubilities in salt solutions at temperatures from 273 K to 363 K". In: *Aiche Journal* 42 (1996), pp. 298–300.

[62] Lien-Chun Weng, Alexis T. Bell, and Adam Z. Weber. "Modeling gas-diffusion electrodes for CO_2 reduction". In: *Phys. Chem. Chem. Phys.* 20 (25 2018), pp. 16973–16984.

[63] Lien-Chun Weng, Alexis T. Bell, and Adam Z. Weber. "Towards membrane-electrode assembly systems for CO_2 reduction: a modeling study". In: *Energy Environ. Sci.* 12 (6 2019), pp. 1950–1968.

[64] Devin T. Whipple, Eryn C. Finke, and Paul J. A. Kenis. "Microfluidic Reactor for the Electrochemical Reduction of Carbon Dioxide: The Effect of pH". In: *Electrochemical and Solid-State Letters* 13.9 (2010), B109.

[65] Kunna Wu et al. "Modeling and Experimental Validation of Electrochemical Reduction of CO_2 to CO in a Microfluidic Cell". In: *Journal of The Electrochemical Society* 162.1 (2014), F23–F32.

[66] Zhuo Xing et al. "Enhancing carbon dioxide gas-diffusion electrolysis by creating a hydrophobic catalyst microenvironment". In: *Nature Communications* 12.1 (2021), p. 136. ISSN: 2041-1723.

[67] Yi Xu et al. "Self-Cleaning CO_2 Reduction Systems: Unsteady Electrochemical Forcing Enables Stability". In: *ACS Energy Letters* 6.2 (2021), pp. 809–815.

[68] Kailun Yang et al. "Role of the Carbon-Based Gas Diffusion Layer on Flooding in a Gas Diffusion Electrode Cell for Electrochemical CO_2 Reduction". In: *ACS Energy Letters* 6.1 (2021), pp. 33–40.

[69] Ziming Yang et al. "Modeling and Upscaling Analysis of Gas Diffusion Electrode-Based Electrochemical Carbon Dioxide Reduction Systems". In: *ACS Sustainable Chemistry & Engineering* 9.1 (2021), pp. 351–361.

[70] Jie Zhang, Wen Luo, and Andreas Züttel. "Crossover of liquid products from electrochemical CO_2 reduction through gas diffusion electrode and anion exchange membrane". In: *Journal of Catalysis* 385 (2020), pp. 140–145. ISSN: 0021-9517.

3

4

OPTIMISATION OF VARIABLE CATALYST LOADING IN CO$_2$ ELECTROREDUCTION

The electrochemical conversion of CO$_2$ is a promising method of carbon-neutral chemical production. However, commercial realisation in aqueous electrolytes is challenging, due to competition with the hydrogen evolution reaction (HER), and the propensity for CO$_2$ to participate in the carbonate equilibrium reactions. These two phenomena are linked through OH$^-$ ions, as both the by-product of the catalytic reactions and the culprit behind the parasitic carbonate reactions. By reducing the local catalyst loading where the CO$_2$ concentration is low, the HER is decreased more than the reactions that are dependent on CO$_2$ as a reactant. Therefore, it is possible to improve reaction selectivity and reactant utilisation while reducing the capital cost of catalyst. We demonstrate this theory through an analytical solution of a 1D flow electrolyser model. We extend this to a comprehensive model of a contemporary gas-diffusion electrode (GDE) setup. We find that the operation costs are dominated by the electrolyser power consumption and, to a lesser degree the cost of CO$_2$ and its recovery at the anode. We numerically obtain the catalyst loading profiles that maximise operating profit. The optimisation process reveals that profits are maximised for high gas flow rates, and consequently low single pass conversions, where the CO$_2$ concentration is as high as possible. However, when lower gas flow rates are used for practical reasons, variable catalyst loadings are shown to lead to significant operational improvements, especially in the production of higher C products that require a greater number of electrons transferred.

4.1. Introduction

As improvements in the fundaments of CO_2 electroreduction (CO_2ER) shift the field closer to industrial readiness, the focus on groundbreaking new insights naturally gives way to a focus on delicate optimisation and pragmatism. Catalysts are expected to be tested in less forgiving conditions [5, 21, 27, 19], cells are expected to be stable even in the presence of feedstock impurities [31, 6], electrolysers are expected to be scalable to industrial sizes [11, 3, 7], and techno-economic assessments (TEAs) are taking centre stage for their insights on realistic limitations. [29]

Even at the laboratory scale, CO_2 electrolysers can exhibit non-uniformity. Simonson et al. showed a significant change in product selectivity over the reactor path in a gas-diffusion electrode (GDE) [28], and computational models have investigated these effects in limiting cases [13, 3]. These non-uniformities are potentially due to a number of changes to the environments of the electrolyte, the catalyst layer, and the diffusion media, as well as due to the inherent reduction in reactant availability in high single-pass conversion setups. Circumventing these issues usually comes at some great cost; reductions in conductivity, reactant utilisation, faradaic efficiency (FE), mass transport, and current density are seldom greater detriments to cell performance than the non-uniformities.

Noting the insights of Kulikovsky into polymer electrolyte fuel cell (PEFC) catalyst optimisation [16, 17], we propose that CO_2 electroreduction can benefit greatly from catalyst loading optimisation. While Kulikovsky's work elegantly homogenises local current along the oxygen channel of a PEFC [18], the CO_2ER is complicated by the bicarbonate buffer system, a variable product spectrum, and an often unwanted hydrogen evolution (HER) side reaction. These effects are susceptible to modification through changes in local catalyst loading, and we propose a surprisingly efficacious model and method of catalyst loading optimisation for CO_2ER.

Many literature studies focus on a single aspect of a system, and often the improvement of such an aspect comes at the great cost of another aspect outside of the scope of that study. This is often the case in CO_2ER, with studies that optimise FE, conversion, cell potential, or reactant utilisation, but only by sacrificing their complementary aspects. For instance, a high single pass conversion necessarily involves reactant depletion, which will lead to a drop in FE. One must consider whether the improvement in one aspect is worth the trade-off in another. This is the core of the idea behind variable catalyst loading, as local reducing the amount of available catalyst will clearly reduce the ability of the system to convert reactant in that region, but in return it can produce a more favourable environment in terms of selectivity and reactant utilisation. There are a large number of interacting aspects relevant when considering a GDE system, so we first lay out the basic idea before continuing.

4.2. 1D flow cell model

In the case of a well-mixed, flow-driven electrochemical reactor with a flow channel of length L, we can approximately model the system with a 1D first-order reaction-advection

equation on the interval [0,L],

$$U\frac{\partial c}{\partial x} + kc = 0, \qquad c(0) = c_0, \tag{4.1}$$

where U is flow velocity, c is reactant concentration, c_0 is initial reactant concentration, and k [s^{-1}] is the (effective, volumetric, first order) reaction rate. To transform this into an equation for CO$_2$ER we must make some assumptions. We first note that the reaction usually takes place in neutral or alkaline media, so we will henceforth assume only the alkaline pathways of reactions. We take c to be the concentration of CO$_2$ and assume reactions of the form:
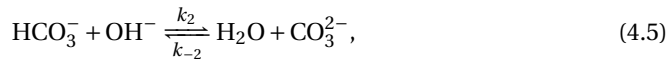
$$CO_2 + ne^- \xrightarrow{k} nOH^- + P, \tag{4.2}$$

where n is the number of electrons transferred per CO$_2$ molecule, k is the first order reaction rate and P denotes the products and, with a negative sign, other reactants like water. While only considering first order reactions may appear to strongly limit the generality, generally n is an integer multiple of two for each product pathway. Therefore, we can safely treat reactions to C$_{2+}$ products that involve two CO$_2$ molecules by halving the reaction terms to preserve the form in (4.2). Furthermore we note that there is also a parallel hydrogen evolution reaction in the form of

$$2H_2O + 2e^- \xrightarrow{k_{H_2}} 2OH^- + H_2, \tag{4.3}$$
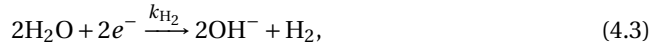
where it is assumed that the concentration of the H$_2$O reactant remains constant and uniform and k_{H_2} [mol m^{-3} s^{-1}] is the zeroth order reaction rate.

Due to the production of OH$^-$ in (4.2) and (4.3), the local environment will be in the neutral to alkaline pH range. The buffer reactions,

$$CO_2 + OH^- \underset{k_{-1}}{\overset{k_1}{\rightleftharpoons}} HCO_3^-, \tag{4.4}$$

$$HCO_3^- + OH^- \underset{k_{-2}}{\overset{k_2}{\rightleftharpoons}} H_2O + CO_3^{2-}, \tag{4.5}$$

convert CO$_2$ to bicarbonate (HCO$_3^-$) and carbonate (CO$_3^{2-}$) in an attempt to reduce the pH. The forward and backward reaction rate constants $k_{1,-1}$ and $k_{2,-2}$ pertain to conversion to HCO$_3^-$ and CO$_3^{2-}$, respectively. The rate constants k_2 and k_{-2} are relatively large, so it is almost always the case that HCO$_3^-$, OH$^-$, and CO$_3^{2-}$ are in equilibrium, but k_1 and k_{-1} are much smaller, so it is often the case that CO$_2$ is out of equilibrium with OH$^-$ and HCO$_3^-$. Moore et al. exploited this disparity to develop simplified models for the buffer system at varying pH ranges [24].

4.2.1. CATALYST LOADING

Catalyst loading is usually expressed in units of mg cm^{-2}, but here the focus is on the relative catalyst loading. We will exclusively use a dimensionless catalyst loading $\theta \in [0,1]$, where $\theta = 1$ corresponds to the maximal catalyst loading at the inlet of the reactor. We assume that the electrochemical reaction kinetics are linear in catalyst loading and

therefore express the (effective, volumetric) electrochemical reaction rates [mol/m^3/s] as

$$R_{CO_2} = \theta c k, \tag{4.6}$$

$$R_{H_2} = \theta k_{H_2} = \frac{\theta c_0 k}{q}. \tag{4.7}$$

Here, $q \equiv c_0 k / k_{H_2}$ is the ratio between the CO_2 and H_2 reaction rate constants at the inlet CO_2 concentration c_0. Larrazábal et al. noted that if the OH^- produced in (4.2) is to immediately and fully react with CO_2 through (4.4) and (4.5), then maximum conversion efficiency is governed by the stoichiometry of the product [19]. That is to say, one mole of CO_2 reactant participating in an electrochemical reaction with n moles of electrons transferred will subsequently cause $\frac{n}{2}$ moles of CO_2 to react with the n moles of electrochemically produced OH^-, limiting conversion efficiency to a maximum of $\frac{2}{n+2}$, with lower values to be expected once the HER is included. Moore et al. cleanly showed that collapsing (4.4) and (4.5) into a single irreversible reaction is valid at high pH, and detailed a simplified model similar to our approach [24]. We still wish to include the effect of OH^- production from the HER (4.3) on the CO_2ER reaction rate. Therefore, we rewrite (4.1) for the evolution of the CO_2 concentration c to

$$\underbrace{U\frac{\partial c}{\partial x}}_{\text{advection}} + \underbrace{\theta c k}_{\text{reduction}} + \underbrace{\frac{n}{2}\theta c k}_{OH^- \text{ from (4.2)}} + \underbrace{\frac{\theta c_0 k}{q}}_{OH^- \text{ from (4.3)}} = 0. \tag{4.8}$$

Here, the $\frac{n}{2}$ term comes from the assumption that each CO_2 electrochemically converted will produce nOH^-, half of which will react with CO_2 via (4.4) and half via (4.5), consuming a total of $\frac{n}{2}$ additional CO_2 molecules. Nondimensionalising gives

$$\frac{\partial \bar{c}}{\partial \bar{x}} + Da\,\theta\left(\left(1+\frac{n}{2}\right)\bar{c}+\frac{1}{q}\right) = 0, \qquad \bar{c}(0) = 1 \tag{4.9}$$

where $\bar{c} \equiv \frac{c}{c_0}$, $\bar{x} \equiv \frac{x}{L}$, and $Da \equiv \frac{kL}{U}$. Da is the initial Damköhler number, representing the ratio between the reaction rate at the inlet (i.e. the reaction rate if the entire channel would have uniform catalyst loading equal to that at the inlet) and convective mass transport. In Ref. [8] an extension of (4.8) is discussed, including the effect of a laminar flow profile and mass transfer resistances between the flow channel and the catalyst layer. The latter can be effected by adding to the inverse of k, in the second and third term, the inverse of a mass transfer coefficient k^t.

The two dimensionless metrics of primary interest are the faradaic efficiency or selectivity, S, and the inlet-normalised yield, Y,

$$S \equiv \frac{\int_0^L \theta n k c \, dx}{\int_0^L \theta (n k c + 2 k_{H_2}) \, dx} \equiv \frac{\int_0^1 \theta n q \bar{c} \, d\bar{x}}{\int_0^1 \theta (n q \bar{c} + 2) \, d\bar{x}} \tag{4.10}$$

$$Y = \frac{1}{U c_0} \int_0^L \theta k c \, dx = \int_0^1 Da\theta \bar{c} \, d\bar{x}. \tag{4.11}$$

In the second expression of (4.10) the rate constants k and k_{H_2} are assumed to be constant. A figure of note is the cumulative catalyst loading, $\Theta(\bar{x})$, defined by

$$\Theta(\bar{x}) \equiv \int_0^{\bar{x}} \theta(\xi) d\xi, \quad \text{or} \quad \Theta \equiv \int_0^1 \theta(\xi) d\xi. \tag{4.12}$$

The yield, Y, is not to be confused with normalised CO_2 conversion X,

$$X = \frac{1}{U c_0} \int_0^L \theta k \left(\left(1 + \frac{n}{2}\right) c + \frac{c_0}{q} \right) dx = Da \int_0^1 \theta \left(\left(1 + \frac{n}{2}\right) \bar{c} + \frac{1}{q} \right) d\bar{x}, \qquad (4.13)$$

which includes the unwanted buffer reactions. The astute observer may note that by the fundamental theorem of calculus and (4.9), it holds that $X = 1 - \bar{c}(1)$.

The solution to (4.9) for $\theta \equiv 1$ (uniform loading) is

$$\bar{c} = \frac{\left(1 + \left(1 + \frac{n}{2}\right) q\right) e^{-\left(1 + \frac{n}{2}\right) Da\, \bar{x}} - 1}{\left(1 + \frac{n}{2}\right) q} \xrightarrow{q \to \infty} e^{-\left(1 + \frac{n}{2}\right) Da\, \bar{x}} \xrightarrow{n=2} e^{-2 Da\, \bar{x}}. \qquad (4.14)$$

While in the limit of no side-reactions, $q \to \infty$, the concentration stays non-negative, this is not guaranteed for general q. Therefore (4.14) only holds when it gives a positive value and should be replaced by 0 for negative outcomes. Equivalently an additional requirement of $X \leq 1$ can be made to ensure that we remain within the domain of validity of the approximation.

As an example case we consider $n = 2$, corresponding to CO_2 reduction to CO. For $\theta \equiv 1$

$$\bar{c} = \frac{1}{2q} ((1 + 2q) e^{-2 Da\, \bar{x}} - 1). \qquad (4.15)$$

For a linearly decreasing loading, $\theta = 1 - A\bar{x}$, the solution is given by

$$\bar{c} = \frac{1}{2q} \left((1 + 2q) e^{-Da\bar{x}(2 - A\bar{x})} - 1 \right), \qquad (4.16)$$

where $A \in [0, 1]$. A full description and derivation of these solutions, and solutions of additional cases can be found in the Supplementary Information, Section SI 4.5.

We note again that the Damköhler number referred to in (4.9) is specifically for the catalyst loading at the entrance of the channel: the final Damköhler number will depend on the total catalyst loading as ΘDa, with more explanation found in SI 4.5.4.

4.2.2. RESULTS

To determine the effectiveness of a proposed catalyst loading profile we must decide on an effectiveness metric. It is clear from (4.10) that maximising the FE is equivalent to maximising $\bar{c}$, which requires minimising θ (see (4.46) or (4.57)). However, maximising yield, Y, defined in (4.11), will likely require maximising θ. We thus propose a metric $\mathcal{E} = YS$, the product of yield and FE, which combines how much product is made with how efficiently it was attained. This is a necessarily simplistic metric, but a much more in-depth metric is discussed in section 4.3.2.

Fig. 4.1 shows the solution of (4.15) for a homogeneous catalyst loading and $n = 2$. As the ratio q between CO_2 and H_2 reaction rate constants increases, the CO_2 concentration increases due to a decrease in parasitic buffer reactions.

Figs. 4.2 (a) and (b) show the solution of (4.16) for a linearly decreasing catalyst loading and $n = 2$ without homogeneous reactions ($n = 0$ and $q \to \infty$), similar to Kulikovsky [18]. The solutions for this case are discussed in the SI. A maximum effectiveness of 1 can be obtained in this case, for high q and Da. At lower q a maximum arises at intermediate Da.
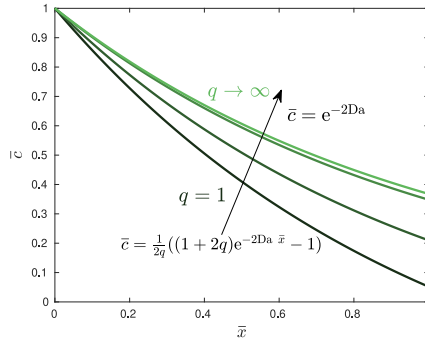
Figure 4.1: The dependency of the normalised concentration $\bar{c}$ in (4.15) on the ratio q of CO_2 and H_2 reaction rates for an $n = 2$ electron reaction with uniform catalyst loading. As q increases, the solution collapses onto the the stoichiometry limited solution proposed in Ref. [19]

Figs. 4.2(c) and (d) include the effect of the homogeneous reactions. It may be noted that the maximum effectiveness does not surpass 0.5. This is due to the maximum yield of 0.5, with OH^- produced by CO_2ER consuming at least half of the CO_2 through the buffer reactions. Otherwise, the results are qualitatively quite similar to those in the absence of buffer reactions.

No direct general improvement in the effectiveness, $\mathcal{E}$, can be obtained by reducing the catalyst loading, but for a fixed Da a decreased catalyst loading can increase the effectiveness. An equal effectiveness can always be obtained using a flat catalyst loading, by choosing the optimal value of Da, and the derivation of optimal values in SI 4.5.4 shows that the reverse is possible too. Any local optimum achieved using a flat catalyst loading can be matched by reducing catalyst loading in a system with a higher fixed Da. Note that, unless q is very large, this optimal Da is typically around or slightly above 1. The reason is that at low Da the concentration varies little and the S is highest. However, at high Da, the conversion and yield are much higher, giving an optimum at intermediate values.

In SI 4.5.4 we also analytically determine the location of the optimal value of the product $Da\Theta$ in terms of q. The solution for the case without buffer reactions can be approximated with a maximum relative error of 11 % by

$$(\Theta Da)_{opt} \approx 1 + \ln\left(\frac{1.2923q}{\ln(1+q)}\right) \tag{4.17}$$

which is exact in the limit $q \to 0$. However, in this limit $\mathcal{E} \to 0$ and for $q \gg 1$ a better approximation is the simple approximation $(\Theta Da)_{opt} \approx \ln(q)$. For the cases with homogeneous reactions, similar results can be found with approximations accurate to about 7 % for low to moderately high $0 \le q \lesssim 10^3$, and exact in the limit of low q,

$$(\Theta Da)_{opt} \approx \frac{2}{3}W(q) \approx \frac{4}{3}\frac{1+q/2}{1+q}\ln\left(\frac{q}{\ln(1+q)}\right), \tag{4.18}$$

and an accurate simple approximation for $q \gtrsim 10^2$ with $(\Theta Da)_{opt} \approx \frac{1}{2}\ln\left(\frac{2q}{3}\right)$ Using (4.17)

and (4.18) the optimal flow velocity can be chosen based on the channel length and reaction rates.

As shown, this approach can reap some benefits in a simple flow reactor. In the most realistic case, Figure 4.2d, it is seen that the same effectiveness can be attained with reduced catalyst loading at a higher Damköhler number, representing a reduction in both capital cost of catalyst and operational pumping costs. We extend the model to a system more suited for industrial CO_2ER to determine the improvements that can be made in the more extreme conditions found in a GDE electrolyser.

4

(a) $\lim\limits_{q\to\infty} \mathcal{E}$, where $\bar{c} = e^{-\mathrm{Da}\,\bar{x}}$

(b) $\mathcal{E}_{q=10}$, where $\bar{c} = e^{-\mathrm{Da}\,\bar{x}}$

(c) $\lim\limits_{q\to\infty} \mathcal{E}$, where $\bar{c} \approx e^{-2\mathrm{Da}\,\bar{x}}$

(d) $\mathcal{E}_{q=10}$, where $\bar{c} = \frac{1}{2q}\left((1+2q)e^{-2\mathrm{Da}\,\bar{x}} - 1\right)$
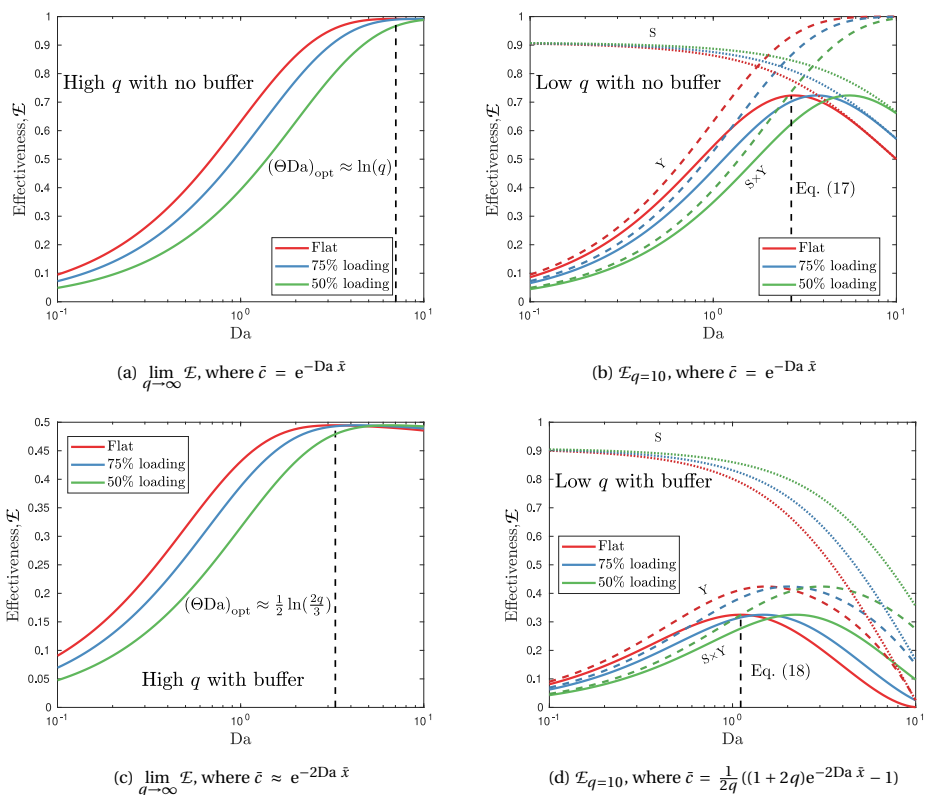
Figure 4.2: A comparison of effectiveness, $\mathcal{E} = \mathrm{YS}$, for linearly decreasing catalyst loadings for the system without homogeneous reactions with high $q \to \infty$, 4.2a, and relatively low $q = 10$, 4.2b and for the system with approximate homogeneous reactions with high $q \to \infty$, 4.2c, and relatively low $q \to \infty$, 4.2d, for an $n = 2$ electron reaction. Red, blue and green colours indicate $A = 0$, 0.5 and 1, corresponding to 100%, 75% and 50% cumulative catalyst loading, respectively. For the low $q = 10$ case, dotted lines show the respective selectivities, S, and dashed lines show the respective yields, Y. In 4.2c and 4.2d the CO$_2$ buffer reactions lower the maximum yield and hence maximum effectiveness to 0.5, although 4.2c still exhibits behaviour similar to 4.2a In the most realistic system, 4.2d, effectiveness remains low throughout due to reaction with OH$^-$ sourced from both the CO$_2$ER (4.2) and HER (4.3).

4.3. GDE MODEL

To overcome the prohibitively low solubility and diffusivity of CO_2 in aqueous electrolytes, GDEs are commonly used to supply gaseous CO_2 as close to the reaction sites as possible, minimising diffusive path length. This means that reactant depletion occurs in a parallel gas channel and we must consider the transport of this depleted reactant to the reaction site. Furthermore, employed electrolytes are commonly optimised for high conductivity (e.g. KOH) or CO_2 saturation and buffer capacity ($KHCO_3$), both of which can affect the local buffer reaction and break the stoichiometric limit of Fig. 4.1. The diagram in Fig. 4.3 shows the normal operation of such an electrolyser, in which gas phase CO_2 is transported from the gas channel through the diffusion medium to dissolve in the electrolyte in the catalyst layer (CL), where it reacts at the catalyst sites. This, along with the undesired HER, produces OH^- ions that then aggressively react with the remaining aqueous CO_2 molecules, forming HCO_3^- and then CO_3^{2-}. Depending on the choice of electrolyte, there are additional sources, or sinks, of CO_2 and OH^- from the electrolyte. If a high pH electrolyte such as KOH is used, the concentration of OH^- in the bulk electrolyte will exceed that in the CL and act as a source, but a lower pH electrolyte can act as a OH^- sink, and in the case of CO_2 saturated $KHCO_3$, even act as a source of reactant CO_2. The extremely high CO_2 mass transfer rate offered by the GDE means that within the CL the CO_2 concentration is often out of equilibrium with the OH^- concentration, although equilibrium is still assumed in (4.5) with CO_3^{2-}. Thus, to model the behaviour upon reducing catalyst loading, as illustrated in Fig. 4.4, we are also required to independently consider the balance of OH^- and gaseous CO_2.

4.3.1. THEORY

First we note that the system is governed by the spatial development of three correlated species: $OH^-_{(aq)}$, $CO_{2(aq)}$, and $CO_{2(g)}$. We also note that there is little variation in the flow-perpendicular in-plane direction, and the characteristic in-plane length scales are far greater than the through-plane length scales, so it is pertinent to reduce the system from 2D to a 1D system with additional relations capturing the through-plane effects. The gas phase is flow-driven and is modelled by a simple ODE. It practically always has a sufficient Péclet number to neglect diffusion in the flow direction, so gas concentration c_g is modelled by

$$-UL_{GC}\frac{\partial c_g}{\partial x} = k_{GC}^t(\mathcal{H}^{cc}c_g - c), \qquad (4.19)$$

with c the average concentration $[CO_2]_{(aq)}$ in the catalyst layer. U is the average flow velocity [m/s] in the gas channel of width L_{GC} and k_{GC}^t is the mass transfer coefficient [m/s] between the gas channel (GC) and catalyst layer (CL). Here, t stands for transport, to make the distinction with reaction rate constants that lack this superscript. $\mathcal{H}^{cc}$ is the dimensionless concentration-to-concentration Henry's constant, which for an ideal gas can be related to the more common partial pressure-to-concentration Henry's constant through $\mathcal{H}^{cc} = \mathcal{H}RT$, where R is the molar gas constant and T is temperature. Introducing an aqueous-equivalent concentration $C \equiv \mathcal{H}^{cc}c_g$ gives

$$-\frac{UL_{GC}}{\mathcal{H}^{cc}}\frac{\partial C}{\partial x} = k_{GC}^t(C - c), \qquad (4.20)$$
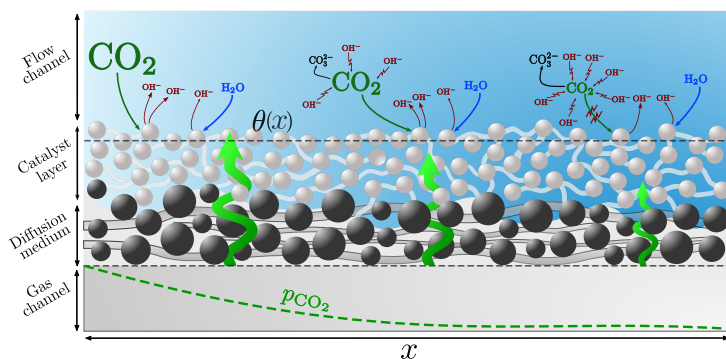
Figure 4.3: A typical GDE flow electrolyser with uniform catalyst loading. High OH$^-$ production leads to high parasitic consumption of CO$_2$ through buffer reactions and severe depletion of both aqueous and gaseous reactant.
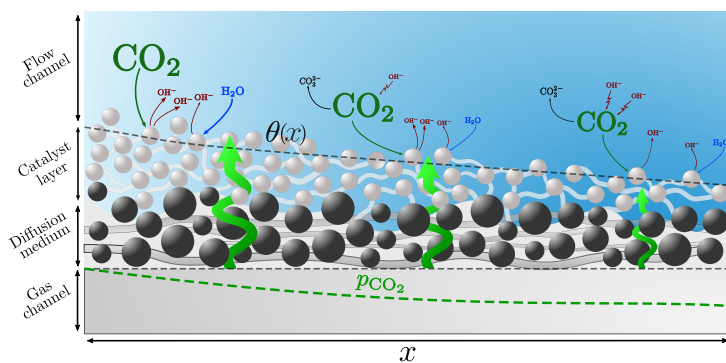
Figure 4.4: A GDE flow electrolyser with progressively decreasing catalyst loading. Lower reduction reaction rates lead to improved CO$_2$ utilisation and reaction selectivity due to lower buffer reaction rates, at the cost of lower single-pass conversion.

We will write the equilibrium concentration in the aqueous phase at the partial pressure of the gas inlet $c_0 = \mathcal{H} p_{\mathrm{CO_2},0} = \mathcal{H}^{\mathrm{cc}} c_{g,0}$. Using this, (4.19) can be nondimensionalised as

$$-\frac{\mathrm{Da_{GC}}}{\mathcal{H}^{\mathrm{cc}}} \frac{\partial \bar{C}}{\partial \bar{x}} = \bar{C} - \bar{c}, \tag{4.21}$$

where $\bar{x} \equiv \frac{x}{L}$, $\bar{C} \equiv \frac{C}{c_0}$, $\bar{c} \equiv \frac{c}{c_0}$. $\mathrm{Da_{GC}} \equiv \frac{U L_{\mathrm{GC}}}{k_{\mathrm{GC}}^{\mathrm{t}} L}$ can be interpreted as a gas channel Damköhler number. Within the catalyst layer there is negligible flow, and the effect of diffusion parallel to the flow channel is minuscule compared to the through-plane interaction with the electrolyte and gas channels. Therefore, we let the spatial variation of the aqueous species along the CL be entirely determined by their local reaction rates and interactions with neighbouring channels. If we again restrict ourselves to the case of $n = 2$, this leads to the following local species balances for $\mathrm{CO_{2\,(aq)}}$ and $\mathrm{OH^-_{\,(aq)}}$ respectively,

$$\underbrace{k_{\mathrm{GC}}^{\mathrm{t}}(C - c)}_{\text{transfer from gas channel}} + \underbrace{k_{\mathrm{CO_2}}^{\mathrm{t}}(c^{\mathrm{B}} - c)}_{\text{transfer from electrolyte channel}} = \underbrace{L_{\mathrm{CL}} \epsilon k c}_{\mathrm{CO_2\,ER\ reaction}} + \underbrace{L_{\mathrm{CL}} \epsilon k_{\mathrm{r}} c_{\mathrm{OH^-}} c}_{\text{homogeneous reaction}}, \tag{4.22}$$

$$\underbrace{k_{\mathrm{OH^-}}^{\mathrm{t}}(c_{\mathrm{OH^-}}^{\mathrm{B}} - c_{\mathrm{OH^-}})}_{\text{transfer from electrolyte channel}} + \underbrace{2L_{\mathrm{CL}} \epsilon k c}_{\mathrm{CO_2\,ER\ reaction}} + \underbrace{2L_{\mathrm{CL}} \epsilon k_{\mathrm{H_2}}}_{\mathrm{H_2\ evolution}} = \underbrace{2L_{\mathrm{CL}} \epsilon k_{\mathrm{r}} c_{\mathrm{OH^-}} c}_{\text{homogeneous reaction}}, \tag{4.23}$$

with $c_{\mathrm{OH^-}}$ the concentration $[\mathrm{OH^-}]_{\mathrm{(aq)}}$ at the catalyst layer. The constants we will use in our model calculations are listed in Table 4.1. Here, $k_{\mathrm{CO_2}}^{\mathrm{t}}$ refers to the mass transfer coefficients [m/s] of $\mathrm{CO_2}$ from the bulk of the electrolyte channel to the CL. The bulk concentrations in the electrolyte channel are given by c^{B} and $c_{\mathrm{OH^-}}^{\mathrm{B}}$, with the B superscript referring to bulk concentration. In each case, mass transfer from neighbouring channels is equated to volumetric sources/sinks due to reactions, averaged across the CL. In (4.22), $\mathrm{CO_2}$ is being supplied by or lost to the electrolyte channel, depending on the value of c^{B} relative to c, and similarly for $c_{\mathrm{OH^-}}^{\mathrm{B}}$ and $c_{\mathrm{OH^-}}$ in (4.23). We note that we will likely see $c_{\mathrm{OH^-}}^{\mathrm{B}} > c_{\mathrm{OH^-}}$ and $c > c^{\mathrm{B}}$ in high pH electrolytes, like KOH, with the reverse being true for neutral pH electrolytes, like $\mathrm{KHCO_3}$. The $\mathrm{CO_2}$ then reacts through the thickness of the CL, L_{CL}, both electrochemically and with $\mathrm{OH^-}$. A similar balance is in (4.23), but with no gas channel transfer. The same homogeneous reaction sink of $\mathrm{CO_{2\,(aq)}}$ on the right-hand side of (4.22) appears for $\mathrm{OH^-_{\,(aq)}}$ on the right-hand side of (4.23). It is doubled due to the second $\mathrm{OH^-}$ ion consumed in converting $\mathrm{HCO_3^-}$ to $\mathrm{CO_3^{2-}}$ in (4.5). The $\mathrm{CO_2\,ER}$ reaction sink $\mathrm{CO_{2\,(aq)}}$ appears doubled and as a source of $\mathrm{OH^-_{\,(aq)}}$, because we consider $n = 2$ in (4.2). Finally, also in the HER source of $\mathrm{OH^-_{\,(aq)}}$ a factor 2 appears, because through (4.3) two $\mathrm{OH^-_{\,(aq)}}$ ions are produced for each $\mathrm{H_2}$.

In non-dimensionalising (4.22) and (4.23) we elect to divide by a characteristic value $\epsilon L_{\mathrm{CL}} k_{\mathrm{r}} c_0 c_{\mathrm{OH^-}}^{\mathrm{B}}$ of the homogeneous term giving

$$\underbrace{\bar{k}_{\mathrm{GC}}^{\mathrm{t}}(\bar{C} - \bar{c})}_{\text{transfer from gas channel}} + \underbrace{\bar{k}_{\mathrm{CO_2}}^{\mathrm{t}}(\bar{c}^{\mathrm{B}} - \bar{c})}_{\text{transfer from electrolyte channel}} = \underbrace{\bar{k}\bar{c}}_{\mathrm{CO_2\,ER\ reaction}} + \underbrace{\bar{c}_{\mathrm{OH^-}} \bar{c}}_{\text{homogeneous reaction}}, \tag{4.24}$$

$$\underbrace{\bar{k}_{\mathrm{H_2}}^{\mathrm{t}}(1 - \bar{c}_{\mathrm{OH^-}})}_{\text{transfer from electrolyte channel}} + \underbrace{\bar{k}\bar{c}}_{\mathrm{CO_2\,ER\ reaction}} + \underbrace{\bar{k}_{\mathrm{H_2}}}_{\mathrm{H_2\ evolution}} = \underbrace{\bar{c}_{\mathrm{OH^-}} \bar{c}}_{\text{homogeneous reaction}}, \tag{4.25}$$
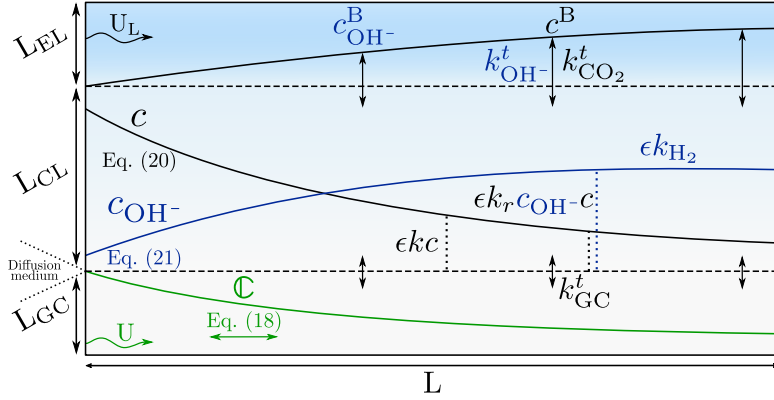
Figure 4.5: Diagram of the numerical system (not to scale). Explicit variation in the flow-wise direction only occurs in the development of $\mathcal{C}$, through (4.20), and in the development of the boundary layer dependent mass transfer coefficients, $k_{OH^-}^t$ and $k_{CO_2}^t$. The concentrations c and c_{OH^-}, governed by (4.22) and 4.23 respectively, depend on these parallel streams, as well as each other and θ.

where $\bar{c}_{OH^-} \equiv \frac{C}{c_{OH^-}^B}$, $\bar{c}^B \equiv \frac{c_B}{c_0}$, $\bar{k}_{GC}^t \equiv \frac{k_{GC}^t}{L_{CL}\epsilon k_r c_{OH^-}^B}$, $\bar{k}_{CO_2}^t \equiv \frac{k_{CO_2}^t}{L_{CL}\epsilon k_r c_{OH^-}^B}$, $\bar{k}_{H_2}^t \equiv \frac{k_{OH^-}^t}{2L_{CL}\epsilon k_r c_0}$, $\bar{k} \equiv \frac{k}{k_r c_{OH^-}^B}$, and $\bar{k}_{H_2} \equiv \frac{k_{H_2}}{k_r c_0}$. Note the division by two in the definition of $\bar{k}_{H_2}^t$, as this will always be a two electron transfer reaction. It is worth noting that $\bar{k}_{CO_2}^t$ and $\bar{k}_{H_2}^t$ are determined by the development of the electrolyte flow channel, and may also be functions of $\bar{x}$ if required, as shown in (4.81).

So far, we have refrained from including the effect of catalyst loading on $\bar{k}$ and $\bar{k}_{H_2}$. This is due to the fact that not all of the HER reaction necessarily takes place on catalyst particles, and some may instead take place on the CL substrate. Yang et al. showed that for catalyst deposited directly onto the GDL, a substantial portion, if not the majority, of HER takes place on the substrate [38]. However, they also showed that for a PTFE-based CL this effect is much less pronounced. HER on the GDL does remain an issue in the case of electrolyte breakthrough and flooding.

We implement the effect of catalyst loading by taking $\bar{k} \to \theta\bar{k}$ for CO$_2$ER but $\bar{k}_{H_2} \to \frac{\theta+\theta_0}{1+\theta_0}\bar{k}$ for HER. Here θ_0 represents the ratio of substrate-based HER to total HER at full catalyst loading. A brief investigation of the impact of nonzero θ_0 is given in SI 4.7.3. Here we will assume that the PTFE content of our CL is sufficient to give $\theta_0 \approx 0$ and so rearrange (4.24) and (4.25) to

$$\bar{c} = \frac{\bar{k}_{GC}^t\bar{C} + \bar{k}_{CO_2}^t\bar{c}^B}{\bar{k}_{GC}^t + \bar{k}_{CO_2}^t + \theta\bar{k} + \bar{c}_{OH^-}}, \tag{4.26}$$

$$\bar{c}_{OH^-} = \frac{\bar{k}_{H_2}^t + \theta\bar{k}\bar{c} + \theta\bar{k}_{H_2}}{\bar{k}_{H_2}^t + \bar{c}}. \tag{4.27}$$

Solving (4.26) and (4.27) for $\bar{c}$ and inserting that into (4.21), we arrive at

$$-\frac{\partial \bar{C}}{\partial \bar{x}} = a\bar{C} + b - \sqrt{\alpha \bar{C}^2 + \beta \bar{C} + \gamma}, \qquad (4.28)$$

where the coefficients are given in (4.89). This equation is solved numerically in MATLAB. Our addition of the additional flow channels requires a more nuanced performance metric, which we will consider now.

4.3.2. PERFORMANCE METRIC

Although the reduction in total catalyst usage will save on electrolyser costs, we focus only on continuous operation efficiency. Factoring in catalyst values would necessitate bold assumptions about total cell material costs and lifespans, both of which are out of the scope of this work. We note that $n = 2$ corresponds to production of CO and consider the following,

$$v_{CO_2}, \quad \text{the price of } CO_2 \text{ in \$ mol}^{-1}, \qquad (4.29a)$$

$$v_{CO}, \quad \text{the price of CO in \$ mol}^{-1}, \qquad (4.29b)$$

$$v_P, \quad \text{the price of electrical energy in \$ J}^{-1}. \qquad (4.29c)$$

We propose the following rough profit metric in units of $ s^{-1}$ m^{-2}

$$Y_\$ = v_{CO}Y^* - v_{CO_2}X^* - v_P(P_e + P_{sep}), \qquad (4.30)$$

which includes the power input per unit area of electrode towards electrolysis P_e and separation P_{sep}, in J s^{-1} m^{-2}. The dimensional product yield and conversion per unit electrode area, Y^* and X^* respectively, in mol s^{-1} m^{-2}:

$$Y^* = \frac{L_H L_{CL}}{A} \int_0^L \theta kc\,dx = X^*_{max} Y \frac{L_{CL}}{L_{GC}}, \qquad (4.31)$$

$$X^* = \frac{U L_H L_{GC}}{A} (c_0 - c(L)) = X^*_{max} X, \qquad (4.32)$$

where L_H is the cell height in the direction normal to the current and the flow and each quantity is normalised by cell area, $A = L_H L$. Here $X^*_{max} = \frac{U L_H L_{GC} c_0}{A} = \frac{U L_{GC} c_0}{L}$ is the maximum conversion per unit area. The faradaic efficiency S remains equal to that in (4.10), inserting $n = 2$. Note that in this $n = 2$ case, producing only CO and H_2, the total rate of electron charge transferred per unit area, C s^{-1} m^{-2}, or the average current density, can be written as

$$j = \frac{2F L_H L_{CL}}{A} \int_0^L \theta(kc + k_{H_2})\,dx = \frac{2F L_{CL} c_0 k}{q} \int_0^1 \theta\left(q\bar{c} + 1\right) d\bar{x} = 2F\frac{Y^*}{S}, \qquad (4.33)$$

where F is Faraday's constant. For a cell potential V, the power per unit area required for electrolysis is

$$P_e = jV = 2F\frac{Y^*}{S}V. \qquad (4.34)$$

Note that separation is currently routinely done through non-electrical means, but we assume future separation equipment will also be electrified. Although the produced H_2 has a value comparable to CO_2 per kg, the low molar mass of H_2 means the market value of the amount produced by HER is almost always negligible ($\approx 1\%$). We include the functionality in the MATLAB code and in the general case of the model, described in SI 4.6.5, but henceforth neglect H_2 in the profit metric. This general case also includes options for non-catalytic HER, electrolyte recombination and recirculation, crossover fractions, and user-defined liquid product separation costs. Often, besides the reactant CO_2 also other species are present at the gas channel inlet. However, for the sake of simplicity, we consider only reactants and products in our outlet gas stream. Therefore, we can approximately consider the energy cost of separation per mole of outlet gas, and then normalise the value by inlet flow rate to get a cost of separation per second. The minimum thermodynamic energy requirement of separation per second and unit area is thus given by

$$P^*_{sep} = -X^*_{sep} RT \sum_i x_i \ln x_i \tag{4.35}$$

where $X^*_{sep} = \left(\frac{UL_H L_{GC}}{A} c_0 (1-X) + \frac{j}{2F} \right) = X^*_{max}(1-X) + \frac{Y^*}{S}$ is the total moles per second to be separated per unit electrode area. The first term represents the amount of CO_2 not converted, and the second term the amount of CO produced, both per second and per unit electrode area. Here x_i are the mole fractions in the outlet gas stream. Note that in SI 4.7.4, where we consider $n > 2$ for multiple product reduction, some fraction of the products may be liquid and thus remain in the liquid stream rather than the gas outlet, see SI 4.6.5. We dampen this ambitious minimum separation energy with an efficiency parameter μ through $P_{sep} = \frac{P^*_{sep}}{\mu}$ and note that for $n = 2$ reduction to CO and H_2

$$x_{CO_2} = \frac{X^*_{max}(1-X)}{X^*_{sep}}, \quad x_{CO} = \frac{Y^*}{X^*_{sep}}, \quad x_{H_2} = \frac{Y^* - Y^* S}{S X^*_{sep}}. \tag{4.36}$$

In addition, we consider the possibility of CO_2 crossover in the form of HCO_3^- and CO_3^{2-}. While often impeded by selective membranes, CO_2 crossover is difficult to fully prevent and leads to high recovery costs as it evolves into the anodic O_2 stream. Average costs are given by $v_A^* \approx 4$ MJ kg^{-1} [1, 37]. We can determine the carbonate production rate by subtracting yield from conversion, and we can also introduce μ_c, the crossover efficiency, to describe the fraction of produced carbonates that cross over, react back to CO_2, and evolve at the anode. Using this in (4.30), along with (4.34) and (4.35), gives a profit per second per unit area of

$$Y_\$ = v_{CO} Y^* - v_{CO_2} \left(X^* - \mu_c \left(X^* - Y^* \right) \right) - v_P \left(2VF \frac{Y^*}{S} + v_A \mu_c \left(X^* - Y^* \right) - \frac{X^*_{sep} RT}{\mu} \sum x_i \ln x_i \right). \tag{4.37}$$

By subtracting the crossed-over carbonate from X^* in the second term, we assume that from it the CO_2 will be fully recovered. However, we note that in the case of high anodic separation costs or low cost reactant, it could occur that $v_{CO_2} < v_P v_A$, in which case it would be preferable to neglect the anodic separation step and simply pay for more reactant, as shown in SI 4.12.

Symbol	Parameter	Value	Unit
L	Channel length	2×10^{-2}	m
L_H	Channel height	5×10^{-3}	m
L_{GC}	Gas channel width	2×10^{-3}	m
L_{EC}	Flow channel width	1.5×10^{-3}	m
L_{CL}	CL width	8×10^{-6}	m
X_{max}^*	Gas flow rate	17	ml min^{-1}
Q_L	Liquid flow rate	0.5	ml min^{-1}
ε	CL porosity	0.4	-
$\mathcal{H}$	CO_2 Henry constant	31.097	$\text{mol m}^{-3}\,\text{atm}^{-1}$
p_0	Initial pressure	1	atm
v_{CO_2}	Price of CO_2	3.1×10^{-3}	$\text{\$ mol}^{-1}$
v_{CO}	Price of CO	1.7×10^{-2}	$\text{\$ mol}^{-1}$
v_P	Price of electrical energy	1.4×10^{-8}	$\text{\$ J}^{-1}$
V	Cell potential	3	V
T	Temperature	293.15	K

Table 4.1: Table of model parameters based on Kenis group flow electrolysers [36, 15, 22, 34]. For a full description of the parameters, refer to SI 4.2, and table SI 4.2.

4.3.3. NUMERICAL METHOD

In optimising the catalyst loading θ we will use (4.37) as the objective function. We will require as a constraint that the loading function, $\theta(\bar{x})$, must return a value on the interval $(0, 1]$, that is to say not including zero, must initially be unity, that is $\theta(0) = 1$, must be nonincreasing, that is $x > y \implies \theta(x) \leq \theta(y)$. integrates to some total catalyst loading value $\Theta = \int_0^1 \theta(\bar{x}) d\bar{x}$. For the sake of optimisation we will assume this function either takes a polynomial form,

$$\theta(\bar{x}) = \sum_{n=0}^{N} a_n \bar{x}^n, \tag{4.38}$$

with coefficients a_n and $a_0 = 1$, or an equally spaced step function form with

$$\theta(\bar{x}) = \sum_{n=0}^{N} (a_n - a_{n-1}) \, \text{H}\left(\bar{x} - \frac{n}{N}\right), \tag{4.39}$$

with $a_{-1} = 0$ and where $\text{H}(\bar{x})$ is the Heaviside function. This allows us to optimise for N coefficients describing the catalyst loading profile. We use a nonlinear optimiser in MATLAB with the above constraints to determine the optimal values of Θ and a_n by solving (4.28) numerically. Functional optimisation of (4.38) is simple due to the smoothness of polynomials, but the discontinuities presented by (4.39) necessitate stiff ODE solvers and spatial mesh refinement in the vicinity of steps, so we use *ode15s*. The resulting code can be freely downloaded as a supporting information file.
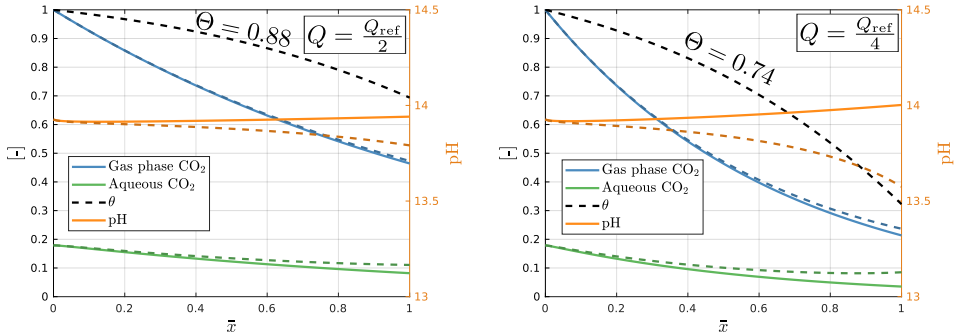
4.3.4. RESULTS AND DISCUSSION

Figure 4.6: Solutions to the numerical system for unoptimised (solid lines) and optimised (dashed lines) catalyst loading showing the normalised gas phase concentration CO$_2$ ($\bar{C}$), aqueous phase concentration CO$_2$ ($\bar{c}$), catalyst loading (θ), and pH, for reduction on an Ag catalyst in KOH. (a) shows that at a flow rate of $Q = \frac{Q_{\mathrm{ref}}}{2}$, or approximately 12 mL min^{-1}, the single pass conversion is only slightly greater than 50% and a slight reduction of 12% in total catalyst loading increases selectivity from 90.4% to 91.3%, at the cost of reducing total current density from 436 mA cm^{-2} to 424 mA cm^{-2}. (b) shows that a lower flow rate of $Q = \frac{Q_{\mathrm{ref}}}{4}$, or approximately 6 mL min^{-1}, the single pass conversion now exceeds 70% and a large reduction of 26% in total catalyst loading roughly doubles the aqueous CO$_2$ concentration at the outlet and increases selectivity from 87.1% to 89.8%, at the cost of reducing total current density from 326 mA cm^{-2} to 303 mA cm^{-2}. In each case a reduced catalyst near the outlet improves selectivity at the cost of current density. The reduction in pH due to decreased HER current and the higher local aqueous CO$_2$ concentration combine to create a more favourable environment for electrochemical reaction of CO$_2$, despite a lower availability of catalyst in that region.

Reference gas flow rate

To date, there are no experimental studies on the effect of flow-wise catalyst loading variation in CO$_2$ER, so our comparison must be between the model with and without optimising catalyst loading. To determine geometric parameters, we take a generic microfluidic setup [15, 22, 34] and its operation conditions. In addition to the parameters in Table 4.1 we take the experimental total current density of $j = 477$ mA cm^{-2} with an FE of 91.2% at a gas flow rate of 17 ml min^{-1} in 3M KOH [34]. We then fit the reaction rate k and ratio q to the reported FE and current density and determine the maximum partial CO$_2$ER current density

$$j_{\mathrm{CO_2},0} = nF k c_0 L_{\mathrm{CL}} \tag{4.40}$$

that would be obtained in case the concentration would be $c_0 = p_{\mathrm{CO_2}}/RT$ through the whole CL. Using this fictitious, but non-arbitrary, high current density, we can write a reference value for flow rates as

$$Q_{\mathrm{ref}} = \frac{j_{\mathrm{CO_2},0} A}{nF c_0}. \tag{4.41}$$

This maximum conversion of all inlet concentration c_0 is completely unattainable, so this flow rate should be seen more as an impartial reference flow rate. For the values in Table 4.1, $Q_{\mathrm{ref}} \approx 24$ ml min^{-1}, and we note that this is in practice quite a high flow rate, so in Figure 4.6 we consider flow rates of $Q = \frac{Q_{\mathrm{ref}}}{2}$ and $Q = \frac{Q_{\mathrm{ref}}}{4}$.

OPTIMISED PROFILES FOR AG

We see that, following (4.22), the aqueous concentration is far lower than the equilibrium concentration, due to the high electrochemical and homogeneous reactions being at comparably high rates to the GDL mass transfer. By reducing the catalyst loading θ, the optimisation process decreases HER rate and thus pH in regions nearer to the outlet, permitting higher CO_2 concentrations. As the CO_2 electroreduction rate is first order in concentration, this increase mostly compensates for the reduction in catalyst availability. For example, in Fig. 4.6(b), $\bar{c}$ more than doubles and θ drops to a third of its initial value, meaning that the CO_2 electroreduction rate is reduced by less than a third while the HER is reduced by two thirds. Note that the optimised catalyst loading lowers the partial CO current density and also leads to a reduction in effectiveness metric $\mathcal{E} = $ YS of Fig. 4.2. However, the metric laid out in (4.37) is increased by roughly 0.6% and 4.5% in Fig. 4.6(a) and (b) respectively, as detailed in Section 4.3.4.

OPTIMISED PROFILES FOR CU

The efficacy of the optimisation is sensitive to reaction kinetics and gas flow rate, so we further investigate the optimisation process on a Cu catalyst cell, with reduction to multiple products with differing values of n. We replace these different reactions with one reaction with an effective n and k, in which different products are disambiguated by their respective experimentally fitted faradaic efficiencies. The value of n is then calculated as an average of electrons transferred for each product, weighted by each the respective faradaic efficiency of that product among CO_2ER products. A bold yet necessary assumption for the model is that reaction rates for each of the products remain first order in concentration. Using this assumption we extract results from the work of Hoang et al. [10] kinetic parameters for the new system. They measured a total current density of 311 mA cm^{-2} and and FE towards CO_2 products of 90.2% at a gas flow rate of 7 mL min. The observed products CO, HCOOH, CH_3OH, CH_4, C_2H_4, and C_2H_5OH on average used $n \approx 5$ electrons transferred per CO_2 converted. Notably, some of these products enter the liquid phase, but liquid separation is a less straightforward process to scale and is neglected from the metric. See SI 4.6.4 for more details. This lower current density and greater n combine to give a value of $Q_{\text{ref}} \approx 0.91$ mL min^{-1}, far lower than that of the Ag based cell. This is relevant, as Fig. 4.7 shows that the Cu based cell already reaches near full conversion of the gas supply at this reference flow rate in KOH, primarily due to the non-electrochemical conversion to carbonates, while the Ag cell does not reach full conversion at flow rates even as low as $\frac{Q_{\text{ref}}}{4}$.

A Cu catalyst based system encounters more issues with reactant utilisation than Ag in KOH as the high n means that the stoichiometric limit of (4.14) instead using $n \approx 5$ becomes

$$\lim_{q \to \infty} \bar{c} = e^{-\left(1 + \frac{5}{2}\right)\text{Da}\,\bar{x}} = e^{-3.5\text{Da}\,\bar{x}}. \tag{4.42}$$

The relatively high average number of electrons transferred, n, used in (4.2) means there are more OH$^-$ ions to parasitically consume the CO_2. This manifests as an extremely high single pass conversion but low yield, motivating the optimiser to drastically decrease θ in the reactant depleted regions. We can track CO_2 in the model to find that in Fig. 4.6 roughly 45% of the reactant that enters the CL is converted to CO, but in each case in Fig. 4.7 only around 15% is converted to products. This means that of the almost unity
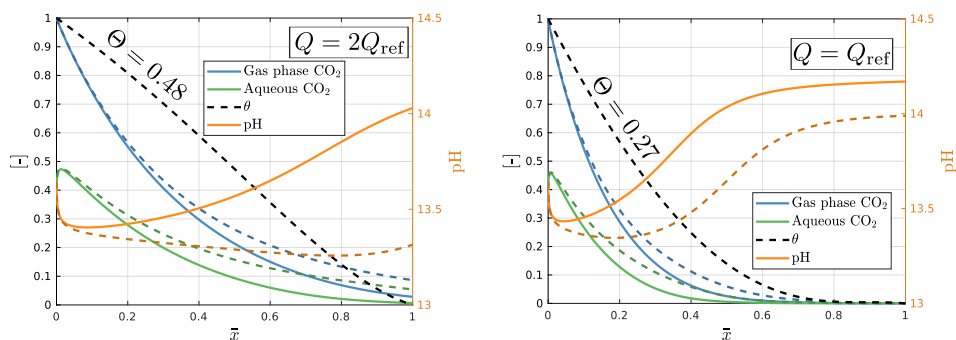
Figure 4.7: Local plots of normalised gas phase CO$_2$ ($\bar{C}$), aqueous phase CO$_2$ ($\bar{c}$), catalyst loading (θ), and pH for reduction on an Cu catalyst in KOH. (a) shows solutions to the numerical system for unoptimised (solid lines) and optimised (dashed lines) catalyst loading at a flow rate of $Q = 2Q_{\text{ref}}$, or 1.82 mL min^{-1}. The relatively low electrochemical reaction rate permits a higher aqueous CO$_2$ concentration near the inlet, but the high value of n means that this still constitutes a large OH$^-$ source. A reduction of 52% in catalyst loading greatly increases the selectivity from 78.8% to 87.4%, with a relatively small reduction in total current density from 141 mA cm^{-2} to 113 mA cm^{-2}. (b) shows solutions to the numerical system for unoptimised (solid lines) and optimised (dashed lines) catalyst loading at a flow rate of $Q = Q_{\text{ref}}$, or 0.91 mL min^{-1}. The effect of the high n and high pH of KOH are sufficient that all reactant is depleted early in the channel, despite Q_{ref} being ostensibly sufficient. The optimiser responds by completely removing catalyst in the depleted regions, fully eliminating the unnecessary HER and greatly improving selectivity from 63.9% to 85.3% with a reduction in total current density from 82 mA cm^{-2} to 55 mA cm^{-2}. High OH$^-$ production from the CO$_2$ reduction as well as HER means that the local pH increases to extreme levels in the unoptimised system, even exceeding the high KOH pH in the latter regions. It becomes preferable for the optimiser to remove large amounts of catalyst to reduce electricity cost from HER, as it is practically impossible for the electrochemical reaction rate to compete with the homogeneous reaction rate and yield more product.
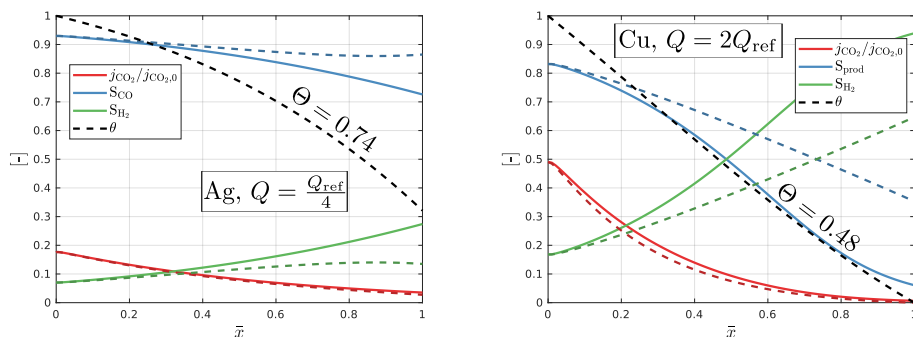
Figure 4.8: Normalised partial CO_2 current densities and product and H_2 selectivities before and after optimisation for (a) the case of reduction on Ag depicted in Fig. 4.6(b), and (b) the case of reduction on Cu depicted in Fig. 4.7(a). The profiles after optimisation, denoted by dashed lines, show that the selectivity towards CO_2 reduction products is significantly increased, the selectivity towards H_2 is significantly reduced, and the normalised current density is relatively unchanged. The effects are far more pronounced in (b), in which the gradient of θ is far steeper and the average number of of electrons transferred, n, is much higher.

single pass conversion, around 80% is simply converted to carbonates, representing a large cost in reactant loss and anodic separation.

COST BREAKDOWN FOR AG

The relevant costs for the Ag and Cu cases discussed above are shown in Figs. 4.9(a) and (b), respectively. From Fig. 4.9(a) we see the change in cost distribution after optimisation is subtle. Despite significant catalyst removal, the distribution and the total costs only slightly change. The majority of the cost comes from electrolysis energy, with reactant and anodic separation costs playing a smaller yet significant role. It is noted that this anodic separation step is to recover CO_2 that has crossed over, so can be viewed as an additional reactant cost. Furthermore, as this process depends on the price of electricity v_P rather than the price of CO_2, v_{CO_2}, so we must be careful to ensure that the step remains feasible. In fact, if v_{CO_2} were to drop by roughly roughly 20%, it would be cheaper to simply purchase more CO_2 rather than waste electricity recovering it from the anode stream. To some extent, this anodic separation cost can be seen as an energy cost due to poor reactant utilisation rather than a direct reactant cost. Improvements in profit margin are 0.6% and 4.5% respectively after optimisation for the used lower and higher flow rates. To these modest improvements a small saving in catalyst costs can be added.

COST BREAKDOWN FOR CU

Fig. 4.9(b) shows a more tempered picture of reduction on Cu. Despite higher normalised flow rates, the profit margins are much smaller (note the different y-axis scaling), and even negative in the unoptimised case using Q_{ref}. Due to the higher value of n, the fraction of cost from converted CO_2 is far smaller and electrolysis energy cost remains dominant. The lower profit is clearly not due to a decrease in conversion, as Fig. 4.7 shows near unity conversion, but is actually due to a low portion of CO_2 being converted to products. The high anodic separation costs represent the overwhelming fraction of CO_2 being converted
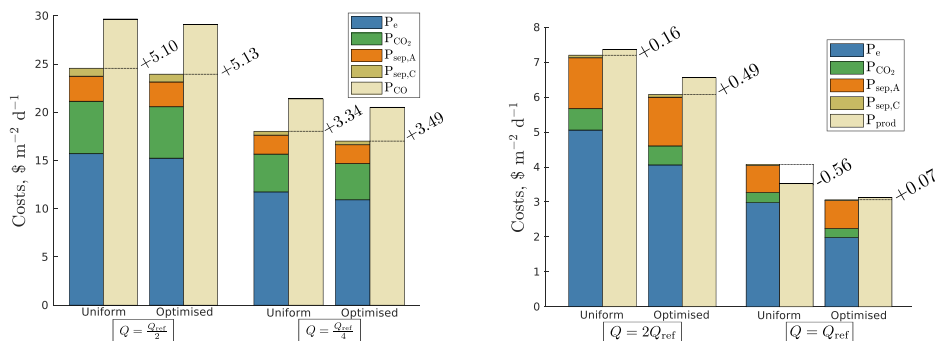
Figure 4.9: Breakdown of the costs associated with electrolyser operation and value of (a) produced CO for reduction on Ag in KOH for the systems in Fig. 4.6 and (b) reduction on Cu in KOH for the systems in Fig. 4.7. The bars represent the costs of electricity, P$_e$, reactant, P$_{CO_2}$, anodic separation, P$_{sep,A}$, cathodic separation, P$_{sep,C}$ and product chemicals, and the revenues P$_{CO}$ and P$_{prod}$, in units of dollars per square metre of electrolyser area per day. The net profits are labelled above the dashed lines. In every case electricity costs dominate, and profit margin is improved by decreasing costs while attempting to maintain high product yield.

to carbonates and crossing over. Notably, the cathodic separation costs are small, for a number of reasons: low outlet CO$_2$ concentrations, due to high single pass conversion; decreased product concentrations for non-CO products, due to higher n values yielding fewer moles of products; and the fact that for reduction on Cu a significant portion of products remain in the liquid phase, so they have no impact on the cathodic gas stream separation cost. The improvements due optimising the catalyst loading in this case are large, from a tripling in profit margin in the higher flow rate case to a recovery from severe loss to minor profit in the lower flow rate case.

4.3.5. DISCUSSION

Across all of Fig. 4.9, we see that a system with a lower gas flow rate is more strongly optimised with a lower value of Θ and a larger improvement in profit margin. However, we also see that simply a higher flow rate leads to a greater profit margin, despite the increase in reactant cost, increase in separation cost, and decrease in single pass conversion. Despite being a serious, even titular, focus in literature studies, single-pass conversion is not always a good metric for CO$_2$ electroreduction performance. In concurrence with more recent techno-economic analyses, we find that anodic separation costs dominate cathodic separation costs [37], but more importantly, electrolyser energy dominates both [23]. Moore et al. neatly show that the energy optima frequently lie at low single pass conversions of less than 10%, and we can similarly show our agreement with this conclusion by manipulating flow rate rather than current density to attain various single pass conversions. Fig. 4.10 shows that indeed, low single pass conversions, achieved by high flow rates, exhibit the highest profit margins, and the largest cost is always P$_e$ by a significant margin.

A recommendation following from this information is to simply make the electrolyser shorter or to increase gas flow rate, both of which have a similar positive effect. Indeed, this is the conclusion found for the simple model in section 4.2. However, from a practical
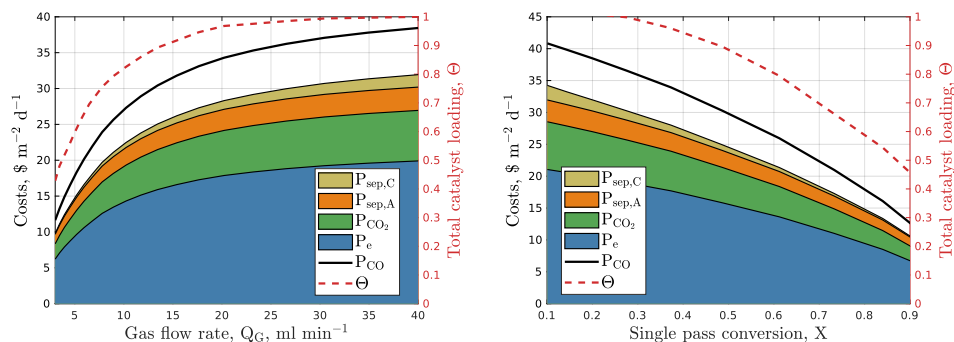
Figure 4.10: Parametric plots of costs, product values, and optimised values of Θ in KOH on Ag against varying gas flow rates in (a) or analogously single pass conversions in (b). Low flow rates correspond to high single pass conversions and low optimised Θ to alleviate reactant shortages, whereas high flow rates yield low single pass conversions, higher optimal catalyst loadings, and, in agreement with Moore et al., higher profit margins. At low single pass conversions, or equivalently very high gas flow rates, Θ reaches unity, meaning that the reactant supply is high enough that the electrolyser is operating effectively along its entire length.

and economical perspective longer electrolysers may be preferred and there are also limitations to the maximum gas flow rate that can be used. High flow rates lead to turbulence and high pressure drops that can lead to pressure-balancing problems that can cause catalyst drying or electrode flooding. Therefore, often sub-optimal flow rates are used in practice for which a variable catalyst loading can generate significant benefits as shown in this work. In some systems that exhibit $\Theta < 1$ even at extremely low single pass conversions, the optimisation process can be degenerate. This can corresponds to systems that are limited by insufficient mass transfer through the GDL or systems that are always economically infeasible. In the former case, Θ becomes independent of flow rate and instead depends on GDL mass transfer rate. This change can be reverted by simply lowering the current density, similar to the conclusion of the 1D model, or by improving mass transfer through the GDL or increasing c_0 by increasing $p_{CO_2,0}$.

4.4. CONCLUSION

We considered first-order reaction systems with competitive secondary reactions, showing how these can be optimised with selective reduction in catalyst. We first derived an analytical solution for simple 1D electrochemical flow cells, in which secondary reactions produce reactant annihilating species. Using analytical solutions for different catalyst loading profiles we show that an improvements are possible at higher Damköhler numbers, corresponding to lower gas flow rates or longer channels. Variable catalyst loading yields greater results in systems with prevalent buffer reactions.

We further the investigation by developing a model of a GDE based CO_2 electrolyser, with a more comprehensive cost metric to consider more realistic operation. In doing so, we find that many typical electrolyser setups can benefit from carefully engineered catalyst distribution, and while some systems may not receive a large benefit it must be reiterated that this benefit is effected by, in fact, a *reduction* in catalyst capital cost.

This means that this optimisation should always be considered. Furthermore we find agreement with recent literature that a singular focus on single pass conversion or reactant utilisation may be misguided, as electrolyser energy is the predominant cost in such cells, and peak performance is reached at low single pass conversions. We further find that, while variable catalyst loading has the greatest impact on high single pass conversion systems, there are parameter spaces in which variable catalyst loading will have a large impact regardless of single pass conversion. As such, we recommend that interested readers use and adapt the provided MATLAB code to investigate the potential benefits of this optimisation process in their own systems.

4.5. Simplest (Single Phase) Model

The simplest model we can use to investigate variable catalyst loading is a 1D reaction advection equation. Without the homogeneous reactions there is no effect of OH^- on c, so terms involving n or q disappear, and Eq. (4.9) reads

$$U\frac{\partial c}{\partial x} + \theta c k = 0, \qquad c(0) = c_0,$$

which is easily solved generally by rewriting it as

$$\bar{c}'(\bar{x}) + \bar{\theta}(\bar{x})(\bar{x})\text{Da}\,\bar{c}(\bar{x}) = 0, \qquad \bar{c}(0) = 1, \tag{4.43}$$

where $\text{Da} = kL/U$, $\bar{c} = c/c_0$ and $\bar{x} = x/L$, with solution

$$\bar{c}(\bar{x}) = e^{-\text{Da}\int_0^{\bar{x}} \bar{\theta}(\bar{x})(\xi)d\xi}. \tag{4.44}$$

This integral represents the total catalyst load up to a fractional length of $\bar{x}$ along the interval, and will henceforth be written as

$$\Theta(\bar{x}) = \int_0^{\bar{x}} \bar{\theta}(\bar{x})(\xi)d\xi, \tag{4.45}$$

with the constant $\Theta \equiv \Theta(1)$ referring to the total catalyst loading. This gives us the general solution of

$$\bar{c}(\bar{x}) = e^{-\text{Da}\,\Theta(\bar{x})}. \tag{4.46}$$

4.5.1. Solutions for n=2

Solutions to the general Eq. (4.9) are possible, but for the sake of brevity we will hereon take $n = 2$ electron reactions, and recommend the reader follow the derivations if greater n is required. Values of interest are the conversion, X, yield, Y, and Faradaic efficiency, S, given respectively by

$$\text{X} = 1 - \bar{c}(1) \tag{4.47}$$

$$\text{Y} = \text{Da}\int_0^1 \bar{\theta}(\bar{x})(\bar{x})\bar{c}(\bar{x})d\bar{x} \tag{4.48}$$

$$\text{S} = \frac{\int_0^1 \bar{\theta}(\bar{x})(\bar{x})\bar{c}(\bar{x})d\bar{x}}{\int_0^1 \bar{\theta}(\bar{x})(\bar{x})(\bar{c}(\bar{x}) + \frac{1}{q})d\bar{x}} = \frac{q\text{Y}}{q\text{Y} + \text{Da}\Theta}, \tag{4.49}$$

where $q = kc_0/k_{H_2}$ is the ratio between the first order primary reaction at concentration c_0 and the zeroth order secondary reaction, in this case the hydrogen evolution reaction, which is another two electron reaction. In the case of Eq (4.43), Eq. (4.47) and Eq. (4.48) are identical by the Fundamental Theorem of Calculus, but in later cases will differ. We identify five key profiles for $\bar{\theta}(\bar{x})(\bar{x})$:

$$\text{Flat:} \qquad \bar{\theta}(\bar{x})(\bar{x}) \equiv 1, \qquad (4.50a)$$

$$\text{Linear:} \qquad \bar{\theta}(\bar{x})(\bar{x}) = 1 - A\bar{x}, \qquad (4.50b)$$

$$\text{Inverse:} \qquad \bar{\theta}(\bar{x})(\bar{x}) = \frac{A^2}{A^2 + \bar{x}^2}, \qquad (4.50c)$$

$$\text{Exponential:} \qquad \bar{\theta}(\bar{x})(\bar{x}) = e^{-A\bar{x}}, \qquad (4.50d)$$

These give cumulative loadings of

$$\Theta(\bar{x}) = \left\{ \begin{array}{ll} \bar{x}, & \text{for } \bar{\theta}(\bar{x})(\bar{x}) \equiv 1 \\ \frac{(2-A\bar{x})\bar{x}}{2}, & \text{for } \bar{\theta}(\bar{x})(\bar{x}) = 1 - A\bar{x} \\ A\arctan\left(\frac{\bar{x}}{A}\right), & \text{for } \bar{\theta}(\bar{x})(\bar{x}) = \frac{A^2}{A^2+\bar{x}^2} \\ \frac{1-e^{-A\bar{x}}}{A}, & \text{for } \bar{\theta}(\bar{x})(\bar{x}) = e^{-A\bar{x}} \end{array} \right\}, \qquad (4.51)$$

The solutions for these profiles are given by

$$\bar{c}(\bar{x}) = \left\{ \begin{array}{ll} e^{-\text{Da}\bar{x}}, & \text{for } \bar{\theta}(\bar{x})(\bar{x}) \equiv 1 \\ e^{\frac{-\text{Da}(2-A\bar{x})\bar{x}}{2}}, & \text{for } \bar{\theta}(\bar{x})(\bar{x}) = 1 - A\bar{x} \\ e^{-A\text{Da}\arctan\left(\frac{\bar{x}}{A}\right)}, & \text{for } \bar{\theta}(\bar{x})(\bar{x}) = \frac{A^2}{A^2+\bar{x}^2} \\ e^{-\frac{\text{Da}(1-e^{-A\bar{x}})}{A}}, & \text{for } \bar{\theta}(\bar{x})(\bar{x}) = e^{-A\bar{x}} \end{array} \right\}, \qquad (4.52)$$

with conversion and yield given by

$$\text{X} = \text{Y} = \left\{ \begin{array}{ll} 1 - e^{-\text{Da}}, & \text{for } \bar{\theta}(\bar{x}) \equiv 1 \\ 1 - e^{\frac{-\text{Da}(2-A)}{2}}, & \text{for } \bar{\theta}(\bar{x}) = 1 - A\bar{x} \\ 1 - e^{-A\text{Da}\arctan\left(\frac{1}{A}\right)}, & \text{for } \bar{\theta}(\bar{x}) = \frac{A^2}{A^2+\bar{x}^2} \\ 1 - e^{-\frac{\text{Da}(1-e^{-A})}{A}}, & \text{for } \bar{\theta}(\bar{x}) = e^{-A\bar{x}} \end{array} \right\}, \qquad (4.53)$$

and Faradaic efficiency S given by inserting (4.53) and (4.51) into (4.49). The effectiveness $\mathcal{E} = \text{YS} = \frac{q\text{Y}^2}{q\text{Y}+\text{Da}\Theta}$ can be immediately obtained from these expressions. For example, for a homogeneous catalyst loading $\mathcal{E} = \frac{(1-e^{-\text{Da}})^2}{1-e^{-\text{Da}}+\text{Da}/q}$. This tends to one for $q \gg \text{Da} \gg 1$.

4.5.2. Homogeneous reactions
The approximate inclusion of homogeneous reactions is expressed as

$$\bar{c}'(\bar{x}) + \bar{\theta}(\bar{x})(\bar{x})\text{Da}\left(2\bar{c}(\bar{x}) + \frac{1}{q}\right) = 0, \qquad \bar{c}(0) = 1, \qquad (4.54)$$

with solutions given by

$$\bar{c}(\bar{x}) = e^{-2\text{Da}\Theta(\bar{x})}\left(1 - \frac{\text{Da}}{q}\int_0^{\bar{x}} \bar{\theta}(\bar{x})(\xi)e^{2\text{Da}\Theta(\xi)}\,d\xi\right), \qquad (4.55)$$

but of course $\bar{\theta}(\bar{x})(\bar{x}) = \Theta'(\bar{x})$, so by noting that $f'(x)e^{f(x)} = \left(e^{f(x)}\right)'$ we can write

$$\bar{c}(\bar{x}) = \frac{1}{2q}\left(2qe^{-2Da\Theta(\bar{x})} - e^{-2Da\Theta(\bar{x})}\left[e^{2Da\Theta(\xi)}\right]_0^x\right), \tag{4.56}$$

simplifying to

$$\bar{c}(\bar{x}) = \frac{1}{2q}\left((2q+1)e^{-2Da\Theta(\bar{x})} - 1\right) \tag{4.57}$$

or in full,

$$\bar{c}(\bar{x}) = \begin{cases} \frac{(2q+1)e^{-2Da\bar{x}}-1}{2q}, & \text{for } \bar{\theta}(\bar{x}) \equiv 1 \\ \frac{(2q+1)e^{-Da\bar{x}(2-A\bar{x})}-1}{2q}, & \text{for } \bar{\theta}(\bar{x}) = 1 - A\bar{x} \\ \frac{(2q+1)e^{-2ADa\arctan\left(\frac{\bar{x}}{A}\right)}-1}{2q}, & \text{for } \bar{\theta}(\bar{x}) = \frac{A^2}{A^2+\bar{x}^2} \\ \frac{(2q+1)e^{\frac{-2Da(1-e^{-A\bar{x}})}{A}}-1}{2q}, & \text{for } \bar{\theta}(\bar{x}) = e^{-A\bar{x}} \end{cases}. \tag{4.58}$$

Importantly, this means that while the definitions of X, Y and S of (4.47)-(4.49) remain unchanged, we can circumvent the need for involved integration by noting that

$$X = Da \int_0^1 \theta(\bar{x})\left(2\bar{c}(\bar{x}) + \frac{1}{q}\right)d\bar{x} \tag{4.59}$$

$$= 2Y + \frac{Da}{q}\Theta \iff Y = \frac{qX - Da\Theta}{2q}, \tag{4.60}$$

so

$$X = \begin{cases} \frac{2q+1}{2q}\left(1-e^{-2Da}\right), & \text{for } \bar{\theta}(\bar{x}) = 1 \\ \frac{2q+1}{2q}\left(1-e^{-Da(2-A)}\right), & \text{for } \bar{\theta}(\bar{x}) = 1 - A\bar{x} \\ \frac{2q+1}{2q}\left(1-e^{-2ADa\arctan\left(\frac{1}{A}\right)}\right), & \text{for } \bar{\theta}(\bar{x}) = \frac{A^2}{A^2+\bar{x}^2} \\ \frac{2q+1}{2q}\left(1-e^{-\frac{2Da}{A}\left(1-e^{-A}\right)}\right), & \text{for } \bar{\theta}(\bar{x}) = e^{-A\bar{x}} \end{cases}, \tag{4.61}$$

and

$$Y = \begin{cases} \frac{(2q+1)\left(1-e^{-2Da}\right)-2Da}{4q}, & \text{for } \bar{\theta}(\bar{x}) = 1 \\ \frac{(2q+1)\left(1-e^{-Da(2-A)}\right)-Da(2-A)}{4q}, & \text{for } \bar{\theta}(\bar{x}) = 1 - A\bar{x} \\ \frac{(2q+1)\left(1-e^{-2ADa\arctan\frac{1}{A}}\right)-2ADa\arctan\frac{1}{A}}{4q}, & \text{for } \bar{\theta}(\bar{x}) = \frac{A^2}{A^2+\bar{x}^2} \\ \frac{(2q+1)\left(1-e^{-\frac{2Da}{A}\left(1-e^{-A}\right)}\right)-\frac{2Da}{A}\left(1-e^{-A}\right)}{4q}, & \text{for } \bar{\theta}(\bar{x}) = e^{-A\bar{x}} \end{cases}. \tag{4.62}$$

4.5.3. Step based loadings

A more practical approach could be to explicitly define uniform loading in subsections of the channel. We assume that these steps are equally spaced and of equal length, with each of the N steps characterised by a catalyst loading, α_n, with $\alpha_0 = 1$. While we could

define this in terms of explicit step functions, most of the expressions are easier to define in terms of the Heaviside step function,

$$H(x) = \begin{cases} 0, & x < 0 \\ 1, & x \geq 0 \end{cases} \tag{4.63}$$

and define $\alpha_{-1} = 0$ to give

$$\bar{\theta}(\bar{x})(\bar{x}) = \sum_{n=0}^{N} (\alpha_n - \alpha_{n-1}) \, H\left(\bar{x} - \frac{n}{N}\right) \tag{4.64a}$$

$$\Theta(\bar{x}) = \sum_{n=0}^{N} (\alpha_n - \alpha_{n-1}) \, H\left(\bar{x} - \frac{n}{N}\right)\left(\bar{x} - \frac{n}{N}\right) \tag{4.64b}$$

$$c(\bar{x}) = \prod_{n=0}^{N} e^{-\mathrm{Da}(\alpha_n - \alpha_{n-1})H\left(\bar{x} - \frac{n}{N}\right)\left(\bar{x} - \frac{n}{N}\right)} \tag{4.64c}$$

$$X = Y = 1 - \prod_{n=1}^{N} e^{-\frac{\mathrm{Da}}{N}\alpha_n} \tag{4.64d}$$

$$\tag{4.64e}$$

Following this, we can use the processes laid out in the following section to derive expressions for the case with reactions.

To conclude, without buffer reactions we have $Y = X$ and

$$\bar{c}(\bar{x}) = e^{-\mathrm{Da}\Theta(\bar{x})} \tag{4.65}$$

with buffer reactions for $n = 2$ we have $Y = \frac{qX - \mathrm{Da}\Theta}{2q}$ and

$$\bar{c}(\bar{x}) = \frac{\left(2q + 1\right)e^{-2\mathrm{Da}\Theta(\bar{x})} - 1}{2q} \tag{4.66}$$

4.5.4. Optimisation
No buffer reactions
We note again that effectiveness is given by,

$$\mathcal{E} = \frac{qY^2}{qY + \mathrm{Da}\Theta}, \tag{4.67}$$

and qualitatively corresponds to the total amount of product we attain multiplied by the efficiency at which we attain it. To determine the optimal value of Θ for a given value of Da, we can set the derivative of $\mathcal{E}$ with respect to Θ to zero. Writing a subscript of Θ to denote a derivative with respect to Θ, we find

$$\mathcal{E}_\Theta = \frac{qY\left(\left(qY_\Theta - \mathrm{Da}\right)Y + 2\Theta\mathrm{Da}Y_\Theta\right)}{\left(qY + \Theta\mathrm{Da}\right)^2} = 0, \tag{4.68}$$

or equivalently

$$Y_\Theta = \frac{\mathrm{Da}Y}{qY + 2\Theta\mathrm{Da}}. \tag{4.69}$$

To find Y_Θ we note that

$$\frac{\partial}{\partial\Theta}Y = \frac{\partial}{\partial\Theta}\mathrm{Da}\int_0^1 \theta(\bar{x})e^{-\mathrm{Da}\Theta(\bar{x})}\,d\bar{x} = \frac{\partial}{\partial\Theta}\int_1^0 \frac{d\left(e^{-\mathrm{Da}\Theta(\bar{x})}\right)}{d\bar{x}}\,d\bar{x} = \frac{\partial}{\partial\Theta}\left(1-e^{-\mathrm{Da}\Theta}\right) = \mathrm{Da}\bar{c}(1). \tag{4.70}$$

Utilising (4.46), (4.47) and (4.70), Eq. (4.69) becomes

$$\mathrm{Da}\bar{c}(1) = \frac{\mathrm{Da}\,(1-\bar{c}(1))}{q\,(1-\bar{c}(1))+2\Theta\mathrm{Da}} \iff e^{\Theta\mathrm{Da}}+qe^{-\Theta\mathrm{Da}} = 1+q+2\Theta\mathrm{Da}. \tag{4.71}$$

Regrettably, the final form in (4.71) is quite insoluble, but in (4.67) and (4.71), only the product of Θ and Da ever appears. This means that Θ successfully acts as a multiplier for Da: that is to say, the optimal value of $\mathcal{E}$ with a flat loading will be identical to the optimal value at a higher Da but optimised Θ. Notably, $Y_{\mathrm{Da}} = \Theta\bar{c}(1)$, or $Y_{\mathrm{Da}\Theta} = \bar{c}(1)$, by symmetry. Therefore, by symmetry, the steps taken in (4.68), (4.69), and (4.71) are identical when considering a given value of Θ and optimising for Da.

When $q \to 0$, $\mathcal{E} \to 0$, so no meaningful value of $\mathrm{Da}\Theta$ can be assigned, and in the case of $q \to \infty$, $\mathcal{E} \to Y$, so the optimum is $\Theta\mathrm{Da} \to \infty$. An approximation for general q with a maximum relative error of 7 % is given by

$$(\Theta\mathrm{Da})_{\mathrm{opt}} \approx 1.256431209 + \frac{1}{2}\mathrm{W}\left(q^2\right) \tag{4.72}$$

where $\mathrm{W}\left(q\right)$ is the Lambert W or product log function satisfying $\mathrm{W}\left(q\right)e^{\mathrm{W}(q)} = q$. A good approximation in terms of logarithms can be found in Ref. [9]. A simple approximation accurate with a relative maximum error of 11 % reads

$$(\Theta\mathrm{Da})_{\mathrm{opt}} \approx 1+\ln\left(\frac{1.2923q}{\ln\left(1+q\right)}\right) \tag{4.73}$$

where $1.2923 \approx e^{1.256431209-1}$, to ensure the exact limit for $q \to 0$ holds. However, for $q \gg 1$ a better approximation is the simple approximation $(\Theta\mathrm{Da})_{\mathrm{opt}} \approx \ln\left(q\right)$.

Including buffer reactions ($n = 2$)

The derivation for the case with buffer reactions is similar. In this case, Eq. (4.70) continues to hold and we have $Y_\Theta = \mathrm{Da}\bar{c}(1)$. Inserting this, $Y = \frac{q\mathrm{X}-\mathrm{Da}\Theta}{2q}$ from Eq. (4.60), and $\mathrm{X} = 1-c(1)$ into Eq. (4.69) gives

$$\mathrm{Da}\bar{c}(1) = \frac{\mathrm{Da}\frac{q(1-\bar{c}(1))-\Theta\mathrm{Da}}{2q}}{q\frac{q(1-\bar{c}(1))-\Theta\mathrm{Da}}{2q}+2\Theta\mathrm{Da}} \tag{4.74}$$

Inserting $\bar{c}(1) = \frac{(2q+1)e^{-2\mathrm{Da}\Theta}-1}{2q}$ from Eq. (4.66) gives

$$(2q+1)^2 e^{-4\Theta\mathrm{Da}} - (2q+1)(2q+4+6\Theta\mathrm{Da})e^{-2\Theta\mathrm{Da}} + 6q + 2\Theta\mathrm{Da} + 3 = 0. \tag{4.75}$$

As before, the final form is quite insoluble, but still only ever includes the product of Θ and Da, meaning that again any optimal value $\mathcal{E}$ found with uniform loading can be attained with variable catalyst loading from a higher initial Da.

Approximations accurate to about 7 % for low to moderately high $0 \leq q \lesssim 10^3$, and exact in the limit of low q read

$$(\Theta\text{Da})_{\text{opt}} \approx \frac{2}{3}\text{W}(q) \approx \frac{4}{3}\frac{1+q/2}{1+q}\ln\left(\frac{q}{\ln(1+q)}\right) \tag{4.76}$$

However, for $q \gtrsim 10^2$ an excellent approximation is the following result that is exact in the limit of high q

$$(\Theta\text{Da})_{\text{opt}} \approx \frac{1}{2}\ln\left(\frac{2q}{3}\right) \tag{4.77}$$

4.6. GDE MODEL

Here we give more details on the GDE model.

4.6.1. ELECTROLYTE BOUNDARY LAYER

Firstly, we address the mass transfer from the electrolyte flow channel, $k_{\text{OH}^-}^{\text{t}}$ and $k_{\text{CO}_2}^{\text{t}}$. The simplest approach is to leave them as single valued mass transfer coefficients, from the Reynolds-Sherwood-Schmidt [35] correlation for instance

$$k_i^{\text{t}} = \frac{D_i}{L}0.664\text{Re}^{\frac{1}{2}}\text{Sc}_i^{\frac{1}{3}}, \tag{4.78}$$

where $\text{Re} = \frac{\text{U}}{\nu}$ is the electrolyte channel Reynolds number and $\text{Sc}_i = \frac{\nu}{D_i}$ are the Schmidt numbers for $i = \text{CO}_2$ and OH^- respectively, with diffusion coefficients D_i and ν the kinematic viscosity of the electrolyte. If however, we wish to include the flow-wise development of the concentration boundary layer, we can use the Lévêque approximation [2, 20] for boundary layer thicknesses, δ, for Poiseuille flow,

$$\delta = 1.607\sqrt[3]{\frac{\text{L}_{\text{EC}}Dx}{\text{U}}}, \tag{4.79}$$

where L_{EC} is the width of the electrolyte channel, or plug flow [4]

$$\delta = 3.643\sqrt{\frac{Dx}{\text{U}}}, \tag{4.80}$$

to arrive at

$$k_i^{\text{t}}(\bar{x}) = k_i^{t,\text{Po}}\bar{x}^{-\frac{1}{3}}, \qquad \text{or} \qquad k_i^{\text{t}}(\bar{x}) = k_i^{t,\text{Pl}}\bar{x}^{-\frac{1}{2}}, \tag{4.81}$$

for Poiseuille and plug flow respectively, where

$$k_i^{t,\text{Po}} = \sqrt[3]{\frac{\text{D}_i^2\text{U}}{4.15\text{L}_{\text{EC}}\text{L}}}, \qquad \text{or} \qquad k_i^{t,\text{Pl}} = \sqrt{\frac{\text{D}_i^2\text{U}}{13.27\text{L}}}. \tag{4.82}$$

This boundary layer thickness is determined for a Dirichlet boundary condition, but a perhaps more relevant description would be for a Neumann boundary condition, whose mass transfer coefficient has been shown to differ by only a numerical factor [32].

4.6.2. DIFFUSION MEDIUM TRANSPORT

Next, we address mass transport from the gas channel side. A simple Fickian approximation of transport through these layers can be made utilising the Bruggeman relation for a porosity and tortuosity corrected diffusivity, giving

$$k_{GDL}^t = \epsilon_{GDL}^{1.5} \frac{D_{CO_2(g)}}{L_{GDL}}. \tag{4.83}$$

Transport through the GDL in the gas phase is extremely fast, but there is still a small distance that must be covered by diffusion in the aqueous phase, and the aqueous diffusivity of CO_2 is low enough that it can be a comparable resistance to crossing the entire GDL in gas phase. The aqueous diffusive distance is an ephemeral property, and difficult to determine, so we choose and determine the mass transfer coefficient with the approach of Weng et al. in their optimally wetted scenario [35], using a characteristic distance of the average pore radius of the material used in Ref. [34] (Sigracet 35 BC) [14],

$$k_{CL}^t = \frac{D_{CO_2(aq)}}{r_p}, \tag{4.84}$$

noting that no diffusivity correction is necessary on the sub-pore scale. Taking a series summation of the mass transfers gives

$$k_{GC}^t = \left(\frac{1}{k_{CL}^t} + \frac{1}{k_{GDL}^t} \right)^{-1}. \tag{4.85}$$

4.6.3. MASS BALANCE

We start with (4.22)

$$k_{GC}^t (\mathcal{H} p_{CO_2} - c) + k_{CO_2}^t (c^B - c) = \epsilon L_{CL} (kc + k_r hc),$$

and divide by $L_{CL} \epsilon k_r c_0 c_{OH^-}^B$ while introducing $\bar{\theta}(\bar{x})$ into the heterogeneous reaction terms and replacing $\mathcal{H} p_{CO_2}$ with $\bar{C}$ to get

$$\bar{k}_{GC}^t (\bar{C} - \bar{c}) + \bar{k}_{CO_2}^t (\bar{c}^B - \bar{c}) = \bar{\theta}(\bar{x}) \bar{k} \bar{c} + \bar{c}_{OH^-} \bar{c},$$

and we take (4.23)

$$k_{OH^-}^t (c_{OH^-}^B - c_{OH^-}) + 2\epsilon L_{CL} kc + 2\epsilon L_{CL} k_{H_2} = 2\epsilon L_{CL} k_r c_{OH^-} \bar{c}$$

and divide by $2 L_{CL} \epsilon k_r c_0 c_{OH^-}^B$ and introduce $\bar{\theta}(\bar{x})$ to get

$$\bar{k}_{H_2}^t (1 - \bar{c}_{OH^-}) + \bar{\theta}(\bar{x}) \bar{k} \bar{c} + \bar{\theta}(\bar{x}) \bar{k}_{H_2} = \bar{c}_{OH^-} \bar{c}.$$

Equating (4.27) and (4.26) gives

$$\bar{c}_{OH^-} = \frac{\bar{\theta}(\bar{x}) \bar{k} \bar{c} + \bar{\theta}(\bar{x}) \bar{k}_{H_2} + \bar{k}_{H_2}^t}{\bar{c} + \bar{k}_{H_2}^t} = \frac{\bar{k}_{GC}^t \bar{C} + \bar{k}_{CO_2}^t \bar{c}^B - (\bar{\theta}(\bar{x}) \bar{k} + \bar{k}_{GC}^t + \bar{k}_{CO_2}^t) \bar{c}}{\bar{c}}, \tag{4.86}$$

which can be solved for $\bar{c}$, and by inserting the positive (physical) solution into Eq. (4.24) we arrive at

$$
\bar{c} = \frac{1}{2(2\bar{k} + \bar{k}_{GC}^t + \bar{k}_{CO_2}^t)}\Big(\big\{\bar{k}_{GC}^{t^2}\bar{C}^2 + 2\bar{k}_{GC}^t((3\bar{k} + \bar{k}_{GC}^t + \bar{k}_{CO_2}^t - 1)\bar{k}_{H_2}^t + \bar{k}_{CO_2}^t\bar{c}^B - \bar{k}_{H_2})\bar{C}
$$

$$
+ (\bar{k} + \bar{k}_{GC}^t + \bar{k}_{CO_2}^t + 1)^2\bar{k}_{H_2}^{t^2} + (2\bar{c}^B\bar{k}_{CO_2}^{t^2} + (2\bar{c}^B\bar{k}_{GC}^t + (6\bar{k} - 2)\bar{c}^B + 2\bar{k}_{H_2})\bar{k}_{CO_2}^t +
$$

$$
2\bar{k}_{H_2}(\bar{k} + \bar{k}_{GC}^t + 1))\bar{k}_{H_2}^t + (\bar{c}^B\bar{k}_{CO_2}^t - \bar{k}_{H_2})^2\big\}^{\frac{1}{2}} + \bar{k}_{GC}^t\bar{C} + (-\bar{k} - \bar{k}_{GC}^t - \bar{k}_{CO_2}^t - 1)\bar{k}_{H_2}^t + \bar{k}_{CO_2}^t\bar{c}^B - \bar{k}_{H_2}\Big).
$$

$$\tag{4.87}$$

and

$$
-\frac{\partial\bar{C}}{\partial\bar{x}} = a\bar{C} + b - \sqrt{\alpha\bar{C}^2 + \beta\bar{C} + \gamma}, \tag{4.88}
$$

where

$$
a = \frac{\widehat{\mathcal{H}}\big(4\bar{\theta}(\bar{x})\bar{k} + \bar{k}_{GC}^t + 2\bar{k}_{CO_2}^t\big)}{2\mathrm{Da}\big(2\bar{\theta}(\bar{x})\bar{k} + \bar{k}_{GC}^t + \bar{k}_{CO_2}^t\big)} \tag{4.89a}
$$

$$
b = \frac{\widehat{\mathcal{H}}\big((\bar{k}_{CO_2}^t + \bar{k}_{GC}^t + \bar{k}_{CO_2}^t + 1)\bar{k}_{H_2}^t + \bar{k}_{CO_2}^t\bar{c}^B - \bar{\theta}(\bar{x})\bar{k}_{H_2}\big)}{2\mathrm{Da}\big(2\bar{\theta}(\bar{x})\bar{k} + \bar{k}_{GC}^t + \bar{k}_{CO_2}^t\big)} \tag{4.89b}
$$

$$
\alpha = \frac{\widehat{\mathcal{H}}^2\bar{k}_{GC}^{t^2}}{4\mathrm{Da}^2\big(2\bar{k} + \bar{k}_{GC}^t + \bar{k}_{CO_2}^t\big)^2} \tag{4.89c}
$$

$$
\beta = \frac{\bar{k}_{GC}^t\widehat{\mathcal{H}}^2\big((3\bar{\theta}(\bar{x})\bar{k} + \bar{k}_{GC}^t + \bar{k}_{CO_2}^t - 1)\bar{k}_{H_2}^t + \bar{k}_{CO_2}^t\bar{c}^B - \bar{\theta}(\bar{x})\bar{k}_{H_2}\big)}{4\mathrm{Da}^2\big(2\bar{\theta}(\bar{x})\bar{k} + \bar{k}_{GC}^t + \bar{k}_{CO_2}^t\big)^2} \tag{4.89d}
$$

$$
\gamma = \frac{\widehat{\mathcal{H}}^2}{4\mathrm{Da}^2(2\bar{\theta}(\bar{x})\bar{k} + \bar{k}_{GC}^t + \bar{k}_{CO_2}^t)^2}\Big\{(\bar{k} + \bar{k}_{GC}^t + \bar{k}_{CO_2}^t + 1)^2\bar{k}_{H_2}^2
$$

$$
+ (2\bar{c}^B\bar{k}_{CO_2}^{t^2} + (6\bar{c}^B\bar{k} + 2\bar{c}^B\bar{k}_{GC}^t - 2\bar{c}^B + 2\bar{\theta}(\bar{x})\bar{k}_{H_2})\bar{k}_{CO_2}^t
$$

$$
+ 2\bar{\theta}(\bar{x})\bar{k}_{H_2}(\bar{k} + \bar{k}_{GC}^t + 1))\bar{k}_{H_2}^t + (\bar{k}_{CO_2}^t\bar{c}^B - \bar{\theta}(\bar{x})\bar{k}_{H_2})^2\Big\}. \tag{4.89e}
$$

4.6.4. DERIVATION FOR ARBITRARY PRODUCT DISTRIBUTION

So long as we maintain that the reaction rates are first order in concentration, we can expand this to greater numbers of electrons transferred and different products. We can rewrite Eq. (4.23) as

$$
\underbrace{k_{OH^-}^t(c_{OH^-}^B - c_{OH^-})}_{\text{transfer from electrolyte channel}} + \underbrace{n\mathrm{L_{CL}}kc}_{\text{CO}_2\text{ER reaction}} + \underbrace{2\mathrm{L_{CL}}k_{H_2}}_{\text{H}_2\text{ evolution}} = \underbrace{2\mathrm{L_{CL}}\epsilon k_r c_{OH^-}c}_{\text{homogeneous reaction}}, \tag{4.90}
$$

noting again that each product transfers at least two electrons per CO_2, so Eq. (4.22) can remain unchanged by simply halving the relevant terms and remembering that this only produces half a product molecule. This only affects one term, so the remaining derivation

can be kept the same as before, only noting that $\bar{k} \implies \frac{n}{2}\bar{k}$ for terms generating OH^-,

$$S = \frac{\int_0^1 \theta n q \bar{c}\, d\bar{x}}{\int_0^1 \theta n q \bar{c} + \theta d\bar{x}}, \tag{4.91}$$

and that n must be increased in the electron cost in Eq. (4.33). The rest of the added complexity comes from determining the outlet product distribution for the sake of separation costs, noting that we only give an expression for gaseous products in this work. The resulting updated expressions are

$$\bar{c} = \frac{1}{2(2\bar{k} + \bar{k}_{GC}^t + \bar{k}_{CO_2}^t)}\Big(\{\bar{k}_{GC}^{t2}\bar{C}^2 + 2\bar{k}_{GC}^t((3\bar{k} + \bar{k}_{GC}^t + \bar{k}_{CO_2}^t - 1)\bar{k}_{H_2}^t + \bar{k}_{CO_2}^t\bar{c}^B - \bar{k}_{H_2})\bar{C}$$
$$+ (\bar{k} + \bar{k}_{GC}^t + \bar{k}_{CO_2}^t + 1)^2\bar{k}_{H_2}^{t2} + (2\bar{c}^B\bar{k}_{CO_2}^{t2} + (2\bar{c}^B\bar{k}_{GC}^t + (6\bar{k} - 2)\bar{c}^B + 2\bar{k}_{H_2})\bar{k}_{CO_2}^t +$$
$$2\bar{k}_{H_2}(\bar{k} + \bar{k}_{GC}^t + 1))\bar{k}_{H_2}^t + (\bar{c}^B\bar{k}_{CO_2}^t - \bar{k}_{H_2})^2\}^{\frac{1}{2}} + \bar{k}_{GC}^t\bar{C} - (\bar{k} + \bar{k}_{GC}^t + \bar{k}_{CO_2}^t + 1)\bar{k}_{H_2}^t + \bar{k}_{CO_2}^t\bar{c}^B - \bar{k}_{H_2}\Big). \tag{4.92}$$

and a derivative equal to (4.88), but with coefficients given by

$$a = \frac{\widehat{\mathcal{H}}\big((n+2)\bar{\theta}(\bar{x})\bar{k} + \bar{k}_{GC}^t + 2\bar{k}_{CO_2}^t\big)}{Da\big((n+2)\bar{\theta}(\bar{x})\bar{k} + 2\bar{k}_{GC}^t + 2\bar{k}_{CO_2}^t\big)} \tag{4.93a}$$

$$b = \frac{\widehat{\mathcal{H}}\big((\bar{k}_{CO_2}^t + \bar{k}_{GC}^t + \bar{k}_{CO_2}^t + 1)\bar{k}_{H_2}^t + \bar{k}_{CO_2}^t\bar{c}^B - \bar{\theta}(\bar{x})\bar{k}_{H_2}\big)}{Da\big((n+2)\bar{\theta}(\bar{x})\bar{k} + 2\bar{k}_{GC}^t + 2\bar{k}_{CO_2}^t\big)} \tag{4.93b}$$

$$\alpha = \frac{\widehat{\mathcal{H}}^2\bar{k}_{GC}^{t2}}{Da^2\big((n+2)\bar{k} + 2\bar{k}_{GC}^t + 2\bar{k}_{CO_2}^t\big)^2} \tag{4.93c}$$

$$\beta = \frac{\bar{k}_{GC}^t\widehat{\mathcal{H}}^2\big(((n+1)\bar{\theta}(\bar{x})\bar{k} + \bar{k}_{GC}^t + \bar{k}_{CO_2}^t - 1)\bar{k}_{H_2}^t + \bar{k}_{CO_2}^t\bar{c}^B - \bar{\theta}(\bar{x})\bar{k}_{H_2}\big)}{Da^2\big((n+2)\bar{\theta}(\bar{x})\bar{k} + 2\bar{k}_{GC}^t + 2\bar{k}_{CO_2}^t\big)^2} \tag{4.93d}$$

$$\gamma = \frac{\widehat{\mathcal{H}}^2}{Da^2((n+2)\bar{\theta}(\bar{x})\bar{k} + 2\bar{k}_{GC}^t + 2\bar{k}_{CO_2}^t)^2}\Big\{(\bar{k} + k_{GC}^t + \bar{k}_{CO_2}^t + 1)^2\bar{k}_{H_2}^2$$
$$+ (2\bar{c}^B\bar{k}_{CO_2}^{t2} + (2(n+1)\bar{c}^B\bar{k} + 2\bar{c}^B\bar{k}_{GC}^t - 2\bar{c}^B + 2\bar{\theta}(\bar{x})\bar{k}_{H_2})\bar{k}_{CO_2}^t$$
$$+ 2\bar{\theta}(\bar{x})\bar{k}_{H_2}(\bar{k} + \bar{k}_{GC}^t + 1))\bar{k}_{H_2}^t + (\bar{k}_{CO_2}^t\bar{c}^B - \bar{\theta}(\bar{x})\bar{k}_{H_2})^2\Big\}. \tag{4.93e}$$

4.6.5. Operation options
While electricity, reactant, and separation remain the only costs considered in the analysis, different operational modes can lead to different costs. We include multiple additional model parameters for the reader to account for these differences.

Firstly, we include the parameter μ_A as the fraction of carbonate species that cross over to the anode. With an anion exchange membrane or no membrane, the diffusion and migration of the negatively charged carbonate species is unimpeded and one would expect a high crossover fraction, but with a membrane more inclined to reject anions,

such as a cation exchange membrane or bipolar membrane, this fraction will be far lower. While this reduction in crossover reduces anodic separation costs, membranes contribute a large amount to capital cost in most electrolyser setups [25] and an increase in electrolysis operation costs linked to the increase in cell potential.

Secondly, we note that the value of the secondary product of H_2 is often neglected in cost analyses. We default to only including the value of the intended product in the analysis as the value of the produced H_2 is usually around 1% of that in systems with reasonably high FE. Nonetheless, we include the option and note that at a high current density, even a small increase in product value can lead to a meaningful increase in profit margin. A switch is included in the model to decide whether or not to include this in the analysis.

Thirdly, a currently null parameter v_L is included for liquid product separation costs. Unlike gas products, liquid product separation is highly dependent on the recirculation of the electrolyte and the stability of the membranes used. Ideally, one would wish to maximise the wt.% of liquid product by recirculating electrolyte, until a balance is reached against the stability of the membrane and the effects on the electrolyte [33]. This is beyond the scope of the model, and is left to the interested reader.

Lastly, we note that it is not unlikely that a small shift in anodic separation efficiency, electricity cost, or reactant cost, could make anodic separation entirely uneconomical. For the parameters in Table 4.2, a reduction of roughly 20% in v_{CO_2} would lead to it being overall cheaper to simply buy more CO_2 rather than recover it from the anode stream. We include a switch in the model to automatically implement this change when relevant.

4

Symbol	Parameter	Value	Unit	Ref.
L	Channel length	2×10^{-2}	m	[34]
L_H	Channel height	5×10^{-3}	m	[34]
L_{GC}	Gas channel width	2×10^{-3}	m	[34]
L_{EC}	Electrolyte flow channel width	1.5×10^{-3}	m	[34]
L_{CL}	CL width	8×10^{-6}	m	[34]
Q_G	Gas flow rate	17	ml min^{-1}	[34]
Q_L	Liquid flow rate	0.5	ml min^{-1}	[34]
ϵ	CL porosity	0.4	-	[34]
$\mathcal{H}$	CO_2 Henry constant	31.097	mol m^{-3} atm^{-1}	[26]
r_p	Average GDL pore radius	0.733×10^{-6}	m	[14]
p_0	Initial pressure	1	atm	[34]
v_{CO_2}	Price of CO_2	3.1×10^{-3}	\$ mol^{-1}	[12]
v_{H_2}	Price of H_2	3.83×10^{-3}	\$ mol^{-1}	[30]
v_{CO}	Price of CO	1.7×10^{-2}	\$ mol^{-1}	[12]
v_{HCOOH}	Price of formate	3.4×10^{-2}	\$ mol^{-1}	[12]
v_{CH_3OH}	Price of methanol	1.86×10^{-2}	\$ mol^{-1}	[12]
v_{CH_4}	Price of methane	2.89×10^{-3}	\$ mol^{-1}	[12]
$v_{C_2H_4}$	Price of ethylene	3.65×10^{-2}	\$ mol^{-1}	[12]
$v_{C_2H_5OH}$	Price of ethanol	4.6×10^{-2}	\$ mol^{-1}	[12]
v_P	Price of electrical energy	1.4×10^{-8}	\$ J^{-1}	[12]
S_A	Anode CO_2 separation energy	1.76×10^{-5}	J mol^{-1}	[1]
μ	Cathode stream separation efficiency	0.15	-	[1]
v_L	Liquid separation cost	0 (neglected)	\$ mol^{-1}	-
μ_A	Anode crossover fraction	1	-	-
V	Cell potential	3	V	[34]
T	Temperature	293.15	K	-

Table 4.2: Table of model parameters based on Kenis group flow electrolysers [36, 15, 22, 34].

4.7. ADDITIONAL RESULTS

4.7.1. STEP LOADING

Step loading can be interpreted as a series of electrolysers with different catalyst loadings, all sharing a single liquid and single gas channel. This means that step loading, while computationally more awkward due to functional discontinuities slowing both individual solutions and precluding the use of many optimisation functions, could be easier to implement in a physical electrolyser. We could elect to simply discretise the existing polynomial fit solutions, but instead use this discretisation as an initial condition and perform additional, albeit inefficient, brute-force optimisation to determine the coefficients a_n for a step loading of N steps. For the cases in Fig. 4.6 we instead solve for a step function catalyst loading, with results in Fig. 4.11 showing that for even a low value of $N = 3$, much of the improvement from a smooth loading profile can be retained. Given the negligible depreciation in performance, step-loading seems a viable alternative when a precisely engineered profile is infeasible, and could also prove a more robust diagnostic tool in the experimental advancement of variable catalyst loading than smooth loading.

4.7.2. REACTANT PRICE SENSITIVITY

We give a brief demonstration of a special case of Eq. (4.37) namely the effect of v_{CO_2} decreasing to equal $v_P v_A$. This represents the point at which anodic CO_2 recovery cost, $v_P v_A$, exceeds the price of CO_2, v_{CO_2}, and it becomes economically preferential to skip the anodic separation step.

4.7.3. SUBSTRATE HER

Yang et al. [38] showed that some or even most of the HER can occur on the substrate. While we otherwise assume that the electrolysers concerned by our model have a sufficient PTFE content to render this fraction negligible, we here entertain the possibility of a catalyst deposition on bare GDL and the occurrence of the HER on regions of the substrate not covered by catalyst. Introduced briefly in the main text, we retain the conversion of

$$\bar{k} \to \theta \bar{k} \tag{4.94}$$

but for the HER use

$$\bar{k}_{H_2} \to \frac{\theta + \theta_0}{1 + \theta_0} \bar{k}, \tag{4.95}$$

where θ_0 is the ratio between catalyst and substrate HER at unit catalyst loading. Given that the majority of the power of variable catalyst loading lies in its ability to improve selectivity by reducing unnecessary HER, it is clear that the larger θ_0 becomes, the less effective this approach will become. In Fig. 4.13 we show parametric studies for the cases depicted in Figs. 4.6(a) and 4.7(a) respectively, increasing θ_0 to show the impact of a greater substrate contribution to HER. These results show that systems with a significant portion of substrate HER can still benefit from variable catalyst loading, provided that portion is not extreme. Nonetheless, optimised performance does still decrease as θ_0 increases, up to the limit at $\Theta = 1$. The inclusion of PTFE in a catalyst layer is usually preferable for other reasons, like stability and controllable wettability, so our observation that a lower θ_0 is preferable and attainable with PTFE adds more support for its inclusion.
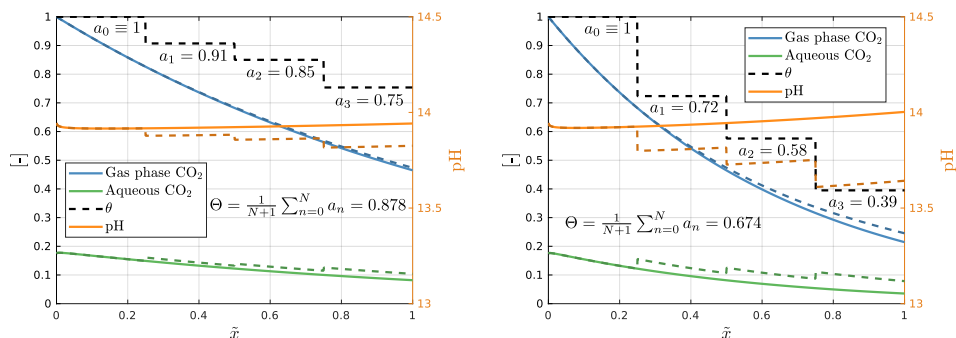
(a) Flow-wise development of pH and dimensionless gas and liquid phase CO_2 concentrations for uniform $\theta \equiv 1$ and dashed concentrations for a step loading with $N = 3$ at a flow rate of $\frac{Q_{ref}}{2}$ in the setup of Fig. 4.6(a).

(b) Flow-wise development of pH and dimensionless gas and liquid phase CO_2 concentrations for uniform $\theta \equiv 1$ and dashed concentrations for a step loading with $N = 3$ at a flow rate of $\frac{Q_{ref}}{4}$ in the setup of Fig. 4.6(b)

Figure 4.11: Step loading analogues of the polynomial loading cases depicted in Fig. 4.6, with $N = 3$. Note the jagged aqueous phase variables, as these are functions only of a through-plane mass balance. The gas phase CO_2 remains continuous, but not smooth, and its lack of smoothness manifests in the discontinuities in the other variables. The system exhibits only a slight performance drop in comparison to the smooth polynomial loading, with optimised profits of 5.12 and 3.47 \$ m^{-2} d^{-1} versus the 5.13 and 3.49 \$ m^{-2} d^{-1} of the polynomial case and similar values of Θ.

Product	n	Value per mole	FE
CO	2	0.017 \$ mol^{-1}	0.065
HCOOH	2	0.034 \$ mol^{-1}	0.03
CH_3OH	6	0.0186 \$ mol^{-1}	0
CH_4	8	0.0029 \$ mol^{-1}	0.016
C_2H_4	6	0.0365 \$ mol^{-1}	0.552
C_2H_5OH	6	0.0461 \$ mol^{-1}	0.259

Table 4.3: Fitted Faradaic efficiencies and prices for Cu products. The remaining current is consumed by HER.

Low values of θ_0 are still permissible, and do not greatly diminish the efficacy of the optimisation process.

4.7.4. Multiple product reduction

Taking a similar setup from the Kenis group, we use parameters and Faradaic efficiencies from Hoang et al. [10] to follow the steps in Sec. 4.6.4 to emulate reduction on a CuAg alloy selective towards C_2H_4 and C_2H_5OH as well as CO, H_2 and a few other low FE products. This is a very rough approximation as it requires us to assume first order reaction for every species, including C_{2+} products, and we further neglect any calculation of liquid product separation cost. We take C_2H_4 and C_2H_5OH prices from Jouny et al. [12]. The largest difference is due to the increased value of reactant averaged (i.e., per CO_2 consumed)
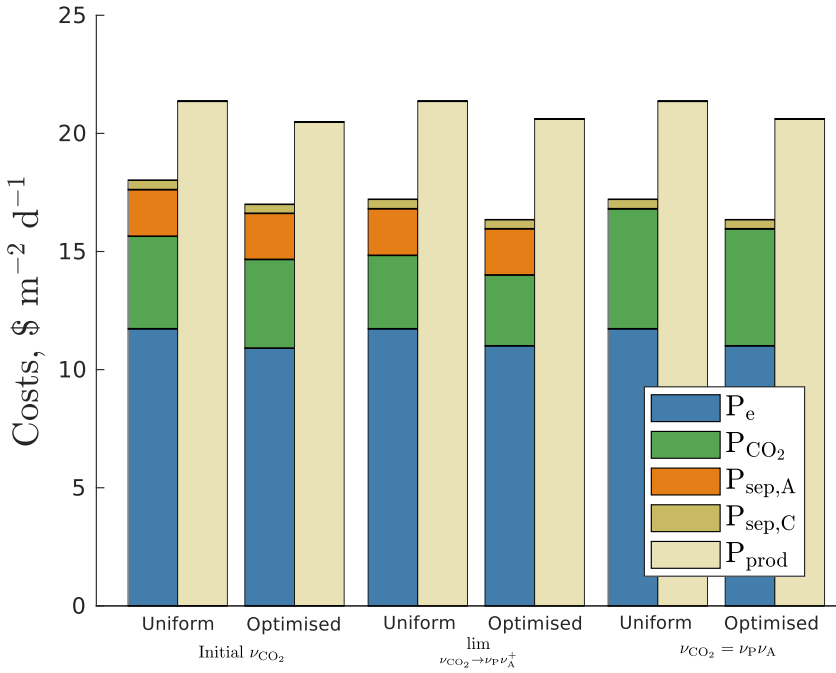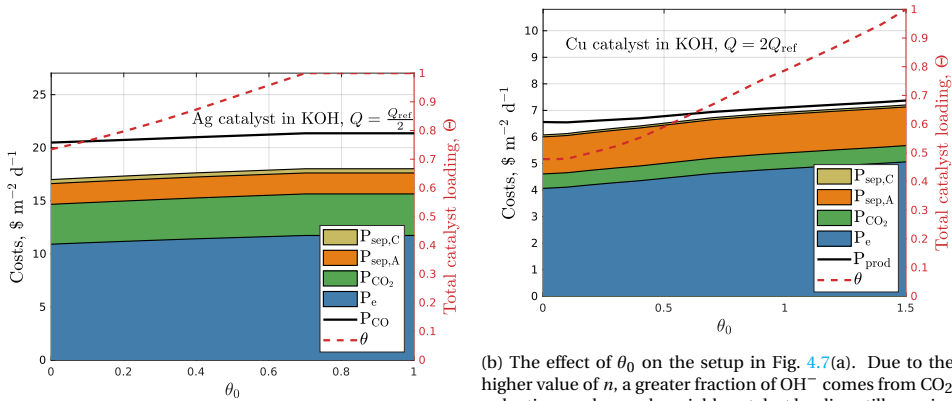
Figure 4.12: Cost breakdowns for three cases: the setup in Fig. 4.6(a), then the same setup but with ν_{CO_2} reduced to approximately $\nu_P\nu_A$, and finally with $\nu_{CO_2} = \nu_P\nu_A$, with the latter two cases distinguished simply to show that this is the value of reactant price at which it becomes infeasible to recover reactant from anode crossover.

(a) The effect of θ_0 on the setup in Fig. 4.6(a). Variable catalyst loading quickly becomes impotent and optimal loading reverts to unity after $\theta_0 \approx 0.7$.

(b) The effect of θ_0 on the setup in Fig. 4.7(a). Due to the higher value of n, a greater fraction of OH^- comes from CO_2 reduction, and as such variable catalyst loading still remains useful up to a larger value of θ_0. For $\theta_0 = 1.5$, 60% of HER is catalyst independent, so the limited effectiveness of variable catalyst loading is to be expected.

Figure 4.13: Parametric studies varying θ_0 for the cases depicted in Figs. 4.6(a) and 4.7(a), in which we clearly see that an increase in θ_0 leads to an increase in optimal Θ along with a decrease in profit margin until Θ reaches unity. After this point, increasing θ_0 has no further effect on the system.

$n \approx 5.2$ compared to the $n = 2$ of reduction to CO. We determine this n through

$$n = \left(\sum_i \frac{S_i}{n_i} \right)^{-1}, \tag{4.96}$$

where i are the different reaction pathways, each transferring n_i electrons with an FE or selectivity of S_i. Looking at the stoichiometric limit of the 1D system in Eq. (4.14), even in the absence of HER this would increase the rate at which reactant depletes from $\tilde{c} \approx e^{-2Da\tilde{x}}$ to $\tilde{c} \approx e^{-3.5Da\tilde{x}}$, entirely due to autoreaction with the OH^- ions produced in the reduction. As such, in the absence of strong buffering electrolytes, the reactant utilisation efficiency is very low, and an excess of 80% of gaseous CO_2 reactant is converted to HCO_3^- and CO_3^{2-}, a portion of which will also cross over and lead to high anodic separation costs as well as reactant costs.

4.7.5. NEUTRAL ELECTROLYTE

For the case in Verma et al. [34] for 3 M $KHCO_3$, we take the highest current density measurement, presumed to be at a cell potential of 3.5 V, and apply the same optimisation process. Despite the increase in cell potential, the decrease in conductivity compared to KOH leads to a much lower total current density of $j = 137$ mA cm^{-2}. Nonetheless, electrolysis energy remains the greatest cost. Other than this, the main difference is the reduced, near-neutral, pH. In KOH, θ can never locally reach very low values unless the reactant supply is also depleted, as this would otherwise lead to costly parasitic consumption of CO_2 through homogeneous reactions with no reduction reaction to compete with it. In $KHCO_3$ however, the aqueous local CO_2 concentration is almost entirely controlled with θ, as both the reduction reaction and homogeneous reaction are dependent on θ as the sole OH^- source is from heterogeneous reactions rather than from the electrolyte. This combines with the fact that electrolyte now also acts a small source of CO_2 rather than sink, and acts as a sink for OH^-, allowing the catalyst loading to have a greater effect. In Fig. 4.14 we see that for similar conditions, the effect of variable catalyst loading is greater in a neutral electrolyte than in an alkaline electrolyte. We note that the investigated current density is lower in this neutral electrolyte case, so in Fig. 4.15 we rescale the electrochemical reaction rates to mimic those of Fig. 4.6(a), while accounting for that in Q_{ref}. In this case, the effect of variable catalyst loading is more extreme, with a large drop in pH, and the interesting phenomenon in which aqueous CO_2 concentration actually increases near the outlet, due to complete lack of sinks in the absence of OH^- and catalyst.

4.7.6. HIGH Q LIMIT

When considering $\lim_{Q \to \infty} \Theta$ in Fig. 4.10 we found that for the setup of Fig. 4.6 and Fig. 4.7 were optimised by a maximised flat loading of $\Theta = 1$. However, there are many setups in which $\Theta_{max} = \lim_{Q \to \infty} \Theta < 1$. For instance, if we increase the cell potential of the setup in Fig. 4.6(a) from 3 V to 3.5 V, to emulate a resistance increase, perhaps due to the deterioration of KOH over time or the inclusion of a more resistive ion-exchange membrane, then Θ_{max} drops significantly (Fig. 4.16b). While a decrease in cell performance leads to this reduction in Θ_{max}, the opposite can also be true. If we double the electrochemical
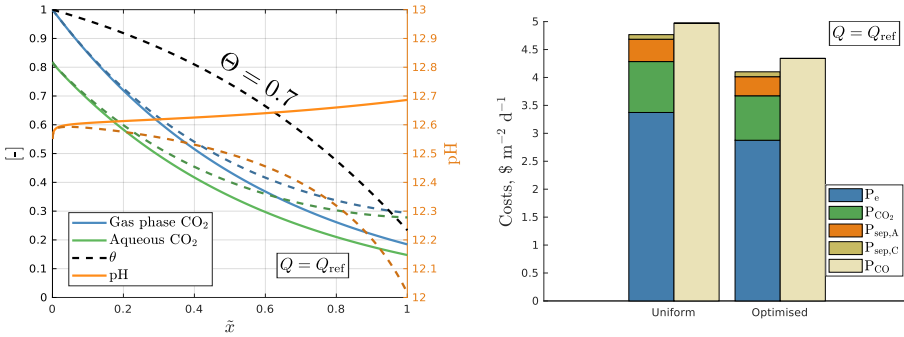
(a) Optimised catalyst loading in 3 M KHCO$_3$ at $Q = Q_{ref} \approx$ 1.25 ml min^{-1}. Despite showing a very similar catalyst loading profile to that of Fig. 4.6(a), the effect on pH and aqueous CO$_2$ concentration is much more pronounced.

(b) Costs associated with the 3 M KHCO$_3$ cell. Despite a lower current density, electrolysis energy is still the largest cost. Furthermore, the low pH allows the anodic separation cost to remain relatively small.

Figure 4.14: Optimised catalyst loading for a 3 M KHCO$_3$ cell. Compared to Fig. 4.6(a), we see a more pronounced effect on pH and aqueous CO$_2$ concentration, despite a very similar catalyst loading profile. This is reflected in the profit margin, as the improvement in Fig. 4.14a is around 17% compared to that of 8% in Fig. 4.6(a), despite the lower current density and higher cell potential.
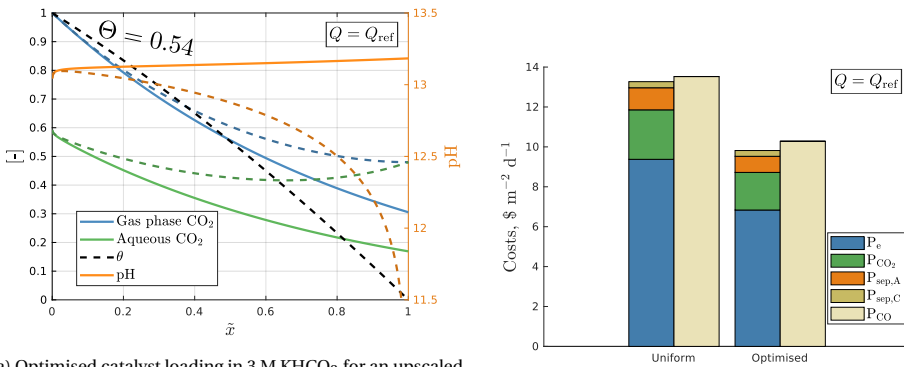
(a) Optimised catalyst loading in 3 M KHCO$_3$ for an upscaled current density and Q_{ref} to match Fig. 4.6(a). Lower Θ leads to lower pH, and the complete absence of both heterogeneous and homogeneous reactions near $\tilde{x} = 1$ leads to the aqueous CO$_2$ concentration rising to meet the gas channel CO$_2$ concentration.

(b) Costs associated with the 3 M KHCO$_3$ cell with upscaled current density. The increase in profit scales with current density, and we here see a 32% increase in profit margin over that of the uniform loading.

Figure 4.15: Optimised catalyst loading for a 3 M KHCO$_3$ cell for an upscaled flow rate and current density. Despite the lack of OH$^-$ from the electrolyte channel, a high pH can still be reached when current density is locally high, so it is vital that θ be reduced as the channel progresses to minimise this unnecessary reaction with OH$^-$.
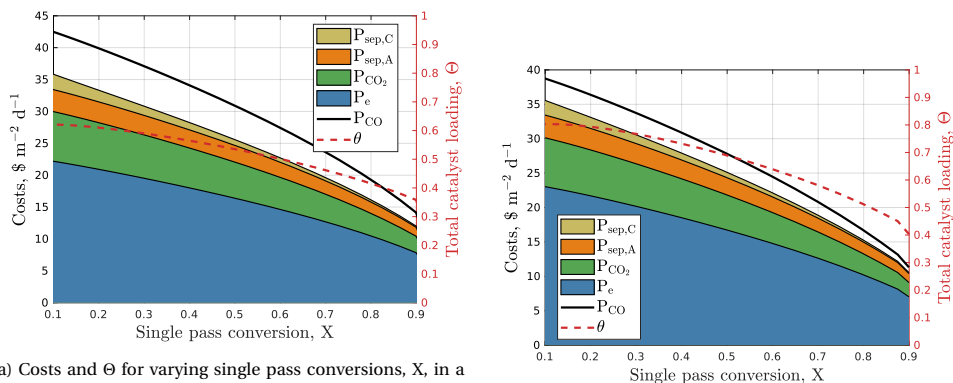
(a) Costs and Θ for varying single pass conversions, X, in a cell with doubled electrochemical reaction rates compared to Fig. 4.6(a). The more pronounced drop in Θ is here due to a limitation in mass transfer from the gas phase. Even with heterogeneous reaction kinetics that dominate homogeneous reactions, the local aqueous CO_2 concentration is never sufficient for Θ to approach unity, and the cell would instead benefit from operation at higher gas pressure.

(b) Costs and Θ for varying single pass conversions, X, in a cell with an increased resistance leading to a total cell potential of 3.5 V. Note that P_e has increased by less than would be expected, and instead P_{CO} has shouldered a portion of the loss, as the optimiser has reduced to Θ to lead to a slightly lower current to account for the increased cell potential.

Figure 4.16: Two cases in which Θ does not approach unity, regardless of gas flow rate. In the former, a high electrolysis cost is limiting due to high resistance, and in the latter the pressure of the gas supply is insufficient to meet the demand for reactant. Both are relevant cases for industrial electrolysis, and show that some issues persist even in perceived abundance of reactant.

reaction rates while retaining the same cell potential and initial Faradaic efficiency, we see a similar effect on $Θ_{max}$ in Fig. 4.16a.

BIBLIOGRAPHY

[1] Théo Alerte et al. "Downstream of the CO2 Electrolyzer: Assessing the Energy Intensity of Product Separation". In: *ACS Energy Letters* 6.12 (2021), pp. 4405–4412.

[2] Ali Belhocine and Wan Zaidi Wan Omar. "Similarity solution and Runge Kutta method to a thermal boundary layer model at the entrance region of a circular tube". In: *World Journal of Engineering* 10 (2018), pp. 1–10.

[3] Joseph W. Blake et al. "Inhomogeneities in the Catholyte Channel Limit the Upscaling of CO2 Flow Electrolysers". In: *ACS Sustainable Chemistry & Engineering* 11.7 (2023), pp. 2840–2852.

[4] William A. Braff, Cullen R. Buie, and Martin Z. Bazant. "Boundary Layer Analysis of Membraneless Electrochemical Cells". In: *Journal of The Electrochemical Society* 160.11 (2013), A2056.

[5] Thomas Burdyny and Wilson A. Smith. "CO_2 reduction on gas-diffusion electrodes and why catalytic performance must be assessed at commercially-relevant conditions". In: *Energy Environ. Sci.* 12 (5 2019), pp. 1442–1453.

[6] Yingying Cheng et al. "CO2 Electrolysis System under Industrially Relevant Conditions". In: *Accounts of Chemical Research* 55.3 (2022). PMID: 35045254, pp. 231–240.

[7] Maxwell Goldman et al. "Bridging fundamental science and applied science to accelerate CO2 electrolyzer scale-up". In: *Current Opinion in Electrochemistry* 39 (2023), p. 101248. ISSN: 2451-9103.

[8] J. W. Haverkort. *Electrolysers, Fuel Cells and Batteries: analytical modelling*. TU Delft Open Publishing, 2024.

[9] JW Haverkort et al. "An analytical flow-by capacitive deionization model". In: *Desalination* (2024), p. 117408.

[10] Thao T. H. Hoang et al. "Nanoporous Copper–Silver Alloys by Additive-Controlled Electrodeposition for the Selective Electroreduction of CO2 to Ethylene and Ethanol". In: *Journal of the American Chemical Society* 140.17 (2018). PMID: 29620896, pp. 5791–5797.

[11] Philippe Jeanty et al. "Upscaling and continuous operation of electrochemical CO_2 to CO conversion in aqueous solutions on silver gas diffusion electrodes". In: *Journal of CO_2 Utilization* 24 (2018), pp. 454–462. ISSN: 2212-9820.

[12] Matthew Jouny, Wesley Luc, and Feng Jiao. "General Techno-Economic Analysis of CO_2 Electrolysis Systems". In: *Industrial & Engineering Chemistry Research* 57.6 (2018), pp. 2165–2177.

[13] Recep Kas et al. "Along the Channel Gradients Impact on the Spatioactivity of Gas Diffusion Electrodes at High Conversions during CO_2 Electroreduction". In: *ACS Sustainable Chemistry & Engineering* 9.3 (2021), pp. 1286–1296.

[14] Ahmad El-kharouf et al. "Ex-situ characterisation of gas diffusion layers for proton exchange membrane fuel cells". In: *Journal of Power Sources* 218 (2012), pp. 393–404. ISSN: 0378-7753.

[15] Byoungsu Kim et al. "Influence of dilute feed and pH on electrochemical reduction of CO_2 to CO on Ag in a continuous flow electrolyzer". In: *Electrochimica Acta* 166 (2015), pp. 271–276. ISSN: 0013-4686.

[16] A.A. Kulikovsky. "A model for optimal catalyst layer in a fuel cell". In: *Electrochimica Acta* 79 (2012), pp. 31–36. ISSN: 0013-4686.

[17] A.A. Kulikovsky. "Optimal shape of catalyst loading across the active layer of a fuel cell". In: *Electrochemistry Communications* 11.10 (2009), pp. 1951–1955. ISSN: 1388-2481.

[18] A.A. Kulikovsky. "Optimal shape of catalyst loading along the oxygen channel of a PEM fuel cell". In: *Electrochimica Acta* 54.27 (2009), pp. 7001–7005. ISSN: 0013-4686.

[19] Gastón O. Larrazábal, Ming Ma, and Brian Seger. "A Comprehensive Approach to Investigate CO_2 Reduction Electrocatalysts at High Current Densities". In: *Accounts of Materials Research* 2.4 (2021), pp. 220–229.

[20] André Lévêque. "Les lois de la transmission de chaleur par convection". PhD thesis. Faculté des Sciences de Paris, 1928.

[21] Yi Li et al. "Atomically dispersed single Ni site catalysts for high-efficiency CO2 electroreduction at industrial-level current densities". In: *Energy Environ. Sci.* 15 (5 2022), pp. 2108–2119.

[22] Sichao Ma et al. "Efficient Electrochemical Flow System with Improved Anode for the Conversion of CO2 to CO". In: *Journal of The Electrochemical Society* 161.10 (2014), F1124.

[23] Thomas Moore et al. "Electrolyzer energy dominates separation costs in state-of-the-art CO2 electrolyzers: Implications for single-pass CO2 utilization". In: *Joule* 7.4 (2023), pp. 782–796. ISSN: 2542-4351.

[24] Thomas Moore et al. "Simplified Models of the Bicarbonate Buffer for Scaled Simulations of CO2 Electrolyzers". In: *Industrial & Engineering Chemistry Research* 62.40 (2023), pp. 16291–16301.

[25] B. Pribyl-Kranewitter et al. "Influence of low-temperature electrolyser design on economic and environmental potential of CO and HCOOH production: A techno-economic assessment". In: *Renewable and Sustainable Energy Reviews* 154 (2022), p. 111807. ISSN: 1364-0321.

[26] R. Sander. "Compilation of Henry's law constants (version 5.0.0) for water as solvent". In: *Atmospheric Chemistry and Physics* 23.19 (2023), pp. 10901–12440.

[27] Mark Sassenburg et al. "Characterizing CO2 Reduction Catalysts on Gas Diffusion Electrodes: Comparing Activity, Selectivity, and Stability of Transition Metal Catalysts". In: *ACS Applied Energy Materials* 5.5 (2022), pp. 5983–5994.

[28]   Hunter Simonson et al. "Direct Measurement of Electrochemical Selectivity Gradients over a 25 cm2 Copper Gas Diffusion Electrode". In: *ACS Energy Letters* 8.9 (2023), pp. 3811–3819.

[29]   Ana Somoza-Tornos et al. "Process modeling, techno-economic assessment, and life cycle assessment of the electrochemical reduction of CO_2: a review". In: *iScience* 24.7 (2021). ISSN: 2589-0042.

[30]   Joshua M. Spurgeon and Bijandra Kumar. "A comparative technoeconomic analysis of pathways for commercial electrochemical CO_2 reduction to liquid products". In: *Energy Environ. Sci.* 11 (6 2018), pp. 1536–1551.

[31]   Di Tian, Zhiguo Qu, and Jianfei Zhang. "Electrochemical condition optimization and techno-economic analysis on the direct CO2 electroreduction of flue gas". In: *Applied Energy* 351 (2023), p. 121787. ISSN: 0306-2619.

[32]   N. Valle and J.W. Haverkort. "Analytical mass transfer coefficients for natural convection from vertical gas-evolving electrodes". In: *International Journal of Heat and Mass Transfer* 225 (2024), p. 125390. ISSN: 0017-9310.

[33]   Sumit Verma et al. "A Gross-Margin Model for Defining Technoeconomic Benchmarks in the Electroreduction of CO_2". In: *ChemSusChem* 9.15 (2016), pp. 1972–1979.

[34]   Sumit Verma et al. "The effect of electrolyte composition on the electroreduction of CO_2 to CO on Ag based gas diffusion electrodes". In: *Phys. Chem. Chem. Phys.* 18 (10 2016), pp. 7075–7084.

[35]   Lien-Chun Weng, Alexis T. Bell, and Adam Z. Weber. "Modeling gas-diffusion electrodes for CO_2 reduction". In: *Phys. Chem. Chem. Phys.* 20 (25 2018), pp. 16973–16984.

[36]   Devin T. Whipple, Eryn C. Finke, and Paul J. A. Kenis. "Microfluidic Reactor for the Electrochemical Reduction of Carbon Dioxide: The Effect of pH". In: *Electrochemical and Solid-State Letters* 13.9 (2010), B109.

[37]   Ke Xie et al. "Eliminating the need for anodic gas separation in CO2 electroreduction systems via liquid-to-liquid anodic upgrading". In: *Nature Communications* 13.1 (2022), p. 3070. ISSN: 2041-1723.

[38]   Kailun Yang et al. "Role of the Carbon-Based Gas Diffusion Layer on Flooding in a Gas Diffusion Electrode Cell for Electrochemical CO_2 Reduction". In: *ACS Energy Letters* 6.1 (2021), pp. 33–40.

4

5

CONCLUSION

5.1. RESEARCH QUESTIONS

The introduction posed a number of research questions, each of which have now been addressed. In Chapter 2 it was found analytically that a thicker CL is poorly utilised unless the cathode potential, or superficial current density, is low enough to not deplete reactant through the CL. This is shown in Eqs. 2.45 and 2.49, where, for a high superficial current density, the effectiveness of the CL will scale inversely with its thickness. As potential increases, the concentration polarisation increases, until the CL near the catholyte performs negligible CO_2 electroreduction, but remains able to perform HER. Ideally, the analytical solution in 2.8 can be used to determine the optimal CL thickness, based on a target j_{CO}, as seen in Fig. 2.4a, but the cost-weighted metric, Eq. 4.37 in Chapter 4 indicates that it is likely preferable to err in the favour of a thin CL, as the cost of CO_2 loss to the catholyte will likely be less than the cost of unnecessary HER in an underutilised thick CL Research Question 1, (RQ1).

The alkalinity problem has often been blamed on HER. High pH catholytes are often used to minimise the availability of H^+ for HER and to maintain high FE to CO_2 reduction products, and even in neutral electrolytes, HER produces OH^- ions that increase the pH. However, the sharp spikes in CL pH found in the simulation of Chapter 3 were found even in neutral electrolytes at high FE to CO_2 products, and were such that the model needed to be logarithmically rescaled for stability. This means that the alkalinity problem cannot be blamed entirely on HER, and the problem would exist in CO_2 electroreduction even with its complete absence. The model shows that the pH stabilisation effect of the catholyte is dependent on aqueous diffusion, whereas the effects that drive pH increase are dependent on extremely fast gas-phase transport of CO_2 with, by design, an extremely small aqueous diffusion pathway, HER notwithstanding. For commercial current densities ($j_{CO} > 500 \text{mA cm}^{-2}$) it should be presumed that the local CL environment will be alkaline, and as seen in Chapter 4, a rough approach is to assume a CO_2 utilisation/consumption ratio dependent on the number of electrons transferred per product, n (RQ2).

As reactant is depleted along the gas channel and the local environment becomes less favourable for CO_2 electroreduction in the CL due to degradation of the electrolyte in the

flow direction, the electrolyser suffers significant drops in j_{CO} and FE. In the metre-long case considered in Chapter 3, the performance in the latter portions was significantly lower than near the inlet, with over half of the total CO_2 electroreduction taking place in the first third of the electrolyser length. A significant portion of this loss of performance came from the widening catholyte boundary layer and increasingly carbonate filled electrolyte, motivating the use of higher flow-rates and lower single-pass conversions when upscaling CO_2 electrolysers. Static mixers to disturb the flow and break up this boundary layer are a notable alternative, but the boundary layer is also the region of highest carbonate concentration. By breaking up the boundary layer, there may be a consequence of improving carbonate transport to and through the membrane, increasing carbonate crossover and subsequent reactant loss RQ3)].

In each chapter, catalyst utilisation has been an issue, but unlike in many electrochemical systems this is not just a case of unnecessary capital expense. The combination of HER and the bicarbonate buffer system means that excess catalyst contributes both a reduction in current utilisation and in reactant utilisation. In Chapter 2, the effectiveness of the catalyst layer was given by roughly $\frac{\tanh M_T}{M_T}$, where M_T is the Thiele modulus, and was essentially governed by how high an average concentration of CO_2 could be maintained in the CL [28]. When the CL is too thick, too much of the CO_2 is reacted away before it can reach the deeper catalyst sites, and as such the CL utilisation is poor. A similar effect is found in Chapters 3 and 4, but in the flow-wise direction rather than the flow-perpendicular direction through the CL. However, in the latter case, this is balanced against a cost-weighted metric, determining that the excess catalyst is actively detrimental to performance unless HER is completely eliminated. In the best case, excess catalyst will attain the same performance as an optimally loaded equivalent, but at a higher capital expense. Of course, underloading is similarly detrimental, but the negatives of underloading of a CL can be somewhat mitigated by increasing applied potential and thus superficial current density, which is a preferable course of action over paying for more catalyst just to operate at a lower current density (RQ4)].

The construction of a cost-weighted metric is motivated by publications detailing the unexpectedly high costs of anode-stream separation and electrolysis energy, compared to other costs [17, 34]. In Chapter 4, a single price for power is used as an input, so for anode and cathode stream separation costs calculation a conversion can be used from $ J^{-1} and J kg^{-1} to $ mol^{-1} based on the same cost of electricity as the electrolysis component. Calculating some values for this metric, it is clear that electrolyser energy dominates in every considered electrolyser of reasonable current density, with anode separation cost placing second. While reactant is a significant cost, its value is comparable to the cost of recovering crossover CO_2 from the anode stream, meaning that it is foreseeable that the advent of low cost direct air capture of CO_2 or utilisation of flue gases could reduce the cost of reactant CO_2 below the cost of recovery. This could shift the place of CO_2 electroreduction from a synthesis process to something more akin to a scavenging process of flue gas, allowing impure mixtures to continue into some later downstream processing. Regardless, cell potential governs the cost of electrolysis in comparison to the other costs, and the outlook for minimising cell potential is grim in comparison to the other components. Reactant cost is reducible through flue gas use or cheaper future direct air capture [8, 25], meaning that carbonate crossover will cost less in ters of reactant

loss. If we consider reactant purification and product separation costs as an energy requirement (J mol^{-1}) then we can compare that to the much higher energy requirement of electrolysis in J mol^{-1} too, assuming that all processes can utilise the same low price local renewable energy sources. It is thus likely that electrolysis will remain the dominant cost in future, even if renewable energy prices decrease (RQ5).

5.2. Areas of future interest

This thesis raises many areas for future interest.

First and foremost is practical experimentation: there is a current lack of experimental literature to compare and contrast with the predictions and recommendations of the models presented here. So far, electrolyser scale-up has only reached an order of 100-250 cm^2 [24], and in the approach to achieving the >400 cm^2 area targeted by literature it would be beneficial to experimentally investigate how well computational predictions of scaling relations match with reality.

As Chapter 2 considers through-plane optimisation of the CL, it could be beneficial to consider an extension of the work of Kulikovsky in fuel cells to the field of CO$_2$ electroreduction [10, 11]. As mentioned, the self-interaction of the bicarbonate buffer system and the influence of HER mean that the potential room for improvement is greater than that of the already advanced fuel cells, in which optimisation considers only catalyst and overpotential utilisation [12]. Considering that Chapter 2 already found optima for CL thicknesses, it is likely that an analogous optimisation could be performed considering the conclusion of the equivalence of 1D catalyst loading and Damköhler number in the analytical model of Chapter, but with a total catalyst loading Θ instead of just CL thickness 4. A natural continuation of the work in Chapter 4 would then be to combine it with the through-plane direction, to create a general unified model of catalyst loading. There is generally a relationship between CL thickness and catalyst loading in mg cm^{-2}, so to treat them as independent is unrealistic. Thankfully, the framework to create such a unified model has already been laid out in this thesis, although it is foreseeable that such a model would become too complicated to treat analytically or with a simple numerical model, and would likely require computational modelling, similar to Chapter 3.
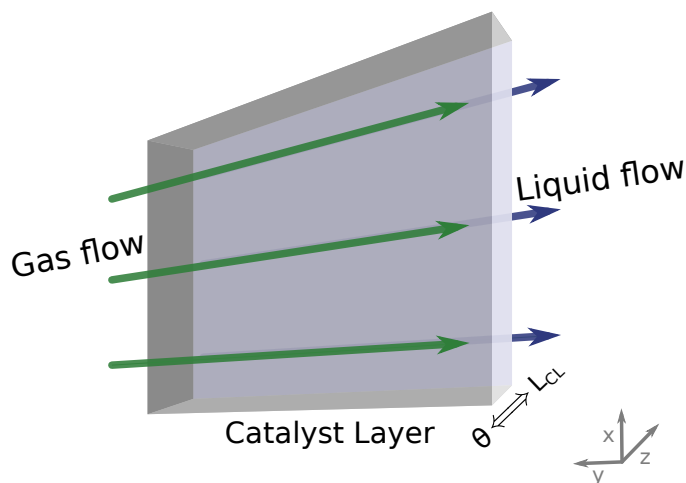
Figure 5.1: The catalyst layer thickness from Chapter 2 is linked to catalyst loading from Chapter 4 and a future unified model could associate them both through a surface catalyst loading (mg cm^{-2}).

5.3. CO$_2$ ELECTROREDUCTION TECHNOLOGY READINESS LEVEL

Technology readiness level (TRL) is a scale from 1-9 that describes how far along the journey from inception to full realisation a technology is. Lower TRLs concern fundamental and mechanistic research, medium TRLs consider upscaling feasibility, and higher TRLs consider commercial and infrastructural viability. A description of the TRLs of a few technologies is shown in Fig. 5.2, in which CO$_2$ electrolysis is assigned a TRL range of 3-4 [7, 5]. This means that CO$_2$ electrolysis is at the stage where the basic principles are well-understood to the point at which the technology has been formulated into tangible designs that have been proven to some degree to work at the proof-of-concept stage in a laboratory [22]. Increasing the TRL requires demonstration that CO$_2$ electrolysis is actually a feasible process (TRL 4) and demonstration that the technology can be operated at sufficient scale and with sufficient stability to be viable to prototype (TRL 5).

The rough targets for development are often given along the lines of

- Current density, $j > 200$-500 mA cm^{-2}

- Faradaic efficiency, FE$_{prod} > 95\%$

- Lifetime, $\tau > 10000$ h

- Cell area, $A > 400$ cm^2,

although it is noteworthy that these figures frequently increase [32, 4, 1]. It is very easy for an experimental setup to meet one or some of these criteria by sacrificing performance in the others. An absurd example from Chapter 4 is that an arbitrarily large and long-lasting cell can be constructed with a (degenerate) FE of 100%, by simply **not turning it on**. While clearly absurd, it is not a far cry from the myriad catalytic studies that laud their high selectivity and stability metrics despite operating at less than a tenth of a lower bound
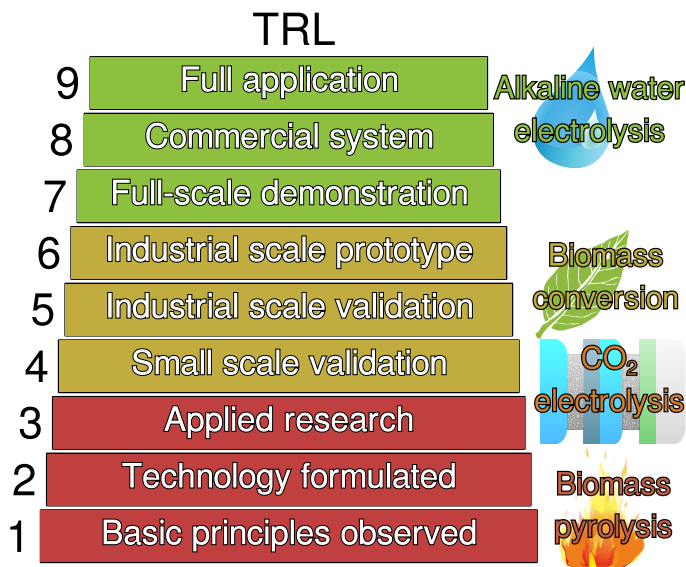
Figure 5.2: A comparison of the technology readiness level of CO_2 electrolysis to that of neighbouring technologies. CO_2 electrolysis sits in a range of 3-4, with some approaches as low as 2 [22]. Meanwhile alkaline water electrolysis sits around 8-9 [31], and biomass conversions vary on the range of 4-6 for gasification and anaerobic digestion or down to around 1 for pyrolysis [18].

minimum current density [15, 20, 33]. Avoiding such pitfalls requires a holistic treatment of design parameters: it is vital to consider realistic environments and conditions when investigating or optimising one aspect of operation.

5.4. PRIORITY ISSUES IN CO_2 ELECTROREDUCTION

Holistic treatment of CO_2 electroreduction as a process does not necessarily mean giving each issue equal weight. Some issues present only minor inconveniences, whereas others are enormous roadblocks to the future feasibility o the technology. The cost metric developed in Chapter 4 provides insight into the predominant contributors to total cost across a range of configurations, and shows that some factors are invariably more important than others.

5.4.1. OPERATIONAL FACTORS

Cell potential, E_{cell}, is the deciding factor behind the economic feasibility: many studies have shown that electrolysis energy is, unsurprisingly, the dominant factor in CO_2 electrolysis [17, 23], and this electrolysis energy is governed by E_{cell}. Any cell operating at significantly more than $E_{cell} = 3$ V is unlikely to be profitable without a large drop in the cost of electricity or increase in product value. Such low electricity costs are locally available, but while versatility is a strength of CO_2 electroreduction, it should not be generally assumed that electricity will be cheap. This means that the additional resistance of a flowing catholyte and/or BPM is seldom acceptable in comparison to AEM-MEA. A BPM

typically adds 1-2 V to E_{cell} in comparison to an AEM [36], but at the low target of E_{cell} = 3 V an increase to e.g. E_{cell} = 4.5 V constitutes a 50% increase in electrolysis energy. For this to be permissible, a BPM must reduce some other costs by a greater amount. Although the reduction in carbonate crossover allows a high cathodic carbon efficiency, the cost of anodic CO_2 recovery is still lower than the additional cost of electrolysis associated with the higher E_{cell} [17]. Any changes that increase the cell potential must be scrutinised intensely before adoption.

Intermittent operation of CO_2 electrolysers will be beneficial or necessary for a few reasons. The first is fundamental to the motivation behind CO_2 electroreduction: it must utilise renewable energy to effectively be carbon neutral, and renewable energy sources are intermittent. In some proposals, it is even the bridge between intermittent renewable sources and stable power grid infrastructure. However, intermittent operation may also be necessary on different timescales to address some of the more pressing matters of stability and feasibility. Catholyte flooding, electrowetting, salt precipitation, and degradation of substrates, are all interlinked and have all been associated with continuous high load operation [13, 1, 6]. Together they form a pervasive group of threats to long term continuous operation, and while some steady solutions have been proposed, such as strict control of electrolyte concentration and cation identity, many clearly effective engineering solutions exist with intermittent operation [26]. By periodically flushing out the electrolyte channel with a solvent or cycling the voltage, cells can maintain a competitive performance for far longer than under constant load, and remain energy efficient despite being held at an inoperative regeneration potential for a third of the time [35]. Rather than averting crossover, the latter approach utilises it, permitting carbonates to cross to the anode side while the cell is idle, away from the vulnerable CL.

Upstream processing must be understood to correctly optimise cell operation. Lab-scale electrolysis experiments utilise high purity CO_2, but this requires expensive separation and purification or direct air capture: separation from industrial sources typically costs around 0.07 \$ kg^{-1}, with direct air capture providing a more versatile option but with early stage technology high costs that are likely to drop [8, 25]. The reactant cost is generally lower than the electrolysis cost, but it can be lowered even further still by the direct use of flue gases as a reactant stream. Van Daele et al. showed that the effects of the main non-CO_2 components of flue gas, that is N_2 (>70%) and O_2 ($\approx$ 5%) are indirect and not entirely unmanageable due to their low solubilities [30]. N_2 effectively only dilutes the CO_2, reducing its partial pressure, and although O_2 actively competes with CO_2 electroreduction by undergoing the far more favourable oxygen reduction reaction (ORR), its low solubility means that it encounters debilitating mass transfer limitations at lower current densities than CO_2. The former issue can be solved by repressurising the flue gas to increase the CO_2 partial pressure, and the latter can be solved by operating far above the ORR limiting current density. In addition, the dreaded SO_x and NO_x impurities were found to be detrimental to FE [19], but only at concentrations far in excess of what is typical for flue gases (<200 ppm) [29]. It should be expected that the cost of reactant CO_2 will plummet as the technology matures, and focus should shift further from efficient CO_2 utilisation to stability, scalability, and energy efficiency.

Single-pass conversion, when viewed in the context of the previous points, becomes less of a priority. Any reduction in CO_2 partial pressure due to streamwise depletion is

associated with a reduction in available CO_2 in the CL and thus a reduction in FE towards carbon products. As electrolysis energy is the dominant cost, this reduction in FE will practically always come at a greater price than the reduction in product stream separation cost, which, in the case of gas products utilising a flue gas source, will be governed by many more constituent gases than just CO_2 and products.

5.4.2. DESIGN FACTORS

When one notes that the majority of physical components used in CO_2 electrolysers are directly ported from adjacent technologies, their shortcomings become less surprising. While the use of components primarily designed for fuel cells has allowed fast progress in experimental work, it is vital for techno-economic assessments to know how much of an improvement bespoke components will bring when the market for them grows. Some futures are clear, like how the scarcity of iridium means that iridium based anode catalysts will remain expensive. Not only is iridium also in high, even bottleneck, demand for PEM water electrolysis, but the global mining rate is around 5-7 t year^{-1} [16], a figure which will likely grow slowly over the next 50 years. Ideally, near unity recycling could be achieved, similarly to other expensive catalysts such as platinum or palladium, but even in such a case the raw demand for iridium in both PEM water electrolysis and CO_2 electroreduction together will take years to meet. If more conductive long-term stable BPMs can be designed, then the acidification of the anolyte can be prevented and non-iridium anode material can be used.

In electrolysers that utilise a flowing catholyte, the delicate pressure balance between liquid and gas is currently difficult to maintain. Materials that are conducive to good gas transport are seldom sufficient to prevent liquid breakthrough and flooding through the gas transport medium. Although MPLs are frequently used to mitigate this flooding, many are prone to the formation of cracks through which electrolyte breakthrough can occur, and even crack-free MPLs often degrade during electrolysis [2]. Prohibitively small differential pressure windows make stable operation difficult to maintain, and these issues will only worsen when scale-up and intermittent operation enter consideration. Either extremely hydrophobic crack-free MPLs may become necessary, incurring a penalty to mass-transfer, or flooding must be controlled, potentially through the use of sacrificial macroporous pathways for liquid to escape through [3].

5.5. THE OUTLOOK FOR CO_2 ELECTROREDUCTION

Carbon capture and storage solutions are expensive enough that the modern term has been updated to carbon capture, **utilisation**, and storage [21], so clearly the future for CO_2 utilisation is bright. However, despite great promise as panacea solution to the problems of the energy solution, CO_2 electroreduction is somewhat late to the party. Both biological processes, with photosynthesis as the engine for biomass based CO_2 conversion, and certain chemical processes, such as mineralisation, carboxylation, and hydrogenation, have higher TRLs than CO_2 electroreduction [9]. Furthermore, none of the main products of CO_2 electroreduction are exclusive to this technology: most can otherwise be formed with reformation, hydrogenation, photochemical reduction or even plasma catalysis.

In a perfect world, there would be ample time to scale, mature, and perfect the

technology for large-scale deployment, but this is not a perfect world. The time required for such development could well be time that we simply do not have. To tackle climate change, immediate, if imperfect, solutions are necessary. A practical first step would be to heavily prioritise the production of CO over other chemicals. Due to the low electron transfer number of two in the case of CO and $HCOO^-$ production, these two products have a significantly higher value per unit electrolysis cost, but CO has the added advantage of at the beginning of the hydrocarbon synthesis chain. When additionally noting that CO will usually be produced alongside the competing H_2, the resultant $CO:H_2$ mix of syngas seems like an obvious candidate for insertion into industrial synthesis routes as a feedstock for the Fischer-Tropsch process alongside H_2 sourced from alkaline water electrolysis.

Nonetheless, it will still be a long time before the direct electrochemical route becomes economically feasible. For instance, a comparable technology for the renewable production of methanol would be the reverse water-gas shift (TRL 6) [14], circumventing the direct need for CO and utilising CO_2 from direct air capture and H_2 from alkaline water electrolysis, then performing the methanol synthesis reaction. However, technoeconomic assessments still show that fossil-based production of methanol, at roughly 450 €/t, costs less than half of what is currently achievable at scale with renewable processes, at 960 €/t [27]. This cost is expected to drop over the next decade, and could become competitive by 2035, provided renewable electricity prices and electrolyser costs decrease, and fossil-based methanol begins to be phased out.

To conclude, there is a clear place in the future for electrochemical CO_2 reduction, but it must compete with far more developed technologies to face pressing contemporary issues with the energy transition. For the present, it would be pertinent to focus on the reduction to CO, which is relatively simple and has a clear place in an existing synthesis chain, rather than focus on complicated direct synthesis of higher value chemicals.

BIBLIOGRAPHY

[1] Lorenz M. Baumgartner et al. "Electrowetting limits electrochemical CO2 reduction in carbon-free gas diffusion electrodes". In: *Energy Adv.* 2 (11 2023), pp. 1893–1904.

[2] Lorenz M. Baumgartner et al. "Narrow Pressure Stability Window of Gas Diffusion Electrodes Limits the Scale-Up of CO_2 Electrolyzers". In: *ACS Sustainable Chemistry & Engineering* 10.14 (2022), pp. 4683–4693.

[3] Lorenz M. Baumgartner et al. "When Flooding Is Not Catastrophic-Woven Gas Diffusion Electrodes Enable Stable CO_2 Electrolysis". In: *ACS Applied Energy Materials* 5.12 (2022), pp. 15125–15135.

[4] Thomas Burdyny and Wilson A. Smith. "CO_2 reduction on gas-diffusion electrodes and why catalytic performance must be assessed at commercially-relevant conditions". In: *Energy Environ. Sci.* 12 (5 2019), pp. 1442–1453.

[5] Wonsuk Chung et al. "Electrification of CO2 conversion into chemicals and fuels: Gaps and opportunities in process systems engineering". In: *Computers & Chemical Engineering* 170 (2023), p. 108106. ISSN: 0098-1354.

[6] Emiliana R. Cofell et al. "Investigation of Electrolyte-Dependent Carbonate Formation on Gas Diffusion Electrodes for CO_2 Electrolysis". In: *ACS Applied Materials & Interfaces* 13.13 (2021). PMID: 33764731, pp. 15132–15142.

[7] Remko J. Detz et al. "Electrochemical CO2 conversion technologies: state-of-the-art and future perspectives". In: *Sustainable Energy Fuels* 7 (23 2023), pp. 5445–5472.

[8] Matthew Jouny, Wesley Luc, and Feng Jiao. "General Techno-Economic Analysis of CO_2 Electrolysis Systems". In: *Industrial & Engineering Chemistry Research* 57.6 (2018), pp. 2165–2177.

[9] Ariane D.N. Kamkeng et al. "Transformation technologies for CO2 utilisation: Current status, challenges and future prospects". In: *Chemical Engineering Journal* 409 (2021), p. 128138. ISSN: 1385-8947.

[10] A.A. Kulikovsky. "A model for optimal catalyst layer in a fuel cell". In: *Electrochimica Acta* 79 (2012), pp. 31–36. ISSN: 0013-4686.

[11] A.A. Kulikovsky. "Optimal shape of catalyst loading across the active layer of a fuel cell". In: *Electrochemistry Communications* 11.10 (2009), pp. 1951–1955. ISSN: 1388-2481.

[12] A.A. Kulikovsky. "Optimal shape of catalyst loading along the oxygen channel of a PEM fuel cell". In: *Electrochimica Acta* 54.27 (2009), pp. 7001–7005. ISSN: 0013-4686.

[13] Mclain Leonard et al. "Investigating Electrode Flooding in a Flowing Electrolyte, Gas-Fed Carbon Dioxide Electrolyzer". In: *ChemSusChem* 13 (Nov. 2019), pp. 400–411.

[14] Christoph Markowitsch, Markus Lehner, and Markus Maly. "Evaluation of process structures and reactor technologies of an integrated power-to-liquid plant at a cement factory". In: *Journal of CO2 Utilization* 70 (2023), p. 102449. ISSN: 2212-9820.

[15] Iván Merino-Garcia, J Albo, and A Irabien. "Tailoring gas-phase CO2 electroreduction selectivity to hydrocarbons at Cu nanoparticles". In: *Nanotechnology* 29.1 (2017), p. 014001.

[16] Christine Minke et al. "Is iridium demand a potential bottleneck in the realization of large-scale PEM water electrolysis?" In: *International Journal of Hydrogen Energy* 46.46 (2021), pp. 23581–23590. ISSN: 0360-3199.

[17] Thomas Moore et al. "Electrolyzer energy dominates separation costs in state-of-the-art CO2 electrolyzers: Implications for single-pass CO2 utilization". In: *Joule* 7.4 (2023), pp. 782–796. ISSN: 2542-4351.

[18] Jude A. Okolie et al. "Waste biomass valorization for the production of biofuels and value-added products: A comprehensive review of thermochemical, biological and integrated processes". In: *Process Safety and Environmental Protection* 159 (2022), pp. 323–344. ISSN: 0957-5820.

[19] Douglas J. D. Pimlott et al. "Impurity-Resistant CO2 Reduction Using Reactive Carbon Solutions". In: *ACS Energy Letters* 8.4 (2023), pp. 1779–1784.

[20] Dan Ren, Bridget Su-Hui Ang, and Boon Siang Yeo. "Tuning the selectivity of carbon dioxide electroreduction toward ethanol on oxide-derived Cu x Zn catalysts". In: *Acs Catalysis* 6.12 (2016), pp. 8239–8247.

[21] Cristina Fernanda Alves Rodrigues, Maria Alzira Pimenta Dinis, and Manuel João Lemos de Sousa. "Review of European energy policies regarding the recent "carbon capture, utilization and storage" technologies scenario and the role of coal seams". In: *Environmental earth sciences* 74 (2015), pp. 2553–2561.

[22] Kosan Roh et al. "Early-stage evaluation of emerging CO2 utilization technologies at low technology readiness levels". In: *Green Chem.* 22 (12 2020), pp. 3842–3859.

[23] Danielle Salvatore and Curtis P. Berlinguette. "Voltage Matters When Reducing CO2 in an Electrochemical Flow Cell". In: *ACS Energy Letters* 5.1 (2020), pp. 215–220.

[24] Angelika A. Samu et al. "Intermittent Operation of CO2 Electrolyzers at Industrially Relevant Current Densities". In: *ACS Energy Letters* 7.5 (2022), pp. 1859–1861.

[25] Eloy S. Sanz-Pérez et al. "Direct Capture of CO2 from Ambient Air". In: *Chemical Reviews* 116.19 (2016). PMID: 27560307, pp. 11840–11876.

[26] Mark Sassenburg et al. "Zero-Gap Electrochemical CO2 Reduction Cells: Challenges and Operational Strategies for Prevention of Salt Precipitation". In: *ACS Energy Letters* 8.1 (2023), pp. 321–331.

[27] Stefano Sollai et al. "Renewable methanol production from green hydrogen and captured CO2: A techno-economic assessment". In: *Journal of CO2 Utilization* 68 (2023), p. 102345. ISSN: 2212-9820.

[28]   E. W. Thiele. "Relation between Catalytic Activity and Size of Particle". In: *Industrial & Engineering Chemistry* 31.7 (1939), pp. 916–920.

[29]   Sam Van Daele et al. "How flue gas impurities affect the electrochemical reduction of CO2 to CO and formate". In: *Applied Catalysis B: Environmental* 341 (2024), p. 123345. ISSN: 0926-3373.

[30]   Sam Van Daele et al. "Influence of the target product on the electrochemical reduction of diluted CO2 in a continuous flow cell". In: *Journal of CO2 Utilization* 65 (2022), p. 102210. ISSN: 2212-9820.

[31]   Christopher Varela, Mahmoud Mostafa, and Edwin Zondervan. "Modeling alkaline water electrolysis for power-to-x applications: A scheduling approach". In: *International Journal of Hydrogen Energy* 46.14 (2021), pp. 9303–9313. ISSN: 0360-3199.

[32]   Sumit Verma et al. "A Gross-Margin Model for Defining Technoeconomic Benchmarks in the Electroreduction of CO_2". In: *ChemSusChem* 9.15 (2016), pp. 1972–1979.

[33]   Jingjie Wu et al. "A metal-free electrocatalyst for carbon dioxide reduction to multi-carbon hydrocarbons and oxygenates". In: *Nature communications* 7.1 (2016), p. 13869.

[34]   Ke Xie et al. "Eliminating the need for anodic gas separation in CO2 electroreduction systems via liquid-to-liquid anodic upgrading". In: *Nature Communications* 13.1 (2022), p. 3070. ISSN: 2041-1723.

[35]   Yi Xu et al. "Self-Cleaning CO_2 Reduction Systems: Unsteady Electrochemical Forcing Enables Stability". In: *ACS Energy Letters* 6.2 (2021), pp. 809–815.

[36]   Kailun Yang et al. "Cation-Driven Increases of CO2 Utilization in a Bipolar Membrane Electrode Assembly for CO2 Electrolysis". In: *ACS Energy Letters* 6.12 (2021), pp. 4291–4298.

5

ACKNOWLEDGEMENTS

"I don't know half of you half as well as I should like; and I like less than half of you half as well as you deserve."

If you have opened this book and immediately skipped to the Acknowledgements to check if your name appears, I urge you to go back and actually read the dissertation. I spent quite a lot of time on it.

The first and greatest acknowledgement must go to my promotors **Johan** and **Willem**. You were the first people I met at TU Delft and frankly everyone else has been a bit of a disappointment in comparison. **Johan**, your inspiringly genuine enthusiasm for a seemingly endless number of topics, scientific or otherwise, is dampened only by the sad reality that you have to spend the lion's share of the day stuck in meetings with fools like me. However, your warm temperament and immense patience are a rarity in academia and there's no one I would rather be supervised by, so I think you will always find your schedule full as there is no shortage of fools like me. **Willem**, you were the bad cop in the good cop, bad cop dichotomy, but let's be realistic: anyone partnered with **Johan** will end up being the bad cop! You kept me grounded in reality and motivated while still allowing room for creativity, and to be completely truthful, if you were not my copromotor I would still be doing this PhD right now (subject to when you are reading this). You are one of the most focused and productive people I have ever met in any walk of life, and I'm sure you sending me paper recommendations at 2 AM is just the tip of the iceberg, so I can only hope you've learnt a hundredth from me of what I have learnt from you. I think your future PhD students will, like me, be daunted in their task of lighting their first candle in the presence of your intense flame. Nonetheless, a reminder to both of you: when you step outside of the professional setting at a borrel or barbecue and find that you are still swarmed by your students, it isn't (just) because we are socially stunted nerds: it's because you are genuinely lovely guys that we are glad to call friends.

I would also like to extend my thanks to the committee, **Dr. Botto**, **Prof. Breugelmans**, **Prof. de Jong**, **Prof. Vreman**, and **Dr. Vermaas** for taking the time to assess my dissertation and be part of my defence.

Also thanks to **Wouter** and **Nikhilesh** for being my paranymphs; everyone else I contacted said "no".

Despite them being the antithesis of academia, I would like to acknowledge the boys from **Arché**: **Floris**, **Mario** and **Robbie**. I joined **Arché** at a dark time after COVID and these guys stuck with me through everything. They reminded me that normal people still exist outside of academia and it is an understatement to say that they kept me sane throughout the latter half of my PhD. Impostor syndrome doesn't survive first contact with a live audience, and perhaps for that exact reason I am more proud of what we have done together than the majority of my PhD work.

Rishabh, thank you for being an encyclopaedic font of graduate advice with your internalised PhD handbook, not that I ever listened to any of it - I'd much rather add to the stack of books I've bought on your recommendation! I'd like to thank **Thanos** for teaching my band how to pronounce their own name and for generally being an all-round cool guy with a great sense of humour and taste in music. **Khatereh**, all I have for you is nostalgia; you make a nice memory. **Marko**, you are one of the few PhDs in P&E that's actually smart and hard-working, and I wish you the best and hope that in the future you find some more time to spend on relaxing and cleaning your grimy ranarrs rather than harassing me during Secret Santa. Cheers to **Heng** for making the best puzzle in Secret Santa too, I properly enjoyed flexing my nerd muscles with that! **Ben** you are the only French anglophile I know, which probably explains why you are the coolest French person I know (sorry **Hugo**), I wish you much beer and cheese in the future. Thanks to **Kate** for always being around for a cheeky beer at PSOR that inevitably gets out of hand.

Thanks to the people that visited me and that made Delft a nicer place to be. Thanks **Abina** for being a reliable friend for my time here and for backing up me and the band at Wolbodo, and a shout-out to **Winston** for being a diamond geezer right upon arrival in the Netherlands. Thanks to **Michael J. Negus**, Enis, and Les for some great visits to Delft and thanks to **Alex**, **Govey**, *Ian*, and Joe for popping by and reminding me why I left the UK. Moreover, thanks to all of you for the small semblance of a social life you provided for me during lockdown.

Although I was never really a bubble boy in reality, I am grateful for being included as one of J. Willy's **Bubble Brigade**. **Sohan** I will miss our coffee and lunch chats littered with ill-fitting Peep Show quotes, and **Jelmer** will likely remain the only person I know to have actually personally benefited from speaking French (incredible). I would especially like to thank **Nico** for always looking out for me: I'm sure your future as an assistant professor will be bright, though I would advise you to revise some of your calculations surrounding coffee quality. Thanks also to **Gilles**, **Mounir**, **Emile** and the rest of Willem's group for always making me feel welcome, and thanks to all of the Master students in P&E that brought some well-needed levity to my time at the department.

My time at P&E was cleaved in twain by COVID, so I must first pay respects to the original office, **Stephan**, **Ivan**, **Rumen**, **Elyas**, and **Rong**. **Ivan** in particular was there to welcome me on day one, despite neither my supervisors nor my office being present at that time. To the rest, thanks for the great times we had in the office and at Physics at Veldhoven. Thank you also to **Aviral** for being there to help with the early days of learning COMSOL, before succumbing to the dark side and becoming **Hackerman**$^{\text{TM}}$. I would also like to acknowledge the post-COVID office, with **Arvind** coming in around 2 PM each day to collect expensive computational hardware and spicy gossip in equal quantities, and **Esaar** popping in once a week to spend the morning reading (bad) manga before diving into a political rant. Thank you to **Ali**, **Fathaah**, and **Vignesh** for making me feel welcome in the office near the end, even when it became quite clear that the department thought I didn't deserve that seat!

I must also mention the great people I have met and worked with from Applied Sciences and e-Refinery. **Lorenz** and **Vojtěch** it was an absolute pleasure to work with you throughout the masters project. I sometimes get the urge to use **Vojtěch's** success as evidence of my excellent performance as a supervisor, but the reality is you never really

needed much help! Thanks also to **Christel**, **Jan-Willem**, **Katie**, and **Kosta** (my greatest ally), for the great times we had together away at conferences or otherwise. My thanks also go **Mark**, **Peter**, and **Dylan**, for making some of those E2CB consortium meetings bearable with copious amounts of smuggled alcohol and lost sleep! A bonus shout-out to **Dylan** for bumping into me for a few minutes at a festival before crowd-surfing off into the distance.

I would like to thank **Masayoshi Takanaka** and **Mike Oldfield**. There is a very good chance that for any words you read from this thesis, one of these two guys was playing guitar in my headphones when I wrote them (including these).

Finally, I would like to thank my brother and my parents for their unwavering support throughout this journey. I hope I've made you proud.

If I forgotten about you, I won't disrespect you with a perfunctory apology.[1]

5

---

[1]"But what about the past? Our past?"
 "We never really shared one... you're not terribly important to me."

LIST OF PUBLICATIONS

1. **J. W. Blake**, J.T. Padding and J.W. Haverkort, *Analytical modelling of CO_2 reduction in gas-diffusion electrode catalyst layers*, Electrochimica Acta, Volume 393, 138987 (2021).

2. **J.W. Blake**, V. Konderla, L.M. Baumgartner, D.A. Vermaas, J.T. Padding and J.W. Haverkort, *Inhomogeneities in the Catholyte Channel Limit the Upscaling of CO_2 Flow Electrolysers*, ACS Sustainable Chemistry & Engineering, Volume 11, 2840 (2023).

3. J.W. Haverkort, B. Sanderse, J.T. Padding and **J.W. Blake**, *An analytical flow-by capacitive deionization model*, Desalination, Volume 582, 117408 (2024).

4. **J.W. Blake**, J.W. Haverkort and J.T. Padding, *Less is more: optimisation of variable catalyst loading in CO_2 electroreduction*, Electrochimica Acta, Volume 507, 145177 (2024).